Nanoscale evolution of silicon electrodes for Li-ion batteries by low-loss STEM-EELS

Maxime Boniface

Communauté
UNIVERSITÉ Grenoble Alpes

THÈSE

Pour obtenir le grade de

DOCTEUR DE LA COMMUNAUTÉ UNIVERSITÉ GRENOBLE ALPES

Spécialité : PHYSIQUE DES MATERIAUX

Arrêté ministériel : 25 mai 2016

Présentée par

Maxime BONIFACE

Thèse dirigée par **Pascale (phys) BAYLE-GUILLEMAUD**
et codirigée par **Said SADKI**, Professeur, UGA

préparée au sein du **Laboratoire Modélisation et Exploration des Matériaux**
dans **l'École Doctorale Physique**

Suivi à l'échelle nanométrique de l'évolution d'une électrode de silicium dans un accumulateur Li-ion par STEM-EELS

Nanoscale evolution of silicon electrodes for Li-ion batteries by low-loss STEM-EELS

Thèse soutenue publiquement le **22 décembre 2017**,
devant le jury composé de :

Monsieur GIANLUIGI BOTTON
PROFESSEUR, UNIV. MCMASTER HAMILTON ONTARIO - CANADA, Rapporteur
Madame LAURENCE CROGUENNEC
DIRECTRICE DE RECHERCHE, CNRS DELEGATION AQUITAINE, Rapporteur
Monsieur OVIDIU ERSEN
PROFESSEUR, UNIVERSITE STRASBOURG, Président
Monsieur CEDRIC HAON
INGENIEUR CHERCHEUR, CEA GRENOBLE, Examinateur

Acknowledgements

I would like to acknowledge all the people without which this manuscript would not have seen the light of day and whose continuous support, be it scientific or else, made my PhD a successful [citation needed] endeavor. This starts with Julien who taught me the ropes and patiently walked me through every bit of experimental procedure. Much of the work reported in this manuscript was initiated by Julien. I also got the chance to be introduced to all the good people at SiNaPS who helped with in situ and especially Eric who was kind enough to make all the little cell modifications I wanted a reality. The same can be said about Nicolas at LEMMA who also had to tolerate my messiness around the lab and that's no small feat.

At LEMMA, I also owe a lot to the good spirits and humor of Pierre-Henri, who didn't hesitate to power through the 8:30PM curfew to try yet another FIB cut, and also to Jean-Luc who took the time to rewrite NPED software on a short notice when results were due for this manuscript. I especially want to thank Hanako for her indulgence despite me mishandling at least one thing for every conference I went to. I also want to warmly thank the good folks I had the pleasure of sharing an office with: Fabio, Miguel, Yannick, Carlos, Deepankar and especially Benedikt who was inspirational and always there when I needed a hand.

One collaboration that really stays with me is that with Samuel and Francois at the synchrotron. This worked out to great results. The same can also be said about everyone in BACCARA: Lucille, Katya, Manuel, Vincent, Nicolas D., Eric, Arnaud, Dominique and of course Philippe who supported and encouraged me and to who I owe numerous tricky interpretations of the data in this work.

Last but not least, I want to express my profound gratitude to my thesis director, Pascale, who believed in this project and in me, got me the opportunity to prove myself and to grow scientifically and personally, pushed me to be better and kept me from getting sidetracked. To Said I also owe a lot, especially for the preparation of this manuscript and the defense.

Over these 3.5 years I learned a ton and I had fun. I owe it to all of you.

Finally, I would like to dedicate this work to Franck, Laurence, Eric, Guillaume, Victor, William, Thibault and Léa.

Introduction

On the 12th of December 2015, 195 countries accounting for over 55% of global greenhouse gases (GHG) emissions adopted the Paris agreements in a historic decision that saw a favorable change of policy from the some of the largest GHG emitters, most notably the United-States, which had until then stayed out of international efforts to regulate emissions such as the Kyoto Protocol. As evidence for climate change accumulates (fig. 1), mitigating the ever-growing global temperatures, sea level, and atmospheric CO_2 levels has become a vital issue rather than a political token as it used to.

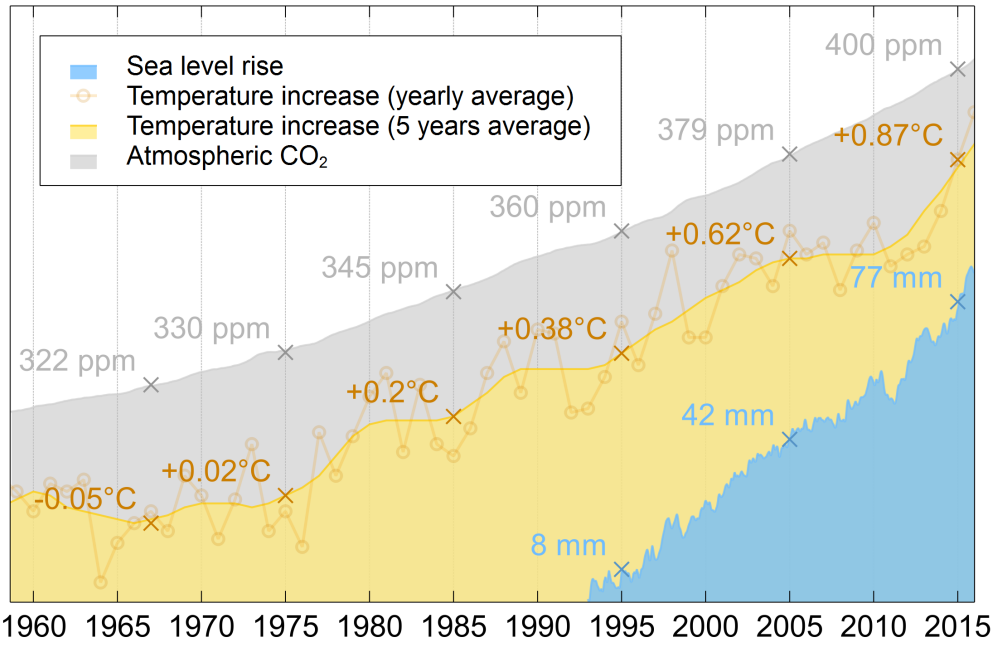

Fig. 1: Average global temperature change, sea level rise, and atmospheric carbon dioxide concentration evolution from 1958 to 2016 [1].

While environmental concerns were largely brushed off as holding back economic growth in the 1990s, a paradigm shift has seen ecology slowly permeate most layers of society and politics,

with many now regarding sustainable growth as an opportunity for bold public investment plans and technological innovation. Nearly 70% of investments in power stations went towards renewables [2] in 2016. A striking example is that of China, the world's largest polluter, for which that same year marked the first ever decline in coal production while the nation's solar capacity rose by 78% [3].

As enormous chunks of the world's population are coming out of poverty, the global electricity demand is expected to rise by more than 69% by 2040, with non-OECD markets accounting for about 85% of the growth (fig. 2). There is a need to skip fossil fuel-based solutions that powered the growth of the West during the 20th century. The Paris Agreements thus acknowledged that it is mutually beneficial for the first world to financially accompany the growing energy demand of the third world in promoting decarbonated, low-environmental impact solutions.

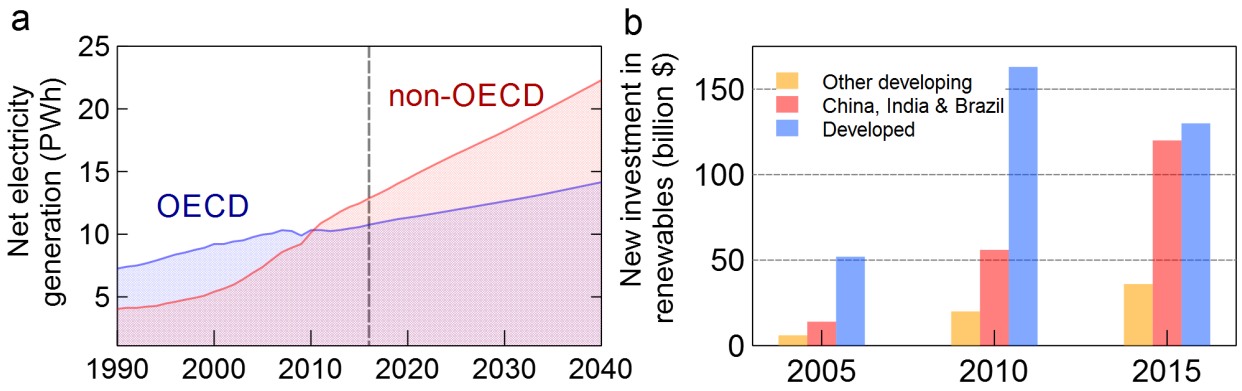

Fig. 2: a. Past and predicted net global electricity generation [4]. b. Investments in renewable electricity generation [5]. Emerging and developing economies are committing to renewable technologies to a greater extent than anticipated.

Foremost in this next-generation renewable energy mix is solar, which is arguably the most scalable and mature available technology [6] to meet the aforementioned challenges. Its modularity and competitive price have helped sprout decentralized production initiatives that saw impoverished rural communities get off-grid electrification [7, 8]. But the share of solar and other relevant renewable energy sources in a country's energy mix is capped to a disappointing 30% because of the intermittent nature of their production. Until cost-competitive grid-wise storage solutions are implemented, this roadblock will remain.

The Lithium-ion battery technology has until now strictly kept to applications where power and energy-density were critical, including electric vehicles (EVs). Those have received a lot of attention from car manufacturers and policymakers alike [9], with 2 million new EVs hitting the road in 2016. This means that the grid is starting to benefit from a large fleet of electric vehicles as a source of available energy storage, while they are cutting away at the emissions of the transport sector - the most oil-centric share of the global energy consumption.

EVs also enjoy an innate advantage to their traditional counterpart, in that the electric powertrain allows a whopping 75% "tank-to-wheel" efficiency, while a conventional gasoline car can only

boast about 16%. When factoring in the efficiency of power plants, conservative estimates have EVs on par with thermal vehicles in the worst case scenario - coal power - in "well-to-wheel" efficiency, with EVs coming out on top in CO_2-equivalent generation [10–12], even accounting for vehicle production. It follows that the environmental rewards of EV deployment are not entirely dependent on an existing decarbonated electricity mix. EV roll-out could in fact support the transition to renewable energies by providing an opportunity to integrate them.

In this landscape the pressure for more cost-effective and energy-dense batteries is enormous. A look at the evolution of Li-ion batteries key metrics shows that volumetric energy density has gone up from 60 $\mathrm{Wh/L}$ to 295 $\mathrm{Wh/L}$ in less than ten years while costs per kWh were slashed from about 1000 \$/kWh in 2010 to a measly 190 \$/kWh according to Tesla's most recent estimates, largely on par with the 2022 objectives laid out by the American DOE, which aims for numbers in the 100-150 \$/kWh ballpark to make EVs on price parity with traditional vehicles.

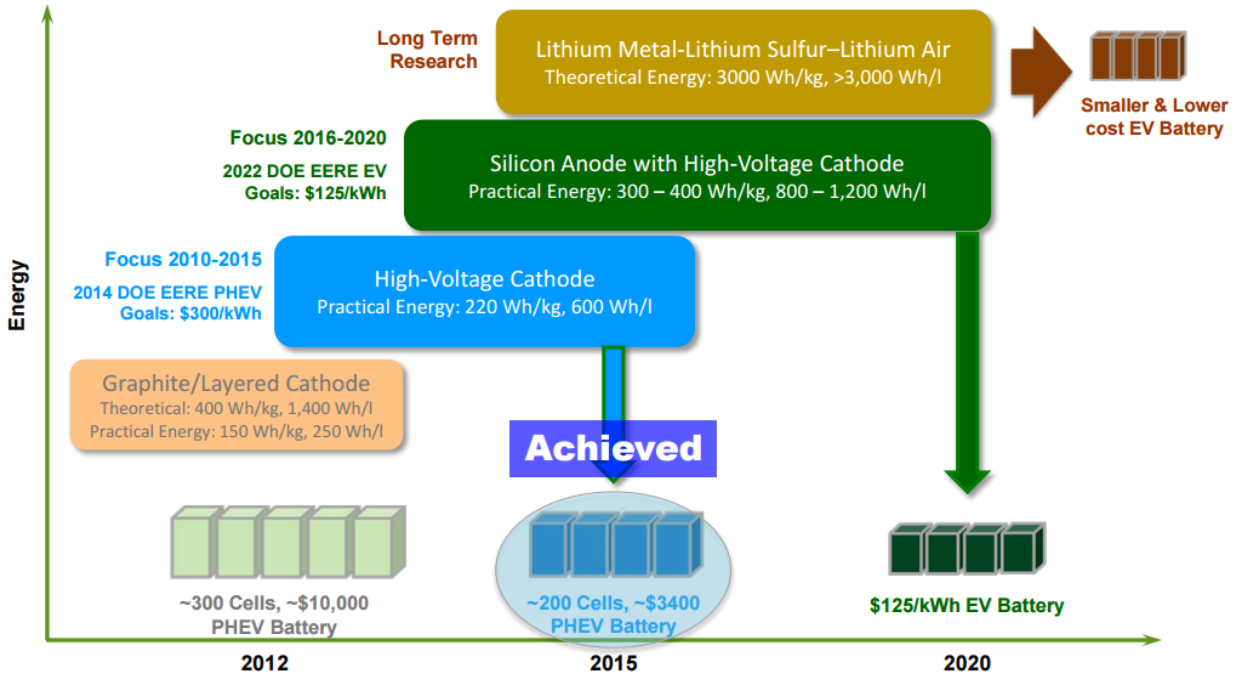

Fig. 3: Li-ion batteries electrode materials roadmap from the DOE's Vehicle Technology Office. [13]

Costs were driven down by economies of scale as well as optimizations on the pack, cell and electrode scale, thanks to the reduction of the share of inactive materials weight and volume. Incremental increases of the operating voltage of cathode and electrolyte materials [13] have also been achieved, and research into Li/Mn rich layered materials are ongoing with the objective of an 80% capacity increase from 120 $\mathrm{mAh/g}$ in 2012 to 200 $\mathrm{mAh/g}$. On the negative side however, graphite electrodes have reached a plateau around 350 mAh/g, and maintaining the current trend of a cell energy density increase of 5% a year [14] appears unsustainable if inherent active material limitations aren't addressed. This has led researchers and engineers to turn to alternative negative electrode materials.

Silicon, which boasts 3579 mAh/g of theoretical capacity, has been pursued as the most low-risk approach to partially replace graphite in commercial anodes in the short term. But designing silicon-based electrodes on par with industry standards has been arduous, although remarkable progress was achieved [15]. Twenty years after Besenhard asked the question *Will advanced lithium-alloy anodes have a chance in lithium-ion batteries?* in his eponymous 1997 paper [16], the field has advanced significantly. Characterizations have notably shed light on the critical role of the Solid Electrolyte Interface (SEI), a composite layer whose abnormal accumulation along the cycling of silicon electrodes limits their lifetime. Yet a lot remains to be explored. The detrimental effect of this ever-growing layer in Si-based electrodes has only been indirectly observed and its local morphology and chemistry remains elusive. Moreover the lithiation process of crystalline silicon itself has not been fully described at a local scale, especially for nanoparticles which have garnered considerable attention [17, 18]. In both topics, chemical sensitivity is needed at the nanoscale.

In **chapter I**, we review current Si-based anode technology and its shortcomings. Characterization efforts on the Li-Si system as well as the SEI are described to outline key issues that remain to be addressed. Low-loss STEM-EELS is then introduced as an promising candidate to study sensitive and heterogeneous systems such as ours. As part of the European BACCARA project, we participated to a collaborative characterization effort around nanoparticle-based electrodes cycled at 30% limited capacity. Cycling conditions and performances, as well as experimental details on sample preparation for the TEM, are presented **chapter II**. Now, prior to the study of these electrodes, a large part of this thesis work was first dedicated to the optimization of low-loss STEM-EELS to mitigate irradiation damage and extract chemical insight from the low-energy region of EEL spectra. These technique development efforts are detailed in **chapter III**.

chapter IV then features our attempt at a custom *in situ* experiment to extend our characterization capabilities to single nano-objects. Results echo those from **chapter V**, where our optimized low-loss STEM-EELS protocol is put to use to describe locally the morphology and chemistry of lithiated silicon nanoparticles and their SEI. A chemo-mechanical model is notably proposed to reconcile the different behavior of Si nano and microparticles. To support that model and debate previous simulation works, we also present local strain measurements on single nanoparticles. Electrode aging is then under scrutiny in **chapter VI**. There, speculative aging mechanisms are challenged at the local scale and a systematic study is proposed. Combining electrochemical data and quantitative STEM-EELS data allows us to propose an in-depth assessment of the evolution of the chemistry of the SEI, and finally propose our own model for the aging of silicon electrodes.

Introduction only

(1) NASA *Vital Signs of the Planet*; tech. rep.; 2016.

(2) IEA *15th International Energy Forum Ministerial Meeting: Background Paper by the International Energy Agency*; tech. rep.; 2016.

(3) BP *BP Energy Outlook*; tech. rep.; 2017.

(4) IEA *International Energy Outlook*; tech. rep.; 2016.

(5) UNEP *Global Trends in Energy Investment 2016*; tech. rep.; 2016.

(6) MIT *The Future of Solar Energy*; tech. rep.; 2015.

(7) Pope, C. *Solar Power Off the Grid: Energy Access for World's Poor*; tech. rep.; 2012.

(8) Smith, M. G.; Urpelainen, J. *Rev. Policy Res.* **2014**, *31*, 17–37.

(9) IEA *Global EV Outlook: Beyond one million electric cars*; tech. rep.; 2016.

(10) Helms, H; Pehnt, M; Lambrecht, U; Liebich, A *18th Int. Symp.* **2010**.

(11) Helmers, E.; Marx, P. *Environ. Sci. Eur.* **2012**, *24*, 14.

(12) Woo, J.; Choi, H.; Ahn, J. *Transp. Res. Part D Transp. Environ.* **2017**, *51*, 340–350.

(13) Howell, D.; Cunningham, B.; Duong, T.; Faguy, P. *Overview of the DOE VTO Advanced Battery R&D Program*; tech. rep.; 2016.

(14) IDTechEx; Gonzales, F. *Advanced and Post-Lithium-ion Batteries 2016-2026: Technologies, Markets, Forecasts*; tech. rep.; 2016.

(15) Zuo, X.; Zhu, J.; Müller-Buschbaum, P.; Cheng, Y.-J. *Nano Energy* **2017**, *31*, 113–143.

(16) Besenhard, J.; Yang, J.; Winter, M. *J. Power Sources* **1997**, *68*, 87–90.

(17) Wilson, A. M. *J. Electrochem. Soc.* **1995**, *142*, 326.

(18) Li, J.-Y. et al. *Mater. Chem. Front.* **2017**, *1*, 1691–1708.

Table of contents

Nomenclature

α	Half convergence angle
β	Half collection angle of the GIF
ΔE	Plasmon damping, in electronvolts. Closely associated to the FWHM of the plasmon peak
λ	Inelastic mean free path of an electron
ν	Poisson's ratio
ρ	Volumetric density
σ_m	Mean stress
σ_{se}	Secondary electron production cross section
θ_c	Cut-off angle for inelastic scattering
θ_E	Characteristic angle for inelastic scattering of energy E
a/b	Core on shell ratio of silicon nanoparticles
a_0	Bohr radius
D_e	Critical electron dose above which a characteristic spectral features falls to $1/e$ of its initial intensity
E	Young's modulus
E_0	Accelerating voltage, in kilovolts
E_p	Plasmon energy, in electronvolts
E_{max}	Plasmon maximum calculated from E_p and ΔE

$FWHM$ Full-width half maximum

I Intensity of the electron beam. Often expressed in picoamperes

M Molar mass

m_0 Mass of the electron

n_e Free electron density

N_{se} Number of secondary electrons

P_{sat} Saturating vapor pressure

r_c Critical core on shell ratio

SoC State of charge

t Thickness

x Lithium on silicon atomic ratio

org phase Group of all non-inorganic SEI components. Mapped as one in STEM-EELS

AES Auger electron spectroscopy

CB Carbon black. Conductive additive in electrode formulations

CMC Carboxymethylcellulose. Binder in electrode formulations

DEC Diethyl carbonate

EC Ethylene carbonate

EELS Electron energy loss spectroscopy

FEC Fluoroethylene carbonate

FIB Focused ion beam

GIF Gatan imaging filter. EEL spectrometer

HAADF High angle annular dark field detector. For STEM imaging

IL Ionic liquid

LEDC Lithium ethylene dicarbonate

MLLS Multiple linear least square algorithm. Outputs the weights (or coefficients) of the contribution of input standard spectra to an experimental spectrum

NMR Nuclear magnetic resonance spectroscopy

NPED Nanobeam precession electron diffraction

poly(FEC) Oxygen-free partially cross-linked polymer. Product of FEC reduction

PSF Point spread function

SE Secondary electron

SEI Solid electrolyte interface

SEM Scanning electron microscopy

SiNP Silicon nanoparticle

SiNW Silicon nanowire

STEM Scanning transmission electron microscopy

ToF-SIMS Time-of-flight secondary ion mass spectroscopy

XPS X-ray photoelectron spectroscopy

ZLP Zero-loss peak

Chapter I

Silicon for Li-ion batteries: a state of the art

This chapter does not aim at an exhaustive state of the art on silicon, but rather to introduce the concepts that will be discussed in this manuscript. With this in mind, our four sections were designed for the following:

- Briefly describe the motivation for silicon in Li-ion batteries.
- Expose the current understanding of lithiation mechanisms at the particle level.
- Give an overview of the solid electrolyte interface (SEI), and how it evolves as silicon electrodes cycle.
- Describe what challenges have held back STEM-EELS for the investigation of Si-based electrodes, and what has been achieved so far.

I.1 An introduction to silicon negative electrodes

I.1.1 Making a case for silicon

Lithium-ion battery technology has been enabling portable electronics and other mobile applications from their introduction in the early 1990s. The steady performance increase that commercial cells have enjoyed over the last 20 years hide an unshifting material landscape, and great challenges remain [1–4]. A succinct overview of the technology's basics is necessary to understand the motivation behind silicon anodes. A typical Li-ion cell is represented figure I.1).

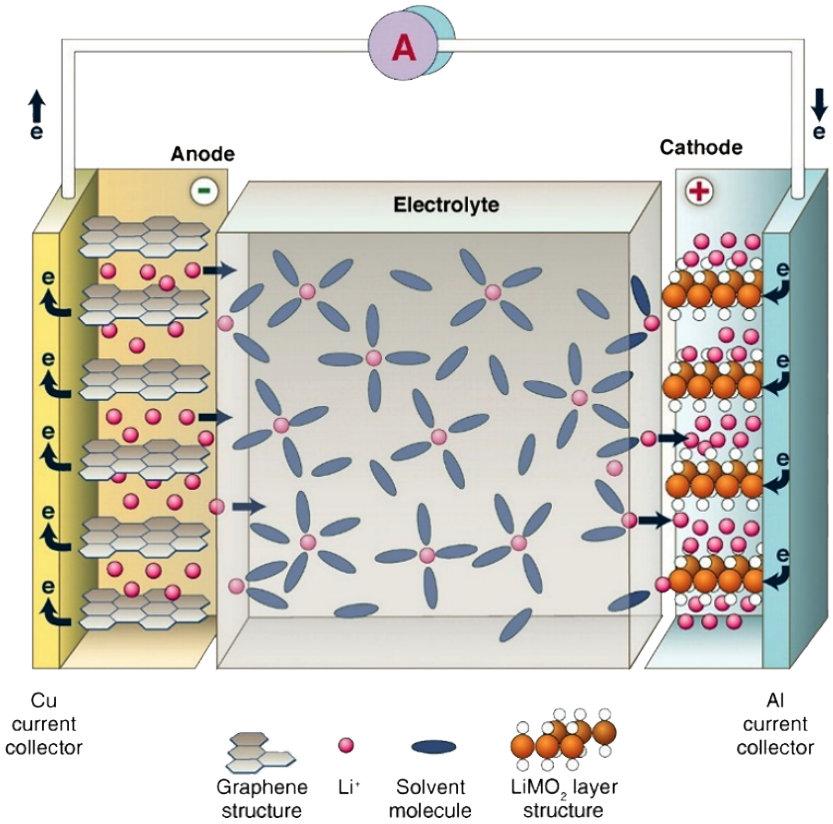

Fig. I.1: Schematic of a Lithium-ion cell during discharge. Reproduced from [5].

Current active materials for Lithium-ion batteries

Lithium is the lightest metal and stands out for its tremendous reductive nature. In Li-ion batteries, this property is harnessed by storing lithium ions in a negative electrode at potentials close to their neutral valence state at 0 $V_{Li^+/Li}$, then allowing upon discharge the Li^+ ions to react with the positive electrode at potentials as high as > 3 $V_{Li^+/Li}$ [6, 7]. In common cells, this exchange takes place between a graphite anode - LiC_6 in its lithiated form - and a layered oxide cathode of

formula $LiMO_2$ with M = Ni, Co, Mn. Lithium ions are shuttled back and forth in an electrolyte made of the salt $LiPF_6$ dissolved in a carbonate solvent as shown figure I.1.

From intercalation to alloying reactions

These host materials allow reversible intercalation - so-called "rocking-chair" process - and feature rigid layered structures, which can only accommodate as much Li^+ ions as their unit cell will allow. This translates to a limited specific capacity of 372 mAh/g for graphite - whose lithiated formula is LiC_6 - and capacity gains from the optimization of inactive electrode and cell components are reaching their ceiling. Stepping away from intercalation materials, towards alloying and conversion reaction pathways [8], opens up an array of metals and semi-metals that could store close to 4 lithium ions per host atom on the negative electrode side, compared to a current 1/6 for graphite (fig. I.2.a).

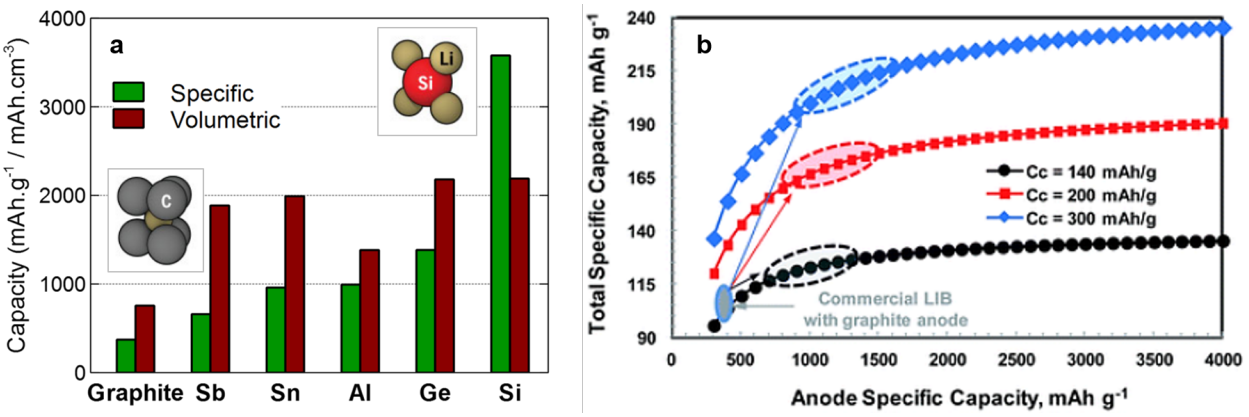

Fig. I.2: a) Specific and volumetric - per fully lithiated element - capacity of negative electrode materials (data from [9]). b) Total specific capacity of a LIB cell as a function of the specific capacity of the anode for 3 cathode specific capacities: (black) current performance of a commercial 18650 LIB cell, (blue) and (red) projections. Reproduced from [10].

Among these materials, silicon combines the highest specific capacity of the lot at 3579 mAh/g with low toxicity and cost. Moreover its operating voltage in the 50 - 400 $mV_{Li^+/Li}$ range translates into good energy densities [11]. As fig. I.2.b shows, using only a third of the capacity of silicon, either by (i) replacing even a fraction of the total graphite content in current negative electrodes or (ii) artificially limit the capacity of pure Si-based electrodes, could realistically increase the specific capacity of the full battery by $\approx 30\%$ [10] and is necessary to harness the full capacity increase enabled by novel cathode technologies.

I.1.2 Capacity retention of silicon electrodes and aging phenomena

A number of issues have kept silicon from going commercial. Indeed, initial attempts to integrate silicon to existing anode technology yielded extremely poor capacity retention [11]. This is illustrated fig. I.3. Unlike graphite and other insertion materials, silicon expands dramatically upon lithiation [12] to close to 4 times its original volume. On the electrode scale, this translates to the pulverization of particles or their disconnection from the percolating network [13]. Addressing pulverization by switching to silicon nanoparticles (SiNPs) [14–16], while absolutely necessary, multiplied the surface area of silicon in these electrodes. As a result, large surfaces are opened up to electrolyte reduction. This is compounded by the SiNPs swelling-contraction cycles along cycling, which leads the layer that forms at the electrode/electrolyte interface, called the SEI, to be repeatedly shed away and reformed, wasting mobile lithium ions and electrons in the process I.4.

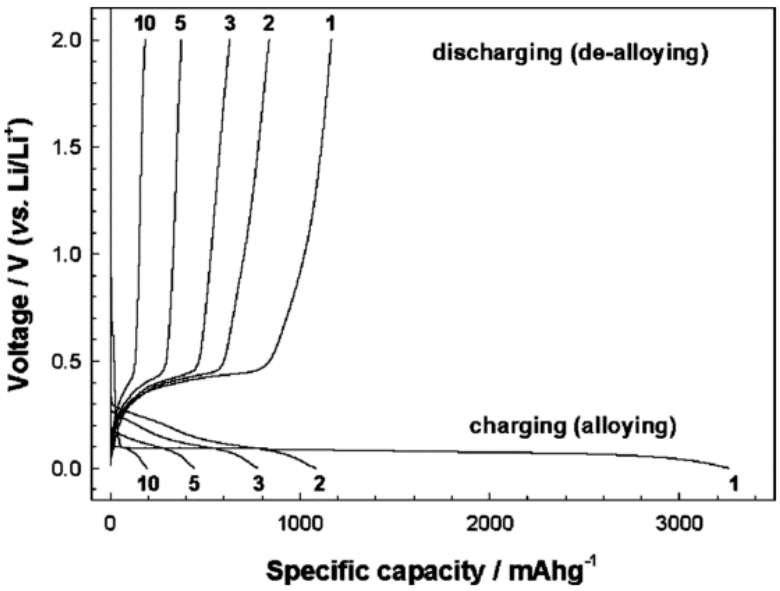

Fig. I.3: Galvanostatic charge-discharge voltage profiles obtained with a silicon powder anode. Numbers correspond to successive cycles. The composite anode was made with a silicon powder of 10 µm average diameter. Reproduced from [11].

Numerous strategies were explored to remedy the issues associated with volume expansion, from the use of electrolyte additives [18] to foster more stable SEIs, to the optimization of binders to prevent particle disconnection [19]. Choi et al. in particular demonstrated very recently tremendous improvement with the use of a sophisticated highly elastic binder [20]. Novel nanostructured silicon architectures were also considered [21], with excellent capacity retentions demonstrated for elaborate hollow nanostructures [22, 23], most notably from the group of Yi Cui [24]. Their sophisticated synthesis protocols have however made scaling up difficult. One practical and successful approach to improve cyclability has been to artificially limit the capacity of silicon electrodes to mitigate their volume change and attenuate the associated electrode degradation [25]. This approach allowed Mazouzi et al. [26] to reach remarkable performance in half-cells (i.e. silicon

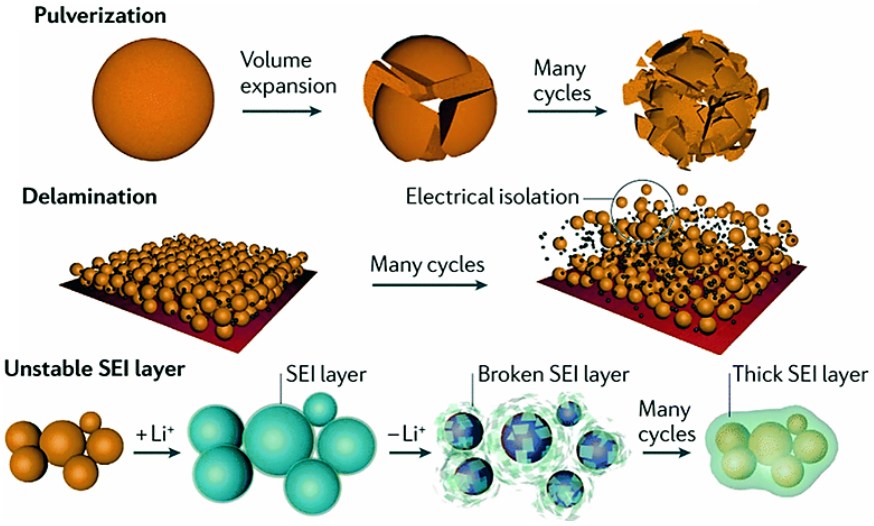

Fig. I.4: Schematic representation of the aging phenomena hindering silicon capacity retention. Upon extensive lithiation the expanding particles can either pulverize or get isolated from the percolating network. The SEI is also thought to delaminate upon particle expansion and will accumulate. Reproduced from [17].

electrode cycled versus lithium metal), maintaining 1200 mAh/g for 700 cycles [27], although the capacity lost to side reactions (called the irreversible capacity, black curve) remains considerable. In full-cells however, the same SiNP-based electrodes exhibit a surprisingly swift capacity decay. This is illustrated fig. I.5. On a side note, studying this discrepancy will be one axis of the study of electrode aging in this manuscript, which can be found in chapter VI.

Delpuech et al. found that the capacity loss in full-cell cannot be fully attributed to the degradation of the electrodes themselves [27]. Electrodes aged in full-cells and whose capacity had dwindled (fig. I.5.b) could in fact, after dismantling the cells, be mounted back in half-cells and cycle efficiently. The root of the poor performance of full-cells is elsewhere. Rather, they point out that there is a growing mismatch between the operating potentials of both electrodes. Electrons extracted irreversibly from the positive electrode are responsible for an internal imbalance in the cell, which results in progressive potential *slippage* of the electrodes and reduces the compositional range of cyclable lithium ions for both electrodes. These findings echo those from Beattie et al. [28] in Si/NCA cells. The authors note that throughout aging an ever-evolving silicon voltage profile that pushes the upper voltage at the cathode to > 4.4 V (vs. Li/Li$^+$). This behavior initially improves cycle efficiency, due to liberation of new lithium, but ultimately reduces cycling efficiency, resulting in rapid capacity fade. This is nicely summarized figure I.7.

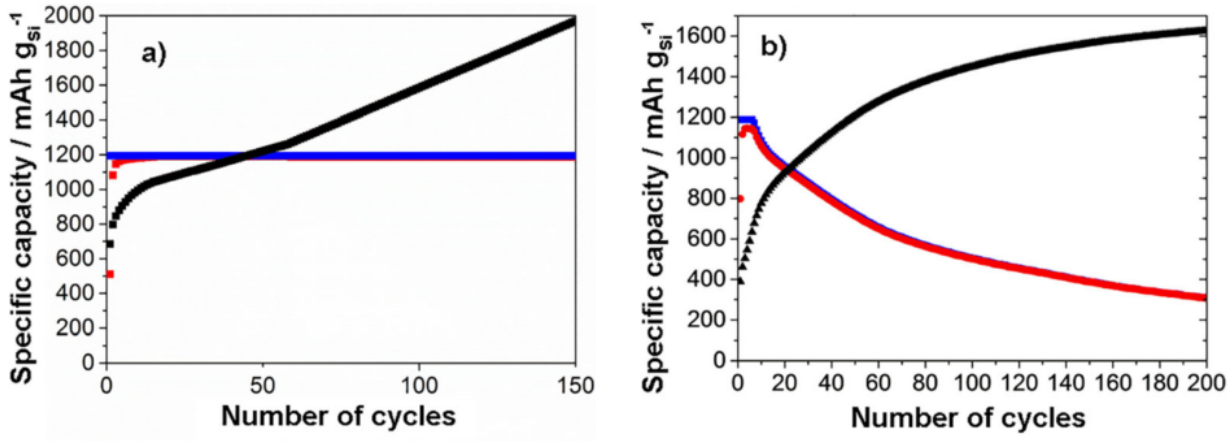

Fig. I.5: Discharge (blue) and charge (red) specific capacities along with the corresponding cumulative irreversible capacity (black) as a function of the number of cycles for (a) a Si/Li half-cell and (b) a Si/$LiCoO_2$ full cell. The electrolyte used in both cases was 1M $LiPF_6$ in EC/DEC/FEC(10%)/VC(2%). Edited from [27].

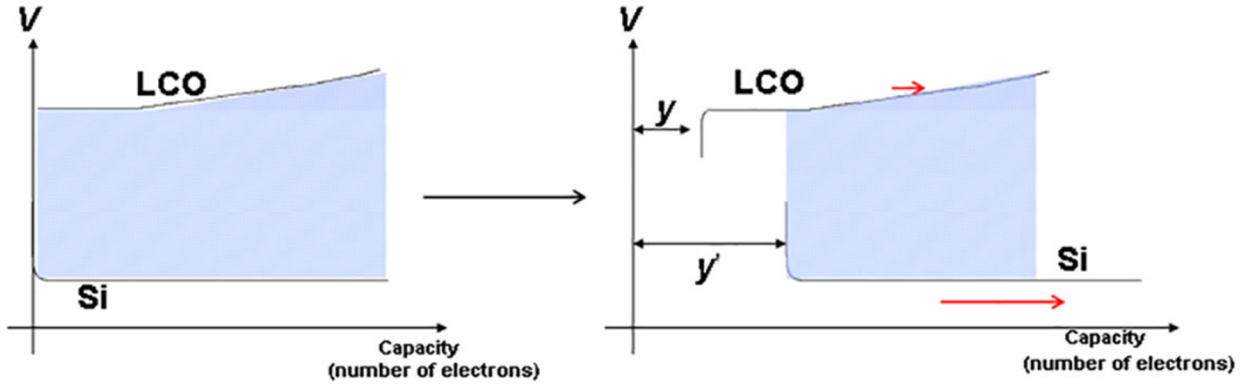

Fig. I.6: Model of galvanostatic curve slippage for positive and negative electrodes. Reproduced from [27].

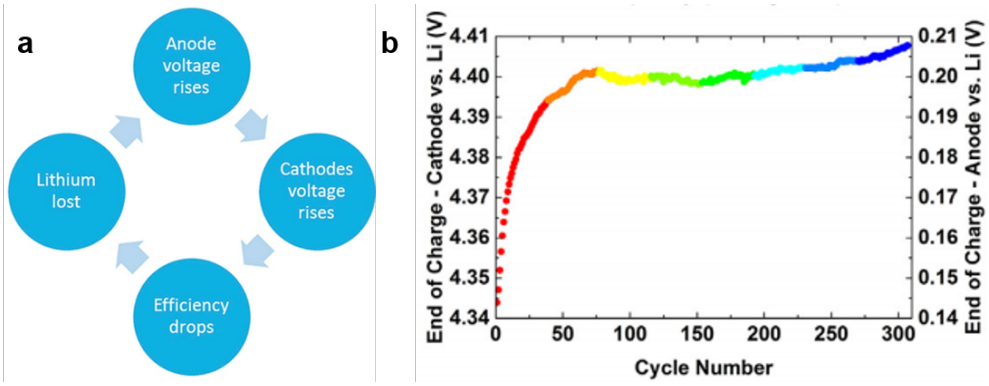

Fig. I.7: a) Schematic of the cause of performance loss of silicon electrodes in full cells. b) Evolution of the potential of both electrodes against a Li/Li^+ reference. Reproduced from [28].

I.2 The Li-Si system

Silicon's alloying reaction with lithium, the very source of its tremendous specific capacity, is intrinsically problematic to electrode design and has received attention proportional to what is at stake: the transition to next-generation Li-ion anodes [29].

I.2.1 Electrochemical behavior and phases of interest

The Li-Si alloy system was first studied in the framework of molten salt batteries operating in the 400 - 450°C temperature range [30, 31]. Several stable intermediate equilibrium phases, $Li_{12}Si_7$, Li_7Si_3, $Li_{13}Si_4$ and $Li_{22}Si_5$, corresponding to as many voltage plateaus, were identified (figure I.8) while the room temperature electrochemistry of Li-Si was left unexplored until the turn of the millennium [32, 33].

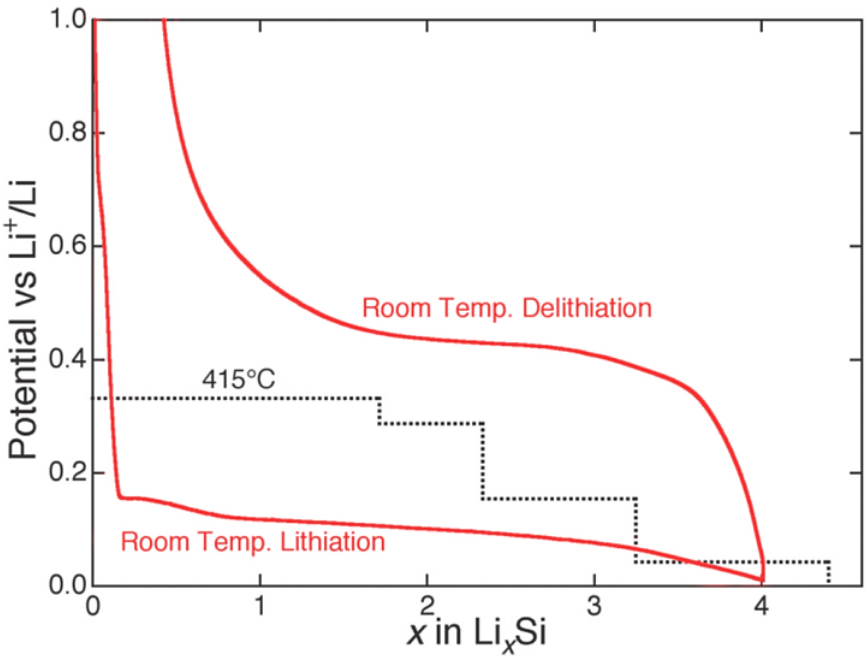

Fig. I.8: Li-Si coulometric titration curve at 415°C (dotted line) and galvanostatic voltage curve of a silicon powder electrode's first cycle in half cell (full line). Reproduced from [34].

Two-phase solid-state amorphization at room temperature

It revealed a radically different behavior. The crystalline alloy phases that were first identified at 415°C do not form at room temperature. Instead, the c-Si phase and an amorphous Li_xSi phase coexist. The latter grows through solid-state amorphization in a biphasic process that corresponds to the voltage plateau around 100 $mV_{Li^+/Li}$ displayed fig. I.8. This dependence on temperature

boils down to Li^+ diffusion kinetics: with the formation of equilibrium phases kinetically blocked, an amorphous, lower-Gibbs free energy phase is formed. The lithium content x of this amorphous phase has been the subject of much debate, part of which has been skewed by a fixation on a true 2-phase mechanism.

While Limthongkul et al. claimed a value around x = 2.2 in their initial study, latter works have put forward a range of compositions [35–40] from $x = 1$ reported by Radvanyi et al. [41] via local Auger spectroscopy measurements, all the way to x = 3.5, in the case of Li, Dahn et al. [42]. However these were not measured for the same state of charge (SoC), current densities (ie C-rates) or particle sizes (microparticle vs. nanoparticles). A closer look at the (pseudo-)plateau shows a downtrend in its voltage as we go up in capacity, possibly corresponding to an increasing lithium content in the amorphous phase as we go up in SoC. This could indicate that a solid-solution reaction process coexists with the 2-phase solid-state amorphization during the first lithiation. The extent of this coexistence and the dependence of y on the SoC during the first lithiation will be under scrutiny in this manuscript.

State-of-charge dependent (de)lithiation mechanism

When the lithiation of silicon is pushed to its full capacity, one can observe a seemingly abrupt transition - from the noticeable dip in voltage profile - to the $Li_{15}Si_4$ phase, identified by Obrovac and Christensen [43]. $Li_{15}Si_4$ eventually crystallizes if electrode potential passes 50 $mV_{Li^+/Li}$, as seen on in situ X-ray diffraction experiments [42]. The delithiation from fully lithiated silicon then proceeds through another biphasic process. That mechanism is out of the scope of this manuscript however, since only partial lithiation is relevant to practical approaches at Si-based electrodes [44], and for all matters lithium-silicon alloys will be understood to be amorphous.

As such, lithium-silicon alloys exhibit pure solid-solution behavior during delithiation and consecutive cycling. This was first deduced from the slopping voltage profiles (fig. I.9) of delithiation and subsequent cycles, which are typical of such a mechanism. Li_xSi phase will undergo a smooth, continuous transition to amorphous silicon upon delithiation, and this is exactly reversed upon the following cycles. From the second lithiation and on, the lithium content x will increase monotonously as the cell potential goes down and the state of charge increases. This behavior was directly witnessed via *in situ* solid-state NMR measurements by Ogata et al. [45] on silicon nanowires (SiNWs). A summary of their result is presented figure I.9. We see that the amorphous Li_xSi phase indeed goes through intermediary Li contents before it reaches the fully lithiated phase $Li_{3.75}Si$. Likewise, the lithiation of amorphous thin films follows a similar pattern as M. Ulldemolins conclusively demonstrated in his thesis work [46]. This shows that the solid solution behavior is intrinsic to silicon, and these findings from thin film and nanowire geometries are equally relevant to the nanoparticles that are the focus of this manuscript.

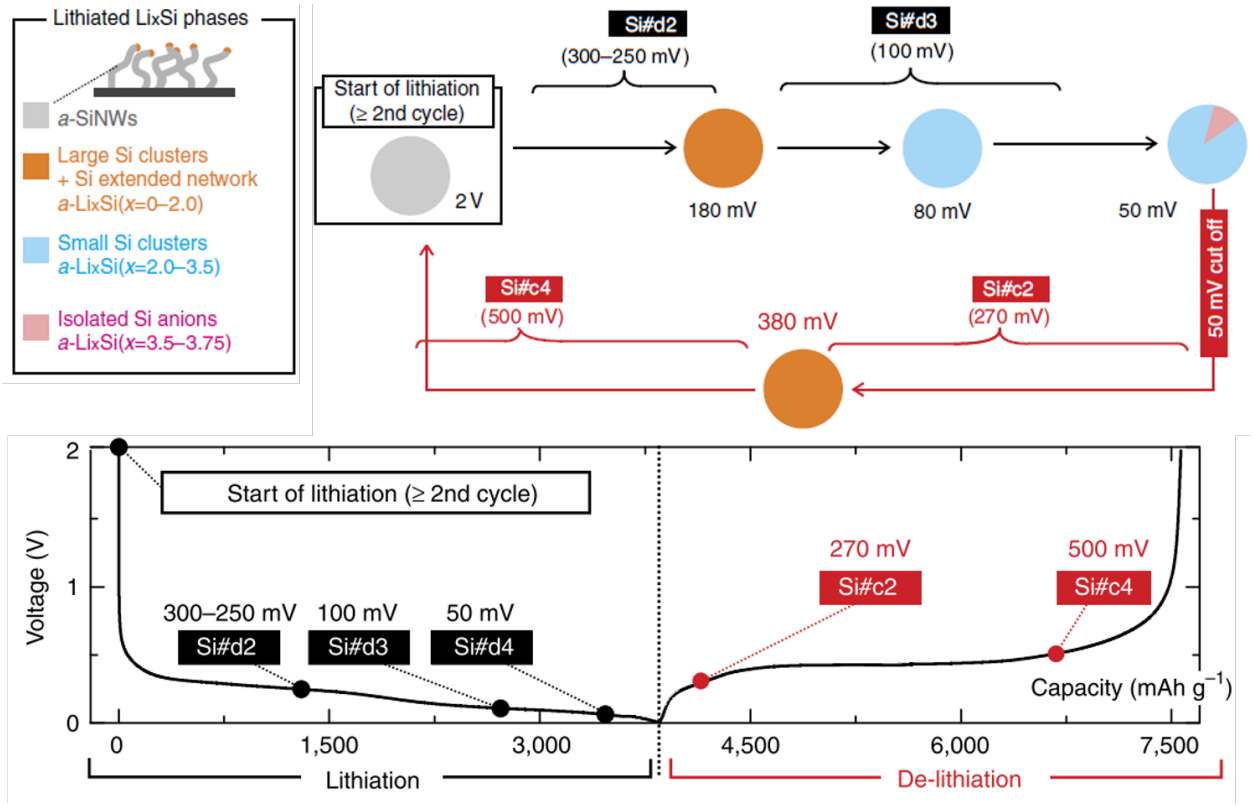

Fig. I.9: Phase transformation during the second cycle of silicon nanowires followed via *in situ* solid-state ^{7}Li NMR measurements. The varying Li_xSi stoichiometry and slopping voltage indicate a solid solution process. Reproduced from [45]

Another striking feature of these curves is the sizable hysteresis i.e. the voltage gap between lithiation and delithiation, which is an order of magnitude higher than what is observed for graphite [47]. Even accounting for polarization losses, there exists a significant difference between lithiation and delithiation at any given SoC. This was demonstrated by Baggetto et al. [48] who allowed cycled electrodes to relax to equilibrium at varying states of charge. Overpotentials of 280 mV (at 1200 mA h/g) to 150 mV (at 3350 mA h/g) were shown to remain - about half of the total potential offset. Insights into the morphological behavior of the Li-Si system are critical to understand its origin.

I.2.2 The morphology of lithiated silicon nanoparticles

Volume expansion and the core-shell structure

During the lithiation of c-Si, solid-state amorphization proceeds along a moving boundary that's been called the reaction front [49]. This yields a core-shell morphology in the case of silicon nanoparticles (SiNPs). Considering that silicon expands dramatically during lithiation - with a linear dependence to the SoC, up to 275% in the case of a-$Li_{15}Si_4$ [12, 50, 51](fig. I.10) - we

observe an a-Li_xSi shell growing outwards and a receding c-Si core. Thanks to the advent of in situ transmission electron microscopy (TEM) experiments, McDowell et al. followed this process in real time (fig. I.11.a).

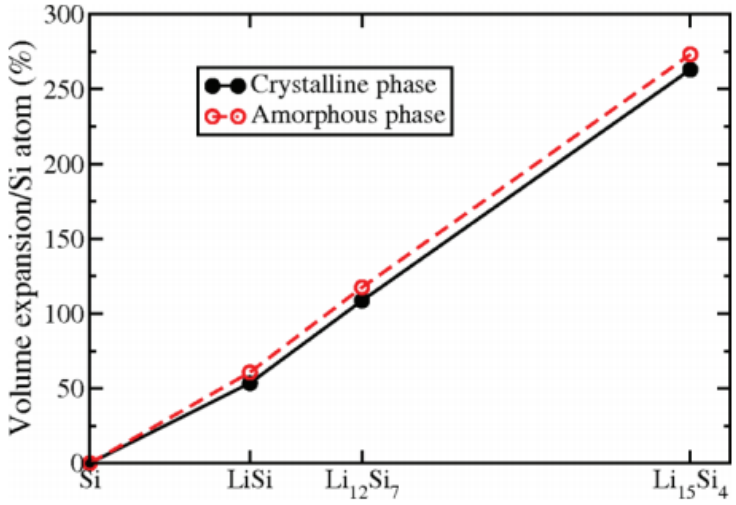

Fig. I.10: Calculated volume expansion of different Li_xSi alloys compared to pure silicon. Reproduced [51].

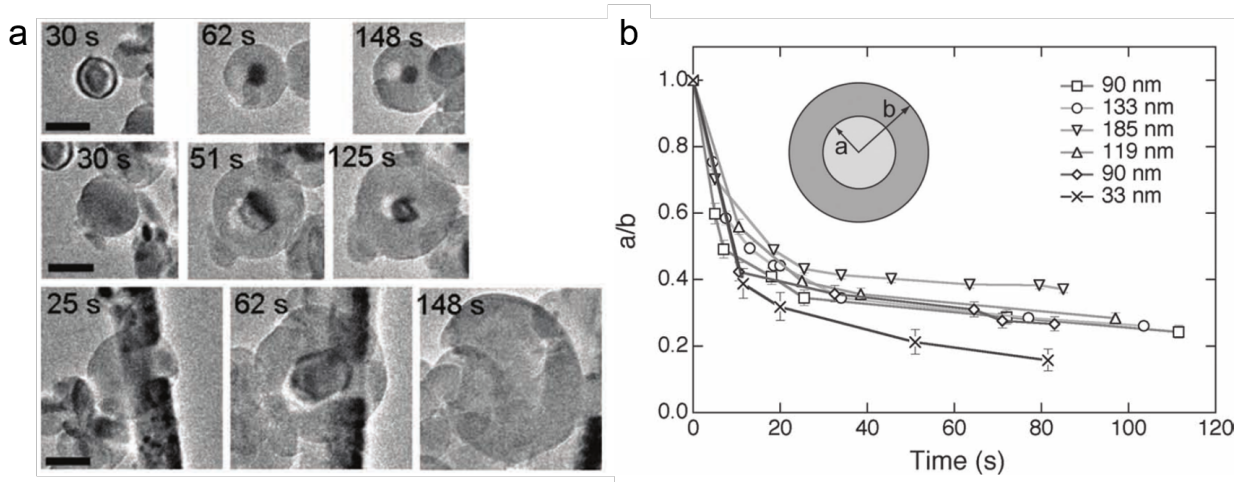

Fig. I.11: *In situ* TEM observations of the lithiation of SiNPs. a) Sample of 3 particles of different sizes, all 3 still featuring a crystalline core after an extended period of time, despite being biased to 0 $V_{Li^+/Li}$. b) Evolution of the core-on-total-diameter ratio in time. Edited from [52].

Evidence of a strain-limited shell growth

These observations show that the reaction front slows down as it progresses, and systematically comes to a halt at a core-on-shell ratio near 0.3 (fig. I.11.b). A phenomenon also identified in nanowires by Liu et al. [53], which clearly outlines a mechanism intrinsic to silicon lithiation rather than to a particular geometry. Furthermore, fractures can appear in the shell in particles that exceed 150 nm of diameter [54]. This hints at a buildup of stresses that could not only

hinder further amorphization, but also tear apart the amorphous shell during its expansion, leading to the pulverization of individual particles and tremendous capacity loss at the electrode scale. Consequently, considerable attention was brought to mechanical stress phenomena in the Li-Si system. Those were indeed demonstrated to influence the kinetics of the reaction front as well as pulverization [49], making an in-depth understanding of stresses critical to the rational design of silicon electrodes. Considerable insight on the matter can be found in a recent review from Xu and Zhao [55].

I.2.3 Behind the voltage hysteresis: stress-potential coupling

Stress profiles predictions and measurements

A tighter silicon lattice under compressive stresses requires a higher bond-breaking energy for lithiation to proceed, which would explain a stress effect on the driving force of the reaction [56, 57]. This was underlined in numerous modeling efforts, with compressive and tensile hoop stress gradients predicted in the crystalline core and amorphous shell respectively [58–60] (fig. I.12.a). To our knowledge, stresses in SiNPs have not been measured experimentally as of yet, a lack that this thesis work will attempt to address. Sethuraman et al. [61–64] did monitor the stress of a silicon thin film in situ during cycling (fig. I.12.b), and measured reversible stresses around ± 1 GPa which were well aligned with predictions. The slight deescalation of this stress at higher SoCs is most likely due to the shell softening with increasing Li content, according to first-principle atomistic models [65–68].

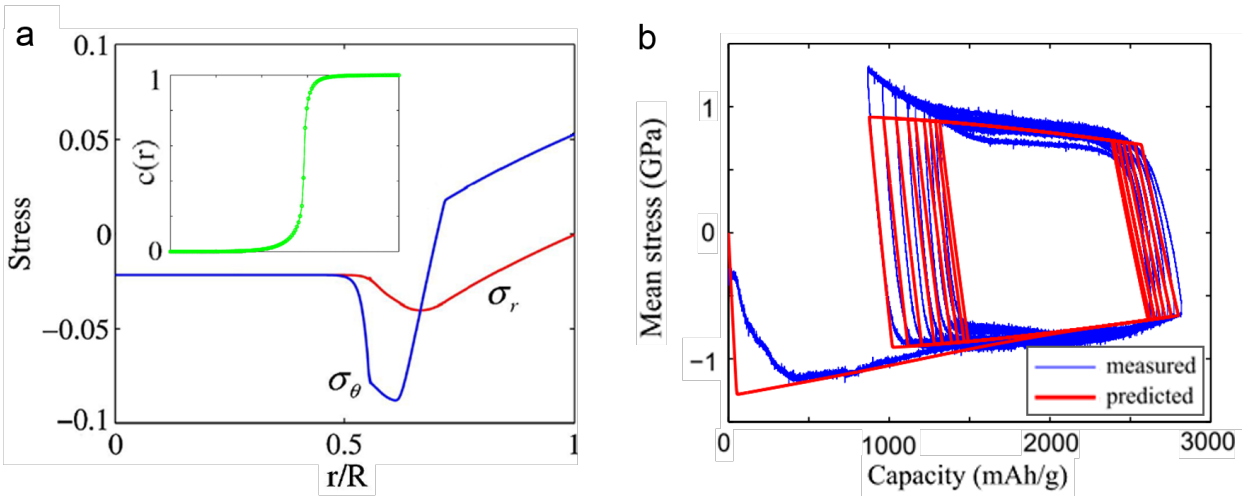

Fig. I.12: a) Radial profile of the hoop stress σ_θ and radial stress σ_r from a numerical simulation of two-phase lithiation of a SiNP that exhibits the Li concentration profile in green. Edited from [59]. b) Measured and predicted stress variation of mean stress during 10 cycles of a silicon thin film in half-cell. Reproduced from [64].

Stress in the Larché-Cahn chemical potential

These large hydrostatic stresses will influence the electrochemical potential of our electrodes, as predicted in the Larché-Cahn formalism [69, 70]. Indeed, an effect near $62\,\mathrm{mV/GPa}$ is expected from the energy dissipated during the plastic deformation of lithium-silicon. If that mechanical factor was to account for the full hysteresis loop however, experimental results ($\sigma_m \approx -1.0 \pm 0.5\,\mathrm{GPa}$, see fig. I.12) point to a coupling as high as $125\,\mathrm{mV/GPa}$ [71]. It follows from the Larché-Cahn equations that compressed phases will exhibit lower potentials, while tensile stresses will mean higher potentials i.e. it is energetically more favorable for lithiation to proceed in tensile areas. Coming back to stress modeling efforts, they could translate to lithium content gradients across particle shells. Experimental confirmation would require local measurements of the $\mathrm{Li_xSi}$ stoichiometry, which have not been reported to date.

Summary and challenges

At room temperature, crystalline silicon is lithiated through a two-phase process and is progressively replaced by an expanding a-$\mathrm{Li_xSi}$ phase. Lithiated particles thus exhibit a core-shell morphology. The amorphization reaction front slows down as c-Si is increasingly compressed however, and the two-phase reaction stops to give way to the solid-solution process that drives the lithiation/delithiation of the newly formed amorphous phase for the subsequent cycles. Despite extensive modeling efforts and abundant circumstantial evidence derived from electrochemical measurements, the lithiation mechanism of crystalline silicon has not been fully elucidated. In particular, the discrepancy there is between microparticles and nanoparticles in the few reported local measurements of the lithium content of the $\mathrm{Li_xSi}$ phase suggests a significant influence of the particle size as D. Robert pointed out [37]. The relation between the lithium content x, the relative shell size and the state of charge has not been elucidated experimentally and deserves our attention. This notably the object of chapter V.

I.3 The solid electrolyte interface

The solid electrolyte interface (SEI), is key to the short lifetime of silicon electrodes. Its complex chemistry and morphology and their evolution along cycling are to be extensively understood to adapt electrode and electrolyte technology. In this section we detail the current understanding of the SEI's chemistry and morphology from works on graphite, before going on to the most recent characterization efforts on silicon. We will solely report results from studies on electrolytes based on the solvent ethylene carbonate (EC) and the $LiPF_6$ salt, as it is the one used throughout the work reported in this manuscript.

I.3.1 SEI morphology models from the study of graphite electrodes

Li-ion cells exhibit a large voltage above 3.6 V, and few electrolytes can withstand such potential gaps. State-of-the-art carbonate solutions [72] - based on ethylene carbonate (EC) - are in fact thermodynamically unstable against reduction at negative electrodes, since the Fermi levels of the latter lie above the lowest unoccupied molecular orbital (LUMO) level of the electrolyte. The product of this reduction reaction is an electronically insulating but ionically conducting layer, akin to a solid electrolyte [73] hence its name of solid electrolyte interface (SEI). The formation of a stable SEI layer is critical to ensure high Coulombic and voltage efficiency [74] which govern the lifetime of a battery. But despite considerable research in the past few decades, the SEI is still a puzzle to be solved [75].

The mosaic model

Early studies of the SEI's morphology suggested an internal bi-layered structure [76, 77], which was later refined to the *mosaic* model [78, 79] (fig. I.13.a). This representation became a cornerstone in the science and technology of lithium batteries. It is worth noting that E. Peled, who authored this widespread model, has recently published a valuable and comprehensive review of the solid electrolyte interface [80]. Regarding the SEI's chemistry, it is tailored of oligomers [81, 82] - such as polyolefins and ethers - and lithium alkyl carbonates [83] loosely clumped in a porous structure on the electrolyte side, whereas closely packed inorganic components [84, 85] - LiF, Li_2O, Li_2CO_3 - lie closer to the electrode surface. Lithium ethylene dicarbonate (LEDC) - $(CH_2OCO_2Li)_2$ - was later identified as the main component of the outer, "softer" part of the SEI [86, 87], with Li_2CO_3 only found in trace amounts [88]. A reaction pathway for LEDC from the reduction of 2 EC molecules was proposed by Michan et al. [89] and it reported figure I.14.

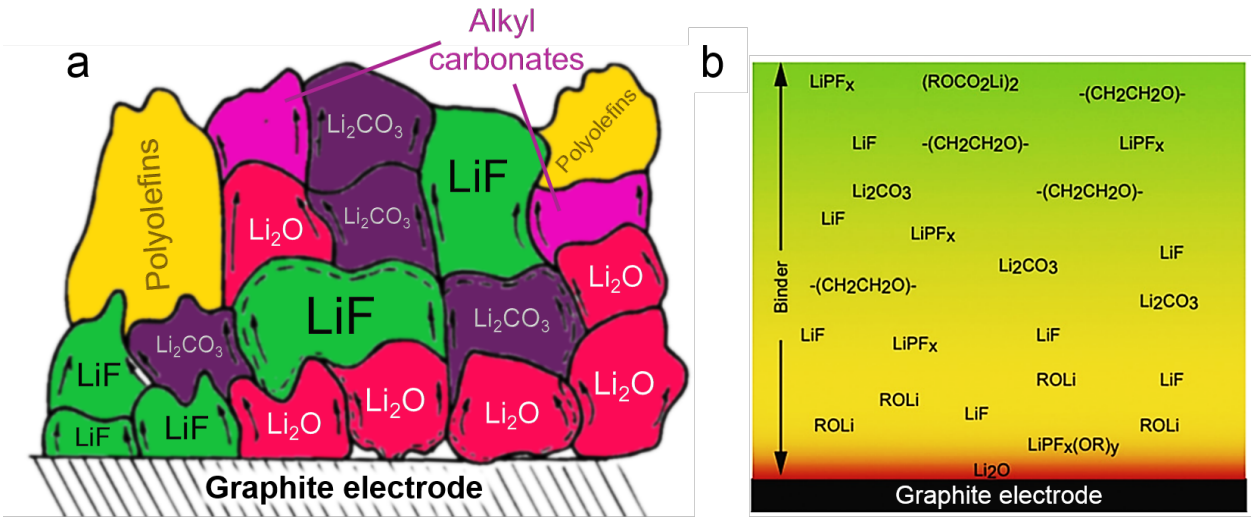

Fig. I.13: a) Schematic of the SEI mosaic model featuring an overstated Li_2CO_3 contribution. Uneven organic and inorganic small domains are preferentially found near the electrolyte and the electrode respectively. Edited from [78]. b) Refined SEI model put together from synchrotron X-ray photoelectron spectroscopy depth profiling. Reproduced from [90].

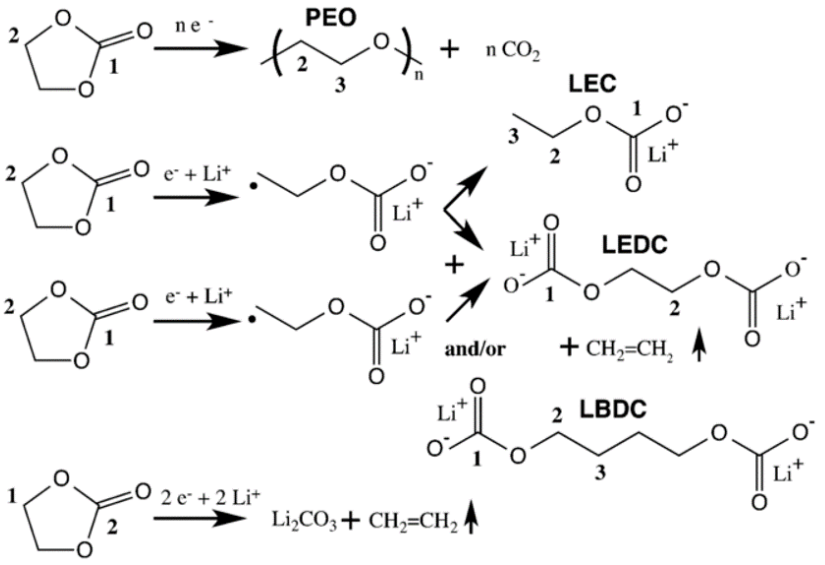

Fig. I.14: Reaction pathways proposed for the reduction of ethylene carbonate (EC) into PEO, LEDC as well as Li_2CO_3. Reproduced from [89].

Domains size and distribution

Although the mosaic model has reached widely within the community, it hasn't fully been established experimentally despite a steady and ongoing research effort. X-ray spectroscopies yield precious depth profiles, but are extremely limited in their lateral resolution. Nevertheless, conclusive evidence was gathered for chemical gradients across the layer, as showcased in the model proposed by Malmgren et al. - fig. I.13.b - which features lithium alkyl oxides and lithium fluoride on the

deeper parts of the SEI, while $C-O$ and $C-C$ containing compounds are more prevalent in its outermost region. The authors estimate a SEI thickness to the tune of 20 nm, well within the 15 nm to 50 nm window from previous reports [91, 92].

The body of results remains however mostly qualitative. Estimating the domain size of individual phases and their quantitative distribution has proven difficult, considering the sensitivity of any such experiment to electrode rinsing, oxygen, water, and electron irradiation in the TEM. LiF stands out however, both for its relative stability and its crystalline nature as an ionic crystal. Chattopadhyay et al. [93] were able to follow a nucleation-growth mechanism in situ, reporting crystallite size growing from 1 nm to 40 nm (fig. I.15).

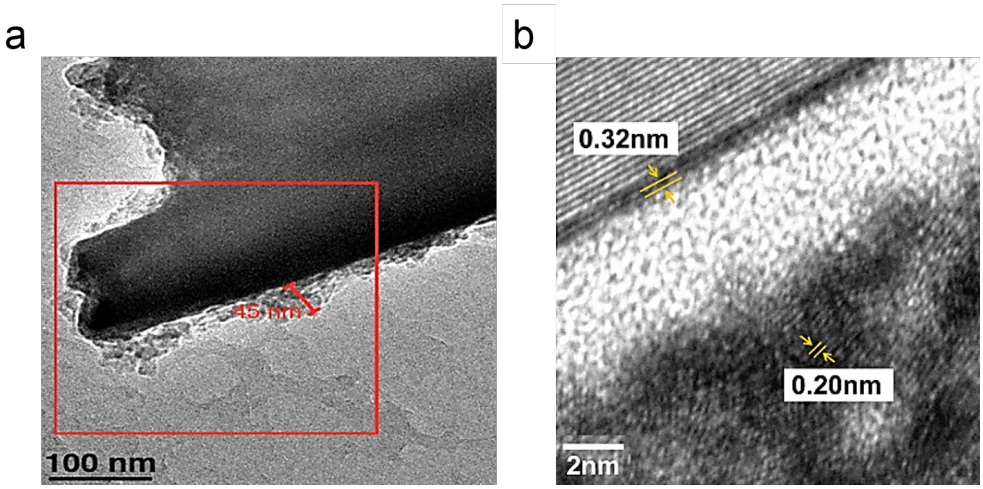

Fig. I.15: Post-mortem TEM micrographs of the SEI formed on carbonaceous surfaces. a) After the first lithiation of graphite, cut-off at 50 $mV_{Li^+/Li}$. The SEI layer features a flaky aspect and an uneven thickness. b) On SiC-supported graphene, LiF nanocrystals - 2Å lattice spacing - are in an amorphous matrix.

This structure sets during the formation phase of the SEI, over the first few cycles on graphite electrodes, which then benefit from its solid electrolyte properties from there on. This balance is upset with silicon: the SEI undergoes tremendous stresses, it cracks and expose fresh surfaces. As a result both its chemistry and morphology evolve throughout the lifetime of the electrode, and this warrants particular attention.

I.3.2 Particulars of the SEI's chemistry on silicon

Electrolyte reduction reactions on silicon surfaces mostly lead to the formation of species similar to those found on graphite [89], and the general "inner inorganic to outer organic" gradient is thought to remain [94]. With two notable exceptions: (i) the degradation of the native oxide, SiO_2 into Li_4SiO_4 [95, 96] and Li_2O [97–99], which sees the original layer triple in volume [100]; as well as (ii) the reduction of fluoroethylenecarbonate (FEC), a popular co-solvent in modern electrolytes for Si-based electrodes.

The FEC additive

In a bet to favor the formation of a more flexible SEI to accommodate the volume change of silicon [101], several additives were screened and FEC was shown to significantly improve electrode lifetimes [102], as outlined by Aurbach et al. in a recent review [103]. During charge FEC reduces first - around $1.1V_{Li^+/Li}$ vs $0.8V_{Li^+/Li}$ for EC - and is continually consumed [104] as electrodes operate. This means that even in moderate concentrations - typically 10% - the additive has a considerable influence on the SEI's composition and properties. Foremost among these properties is an improved ability to sustain the mechanical stresses associated with the lithiation of silicon. Shkrob et al. [105] propose that this is explained by the elastomeric properties of the cross-linked polymer that forms after the radical polymerization of FEC. The associated reaction pathways are reported figure **??**. This compound, later labeled $\mathrm{poly(FEC)}$ in several studies [106, 107], was also identified experimentally (fig. I.16) by XPS [108]. According to Etacheri et al. [109], it seemingly overtakes LEDC as one of the main building block of the SEI.

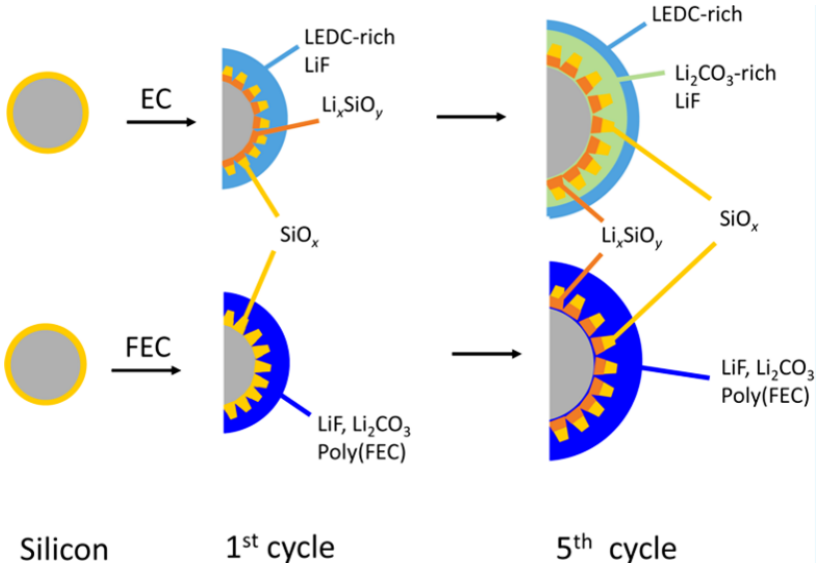

Fig. I.16: Schematic depiction of SEI on SiNPs from the decomposition of EC and FEC [106]. The presence of Li_2CO_3 has been attributed in other works to the decomposition of LEDC [**Seo2014**].

It is also worth noting that LiF is often quoted as a byproduct of these reactions and, as a result, the LiF content of the SEI is typically higher when FEC is added [110]. Edström and coworkers [107] have reported that this is compounded as the electrode age, as the continuous reduction of FEC [104] causes an accumulation of LiF in the electrode. This is however disputed by XPS analyses from the group of Shirley Meng [111]. There the atomic ratio for LiF in the SEI would go from almost 50% after the 1st cycle to 15% after 100 cycles. We will challenge this assertion in the aging study of chapter VI.

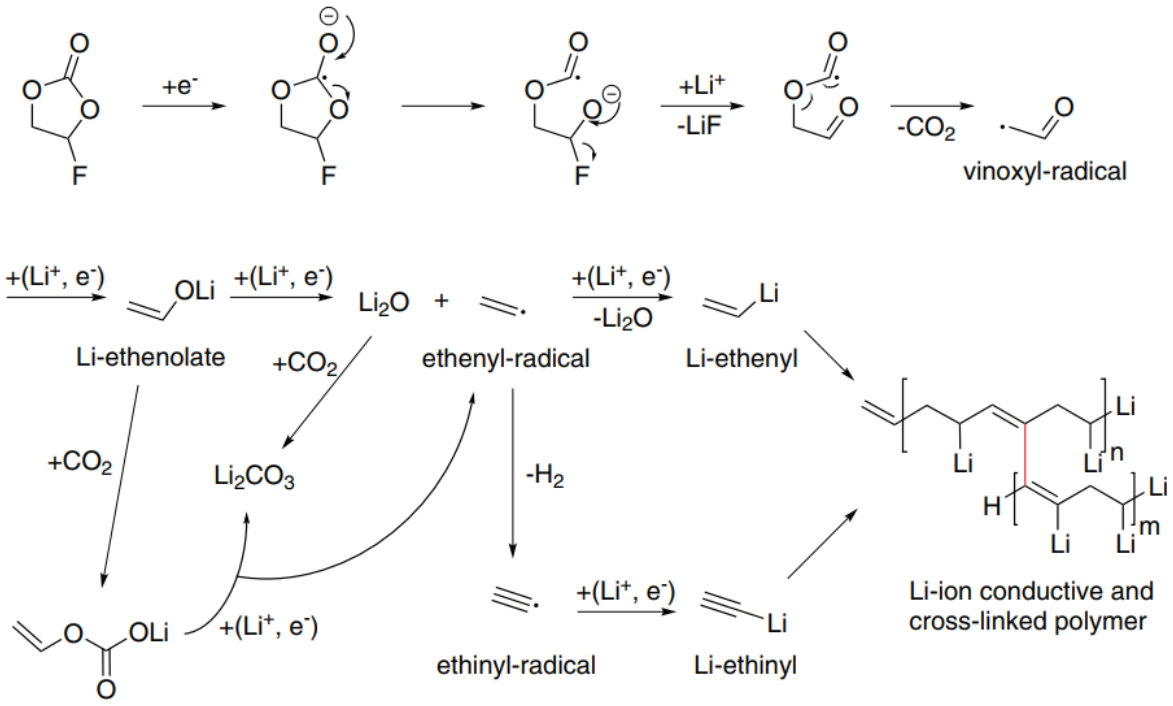

Fig. I.17: Reaction pathways proposed for the reduction of ethylene carbonate (FEC). Reproduced from [104].

I.3.3 Instability of the layer on silicon

SEI accumulation

In silicon electrodes, the SEI's unstable nature causes severe electrolyte degradation and was rapidly pointed to as one the main cause of irreversible capacity [112]. Consequently several studies attempted to quantify the SEI's continuous growth along cycling. Gravimetric measurements in fact showed an increase of 210% in electrode mass after 100 cycles [41] at a limited capacity of 1200 mA h/g, in line was an earlier report of 150% in the same conditions by Mazouzi et al [26]. That sheer amount is already relevant to start understanding performance loss as (i) charges as well as Li^+ ions are lost is the reduction process and (ii) the thickening SEI will hinder Li^+ transport, at the particle scale and at the electrode scale by clogging its pores and restricting diffusion to surface regions. In this scenario, a Li_xSi gradient would develop, leaving surface SiNPs over-lithiated [41, 89]. Yet the experimental evidence for this is scarce. That phenomena will be under scrutiny in chapter VI of this manuscript.

As previously mentioned, the instability of the SEI is mostly associated with the mechanical stresses applied by the swelling/contraction cycle of silicon particles during lithiation/delithiation. Tensile stresses at the silicon/electrolyte interface result in cracking and partial delamination of the layer, as shown by Kumar et al. [113, 114] from *in situ* atomic force microscopy (AFM) measurements. Those findings are illustrated figure I.19.

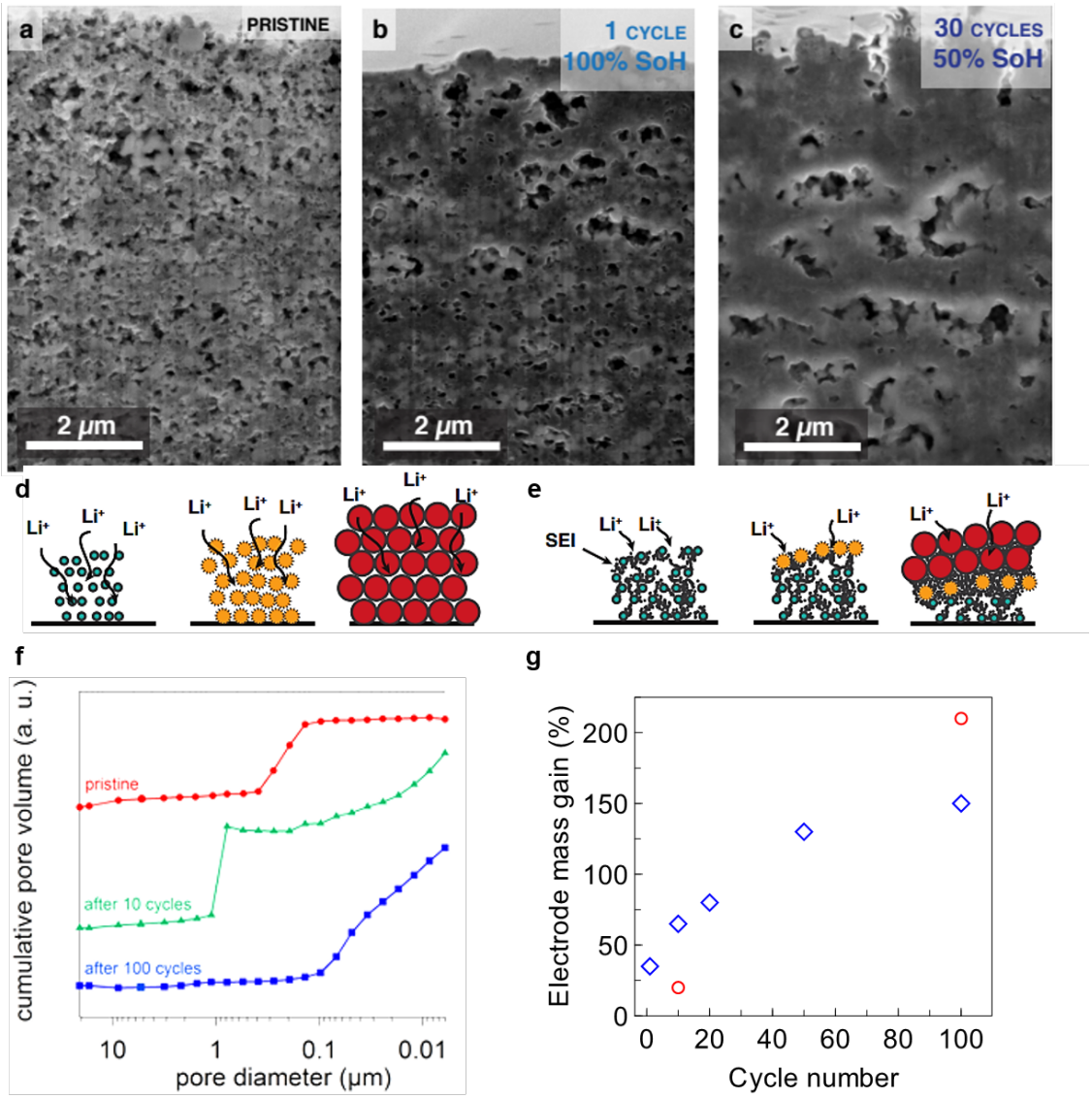

Fig. I.18: a-c) FIB/SEM cross-sections of a Si electrode cycled in half-cell showing SEI accumulation and pore clogging. d-e) Schematic of the influence of the growing SEI on lithiation kinetics. A lithiation gradient develops across the depth of the electrode in later cycles [89]. f) Hg porosimetry of an electrode after 1, 10 and 100 cycles to 1200 mAh/g showing progressive blockade of the ionic conduction network [41]. g) Electrode mass gain after delithiation from [26] (blue diamonds) and [41] (red circles).

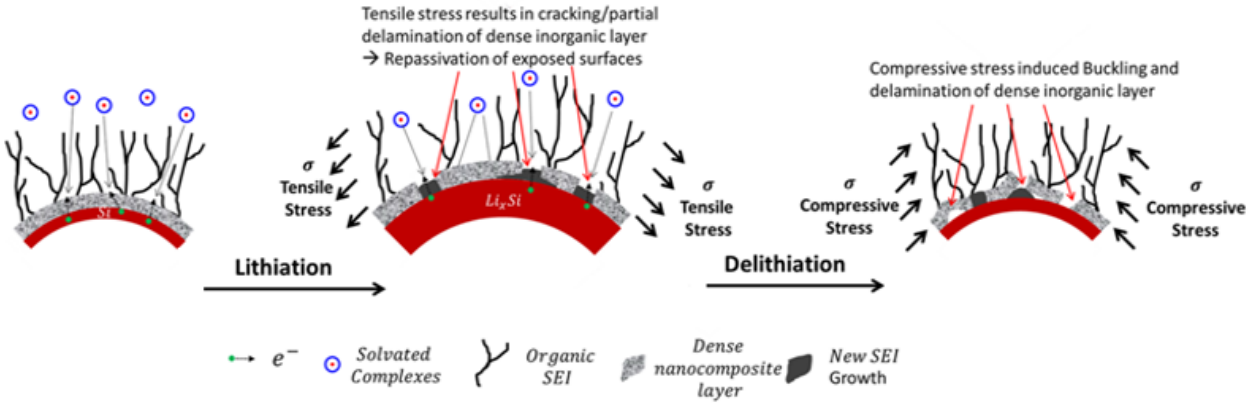

Fig. I.19: Schematic representation of the SEI evolution with strain. In practical electrode geometries such as silicon particles, expansion (contraction) of the underlying silicon stretches (compresses) the SEI layer, and causes in-plane tensile (compressive) stress in the film. Reproduced from [114].

Chemical evolution

There is however more to the SEI than its raw mass. Further understanding of electrode aging requires us to dwelve into the chemistry of this newly formed SEI. By correlating ^{7}Li NMR observations with electrochemical data, Delpuech et al. [115] showed that the formation of lithium-containing species occurred continuously but couldn't account for more than about 15% of full irreversible capacity loss. They estimate that two-thirds of the electrode mass gain could be attributed to oligomers and polymers. A statement supported by other spectroscopy studies [89, 109, 116]. It is also likely that the electrode's operating voltage will play a significant role in the composition of the SEI that forms [89, 117]. This voltage has in fact been shown to drop in half-cells - higher polarization to overcome with accumulating SEI - and rise in full cells [27, 28, 118].

The *breathing* effect

In addition to its build-up cycle after cycle, the SEI of silicon exhibits a significant dynamic behavior from charge to discharge, akin to previous results on graphite [119] but to a greater extent. Qualitative trends were identified in early characterization efforts through AFM measurements and SEM observations [94] which reported a dissolution, or contraction of the layer during delithiation [120]. This is supported by recent findings from Veith et al. [121], who followed the growth of the SEI layer via *in situ* neutron reflectometry and observed a decrease of about $\approx 25\%$ in SEI thickness after delithiation. Moreover complementary XPS measurements allow the authors to show that the inorganic part of the SEI does not evolve upon electrode delithiation. Rather, the polymeric component is the sole responsible of SEI *breathing*, as illustrated figure I.20.

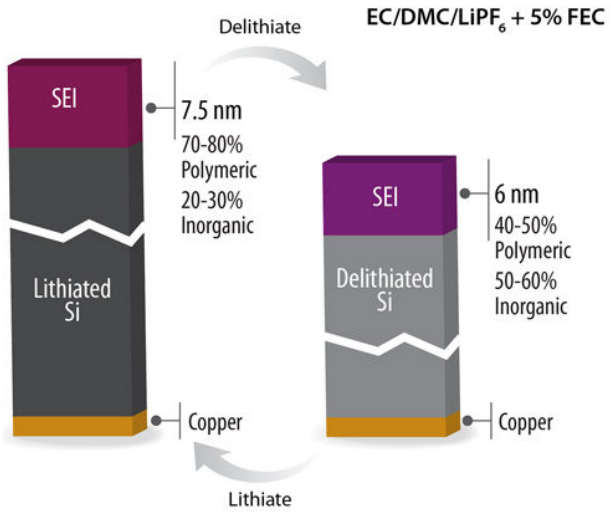

Fig. I.20: Graphical summary of SEI layer chemistry grown on silicon before and after delithiation. Edited from [121].

Conclusion and objectives

State-of-the art electrolytes are unstable at the working potentials of anodes and reduce to form the SEI layer. On graphite, a sustained research effort narrowed down the overall structure of this intricate structure to an inner tightly-packed inorganic film rich in LiF, Li_2CO_3 and Li_2O, and an outer layer composed of both oligomers and alkyl-carbonates, among which lithium ethylene dicarbonate (LEDC) is foremost. While this pattern is mostly unchanged in silicon electrodes, with the notable addition of products of the reduction of FEC, characterizations identified a dramatic increase in the overall SEI content of aged electrodes as a result of the continuous solvent reduction along the electrode's lifetime. Although these overall trends in accumulation are well described, they have so far only been observed from at the electrode scale, and direct observations of the SEI's morphology are few. Studying the layer at the particle scale could not only allow us to compare local observations to established bulk phenomena, but also to probe the SEI's influence on local cycling performance. In addition, the widespread framework of the mosaic model can itself benefit from being challenged experimentally.

I.4 Electron energy loss spectroscopy on negative electrode materials

The advent of nanomaterials and the importance of surface chemistry in lithium-ions batteries have made TEM a tool of choice for this application. Regarding silicon anodes, we have seen that lithiation mechanisms are yet to be fully elucidated, with current models mostly relying on inductions from the electrochemistry of the system. Likewise, the SEI's fine morphology has yet to be understood. If its total thickness is a few dozen nanometers, we can expect domains to be as small as a nanometer, an ever smaller scale than what is necessary to study lithiation. Those resolutions can only be probed by transmission electron microscopy (TEM). This section reviews previous attempts at characterizing lithiated negative electrodes in the TEM by electron energy loss spectroscopy (EELS), before introducing the method of interest to this manuscript called *low-loss* EELS. We show that this technique is better suited to handle the great sensitivity of both lithiated species and the soft materials of the SEI, a major experimental roadblock for classical EELS experiments. Particular attention will be paid to the approach that was pioneered in the thesis of J. Danet [122], and which we build upon.

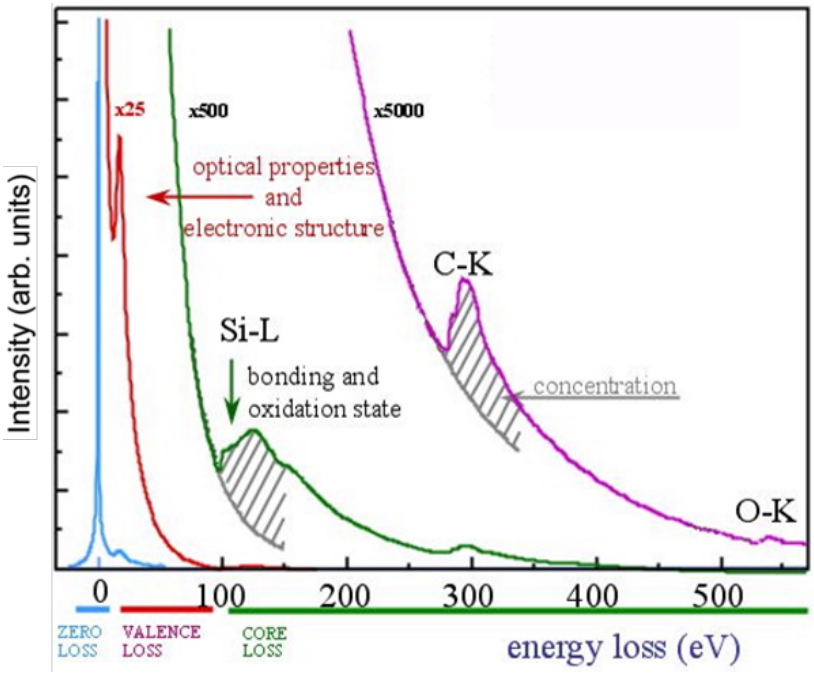

Fig. I.21: Typical electron energy-loss spectrum, with the low-loss ($< 100\,\text{eV}$, also called valence loss) and core-loss regions clearly delimited.

I.4.1 Core-loss EELS on graphite and silicon particles

Scanning transmission electron microscopy (STEM) combined with electron energy-loss spectroscopy (EELS) provides spatial resolution that can be less than 0.1 nm in modern TEMs, with chemical and atomic bonding investigation. EELS ionization edges - or core-loss edges - are known to contain quantitative information on both elemental composition as well as chemical environment in their fine structure, as illustrated on the typical EEL spectrum represented figure I.21. This has allowed numerous high resolution studies on the transition metal oxides of the positive electrode [123, 124]. However attempts to replicate this success on negative electrode materials [125], notably to probe the SEI's complex chemistry [111, 126], have had to deal with the extreme reactivity of lithiated species. Besides the necessity of having the appropriate instrumentation to protect samples from oxygen and moisture, there remains the issue of the sensitivity of lithiated compounds and the SEI to electron radiation in the TEM. Indeed, common experimental protocols involve electron doses that cause the loss of chemical information in these sensitive species, and EELS has scarcely been used to study the negative electrodes as a result. Nevertheless, a few works took advantage of the unique possibilities offered by EELS on negative electrodes, giving us a glimpse of what could be achieved if acquisition protocols were tailored to the sensitive species of interest.

Investigation of the Li-K edge core-loss edge

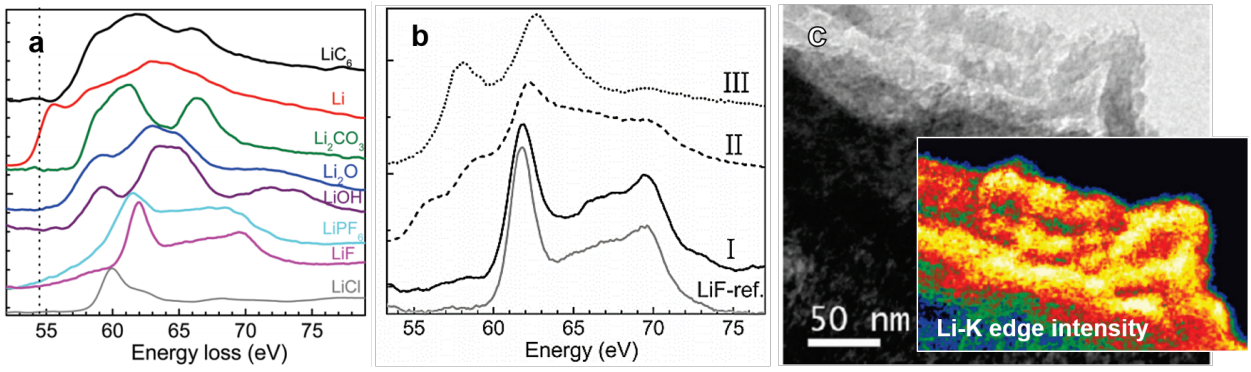

Fig. I.22: EELS observation of a lithiated graphite microparticle. a) Reference Li-K edges of standard SEI compounds. b) Experimental EEL spectra of the SEI for three acquisition times [125]. c) TEM micrograph of the surface layers of lithiated graphite. Li-K integrated edge intensity from EFTEM observation in insert. Edited from [125].

One of such attempts comes from Wang et al. [125] who looked at lithiated graphite - LiC_6 - and its SEI. By comparing their SEI Li-K edge to experimental references (fig. I.22.c), the authors note that the porous, "spongy" aspect of the SEI (fig. I.22.a) can be attributed to damaged organic components. Moreover LiF is the only detectable compound, unsurprisingly as it is the least beam sensitive of the SEI components. LiF is nonetheless observed to decay to metallic Li then Li_2O under the electron beam (fig. I.22.b), as expected from earlier studies on similar compounds [127].

The authors also report elemental mapping from the Li-K edge intensity, figure I.22. This is achieved via energy-filtered TEM (EFTEM), which consists in the introduction of an energy slit to only gather electrons that have here lost the energy corresponding to the lithium edge. We see that mapping this single element yields little insight here, as lithium is present in both the SEI and the active matter of electrodes. As a result the contrast of the insert of figure I.22 is essentially the sample thickness.

Wang's approach was replicated by Sina et al. [111] on silicon nanoparticles, notably in an effort to analyze the influence of the FEC additive on the SEI's chemistry. As we can see figure I.23.a, two different Li-K edge shapes are observed, indicating a prevalence of LiF in the SEI when FEC is added to the electrolyte, and a signal closer to that of the Li_2CO_3 standard otherwise. This represents a noticeable technique improvement given the sensitivity of this last compound. Likewise, from the Si-L edge, Li_ySiO_x species are shown to be suppressed when FEC is used. Besides this local chemical analysis, the authors also demonstrate an ability to probe the SEI morphology by mapping elemental concentrations by STEM-EELS as illustrated I.23.c-d. However, the high lithium concentration at the particle's surface likely results from the degradation of Li-Si alloys, as detailed later on. Thus developing a low-dose protocol for STEM-EELS is critical to analyze the system at hand.

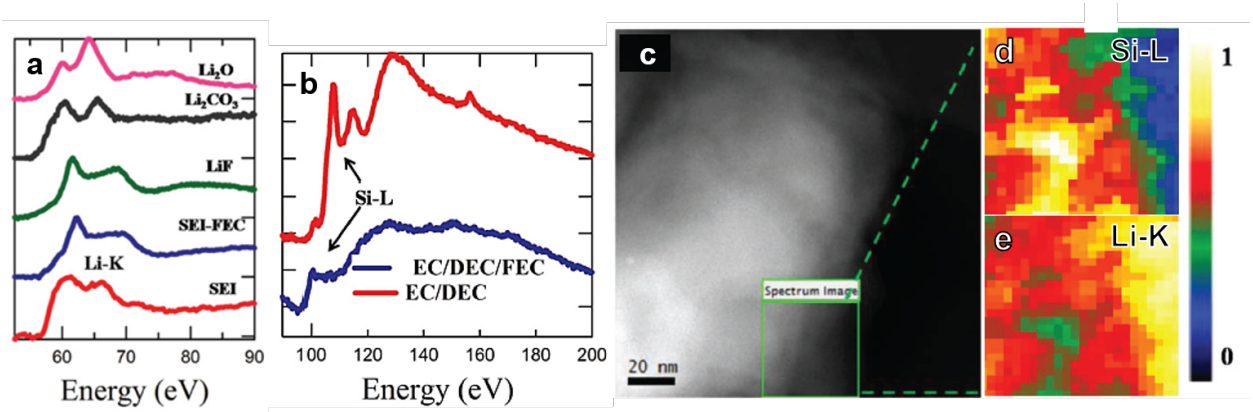

Fig. I.23: EELS analysis of lithiated silicon nanoparticles from electrodes cycled with and without the FEC additive. a) Reference Li-K edges of standard compounds next to experimental Li-K edges of the SEI. b) Experimental Si-L edges from EEL spectra averaged over line scans. The difference between the two edges reveals that Li_ySiO_x is suppressed with FEC. c-e) STEM-EELS maps of silicon and lithium relative concentrations from their respective Si-L and Li-K core-loss edges. Edited from [111].

Phase mapping with multiple edges

Another approach was to simultaneously acquire silicon, carbon and lithium edges to encompass all compounds present and map their morphology relative to one another. Each experimental spectrum can be decomposed into reference components - in this case, different edge structures - fed into a multiple least-square fitting (MLLS) algorithm. The output is a series of components

maps that can be stacked in a composite phase map, as illustrated fig. I.24. This method is detailed and developed in chapter III.2.

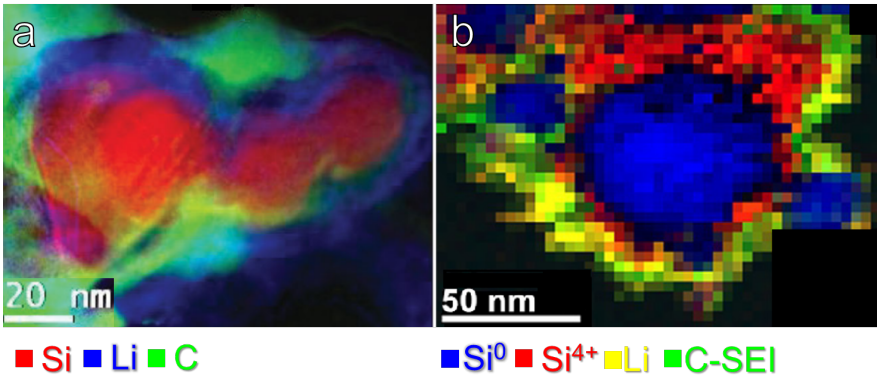

Fig. I.24: Phase mapping in lithiated silicon nanoparticles from EFTEM and STEM-EELS experiments. a) EFTEM composite color map. Reproduced from [38]. b) Core-loss STEM-EELS composite color maps of Si^0 (blue), Si^4+ (red), Li (yellow) and the C-K edge of Li_2CO_3 (green). Reproduced from [128].

This represents noticeable progress when it comes to probing the morphology of our system. However any form of electron-dose limitation has been neglected. The total dose applied borders upon $10^5\, e\,\text{Å}^{-2}$. This is orders of magnitude above the critical dose (total dose above which a distinctive spectral feature is suppressed) of $D_e = 750\, e\,\text{Å}^{-2}$ for Li_2CO_3 at room temperature [129]. The results are a snapshot of degraded materials, rather than an accurate depiction.

I.4.2 Low-loss STEM-EELS for sensitive materials

Since the electron doses associated with the study of core-loss edges are unsuited to the study of both the SEI and Li-Si compounds, one has to look to the low-energy part of the EEL spectrum (<50 eV) called plasmon losses or low-loss for short. Indeed, the intensity of the electron energy loss scales with 1/E. Considering that the C-K edge - the most relevant to study the SEI - stands at 284 eV, an equivalent low-loss signal can be acquired for doses 15 times lower. Consequently, one can observe smaller areas without passing the dose threshold - called the critical dose D_e, see II.2 - above which chemical information is lost. As a result, in the case of radiation-sensitive materials, using plasmons rather than edges greatly improves the achievable spatial resolution. Shorter acquisition times also enable the acquisition of large field of views which are necessary when characteristic domain sizes are larger than a few nanometers and samples are not homogeneous.

A lever for quick phase mapping

Although plasmons cannot usually be used for quantitative chemical analysis, their shapes vary substantially between specimens and provide an additional characteristic fingerprint [130, 131]. If

one gathers a database of the low-loss spectra of the species of interest, phase domains can easily be distinguished in a spectrum image. For example, Sigle et al. [132] report the phase mapping of SiC and Si_3N_4 grains using the difference of their plasmon peak energy (fig. I.25.a), while Yurtsever et al. [133] used the energy shift between the SiO_2 plasmon ($\approx 23\,eV$) and the silicon plasmon ($\approx 16.6\,eV$) to outline the position of Si grains embedded in a silica matrix (fig. I.25.b). Tomographic reconstruction then allowed them to present a 3D structure, a feat replicated in an organic semi-conductor by Pfannmöller et al. [134]. Similar experiments with core-loss EELS would involve impractical acquisition times and are impossible.

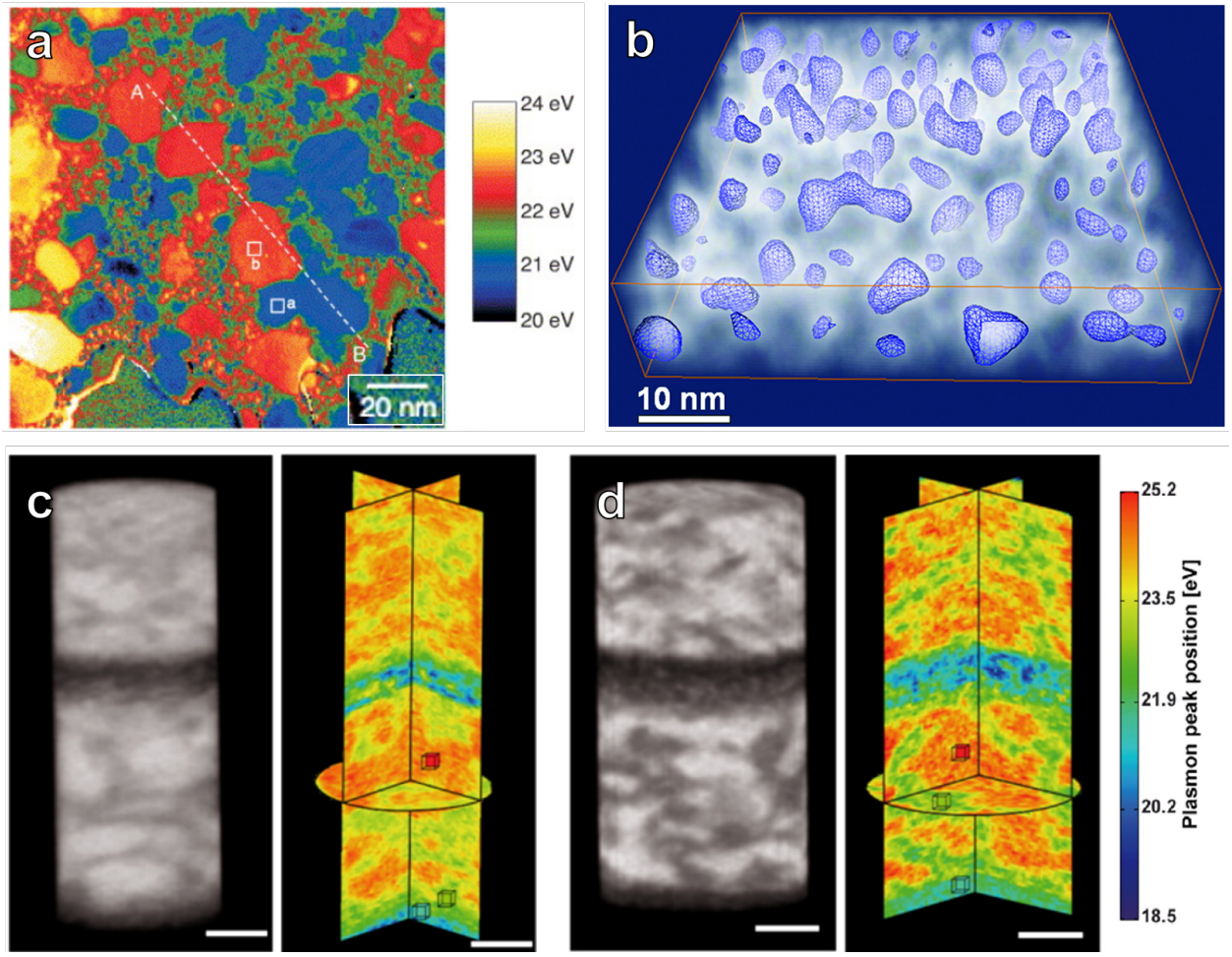

Fig. I.25: a) Plasmon energy mapping from a filtered transmission energy microscopy (EFTEM) experiment, revealing Si_3N_4 and SiC grains [132]. b) Tomographic reconstruction of silicon particles in silicon oxide from EFTEM acquisitions [133]. c) Reconstruction of nanoscale morphology of a photoactive layer by 3D plasmon peak mapping. Bright regions correspond to fullerene-rich domains and dark regions to polymer-rich domains. Scale bars in all images represent 50 nm. Edited from [134].

In other systems, the full low-loss spectrum has to be used to identify a particular phase, and considering only the plasmon peak is not sufficient. This is most notably demonstrated for the $LiFePO_4/FePO_4$ cathode material by examining a characteristic spectral feature at 5 eV, an approach pioneered by P. Moreau and coworkers [135] (fig. I.26). This follows a milestone paper

from V. Mauchamp [136] which advocates for low-loss EELS as a characterization tool of electrode materials. Both lithiated and delithiated phases can easily be distinguished on large field of view images thanks once more to the low acquisition times allowed by the increased intensity of the low-loss spectrum compared to core-losses.

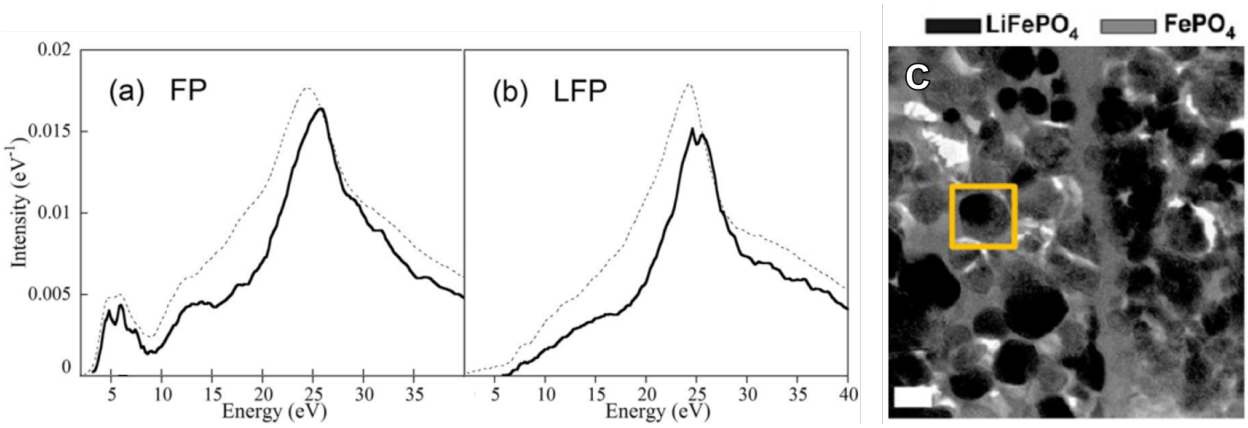

Fig. I.26: a-b) Experimental low-loss spectra of (a) $FePO_4$ and (b) $LiFePO_4$. Edited from [135]. c) EFTEM phase map obtained by a ratio of two filtered images centered at 5 and 25 eV [137].

Cryo low-loss EELS for sensitive phases

In the field of cryo electron microscopy, driven by the life sciences [138, 139], radiation damage was rapidly identified as a major hurdle to the study of organic compounds. Indeed, researchers noticed a strong temperature dependence of radiation damage [140]. The electron doses associated with significant chemical damage in samples (the critical dose D_e, see II.3) were shown to go down by 3 orders of magnitude when cooling from 300 K to 80 K. This motivated the application of cryo TEM to samples for which (electron-)beam-induced damage had been an issue such as delicate polymers [141] as well as fragile inorganics [126], especially with spectroscopies that require higher electron doses. Using the low-loss part of the EEL spectrum brings even further improvement, with led Kim et al. to accurately distinguish organic domains in block copolymer with a resolution of 10 nm (fig. I.27) [142, 143]. This strategy was notably continued by Yakovlev et al. to study the Nafion fuel cell membrane [144, 145]. A similar approach could be applied to observe the sensitive compounds of the SEI in silicon electrodes.

LN_2 cooling is however impractical when coupled with the necessity of vacuum transfer and could not be set up for the experiments reported in this manuscript. We expect that it could only improve the performance reported in chapter III. Nevertheless, low-loss EELS with MLLS fitting can advantageously replace classical protocols to map sensitive phases, making it a tool of choice to study the SEI. By cooling samples to liquid nitrogen temperatures to temper beam damage.

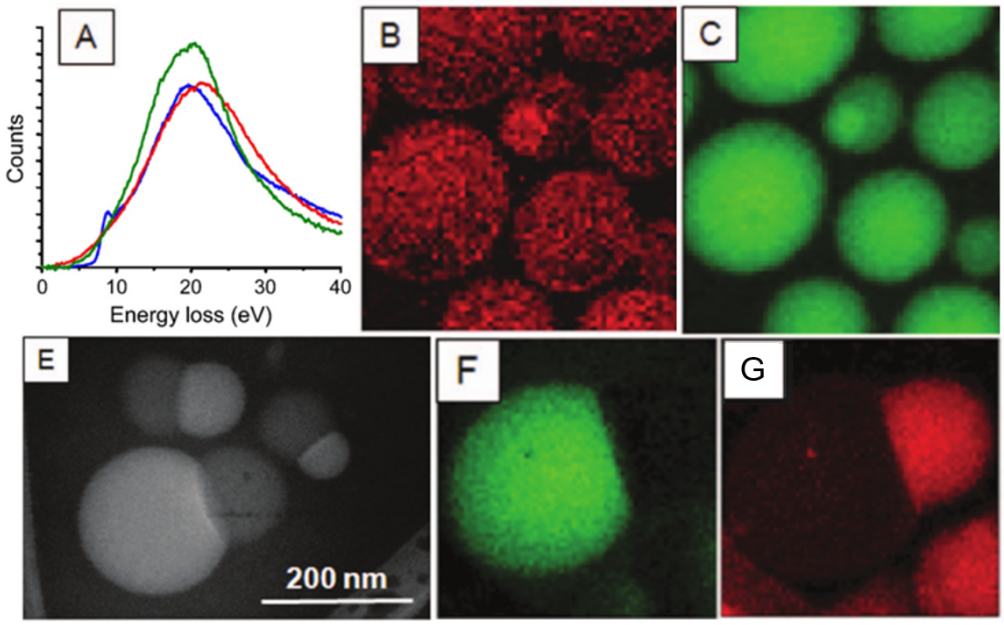

Fig. I.27: A) Reference plasmon spectra for the PDMS (green), acrylate monomer (red) and background amorphous ice (blue). B-C) Components maps before polymerization. E) TEM image after polymerization. F-G) Component maps after polymerization. The electron dose is reported to be $12\,e\,\text{Å}^{-2}$. Edited from [131].

I.4.3 Application to the Lithium-Silicon system

Besides phase mapping, the low-loss EEL spectrum can be used to probe a variety of physical properties by examining the plasmon peak whose energy contains information on the electronic structure of specimen. Plasmon energy values can even be directly correlated with the microstructure of a specimen [130]. A prime example comes from the work of J. Gilman [146] and Monthioux et al. [147] to determine the Young's and bulk modulus of carbonaceous materials.

For the scope of this manuscript, we are particularly interested in the dependence of the plasmon peak energy E_p on the free electron density of conductors [148]. In binary alloys, this means a relation can be drawn between E_p and the stoichiometry of the specimen. This was first demonstrated for the Al-Li system [149], where a linear relationship between the plasmon energy and the lithium content could be extrapolated. Danet et al. [35] successfully applied the same strategy to Li_xSi alloys. The synthesis of Li_xSi alloys of known stoichiometry yielded a database of alloy plasmons (fig. I.28). From there, a relation between the lithium content x and the plasmon energy can be extrapolated (fig. I.29.a). Therefore the plasmon of any given Li-Si alloy can then be traced back to the lithium content [35], provided its peak energy can be fitted through a physically-relevant model. This is done via the Drude-Lorentz formula [150].

The protocol was subsequently applied pixel-wise (i.e. on each spectrum) of large spectrum images to produce lithium content maps of resolutions as high as 3 nm (fig. I.29.b). These observations are experimentally challenging however, as the high incident electron doses they involve

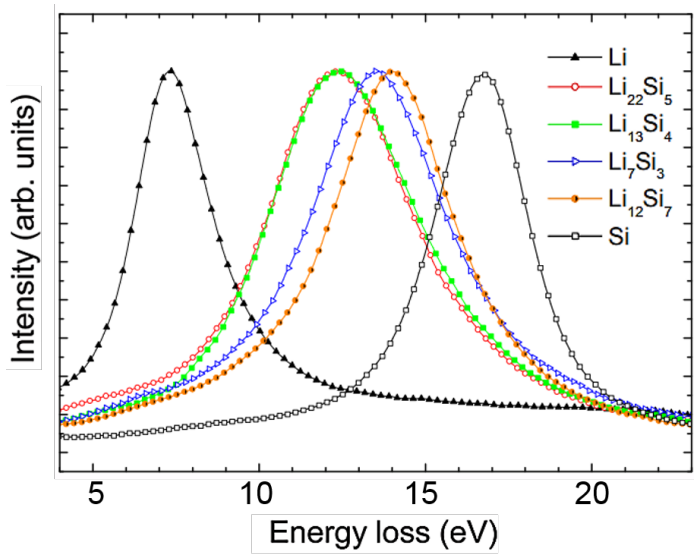

Fig. I.28: Low-loss EEL spectra of Li_xSi alloys of different stoechiometries. The plasmon peak energy goes down with increasing lithium content. Reproduced from [122].

(above 5000 $e\,\text{Å}^{-2}$ in D. Robert's work [37]), can affect the very chemistry one tries to determine. An in depth investigation of this phenomena can be found in chapter III.1.1. We see here that the issues surrounding the observation of lithium alloys and soft matter converge, and that controlling the electron dose will be critical to successful experiments.

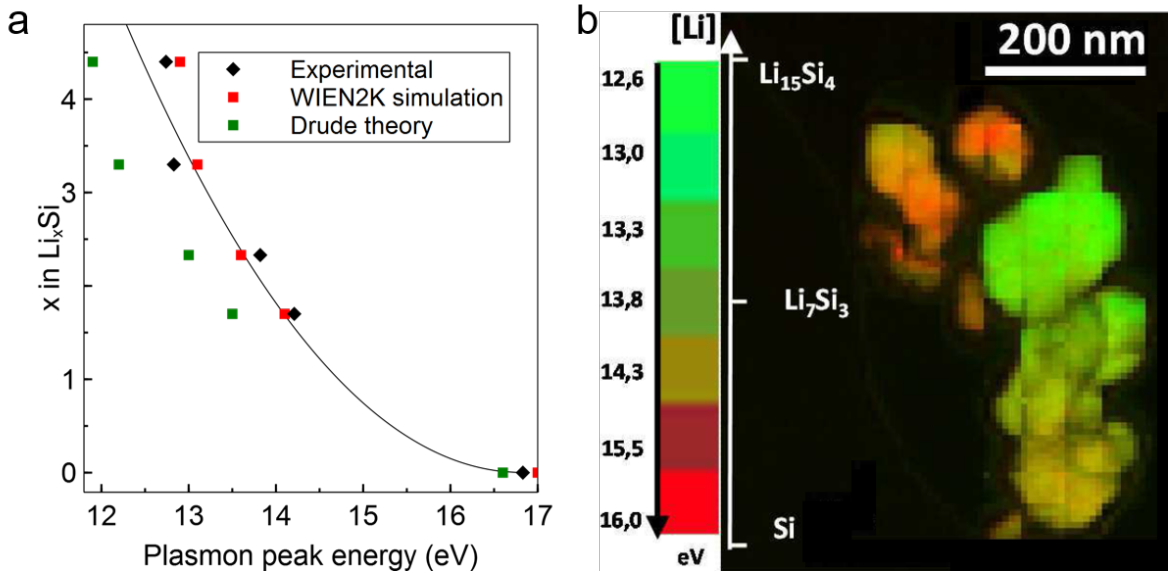

Fig. I.29: a) Fit of Danet et al. [35] experimental plasmon positions determined using the Drude model. b) Lithium content map calculated from a spectrum image with the fitted $x = f(E_p)$ relationship [37].

Going further

EELS on negative electrodes has come a long way and was shown to be a versatile tool that can, in principle, simultaneously probe the delicate organics of the SEI as well as Li-Si alloys. Acquiring decent plasmons while keeping doses low enough is however by no means straightforward. A sustained development effort of experimental acquisition protocols is required to turn those proofs of concept into a reliable characterization technique. Even more so for the spectral analysis methods so as to extract as much chemical information as possible from the large datasets the technique yields. Both these challenges will be tackled in chapter 3.

I.5 Objectives of this thesis work

Silicon's theoretical specific capacity, operating potential and cost make it an promising candidate for future anodes, but state-of-the-art electrode lifetimes are not on par with industrial standards. The volume expansion of silicon causes active matter to be lost and destabilizes the solid electrolyte interface sufficiently to cause rapid electrode failure, even with the best mitigation strategies. The effect of these phenomena has been well assessed on the electrode scale. Yet they have not been described on the scale to which they effectively take place, at the particle level. For the SEI especially, microscopy techniques have struggled with radiation damage and delivered partial or inaccurate descriptions of the layer, whose morphology stays elusive to this day.

Developments in instrumentation and methods have opened new characterization opportunities. Exploiting the plasmon peaks of the EEL spectrum has shown great promise for mapping sensitive species and Li-Si alloys alike to unmatched resolutions. Building upon this approach pioneered over the last 10 years could yield a powerful tool to study up close the aging phenomena that have plagued Si-based anodes until now. Our aims are as follows:

- Push low-loss STEM-EELS to the best spatial resolutions our instruments can achieve at electrons doses SEI compounds and Li-Si alloys can withstand. Propose new analysis protocols to go further in chemical analysis from plasmons.
- Design and operate a custom *operando* experiment that adresses the limitations identified in previous *in situ* works on model systems. Dynamic measurements on single objects could add a second perspective of aging phenomena to the *post mortem* approach pursued in this manuscript.
- Elucidate the lithiation mechanisms of silicon nanoparticles as a function of their crystallinity, the electrode state of charge, and investigate the role of stress.
- Make plain the morphology of the SEI and challenge the mosaic model. Use focused ion beam (FIB) sample preparation to verify previous reports of electrode-scale chemical gradients
- Study the aging of those newly identified structures upon cycling in full and half-cells. By correlating STEM-EELS and electrochemical cycling data within that framework, we propose a comprehensive scenario for electrode failure.

Chapter II

Materials and methods

This chapter details the experimental aspect of this thesis's work. A first section describes what went into making the TEM samples analyzed in this manuscript, while the second succinctly describes STEM-EELS and introduces the experimental parameters of interest, without dwelling on the development of low-dose STEM-EELS which is presented in chapter 3. We notably report the capacity curves of silicon electrodes cycled in full and half cells, which are instrumental to the study reported chapter 5 and 6.

II.1 From electrodes to TEM samples

In the framework of the European BACCARA project, a collaborative effort got together the expertise on silicon-based electrode formulations from IMN Nantes [25, 26, 115, 151–154] with our characterization capabilities. Thus electrode and electrolyte formulations as well as cycling conditions are similar to those used in other reports from this group, most notably [26],[118] and [27] which contain in-depth studies of the electrochemistry of our electrodes. Both formulations and the conditions of galvanostatic cycling (rate, cut-off, limited capacity) went unchanged throughout this thesis, so as to restrict the number of variables and present a coherent aging study.

II.1.1 Electrode formulations

The following paragraphs sum up electrode preparation. Opposite our silicon electrodes we used NMC-based electrodes for full-cell cycling and a lithium disk of 1 cm^2 in half-cells. All composite electrodes were prepared by the slurry technique.

Positive electrode

The positive electrode was prepared in organic dispersion. The slurry contained 7 w% of polyvinylidenedifluoride (PVdF)-based binder, 88 w% cathode active material (NMC) and 5 w% of

the conducting agent (Super P carbon black) in the N-ethyl-2-pyrrolidone (NEP) solvent. It was coated on an aluminum current collector, adjusting the mass loads so that the specific capacity was between 0.9 and 1.1 $mAh\,cm^2$. After a drying step the resulting electrodes were calendered resulting in a reduction of the coating thickness by approximately one third. The mass loading of the NMC (calendered) electrodes is 6.49 $mg\,cm^2$ for an average theoretical capacity of 0.9 $mAh\,cm^2$.

Negative electrode

Negative electrodes were prepared from an aqueous dispersion. The slurry contained 8 w% binder material - sodiumcarboxymethylcellulose (CMC), 80 w% silicon nanoparticles and 12 w% conducting agent (Super P carbon black). We obtained a specific capacity of 0.8 $mAh\,cm^2$ based on a capacity limit of 1200 $mAh\,g$. The equivalent mass loading is therefore about 1 $mg\,cm^2$. Calendering was avoided so as to engineer sufficient porosity to accommodate for the volume change of SiNPs, yielding an electrode thickness of about 20 m.

The silicon powder

The silicon power used for this study was bought from Nanostructured & Amorphous Materials (NAM). HRTEM analysis (II.1) indicates a bimodal distribution of nanoparticle sizes, with smaller - 20 nm to 40 nm - polycrystalline SiNPs sintered in long chains and larger 70 nm to 150 nm mostly monocrystalline ones. As we will see in V.2, this insight is especially relevant to the understanding of lithiation kinetics. Discrepancies in the size and crystallinity of pristine nanoparticles will indeed result in inhomogeneities in lithiated electrodes.

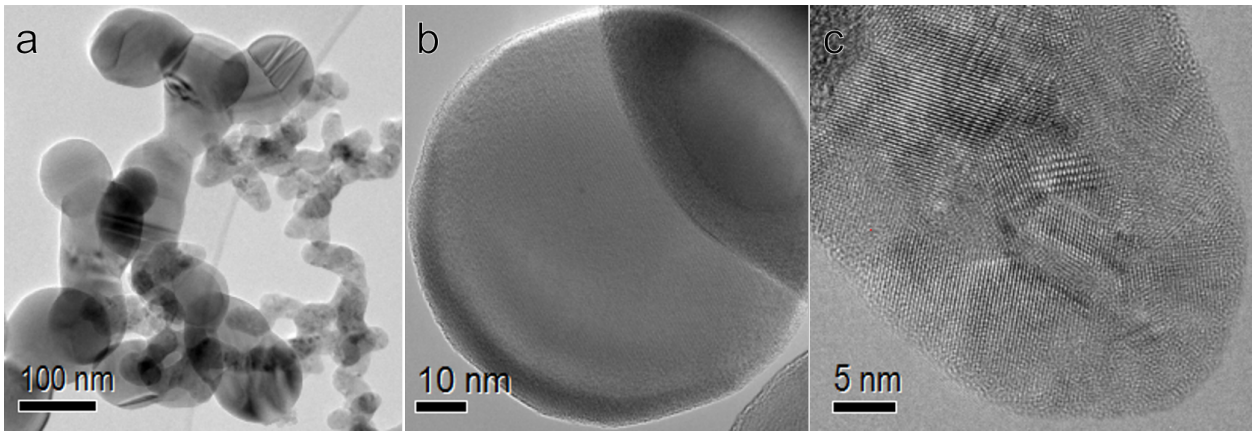

Fig. II.1: HRTEM observation of the pristine silicon powder. a) Wide view of the two SiNPs populations. b) Monocristalline particle of diameter 90 nm. c) Polycristalline particle of diameter 35 nm.

Electrolyte

All cells were cycled using 1 M $LiPF_6$ in EC:DEC carbonate electrolyte with 10 w% FEC additive. The motivation behind that additive is detailed section I.3.2.

II.1.2 Swagelok setup, cycling conditions and performances

Capacity limit and C-rate

An artificial limit was set to the capacity of our negative electrode to one third of silicon's full capacity - 1200 mAh g, in a bid to prolong cell lifetimes by mitigating volume expansion [25]. We used a single current density for galvanostatic cycling corresponding to C/2.5 or "1 Li in 2 h". If ones assumes the full capacity to correspond to the stoechiometry, this would correspond to C/7.5. Full batteries (Si vs NMC) were prepared in 3 electrodes Swagelok cells illustrated figure. II.2, using $FePO_4$/$LiFePO_4$ as a reference, taking advantage of the flat voltage plateau - 3.43 $V_{Li^+/Li}$ - of the delithiation of this material. The cell balancing factor was 1.4. For half cells, a two-electrode setup was used where a Li metal disk acted as counter and reference electrode.

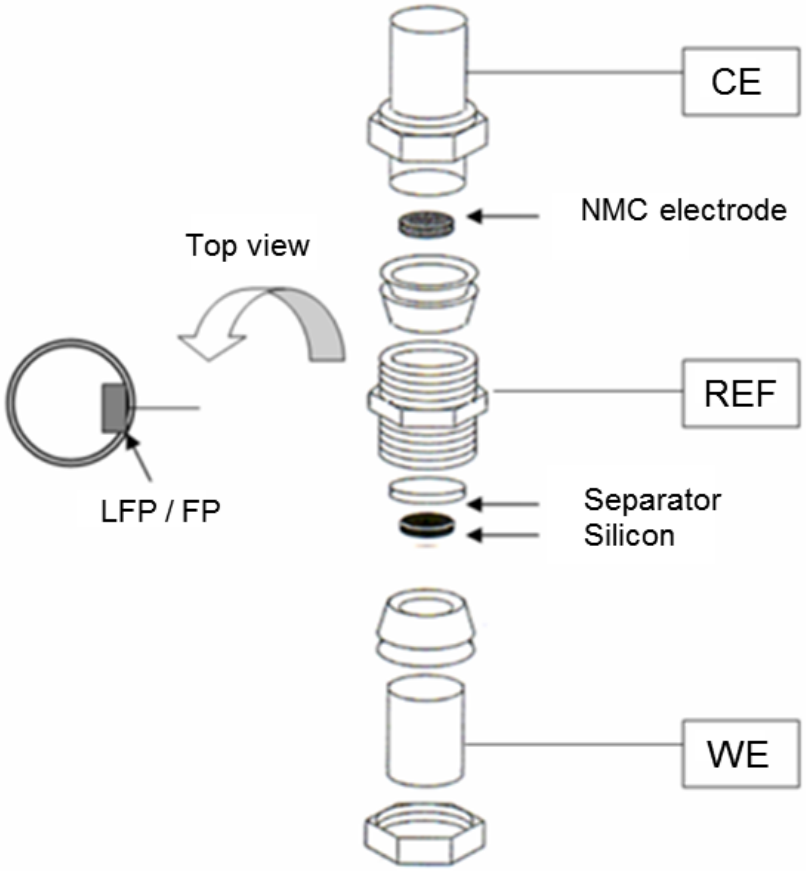

Fig. II.2: Schematic of the 3-electrode cell setup used for the galvanostatic cycling of full-cells.

Galvanostatic cycling

The potential-composition and capacity curves of 2 silicon electrodes analyzed in this manuscript, cycled in full and half-cells respectively, are reported figure II.3. A swift capacity fade is observed in full cells, with 20% of the nominal capacity lost after only 20 cycles, whereas longer electrode lifetimes are expected in half cells, to the tune of several hundreds of cycles in the present conditions [27]. This behavior could not be conclusively replicated in the present thesis however, as only two electrodes were extensively cycled in half cells. One, cycled to 100 cycles and hereby referred to as "Half cell L100" showed a early onset of its capacity decay, after 45 cycles, and an unusually high irreversible capacity compared to other cells (see fig.II.3.c). Therefore it will be considered separately in chapter 6, and we will rather regard the electrode cycled to 30 cycles as representative of half cell behavior, given its irreversible capacity is in line with that of our full cells and the results from Delpuech et al. [27].

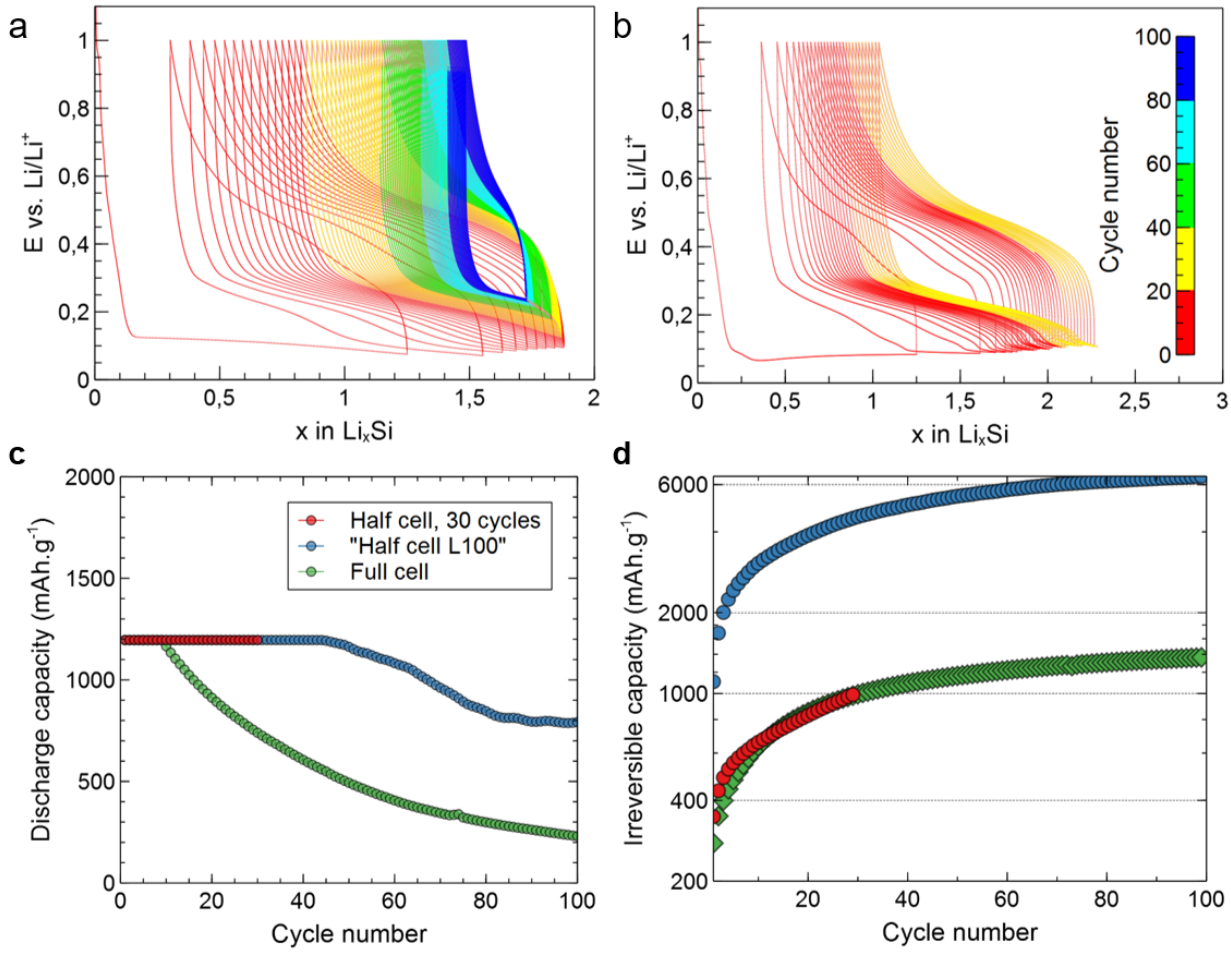

Fig. II.3: Potential-composition curves for the galvanostatic cycling of (a) full-cells, 100 cycles and (b) half-cells, 30 cycles. c) Capacity curves for the galvanostatic cycling of our silicon-based electrodes in a full-cell to 100 cycles (green) and in a half-cell to 30 cycles (red) and 100 cycles (blue). d) Irreversible capacity profiles for these same electrodes.

Importantly, we also witness an upward shift of the operating potential of silicon electrodes cycled in full cells but not in half cells, in agreement with the *slippage* phenomenon outlined by Delpuech and coworkers [27]. This is illustrated figure VI.24. Once again "Half cell L100" shows a singular profile. The drop is similar to those reported by Mazouzi et al [26] although faster and with a much earlier onset.

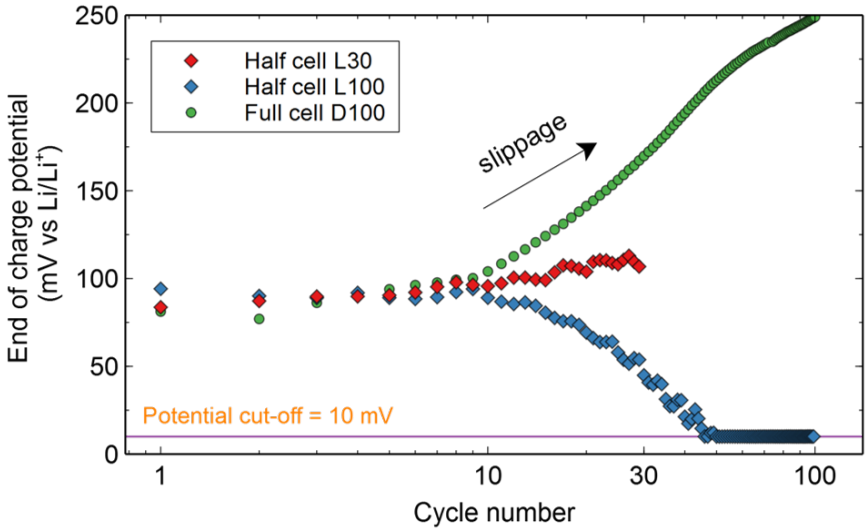

Fig. II.4: Evolution of the end-of-charge potentials of the silicon electrode in full and half-cells over 100 cycles.

II.1.3 Sample preparation and vacuum transfer

From cells to grid

Swagelok cells were dismantled in the glovebox and the silicon electrodes were allowed to dry for a minimum of 12 h. Rinsing was decided against for the scope of our study, as it has been demonstrated to have a significant influence on the SEI [125, 155]. Dry electrodes were subsequently scratched onto copper grids covered with a lacey carbon film.

Vacuum transfer apparatus and FIB lamellas

In order to protect lithiated compounds from moisture and oxygen, the grids were mounted onto a Gatan vacuum transfer holder (fig. II.5) inside the glovebox then swiftly transferred to the TEM. The same procedure was used for half-grids holding FIB-prepared electrode lamellas. In that case, electrodes were attached inside the glovebox to a dedicated self-sealing transfer chamber from ZEISS which opens under a particular vacuum threshold in the FIB chamber. Large lamellas

of dimensions 5 (depth) x 35 (width) x 25 µm (height) were cut out then thinned until porosities revealed electron transparent areas suitable for TEM observation.

Fig. II.5: Schematic representation of the head of a vacuum transfer holder for FEI microscopes. After loading a TEM grid, the head can retract and hermetically seal the sample from ambient conditions.

II.2 The STEM-EELS technique

In this thesis work, we made heavy use of the TEM handbook of Williams & Carter [156] as well as the reference publications of Egerton [157] on EELS. Numerous descriptions and diagrams in this section were directly inspired from these publications. Descriptions of the technique and their underlying physics were voluntarily kept brief, so as to avoid redundancy with the notions introduced in chapter III, as well as to keep this manuscript centered on personal work.

II.2.1 Electron energy-loss spectroscopy

Electron energy-loss spectrometry (EELS) is the analysis of the energy distribution of electrons that have come through a specimen. These electrons either have lost no energy (zero-loss peak) or have suffered inelastic collisions (electron-electron interactions where they have lost energy). The distribution of these energy-loss events tells us a about the chemistry and the electronic structure of the specimen atoms, as well as the specimen thickness. To examine the spectrum of electron energies, we invariably use a magnetic-prism spectrometer, often referred to by its modern commercial name, Gatan imaging filter (GIF), in our case. The EELS technique, compared to the somewhat simpler Energy dispersive X-ray spectroscopy (EDX), offers substantially more information than simple elemental -identification and is well suited to the detection of light elements such as Li, O, C and F, which are prevalent in negative electrodes and difficult to analyze with EDX.

Although a typical EEL spectrum can extend to energy losses of 2000 eV, we are exclusively interested in the low-loss (below 100 eV) part of the spectrum in this work. This is because, as introduced in chapter I.3, working with high-energy-losses (core-losses) involves large electron doses that are not compatible with the sensitivity of the lithiated species considered here.

Plasmon excitation

As an electron passes through a solid, the nearby atomic electrons are displaced by Coulomb repulsion, forming a region of positive potential that trails behind the electron. The response of the atomic electrons is oscillatory, resulting in regions of alternating positive and negative space charge along the electron trajectory, as illustrated figure II.7. The effect is known as a plasmon wake.

The periodicity of the wake along the electron trajectory can be expressed as:

$$\omega_p = \sqrt{\frac{n_e e^2}{\varepsilon_0 m_0}} \tag{II.1}$$

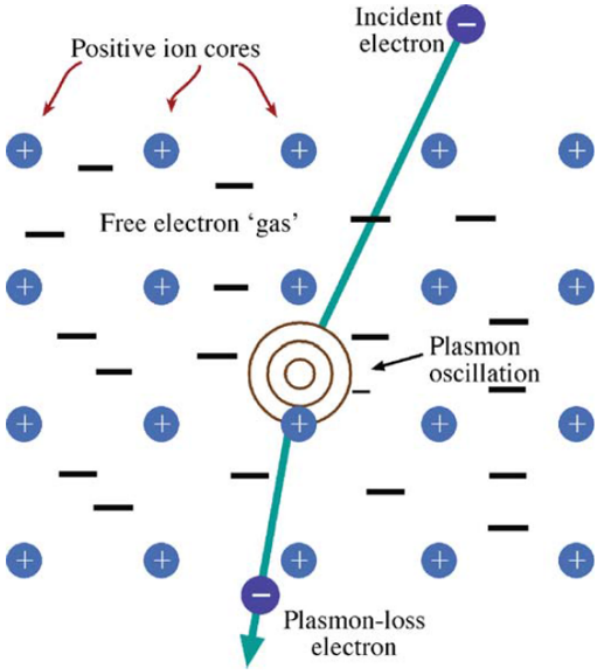

Fig. II.6: Schematic diagram of a high-energy beam electron exciting a plasmon oscillation in a free-electron gas that permeates the ion cores in a metal. Reproduced from [156].

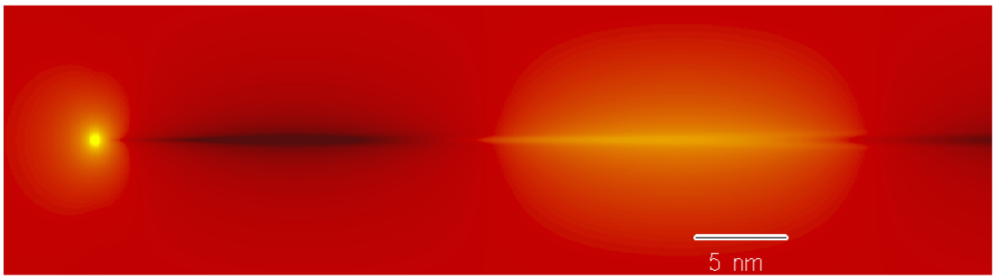

Fig. II.7: Plasmon wake of a 100 kV electron traveling through aluminium, calculated from the dielectric properties. The electron is represented by the bright dot on the left; alternate dark and bright bands represent positive and negative regions of space charge that trail behind the electron. Reproduced from [157].

Here n_e is the density of the outer-shell electrons and m_0 their mass. When an electron passes through the solid, the backward attractive force of the positive potential results in energy loss. The process can be viewed in terms of the creation of pseudo-particles named *plasmons*, each of which carries an energy often written E_p, with:

$$E_p = (h/2\pi)\omega_p \tag{II.2}$$

Inelastic scattering can then be interpreted as the creation of a plasmon at each scattering "event" of the transmitted electron, giving an energy-loss spectrum consisting of a peak at an energy loss

$E = E_p$ and at multiples of that energy when the specimen is thick enough. This last phenomenon, multiple scattering, is illustrated figure II.8.

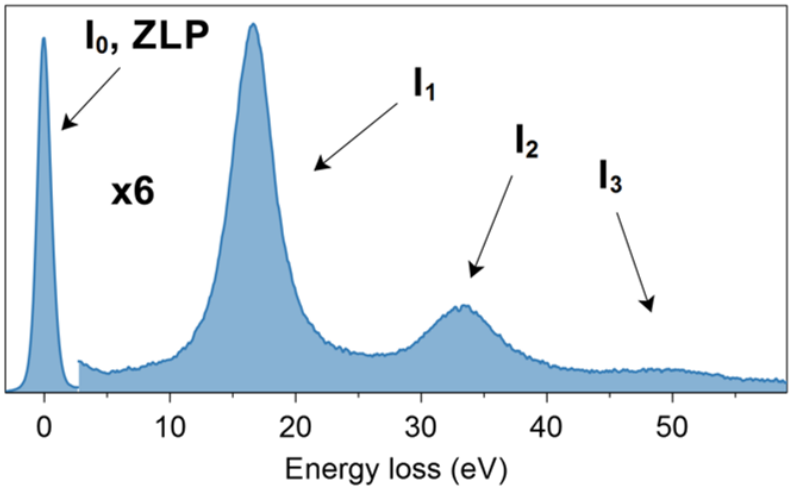

Fig. II.8: Experimental EEL spectrum of 2 stacked silicon nanoparticles. The total is 250 nm-thick. The zero-loss peak and the primary, secondary, and ternary scattering events can clearly be distinguished.

The probability P_n of n plasmon-loss events in a specimen of thickness t is given by Poisson statistics:

$$P_n = (1/n!)(t/\lambda)^n exp(-t/\lambda) \tag{II.3}$$

Where the electron mean free path (MFP) λ is the average distance between scattering events. It is heavily dependent on the specimen composition. The integrated intensity I_n of each plasmon peak is then given by:

$$I_n = (1/n!)(t/\lambda)^n I_0 \tag{II.4}$$

We see here that if I_n and I_0 (the intensity of the zero-loss-peak) can be measured from the EEL spectrum, and if λ is known, the thickness of a specimen can easily be calculated. This introduces the log-ratio method, or "t/λ" method, used in chapter III.3.

The low-loss EEL spectrum

In addition to the plasmon excitation described above, the low-loss energy part of the spectrum contains several other features, which are illustrated on an experimental LiF spectrum in figure II.9:

- Interband transitions: In a non-metal, the low-loss fine structure represents interband transitions. The spectral intensity is related to the joint density of states between conduction and valence bands.
- Surface plasmons: Even before a beam electron enters the specimen, its electric charge polarizes the entrance surface. Thus the energy-loss spectrum will include a surface-plasmon peak centered about an energy E_s given by $Es = E_p/sqrt2$
- Core-loss ionization edges: The atomic electrons that are located in inner shells (labeled K, L etc from the nucleus outwards) have binding energies that are mostly hundreds or thousands of electron volts. Their excitation by a transmitted electron gives rise to ionization edges in the energy-loss spectrum. Since core-electron binding energies differ for each element and each type of shell, the ionization edges can be used to identify which elements are present in the specimen, and their fine structure is linked to their chemical environment. In our case, the Si-L and Li-K edges can be acquired alongside plasmons since they are at sufficiently low energies (approximately 100 eV and 60 eV respectively) to be part of the low-loss spectrum.

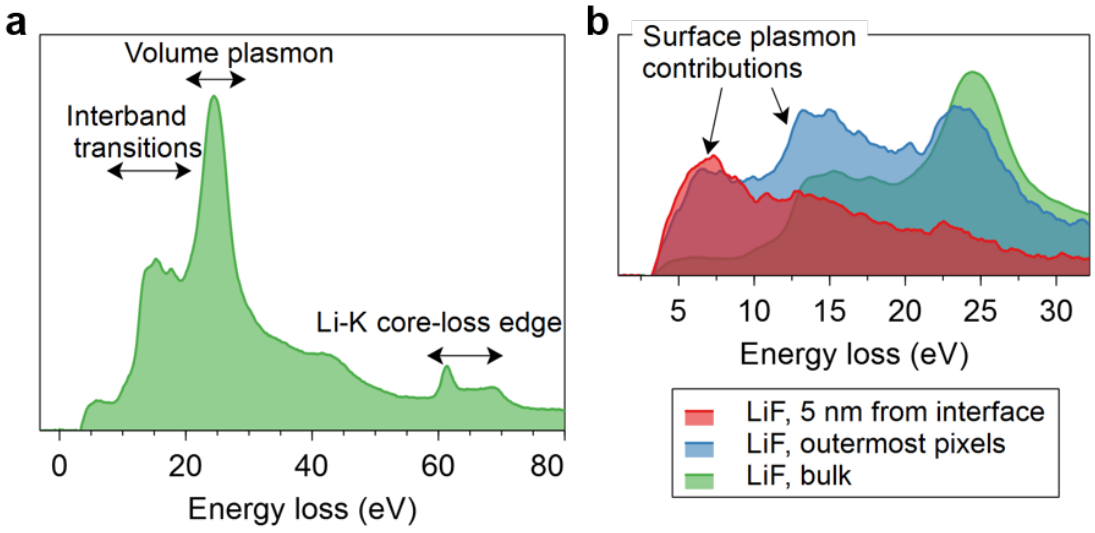

Fig. II.9: a) Illustration of the features of the low-loss EEL spectrum on an experimental EEL spectrum acquired on bulk LiF. b) Contribution from surface plasmons as we approach the interface.

Irradiation damage

As energetic electrons pass through a specimen, they will deposit energy which can destabilize fragile chemical bonds. Thus in many materials, the practical limit to spatial resolution is set by radiation damage, which occurs *via* two mechanisms:

– Radiolysis: Inelastic scattering breaks the chemical bonds of certain materials such as polymers and alkali halides. In our case, the oligomers and alkyl carbonates of the SEI,

as well as some inorganics such as Li_4SiO_4 and Li_2CO_3, are particularly susceptible to radiolysis.

– Knock-on damage: The displacement of atoms from head-on collisions with incoming primary electrons. This is the main damage mechanism for conductive specimens. σ_e, the cross-section for knock-on damage, will scale with the inverse of the displacement energy E_d, itself proportional to the atomic number Z. Thus light atoms such as Li are especially susceptible to knock-on damage.

Both of those damage mechanisms will be illustrated in the study reported chapter III.1.1. Egerton, Libera et al. recently shed light on a damage mechanism that is specific to STEM-EELS [158]. At fixed electron dose, they observed increased damage when the scanning step was reduced, as illustrated figure II.10. This suggests that damage could occur outside the area directly under the probe, possibly through the generation of *fast secondary electrons*. That phenomenon will be the focus of part III.1.2.

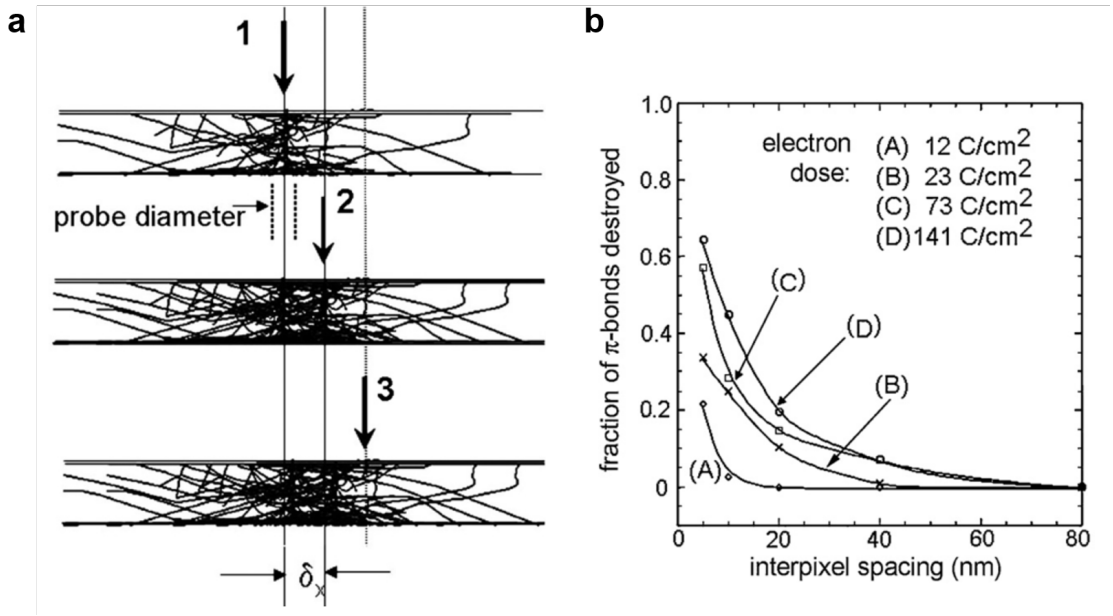

Fig. II.10: a) Monte-Carlo calculations illustrating the trajectories of fast secondary electrons and the first three positions (1–3) of a 3-nm electron probe with 5-nm interpixel spacing. b) Damage as a function of distance from the centre of a 3-nm probe, deduced from 200-kV digital linescans on 50-nm DGEBA polymer samples. Reproduced from [158].

II.2.2 Principle of STEM imaging and instrumentation

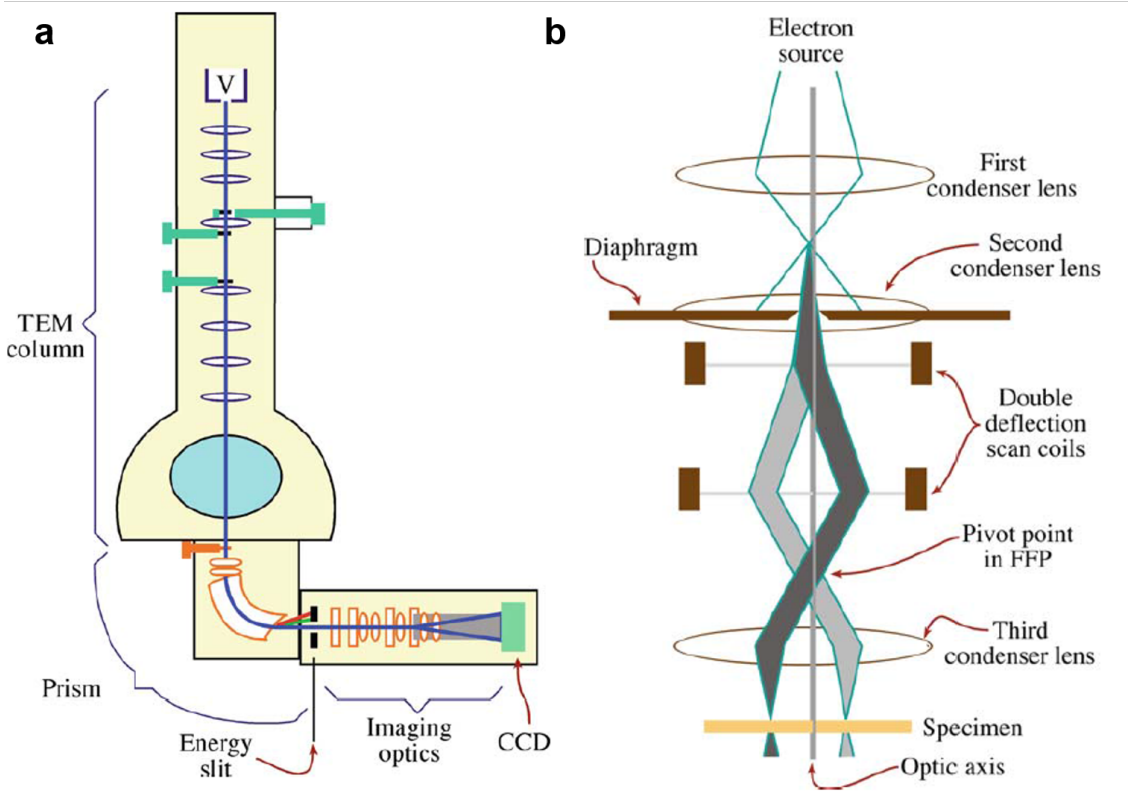

Fig. II.11: a) Schematic of the main elements of the transmission electron microscope equipped with an imaging energy filter, or GIF. b) Scanning the convergent probe for STEM image formation. The double deflection process ensures that the probe remains parallel to the optic axis as it scans across the specimen surface. Reproduced from [156].

Image formation in the scanning TEM (STEM) mode is fundamentally different from static-beam TEM image formation. Rather than being parallel, the electron beam is here convergent and called the *probe*. Simply stated, we scan the electron beam on the specimen by adjusting the scan coils (fig. II.11.b); these same coils are used to scan a computer display synchronously. An electron detector acts as the interface between the electrons coming from the specimen and the image viewed on the display screen. The whole process of creating a STEM image is much slower than TEM imaging: it's serial recording instead of parallel recording. This process is exactly the same principle as used in an SEM.

EELS acquisition and main experimental parameters

To acquire EELS with an incident STEM probe of half-convergence angle α, electrons enter the spectrometer through an aperture that, in addition to the camera length h, defines the half-collection angle β. Choosing β is critical to optimize the signal-on-noise ratio of experiments. It has to be

adjusted to as to acquire all the inelastic scattering signal. If it is too large, additional noise will needlessly deteriorate the signal. If too narrow, part of the signal will be cut-off and lost. The choice of β for our system is detailed in III.1.2.

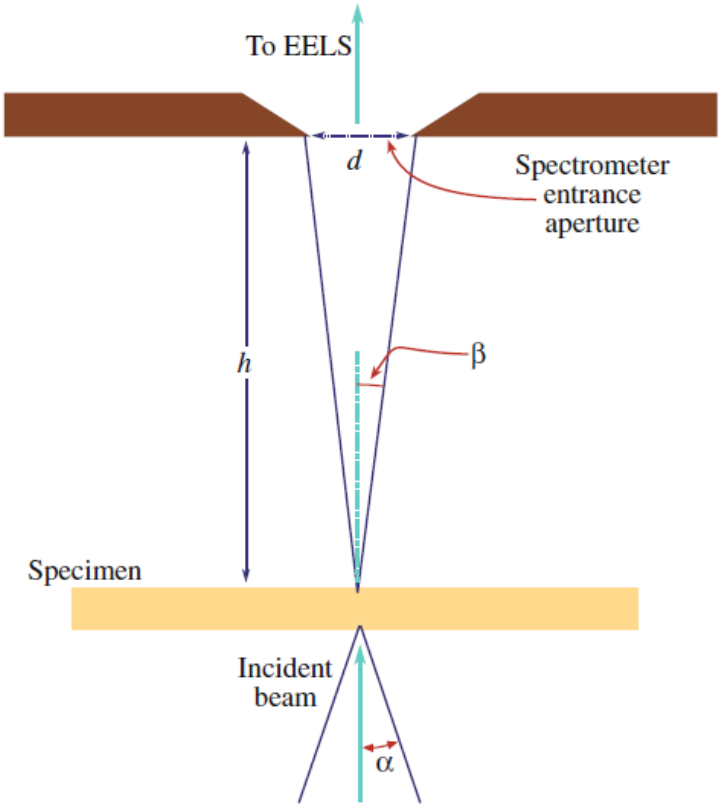

Fig. II.12: Definition of the major angles (i.e., semi-angles) in TEM. All the angles are measured from the optic axis, an imaginary line along the length of the TEM column. Reproduced from [156].

In the GIF itself, The electrons travel down a "drift tube" through the spectrometer and are deflected through by the magnetic field. Electrons that have lost energy are deflected further than those suffering zero loss. A spectrum is thus formed in the dispersion plane, consisting of a distribution of electron intensity (I) versus energy loss (E). This process is closely analogous to the dispersion of white light by a glass prism shown in the inset.

Instruments used in this work

Three TEMs were used in this thesis work: the JEOL 3010 for *in situ* experiments reported in chapter IV, the Tecnai Osiris which was used during the first half of this thesis, as well as the Titan Themis. Those last two microscopes were equipped with the spectrometers *Quantum SE* and *ER* respectively

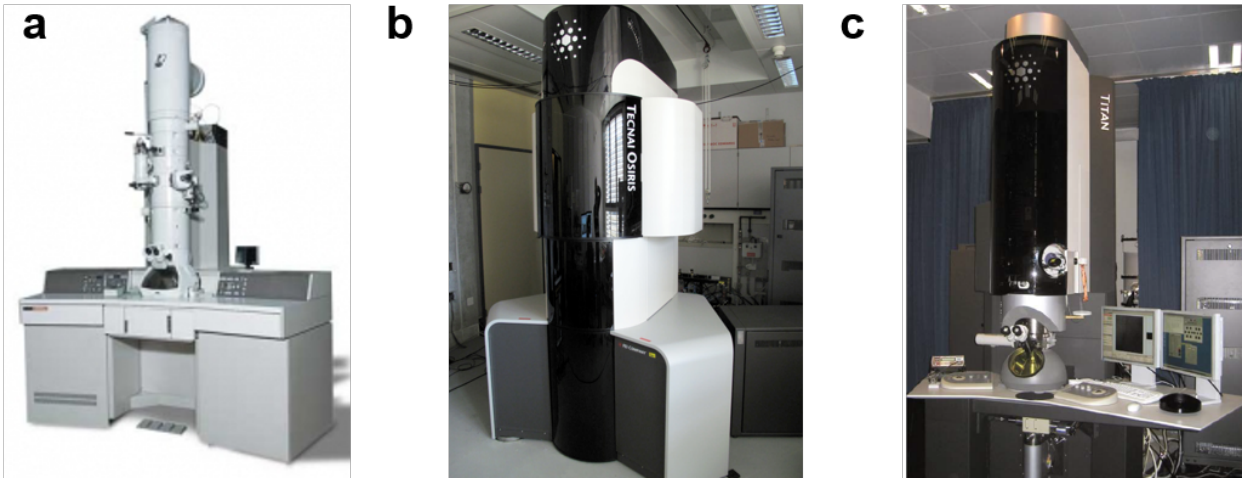

Fig. II.13: Photographs of the TEM instruments used throughout this thesis work. a) JEOL 3010. b) FEI Tecnai Osiris. c) FEI Titan Themis.

II.2.3 Spectrum imaging

Data-Cube acquisition

In spectrum-imaging mode, the precise scanning pattern of STEM imaging is leveraged to acquire an array of EEL spectra at known positions in space. The result is a 3D dataset that contains a trove of chemical information resolved at nanometer resolution. The resulting $(x, y, \Delta E)$ dataset is often referred to as a *datacube*. Each "column" of the datacube is an EEL spectrum.

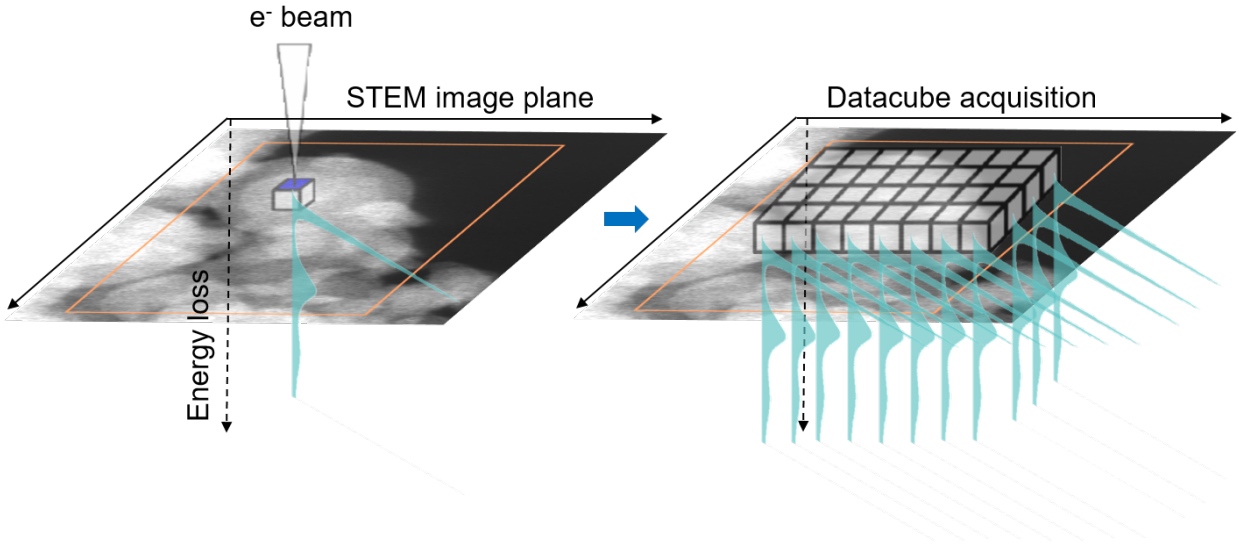

Fig. II.14: Schematic of the STEM-EELS acquisition process. A condensed STEM probe is scanned across the specimen and an EEL spectrum recorded at each specimen.

Datacubes are visualized in the form of energy *slices*, or planes, which are equivalent to filtered energy images. An example is provided figure II.15. There, 2 energy orthoslices are reported: one

at 17 eV, close to the energy of the silicon plasmon (16.6 eV), the other centered on 24 eV, around that of the plasmons of LiF and carbon black.

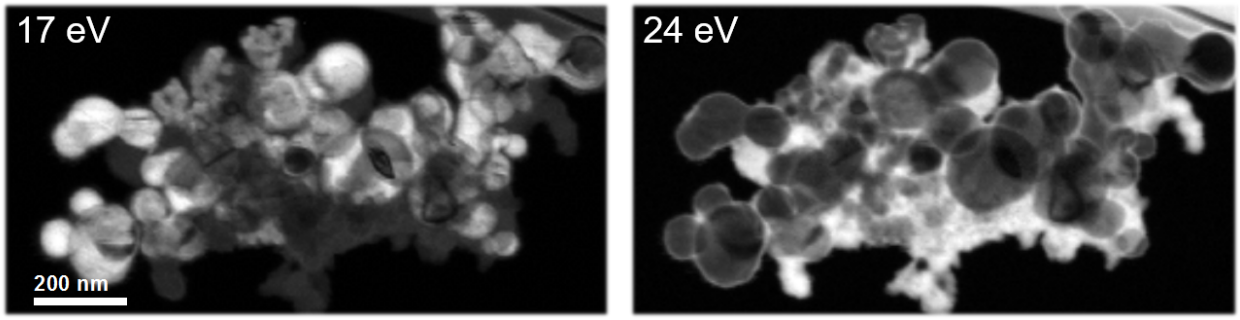

Fig. II.15: Energy slices at 17 eV and 24 eV of the same datacube.

Deconvolution and denoising routines

Prior to being exploited for phase mapping and chemical analysis, datacubes are subject to the following routine:

- Alignment: Since the GIF is never perfectly aligned, EEL spectra have to be manually aligned on the proper energy. The ZLP is aligned to 0 eV for all pixels of the datacube.
- Calibration: The chosen energy dispersion, 0.1 eV per channel in this work, can vary significantly from that reported by instrument manufacturers and from one experiment to the next. It is manually measured of the start of each session to calibrate all datacubes. This is critical, as a 3% error results, for example, in a 0.5 eV offset for the silicon plasmon.
- Deconvolution: a correction of the effect of multiple scattering, as demonstrated figure II.16.
- PCA decomposition: Principal components analysis is performed as a denoising step. The algorithm used for the decomposition, and the number of components kept in the final reconstruction are critical to the robustness of the method. An example is provided figure II.17.

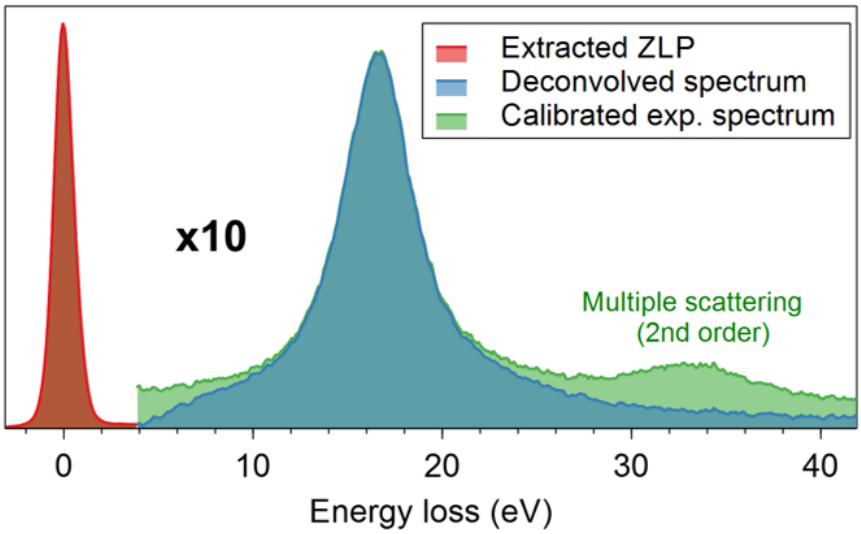

Fig. II.16: Experimental EEL spectrum (green), extracted zero-loss peak by the logarithm-tail model (red) and deconvolved spectrum by the fourier-log method (blue).

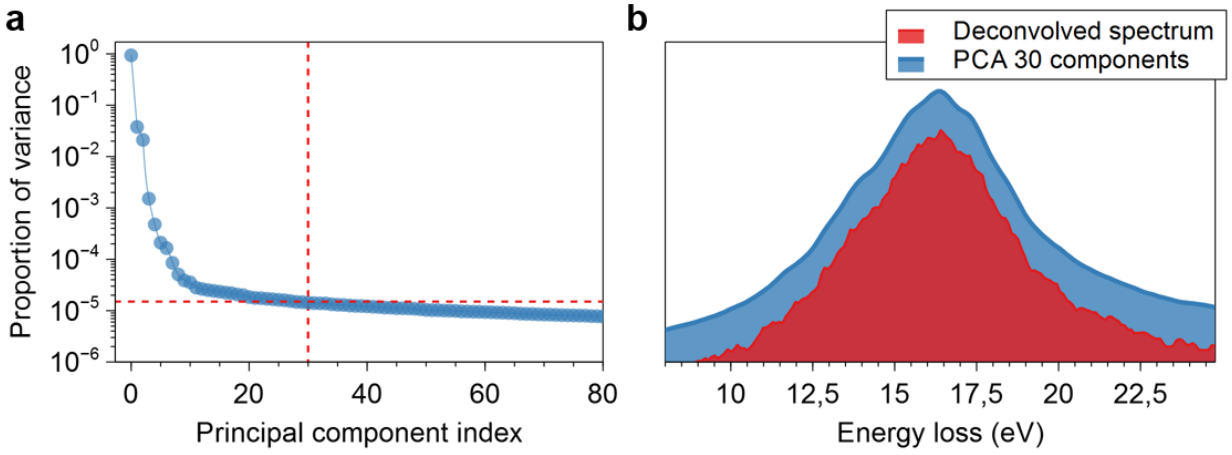

Fig. II.17: a) Scree plot of the PCA decomposition performed with the NMF algorithm of the Hyperspy Python package. b) Example of denoising by selecting 30 PCA components.

Chapter III

Low-dose STEM-EELS development

As introduced in section I.4.2, using the low-loss part of the EEL spectrum opens up a new field of possibilities to study nano-sized negative electrode materials. Given the sensitivity of the compounds of interest, which is the first item of this chapter, we will see that it is of utmost importance to develop this characterization potential to its fullest so as to offer a robust characterization of the heterogeneous system at hand.

To this effect, we will detail in this chapter the progress made in further developing te low-loss STEM-EELS methodology, from optimizing the acquisition protocol to ensure observations reflect an undamaged sample, to refining analysis routines to extract the most chemical data from limited signals [159]. The superposition of the signals of Li-Si alloys and of all SEI species makes the interpretation of experimental spectra arduous, but performing decomposition with the MLLS algorithm can reveal the morphology of individual phases, provided the proper input is chosen. Novel quantification efforts are then detailed, with the aim of calculating the thickness of each phase and combining multiple measurements into statistically relevant results at the electrode scale. At the particle level, chemical gradients can further be identified by fitting spectra with the Drude model to measure the plasmon energy E_p, for which interpretations are proposed based on empirical and theoretical models. Finally, we show that MLLS and Drude model fitting can be used jointly to make low-loss STEM-EELS an even more efficient and versatile characterization technique for sensitive and heterogeneous systems.

III.1 A gentle acquisition protocol

SEI compounds and Li-Si alloys alike are susceptible to irradiation damage. This sensitivity warrants an extensive effort to optimize our acquisition protocol, lest irradiation damage invalidates our study. In the organic species of the SEI especially, characteristic doses (defined in part II.3) have been speculated to be as low as $D_e = 100\,e\,\text{Å}^{-2}$ [160]. Tuning experimental parameters to stay within that order of magnitude appears straightforward, but acquiring low-loss spectra of acceptable signal for incident doses as low is not, and that does not only mean optimizing detection. One has to mind irradiation at all steps of the acquisition process, including camera readout. Furthermore, a thorough understanding of radiation damage mechanisms is necessary. The spatial distribution of irradiation damage needs to be grasped in full to design successful spectrum imaging experiments on such sensitive materials, as the same electron dose can result in either mild or critical specimen damage depending on the accelerating voltage, probe shape and spectrum image step size. The impact of all those factors is studied systematically and allow us to confidently chose the following experimental parameters:

Table III.1: Summary of experimental STEM-EELS parameters chosen for the study reported in this manuscript.

Parameter	Symbol	Value
Accelerating voltage	E_0	200 kV
Convergence half-angle	α	3 mrad
Collection half-angle	β	$\approx$ 10 mrad
Probe current	I	4 pA to 6 pA
Dwell time		10 ms to 15 ms
Readout time		3 ms to 5 ms
Energy dispersion		0.1eV/channel
Step size		5 nm
Electron dose	D	$\approx 130\,e\,\text{Å}^{-2}$ to $300\,e\,\text{Å}^{-2}$

III.1.1 Irradiation of Li-Si alloys and SEI compounds

Both Li_xSi alloys and the SEI are electron-sensitive, albeit to different extents. Examples of irradiation damage were obtained experimentally. They reveal telltales of degradation we can look for after STEM-EELS experiments on electrodes (fig. III.3) and help us define dose thresholds for our acquisitions.

Knocking Li out of Li_xSi alloys

At the electron doses relevant to the study of the SEI - $D < 300\,e\,\text{Å}^{-2}$, Li-Si alloys are stable and will not be our primary concern, although they remain very sensitive to irradiation by EELS standards and warrant investigation. Since Li_xSi alloys exhibit quasi-metallic behavior [161], damage occurs through the knock-on (or sputtering) effect [140] which represents the elastic scattering of incident electrons (i.e. electron-nucleus collisions). Knocked Li atoms will gather on the surfaces of nanoparticles to form Li clusters (fig. III.1.a-b) that are easily detected thanks to the low plasmon peak energy of metallic lithium at 7.5 eV. Furthermore we notice an additional phenomenon in spectrum imaging experiments. In the case of dose-heavy observations of lithium-silicon alloys (fig. III.1.c), lithium content appears to follow a gradient along the scanning pattern (top to bottom), with the last pixel reflecting an exceedingly damaged specimen more than 500 nm away from the first pixel acquisition. Since elastic scattering i.e. sputtering damage is fairly localized in space - within a ≈ 3.5 nm diameter around the probe position if we account for both elastic scattering delocalization in Li_xSi [160] and beam spread - this sort of long-range cumulative damage is puzzling.

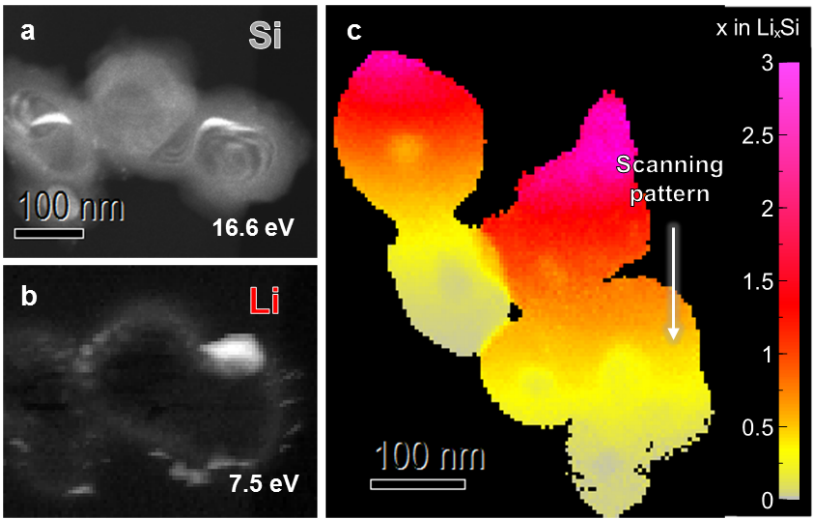

Fig. III.1: Telltales of irradiation damage in Li_xSi. a-b) Filtered energy maps from a spectrum image taken with $D \approx 500\,e\,\text{Å}^{-2}$ showing metallic lithium deposition at the surface of SiNPs. c) Top-down gradient in lithium content map showing long-range irradiation damage.

To quantify the severity of sputtering damage in Li-Si alloys and study this "cumulative" damage, consecutive measurements were performed on a lithiated nanoparticle among a larger two-particle aggregate (fig. III.2). We were able to follow continuous lithium depletion in alloys as electron dose accumulates all the way from Li_2Si to a floor value of $Li_{0.4}Si$. This last value was systematically observed in other observations of extensively irradiated lithiated nanoparticles. No degradation seems to occur below a threshold of $200\,e\,\text{Å}^{-2}$. The non-linear relation bears good resemblance with reports from D. Robert's [37] and J. Danet's [122] PhDs and hints at a higher electron sensitivity for

Li-rich alloys, which is not surprising considering the Li-Li bond is weaker than Li-Si [162]. After applying 1200 $e\,\text{Å}^{-2}$ to the nanoparticle of interest, spectrum imaging was once again performed on both particles (fig. III.2.c) and showed that the area that wasn't included in the consecutive measurements had undergone similar depletion, despite having been spared from sputtering damage. This could indicate that the SiNP aggregate is homogeneously lithiated at any given time. Baring that a previously unknown long-range irradiation phenomena is at play, a possible explanation is that Li will diffuse to lithium-poor areas as they deplete to maintain thermodynamical equilibrium, with the incoming electron flux providing the driving force for the electrochemical reaction. Considering that the low end of the diffusion coefficients reported for Li^+ in Li_xSi is about 10 nm^2/s [163–165], the timescales necessary for such transport are well below the acquisition times of spectrum images.

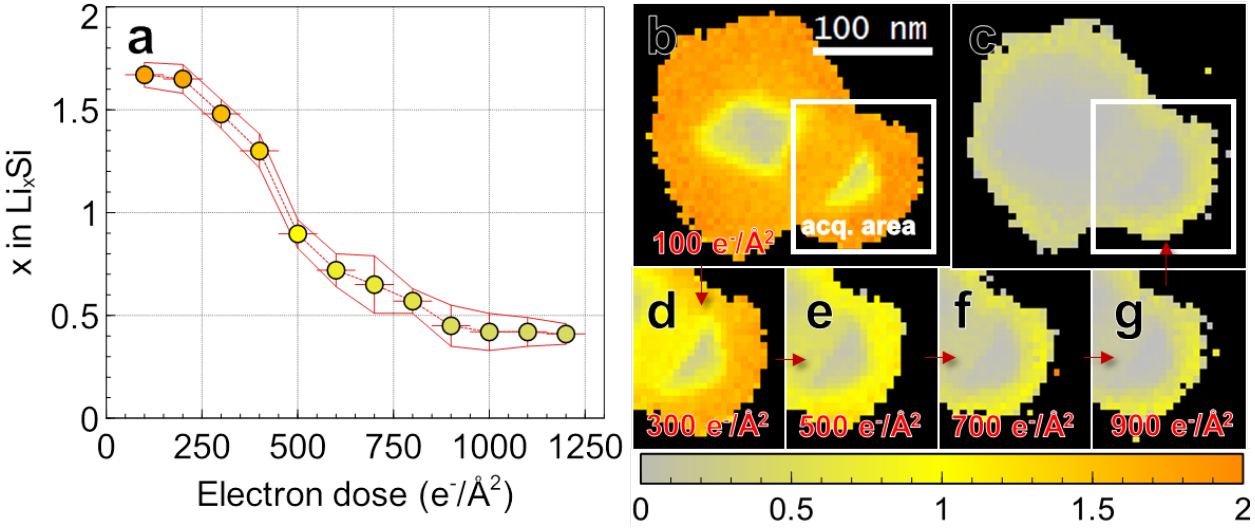

Fig. III.2: Irradiation damage on a lithiated silicon nanoparticle. Consecutive spectrum image acquisitions were performed in the area highlighted. a) Evolution of the lithium content against electron dose. b) Prior observation of the 2-SiNPs cluster. c) Observation of the cluster after measurements in the highlighted area. Lithium depletion occurs to the same extent in areas that are not irradiated. d-g) Progressive lithium depletion under the electron beam.

Radiolysis of SEI compounds

In insulating compounds such as most of the SEI, the most prevalent source of damage is radiolysis - or ionization damage - which causes bond breaking [157] and whose processes are further detailed in the next section. This chemical damage causes the loss of the characteristic spectral features necessary to identify a compound. To study the impact of radiolysis on the SEI and determine threshold doses experimentally, we performed successive reference measurements on Li_2CO_3 and LiF. For the former, the shouldering at 10 and 14 eV due to the interband transitions as well as the sharp shape of the plasmon disappear completely between 500 $e\,\text{Å}^{-2}$ to 1000 $e\,\text{Å}^{-2}$ (fig. III.3.a), in line with previous reports of a characteristic dose of $D_e = 750\,e\,\text{Å}^{-2}$ [129]. On the

other hand, LiF is stable for those electron doses, as expected [166], and measurements showed no modification of the low-loss spectrum for D below 2000 $e\,\text{Å}^{-2}$ (fig. III.3.b). Interestingly, these same electron doses correspond to heavy specimen damage in spectrum images (fig. III.3.c-e). After applying 300 $e\,\text{Å}^{-2}$ the fine structure of single spectra are preserved, including the Li-K edge fine structure in Li_2CO_3, whereas for that same value specimen thinning as well as metallic Li deposition appears in spectrum imaging mode with a 5 nm step. This effect needs to be fully understood as spectrum-imaging is the one mode relevant to our work.

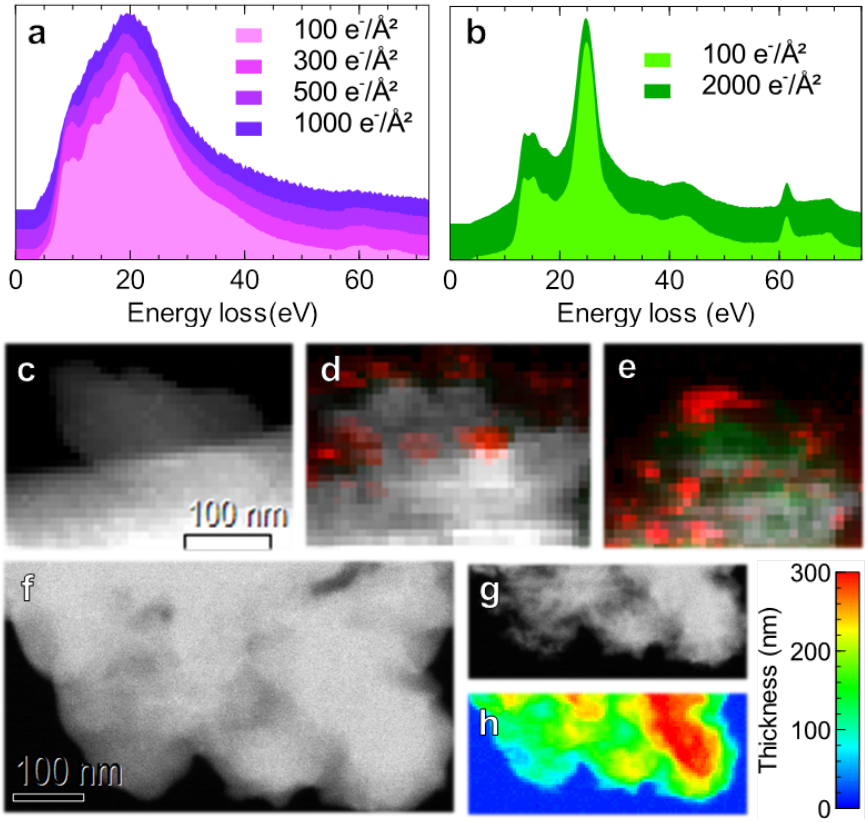

Fig. III.3: Radiolysis damage as a function of applied electron dose on Li_2CO_3. a) Consecutive measurements showing the loss of characteristic spectral features as dose accumulates on Li_2CO_3. Several spectra were summed to improve the signal-on-noise ratio. b) No significant irradiation damage is observed on LiF. c-e) Thickness maps from consecutive spectrum-image acquisitions 200 $e\,\text{Å}^{-2}$ apart on Li_2CO_3 (white) showing specimen thinning and Li (red) as well as Li_2O (green) deposition. f-g) STEM observations before and after a 200 $e\,\text{Å}^{-2}$ spectrum image acquisition on a thick ($\approx$ 50 nm) SEI layer.

Numerous other compounds compose the SEI, as described in part I.2. Most of those are alkyl-carbonates and oligomers, which we'll refer to as the "organics" of the SEI. In these organics, such as LEDC and poly(FEC), the energy deposited by inelastic scattering isn't quenched by as many valence electrons as is the case in inorganics Li_2CO_3 and LiF. As a result this energy is even more likely to cause bond breaking and organics are among the most sensitive species to beam damage [167]. Since they could not be obtained in pure form for reference experiments, their behavior under irradiation was deduced from analysis on cycled electrodes. Large SEI layers

($\approx$ 50 nm to 100 nm) present on particles that have seen extensive cycling are an ideal case study (fig. III.3.f-g). Those showed significant specimen thinning for doses as low as 200 $e\,\text{Å}^{-2}$ in spectrum image acquisitions, although it does not significantly impact EELS data (fig. III.3.h).

III.1.2 Delocalization of damage and spectrum imaging

The discrepancy between the beam damage in single-spectrum and spectrum-imaging mode suggests that radiation damage is not limited to the area under the electron probe [168]. In radiolysis, two phenomena are in fact at play to transfer energy to the specimen. The first is the inelastic interaction itself, and the second is the creation of secondary electrons (SE). Both are delocalized and will affect an area well beyond the diameter of the electron probe. SEs are created nearly perpendicular to the optical axis and will travel across the specimen to cause further damage. In STEM-EELS experiments, this means that each spectrum acquisition could impact the next few. This overlapping has disastrous consequences on our material ability to sustain irradiation. Consequently, understanding how these two damage components affect the specimen is critical to determine the best choice of probe size and step size for our spectrum imaging experiments. For this, we gathered theoretical approaches from the literature for both damaging processes.

Modeling the spatial distribution of radiolysis

Our model makes use of equations developed by Egerton [169] and Wu et al. [170] who studied SE energy deposition for electron lithography applications. The aim is to simulate the energy deposited around the probe for different probe shapes to help us determine which is best to limit radiolysis damage. From Egerton, we have the deposited energy per unit volume per secondary electron as function of a distance r from the probe in a sample of thickness t:

$$\frac{dQ_{se,se}}{dV}(r) = \frac{\langle E\rangle_{se}}{2\pi t}\frac{1.41\,\text{nm}}{r^3} \tag{III.1}$$

Where $\langle E\rangle_{se}$ is the mean energy of a traveling SE. Since a good approximation of bond energy the compounds of interest is 5 eV, we consider SEs that yield at least 5 eV per interaction. According to Egerton this corresponds to SEs whose starting energy is above 10 eV, resulting in $\langle E\rangle_{se} = 30\,\text{eV}$ [169]. Now to get the damage deposited per primary electron (PE) we use Wu's approach to calculate the N_{se}/N_{pe} ratio with the SE-production cross-section σ_{se} and t, canceling in passing the thickness dependence.

$$\frac{dQ_{se,pe}}{dV}(r) = \frac{N_{se}}{N_{pe}}\frac{dQ_{se,se}}{dV}(r) = \frac{\sigma_{se}n_e 1.41\,\text{nm}\times 30\,\text{eV}}{2\pi}\frac{1}{r^3} \tag{III.2}$$

With n_e the electron density in a chosen material which we'll consider as Li_2CO_3. Finally we have the spatial distribution of energy deposited by secondary electrons for each PE:

$$\frac{dQ_{se,pe}}{dV}(r) = \frac{2.77 \times 10^{-3}}{r^3} \quad (\text{eV.nm}^{-3}) \tag{III.3}$$

To reach a full assessment of radiolysis, energy deposition by inelastic scattering also needs to be described mathematically. For this, we make use of Egerton's description from a recent published work [171]. The spatial dependence of the energy deposited is obtained by integrating the product of the inelastic scattering point spread function $PSF(E,r)$ and the energy lost by each electron during a scattering event E, over the low-loss energy range.

$$PSF(E,r) = (\pi^2 a_0 m_0 v^2)^{-1} \frac{exp(-2r/b_{max})}{(r^2 + b_{min}^2)} Im\left[\frac{1}{\varepsilon(E)}\right] EdE \tag{III.4}$$

$$\frac{dQ_{scattering}}{dV}(r) = \int_{5\,\text{eV}}^{100\,\text{eV}} PSF(E,r)\, EdE \tag{III.5}$$

Where b_{min} and b_{max} are functions of the characteristic and cutoff angles θ_e and θ_c for which full expressions can be found in [171]. The spatial distribution of both contributions to radiolysis can now be compared by plotting equations III.3 as well as III.5 and results are reported fig. III.4.a. Moreover these formulas can be used to predict the effective energy deposition in experiments. To do so accurately one has to consider that primary electrons are not concentrated in a single point but are distributed unevenly over the width of the probe. For this reason, we took a CCD image of our probe - $\alpha = 3\,\text{mrad}, d = 1\,\text{nm}$ and used this profile to simulate the distribution of the total energy deposited in our experiments. Eq. III.5 was integrated on a volume $2\pi trdr$ to obtain the energy deposition at a distance r of the center of the probe. Results are plotted fig. III.4.b.

$$Q_{scattering}(R) = \int_{probe} \int_{R-\varepsilon}^{R+\varepsilon} 2\pi trdr \int_{5\,\text{eV}}^{100\,\text{eV}} PSF(E,r)\, EdE \tag{III.6}$$

At a glance, damage from secondary electrons appears to dominate both at long range - over 20 nm, although this accounts for very little of total damage - and in the immediate vicinity of primary electron incidence, below 2 Å (fig. III.4.a). Secondary electrons damage accounts for 77% of the total energy deposited, but most of it is right at the center of the area exposed to the electron probe. This is reflected in the quantities $r_{0.5}$ and $r_{0.9}$ - 50% and 90% of damage deposited within those radii - which are below 1 nm. Range values are summarized table III.2. The energy deposited by inelastic scattering however is distributed along a wider area, as reflected in the $r_{0.9}$ values that exceed 3 nm.

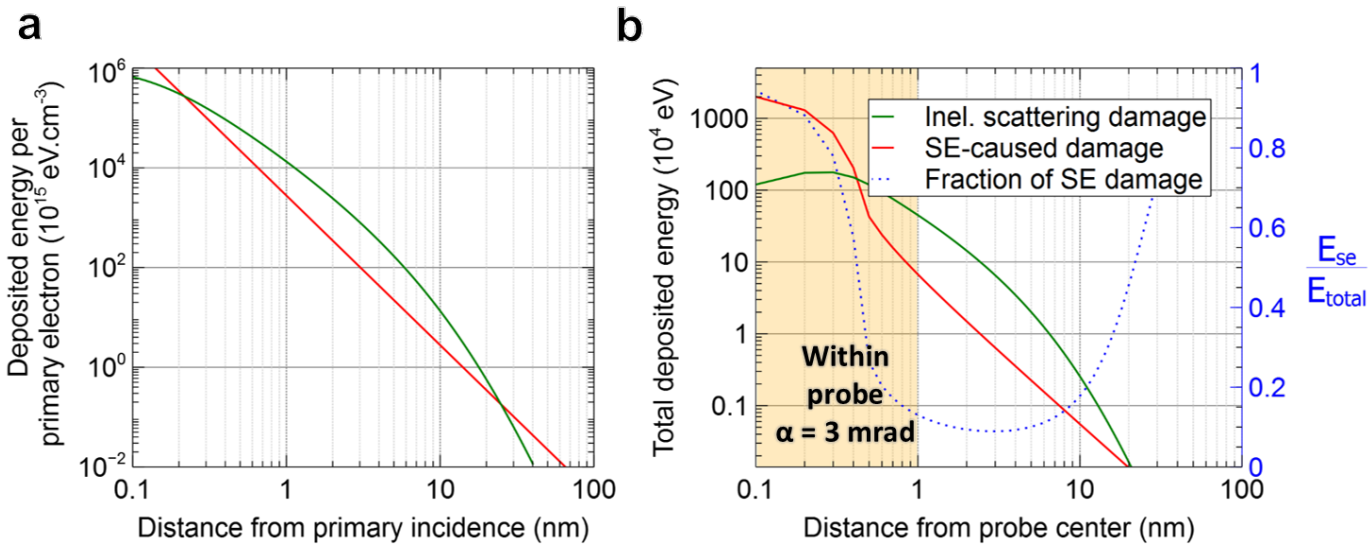

Fig. III.4: Comparison of the spatial distributions and relative weight of the two contributions to radiolysis. a) Deposited energy by unit volume per incident primary electron. b) Total energy deposited in experiments with a probe $\alpha = 3\,\mathrm{mrad}$ at a dose of $100\,e\,\text{Å}^{-2}$, obtained by integrating III.4 over a volume $2\pi trdr$ (red and green lines), and proportion of the damage caused by secondary electrons (blue line).

Table III.2: Comparison of the two contributions to radiolysis

Contribution	Fraction of total damage	$r_{0.5}$ (nm)	$r_{0.9}$ (nm)
Inel. scattering	23%	0.7	2.7
SE-caused damage	77%	0.2	0.4
Total	100%	0.3	0.8

Keeping in mind that the inelastic interaction is the very origin of the EEL signal, we see that signal and total radiolysis damage will only overlap but not superpose. Most of the damage is caused by secondary electrons and will be kept in a narrow area under the probe while the signal will come from larger, less damaged surroundings.

Probe diameter and signal-on-damage ratios

Therefore by tuning the probe size wisely, one can confine secondary electron damage. Having a very small, point-like probe sounds advantageous as the signal-emitting area will be comparatively larger than the very damaged area under the probe. This is rather counter-intuitive, as one might have favored spreading the dose over a larger probe to allow more of the specimen to quench as many electrons. But this strategy is invalidated by experimental evidence which also suggests that decreasing the probe diameter d is beneficial, as the characteristic dose D_e reportedly scales with $1/d^2$ [167]. Taking advantage of the delocalization of inelastic scattering might be the better tactic to limit the impact of irradiation on the EELS data we collect.

To verify these claims and determine the most appropriate probe size for our experiments, we have set out to simulate how signal and damage overlap for different probes and calculate which one yields the best signal-on-damage ratio (SND). A higher SND will reflect a "better use" of the dose applied. The signal profile shows a very similar radial dependence to the energy deposited from inelastic scattering since it will also result from integrating the inelastic scattering point-spread function, only we'll solely consider bounds 10 eV to 30 eV.

$$S_{EELS}(R) = \int_{R-\varepsilon}^{R+\varepsilon} 2\pi t r dr \int_{10eV}^{30eV} PSF(E,r)dE \tag{III.7}$$

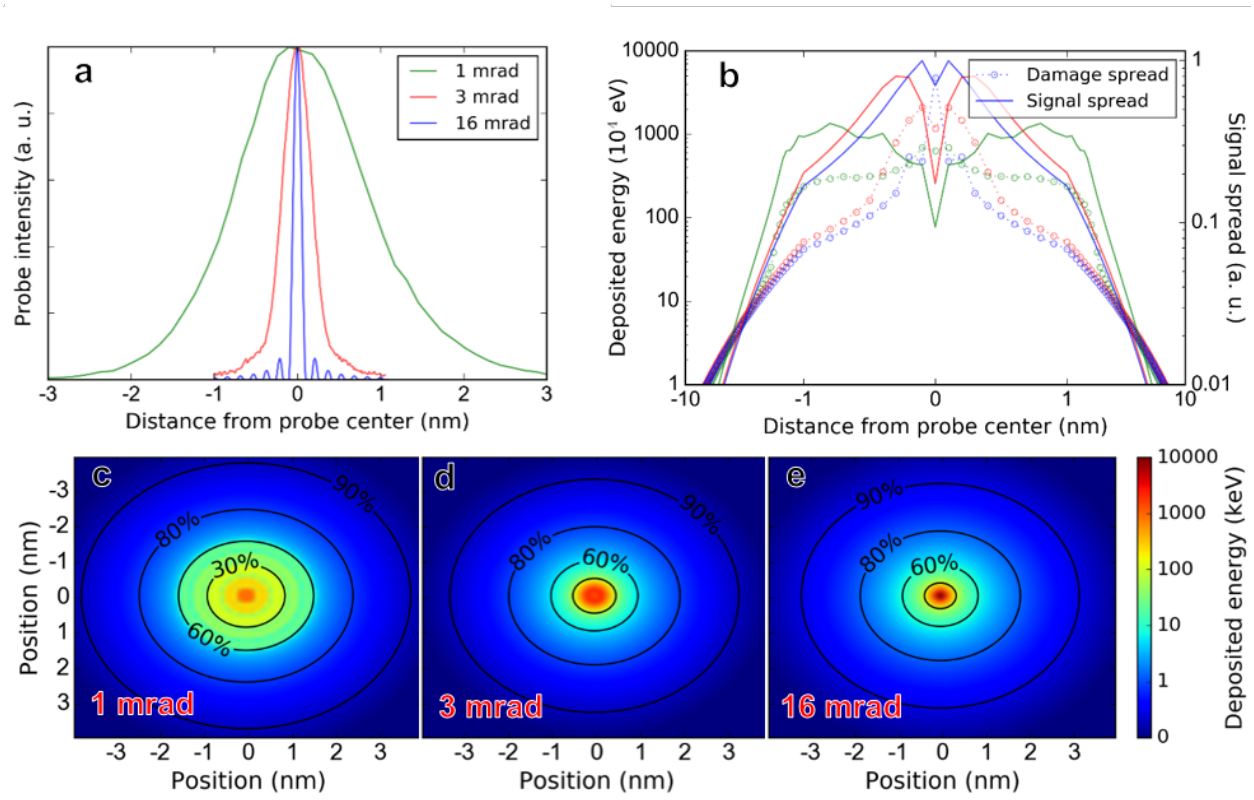

Fig. III.5: Damage and signal profiles for 3 different electron probes. a.) Intensity profiles. For $\alpha = 16$ mrad the electron distribution was approximated by the Airy function [172]. b) 1D damage profiles. c-e) 2D damage profiles, signal levels are drawn in black contour lines.

The results of eq. III.7 were overlaid onto damage profiles calculated for probes of convergence half-angles $\alpha = 1$, 3 and 16 mrad (fig. III.5). In the 1D representation, damage and signal profiles show the same trend for $\alpha = 1$ mrad whereas, as expected, they are shifted from one another for smaller probes. This can be visualized more easily in the 2D profiles fig. III.5c-e), where black contour lines represent levels for the EEL signal - i.e. 60% of signal originates from within the "60%" circle. The smaller the probe, the larger the relatively undamaged area that gives out signal. We can evaluate that quality by calculating the average SND across the signal (eq. III.7). Results are reported table III.4.

Table III.3: Range of signal and damage in single-spectrum EELS measurements for different probes

α	d	Signal range (nm)		Damage range (nm)		SND
		$r_{0.5}$	$r_{0.9}$	$r_{0.5}$	$r_{0.9}$	
1 mrad	22 Å	1.3	3.7	0.7	1.5	14.5
3 mrad	10.4 Å	0.7	2.7	0.2	0.7	17.5
16 mrad	2 Å	0.6	3.1	0.1	0.6	20.4

$$\langle SND \rangle_{signal} = \frac{\int_0^{r_{0.99}} S_{EELS}(R) \times SND(R) dR}{\int_0^{r_{0.99}} S_{EELS}(R) dR} \tag{III.8}$$

According to those calculations, going from $\alpha = 1$ mrad to $\alpha = 16$ mrad could not only improve the SND by a factor close to 30% in the case of single-spectrum acquisitions, but also decrease the absolute range of radiolysis. This is critical in the case of spectrum images, where damage could extend to neighboring pixels. Any spectrum would then be pre-damaged before EELS acquisition and a larger probe could once again be detrimental. To study the extent of this effect, we have simulated the energy deposited on the next pixel half-way through a spectrum image acquisition to evaluate how much are areas damaged prior to acquisition. Damage levels were drawn in white contours in units of a critical dose D_e, which we attempt to define from the total number of chemical bonds in a volume $A \times t$ where A is the area of an element of the mesh used in the simulation. According to Wu et al. [170] the number of bonds broken by a number of electrons N_e carrying an average energy $\langle E \rangle$ can be calculated from an exposure cross-section σ_{exp} which depends on the bond energy E_{bond}, and the bond density n_{bond}.

$$\%D_e = \frac{\text{Bonds broken by the energy deposited}}{(1-\frac{1}{e})\text{Total number of bonds}} = \frac{N_e \sigma_{exp}(E_{bond} = 5\,\text{eV}) n_{bond} t}{(1-\frac{1}{e}) n_{bond} A t} \tag{III.9}$$

$$\%D_e = \frac{E_{dep}}{\langle E \rangle} \frac{\sigma_{exp}(5\,\text{eV})}{(1-\frac{1}{e})A} \tag{III.10}$$

Results of the spectrum imaging simulation are reported fig. III.6. The total dose in each spectrum image was normalized for its step-size so that they can be compared at a constant areal dose. When the step size exceeds the range of radiolysis damage, such as in the 8 nm step case, the choice of the probe is no more important than in the single-spectrum case, as damage in each pixel prior to acquisition will be negligible. As step size decreases to intermediate values such as 5 nm, next signal and prior damage start to overlap, and to greater extent for larger probes. When the step size

reaches 3 nm especially, a significant part of the signal is bound to come from extensively damaged areas ($D > 2D_e$). This shows that regardless of the probe and the dose chosen the absolute range of radiolysis damage puts a cap on the step size - i.e. resolution - we can use without damaging nearby pixels, to around ≈ 4 nm, as demonstrated experimentally (fig. III.7). Hence we have chosen 5 nm to study our electrodes as a compromise between spatial resolution and damage mitigation. In all cases a small probe is desirable to limit the signal on damage overlap and achieve higher SND values, which are reported table III.4.

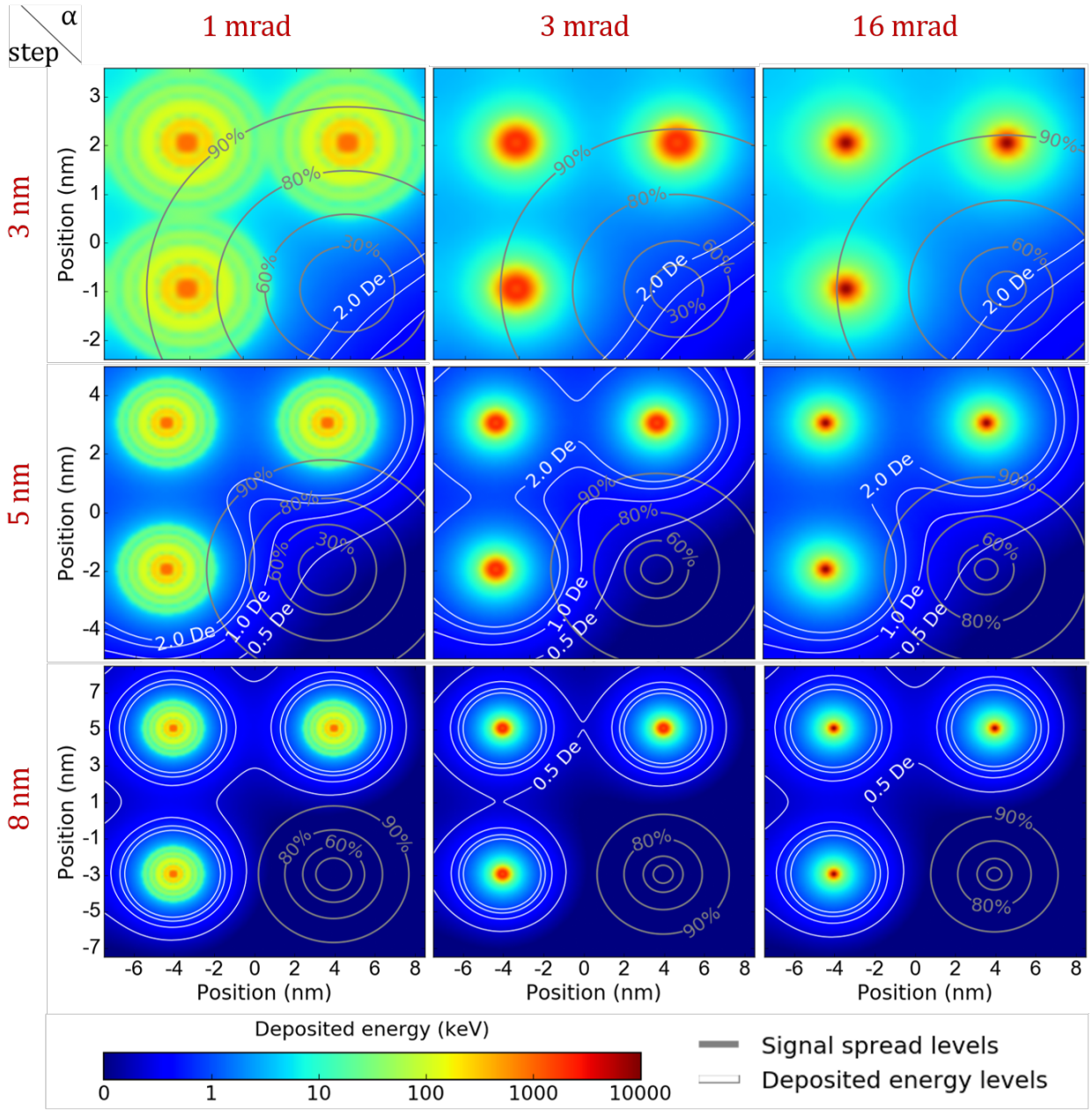

Fig. III.6: Simulation of the distribution of the inelastic scattering signal (grey contours) of the next pixel acquisition in spectrum imaging mode for different probes and step sizes. White contours represent the energy deposited by previous pixel acquisition, in units of critical dose (see eq. III.10). An areal dose of $\approx 200\,e\,\text{Å}^{-2}$ was maintained in all simulations, regardless of the step size.

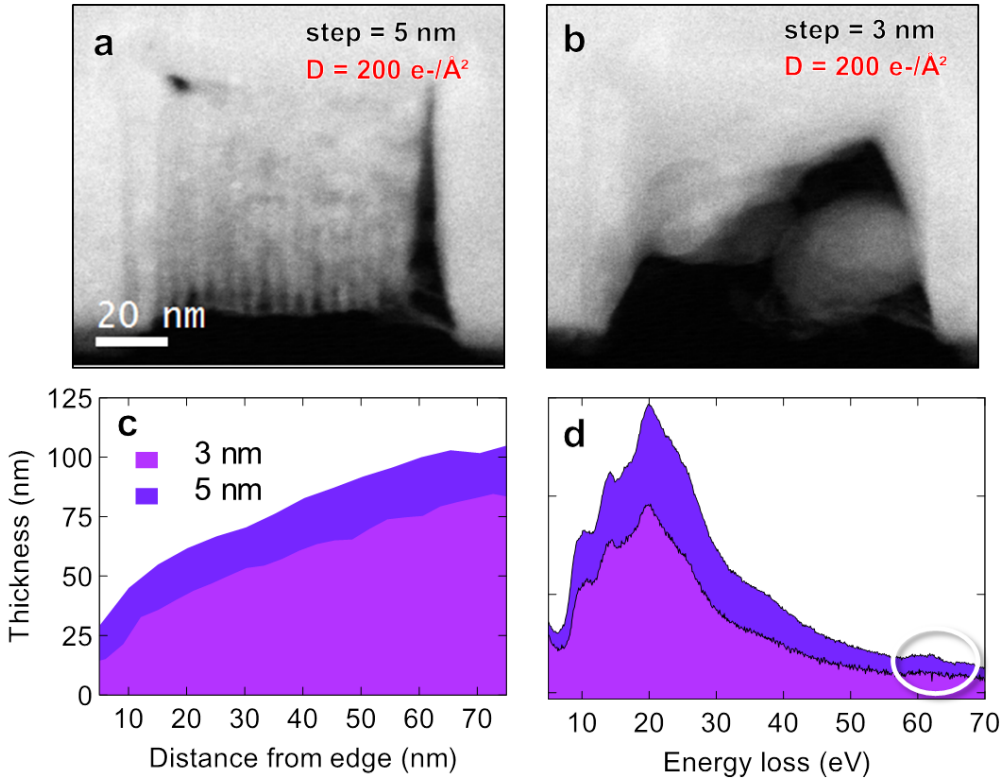

Fig. III.7: Threshold effect of the step size in spectrum imaging at constant areal dose. a-b) STEM observation after spectrum imaging showing greater specimen thinning for a step size of 3 nm. c) Thickness profiles of both spectrum images. d) Summed spectra for both spectrum images. Both results demonstrate lesser damage with higher step sizes.

For the step size of 5 nm which was routinely used in this manuscript, SND values are improved from 14.7 to 17.5, a 20% increase, if a 16 mrad probe is used rather than our pick of 3 mrad. In the scope of this thesis we have sticked to this last value however, for two reasons: (i) beam broadening. The mean probe diameter accross a sample's thickness t is proportional to αt. For specimen thicknesses above ≈ 70 nm, which we encounter often in lithiated silicon nanoparticles and thick SEI layers, a 3 mrad probe is in fact smaller than a 16 mrad one. (ii) The signal-on-noise ratio will suffer from increasing the convergence angle α, as we discuss in the following section.

Table III.4: Signal-on-damage ratios of a spectrum acquisition in spectrum-image mode depending on the probe used and the step size.

α	SND		
	3 nm	5 nm	8 nm
1 mrad	6.7	10.8	12.9
3 mrad	12	14.7	16.3
16 mrad	14.7	17.5	19.1

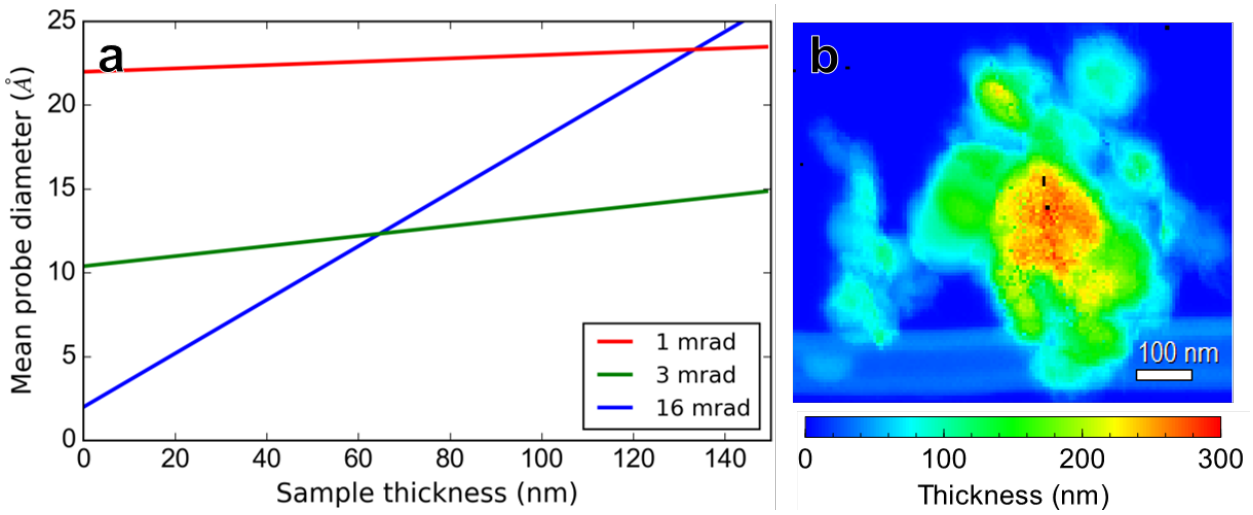

Fig. III.8: a) Mean probe diameter as a function of specimen thickness. b) Thickness map of a representative lithiated silicon nanoparticles cluster.

III.1.3 Collection angle, probe current and accelerating voltage

This section addresses the remainder of the important experimental parameters we have optimized for our low-dose STEM-EELS protocol, reported beforehand table III.1. Each of those is involved in one or multiple sub-issues surrounding STEM-EELS acquisitions, and we can prioritize these issues so that parameters can be optimized independently. We have defined this work-flow as follows:

- Optimizing detection of the EEL signal: β
- Minimizing specimen damage during irradiation: E_0, α
- Limiting irradiation throughout CCD readout: probe current I

Collection angle β and signal-on-noise ratio

From a practical point of view, there is a lower limit on the signal-on-noise ratio needed to perform meaningful analysis. We have empirically set this condition as $SNR \geq 20$. Signal detection then needs to be optimized so that this target SNR is reached for as little dose as possible. A general rule-of-thumb to maximize the SNR is for the collection half-angle to not exceed the cutoff angle θ_c, above which no inelastic scattering occurs and only noise is gathered. θ_c will be a function of the plasmon energy E_p, and can be roughly approximated by the formula found in Egerton's 2011 book [173] as:

$$\theta_c = \frac{E_p}{\hbar v_F k_0} \tag{III.11}$$

Where v_F is the Fermi velocity, calculated from the electron density n_e and $k_0 = 2\pi/\lambda$ is the momentum of incident electrons. Using experimental E_p values (whose determination is detailed part III.3), we can now calculate θ_c for a few significant compounds (fig. III.9). To put forward a value for the organic component of the SEI despite its complex and elusive composition, calculations were carried out using a rough estimate of $n_e = n_{e,FEC}$ the electron density of the electrolyte additive fluoroethylene carbonate whose reduction accounts for most of the SEI (see I.2.2). Now, since cutoff angles vary dramatically, a choice needs to be made as to which species takes priority. Naturally the most radiation sensitive compounds takes precedence, since the very reason the SNR is considered is to keep our input dose to a minimum. Those will be the alkyl-carbonates that were shown to be particularly prone to radiolysis in the previous section. Therefore a cutoff angle $\theta_c = 7\,\text{mrad}$ is picked. Since we have $\theta_{c,LiF} < \theta_{c,org} < \theta_{c,LiSi}$, detection will not optimized for Li-Si alloys and LiF. However the signal decrease of Li_xSi alloys as well as the additional noise gathered for LiF are inconsequential since these compounds give sharp, easily-interpretable spectra. The *org* phase however is not only more sensitive but also stacked in chemical information as we'll see in the following sections. Hence the emphasis on the SNR obtained from this phase rather than the others.

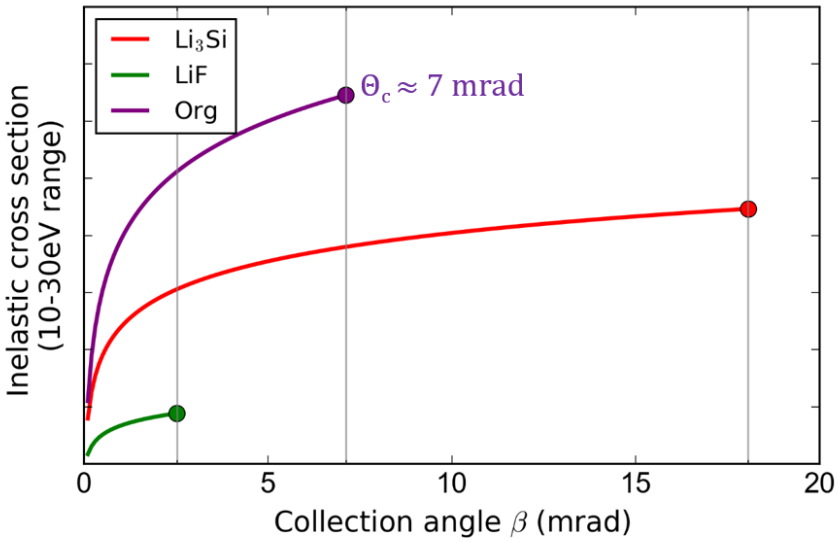

Fig. III.9: Inelastic scattering cross section as a function of the collection angle β. Data points indicate cutoff angles calculated from eq. III.11.

Once again, the distribution of electrons across the probe of angular width α should be minded. Electrons will be scattered to a maximum angle of $\alpha + \theta_c$, and β should be set near this value to ensure all signal is collected, at $\beta \approx 10\,\text{mrad}$ in our case of using $\alpha = 3\,\text{mrad}$.

Minimizing damage during irradiation: E_0 and α

From there, the main concern driving the choice of our parameters will be to minimize specimen damage regardless of dose. Two parameters will impact the damage done by a given number of incident electrons: (i) the energy they carry, i.e. the microscope's accelerating voltage E_0 and (ii) their spatial distribution i.e. the probe shape controlled by the convergence half-angle α. Since $\alpha = 3\,\text{mrad}$ was already set as a compromise between SND and beam broadening, our focus is shifted to E_0. Higher accelerating voltages are generally considered more harmful for sputtering damage [167]. But a closer look at the displacement cross section for Li actually suggests the opposite trend above 30 kV (fig. III.10.a) because of lithium's light atomic weight and loose bonding. This was demonstrated experimentally by D. Robert [37] who showed faster Li depletion at 80 kV than at 200 kV at equal electron dose in Li_xSi alloys.

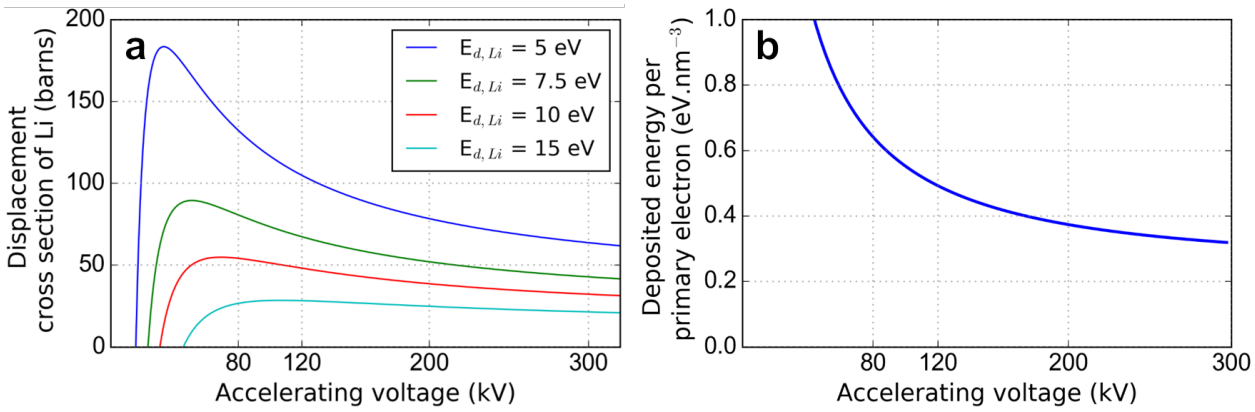

Fig. III.10: Dependence of irradiation damage on accelerating voltage. a) Displacement cross section of Li atoms for different binding energies. Practical behavior is most likely between 5 eV to 7.5 eV. Results were obtained thanks to the formula from [125] b) Energy deposited by inelastic scattering per unit volume.

Regarding radiolysis, increasing E_0 will reduce the likeliness of an inelastic interaction, which means less damage but also less signal at the same time [157] which amounts to no effect overall. The energy deposited through each inelastic event shows however a strong dependence on the accelerating voltage, as shown fig. III.10.b. Moreover, the cross section of secondary electron generation, which is largely responsible for radiolysis damage, will also follow $\sigma_{se} \propto 1/E_0$ [170]. Higher energies are thus desirable in all cases and for both TEMs used in the scope of this thesis $E_0 = 200\,\text{kV}$ was the maximum available. We nonetheless recommend 300 kV experiments whenever possible.

Effective dose and CCD readout: probe current I and dwell time

Foremost among the remaining possible improvements is slashing the part of irradiation that does not contribute to the signal: CCD readout time. This parameter for irrelevant in single spectrum

acquisition but critical in spectrum images. In this mode, the electron beam stays idle in the same position on the sample throughout the readout time, which can easily exceed the dwell time for low-loss EELS (≈ 10 ms in our case). Since irradiation damage is delocalized, the damage that occurs during readout will impact the following acquisitions. Consequently it is critical that this term is accounted for when in spectrum imaging mode, as demonstrated experimentally (fig. III.11).

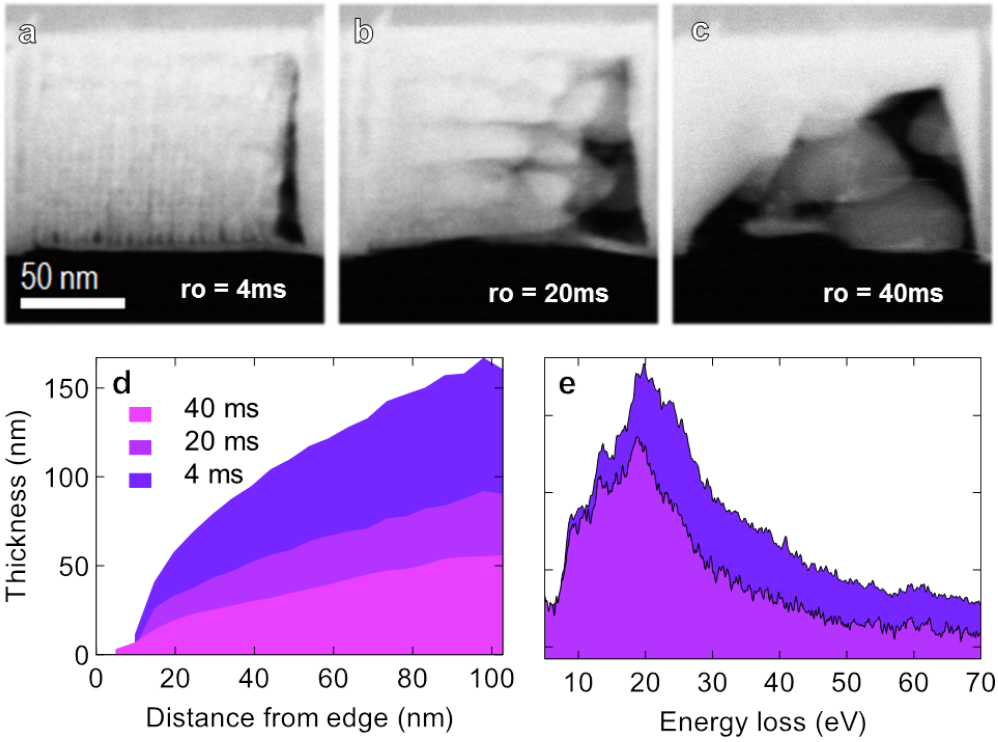

Fig. III.11: Impact of the readout time on the radiolysis undergone by a Li_2CO_3 layer with $I = 5$ pA and dwell time = 10 ms. a) Thickness profiles showing specimen thinning proportional to the readout time. b) Spectra extracted from the same position of spectrum images taken with readout times 4 ms an 20 ms. Changes in the total scattered intensity, Li-K edge and interband transitions show increased damage. c-e) Post-acquisition STEM observation.

The total electron dose is simply the product of the dwell time and the probe current I. If we now define the *effective dose* D as the sum of the electron dose applied to the sample during the user-chosen dwell time **and** the CCD readout time, we have:

$$D = D_{acq.} + D_{readout} \propto I \times (dwell\ time + readout\ time) \tag{III.12}$$

The term $D_{readout}$ should be kept as small as possible. This can be expressed as:

$$\frac{D_{acq.}}{D_{readout}} \gg 1 \quad \text{e.g.} \quad dwell\ time \gg readout\ time \tag{III.13}$$

Using a vertical binning of 10 ×, digiscan's hardware sync and the "High-speed" mode of the GIF, we can go down from ≈ 100 ms to under 5 ms. As a side note, low readout times are not only beneficial to irradiation damage, but also to allow for fast acquisitions. With the current setup, spectrum imaging can be performed on areas as large as a few µm² in less than 10 minutes. This is instrumental to multiply measurements and guarantee statistical significance in such heterogeneous samples. Now to satisfy equation III.13 we need to use an accordingly high dwell time of approximately 15 ms and a correspondingly low probe current $I = 5\,\mathrm{pA}$ so as to meet our total dose target. For a resolution of 5 nm our experimental electron dose is then:

$$D = \frac{20\,\mathrm{ms} \times 5\,\mathrm{pA}}{e \times 50\,\mathrm{\AA}^2} = 200\,e\,\mathrm{\AA}^{-2}$$

Another way to look at the problem is that since the specimen is exposed anyway during readout, a low probe current is preferable to minimize damage. Arguably, a case could also be made for the influence this has on the *dose rate*, which reflects how fast our dose is applied, but no dependence was found between the characteristic dose D_e and the dose rate in organic samples [168]. Naturally, this is optimization process is moot if the beam can be automatically blanked during camera readout. This is possible when a pre-specimen shutter is available. This equipment is specific and mostly found on systems fully dedicated to the study of sensitive materials.

Conclusion

Both Li-Si alloys and SEI compounds show great radiation sensitivity. In alloys, sputtering causes lithium depletion which affects nanoparticles clusters as a whole due to lithium ionic mobility. Limiting the size of spectrum images and keeping doses below a threshold of $\approx 200\,e\,\mathrm{\AA}^{-2}$ can help us mitigating this phenomena. Regarding SEI compounds, radiolysis will cause bond breaking and specimen thinning which, although inevitable, can be kept to reasonable limits as demonstrated. This is achieved by combining modeling efforts and empirical observations of irradiation damage to optimize our acquisition parameters, among which the choice of the probe is key in order to mitigate pre-acquisition damage during spectrum imaging. A lower limit on the achievable spatial resolution was found at around 4 nm in simulations, in good agreement with reference experiments on Li_2CO_3. Regarding the rest of our parameters, a carefully chosen collection angle allows us to acquire workable spectra for doses as low as possible, while using the proper probe shape and accelerating voltage can limit the damage done for a given dose. Finally, a combination of low probe current and high dwell time is favored in order to minimize the damage done during CCD readout.

Our approach to optimize the experimental protocol can be summarized in the diagram presented fig. III.12.

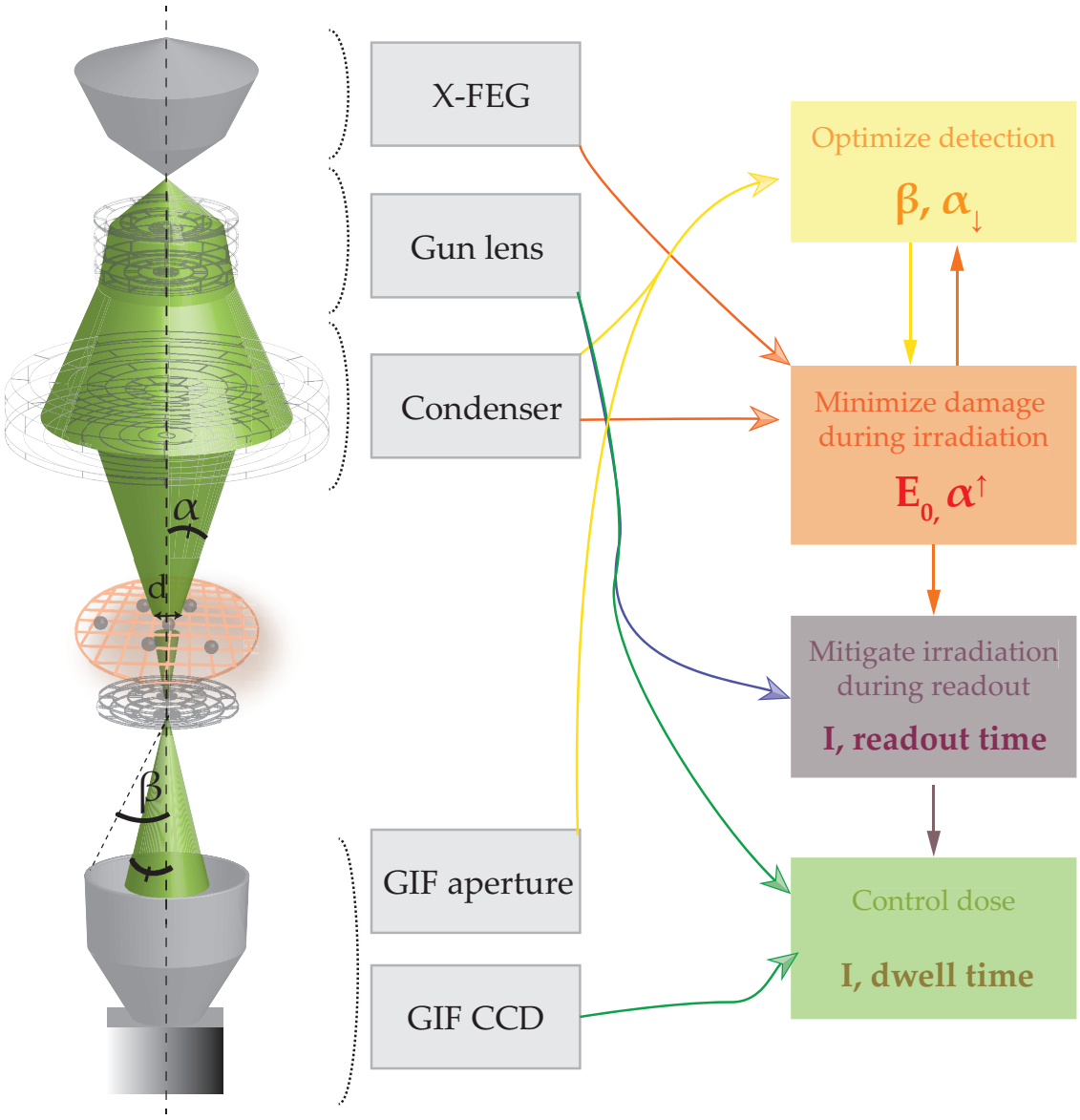

Fig. III.12: Schematic summary of the experimental parameter optimization workflow.

III.2 Phase mapping: the MLLS approach

III.2.1 Methodology and interpretation

While a refined experimental protocol is necessary to keep radiation damage in check, clever analysis methods are equally important for successful low-dose STEM-EELS experiments. To understand electrode aging, insight needs to be gathered on the morphology of the different Li-Si alloys and SEI phases from spectrum images where the contributions of all of those phases are superposed. To extract each of these contribution we use the multiple linear least square fitting (MLLS) algorithm. This method determines the weights $\{a_0,...,a_n\}$ of a set of input spectra $\{s_{ref,0}(E),...,s_{ref,n}(E)\}$, to satisfy in each pixel of coordinates x,y and spectrum $s_{exp}(E)$ the relation:

$$\int s_{exp}(E,x,y)dE = \sum_{i=0}^{n} a_i(x,y) \int s_{ref,i}(E)dE \tag{III.14}$$

Which can also be written in terms of the total inelastic scattered intensities I_1:

$$I_1^{exp}(x,y) = \sum_{i=0}^{n} I_1^{ref,i}(x,y) \tag{III.15}$$

This approach has already been successfully demonstrated in several low-loss EELS works such as those reported section I.3.2 [143] and is instrumental to the study of low-loss spectra which, unlike core-losses, cannot be directly linked to specific chemical elements or bonding environments. Therefore a database of reference spectra, or fingerprints, should be built to feed the MLLS algorithm. Maps of the weight of each input component can then be combined into a composite phase map by attributing a color to each compound, as demonstrated figure III.13. This methodology yields the morphology and relative proportion of SEI as well as Li-Si compounds to a spatial resolution corresponding to our step size of 5 nm and is the foundation of our study of silicon electrode aging.

In their raw form, maps obtained from MLLS decompositions can only be interpreted qualitatively as intensity values do not reflect absolute thicknesses. However those do correspond to inelastic scattering intensities I_1 as described eq. III.15. As described section II.2, for each MLLS component i, I_1^i is related to the total zero-loss peak intensity I_0, sample thickness t and electron mean-free path λ_i according to III.16 [157].

$$\frac{I_1^i}{I_0} = \frac{t_i}{\lambda_i} \tag{III.16}$$

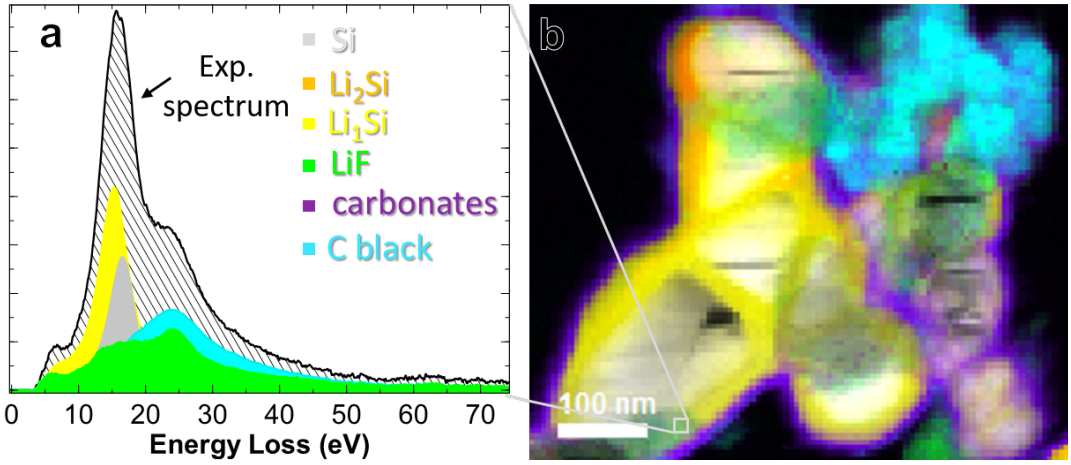

Fig. III.13: Example of phase mapping through MLLS decomposition. a) The inelastic scattered intensity of each MLLS component is extracted from experimental spectrum in each pixel of the spectrum image. b) Maps of these intensities combined into a composite color map that outlines the overall morphology.

This means that in individual component maps, intensity ratios i.e. contrasts will be equal to thickness ratios and can be used to deduce the morphology of layers in 3 dimensions. As to composite maps, the dependence on λ_i makes comparing the thickness of different components difficult at a glance but since λ values do not differ by more than 30% from one compound to the next [174], component maps can be reasonably combined in composite phase maps for a rough estimate of the overall morphology. Performing absolute thickness measurements through eq. III.16 is not out of reach, but requires prior knowledge of λ_i. This is discussed in sub-section *electrode-scale quantification*.

III.2.2 Choosing the right input

Gathering an extensive set of reference spectra that is representative of the experimental data is key to obtaining reliable results from MLLS. Failing to account for a given compound can result in the severe over-representation of the rest of input components. This makes prior knowledge of the system at hand indispensable. For example, limiting SEI components to LiF and Li_2CO_3 does not decently describe the variety of organic and semi-organic compounds in the SEI, which are characterized by extremely broad plasmon peaks in the 18 eV to 22 eV region [143, 157]. Without additional input components, the MLLS decomposition will compensate with an exaggerated contribution of the reference spectrum closest to the experimental one which here is the inactive additive carbon black. Thus MLLS can effectively fail to accurately portray the SEI phase if the proper input is not used, as demonstrated fig. III.15. Likewise, trying to analyze all Li_xSi alloys by only feeding Si and $Li_{3.75}Si$ to MLLS will result in a result split between these two extremes, where intermediate x values are under-represented (fig III.14). This is particularly damageable

when studying partially lithiated electrodes, for which more agreeable fits are obtained with a fuller array of Li_xSi alloys.

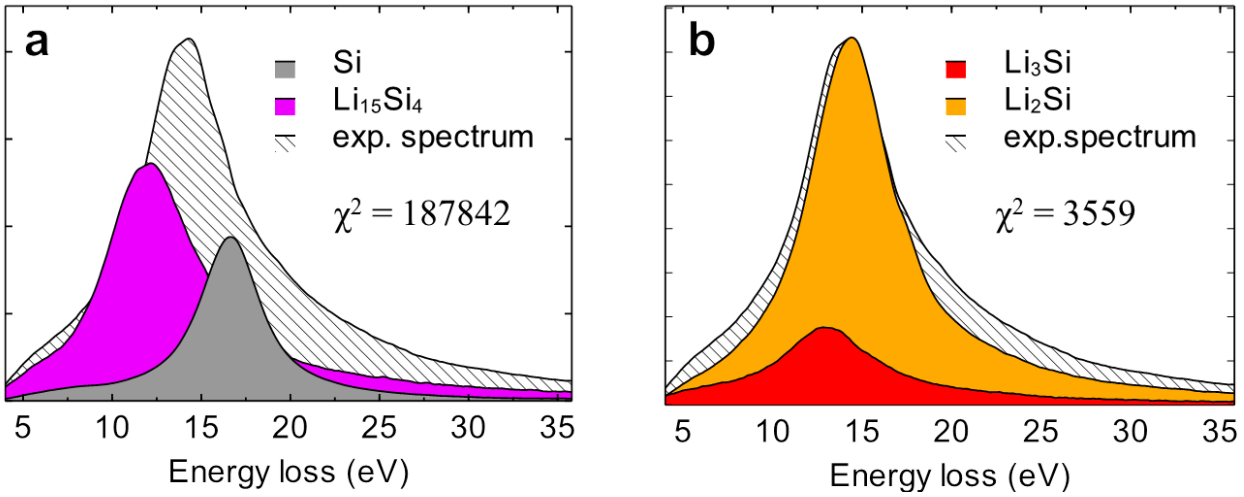

Fig. III.14: MLLS decomposition on a lithiated SiNP with two different set of reference spectra as input. a) Being limited to Si and $Li_{3.75}Si$ leads to an overestimate of $\approx 25\%$ of the lithium content. b) Including Li_1Si, Li_2Si and Li_3Si allows for a reliable fit. Insets are maps of the lithium content calculated from the weight of Li_xSi components output by MLLS.

Therefore it is preferable to use numerous components, even it means straying away from pure reference experiments. Reference spectra can be taken directly from experimental data in regions where a single phase is present. For the SEI especially, this is made necessary by the difficulty to isolate compounds such as alkyl carbonates LEDC or polymeric species like poly(FEC) that we strongly expect in the SEI (see part I.2). The correspondence of these experimental MLLS components to a given chemistry is unknown. Incorporating them in the MLLS database aims at a more accurate portrayal of the morphology of the "organic" SEI phase by fostering a better MLLS fit, rather than a precise determination of the composite chemistry of the SEI. With that in mind, 3 such spectra were added to the MLLS database, all extracted from experimental data to cover the 18 eV to 22 eV described earlier.

Introducing many more spectra can however lower the accuracy of our fit, especially when trying to account for components present in trace amounts or whose EEL spectra is too similar to those already used. A notable absent of our results is for example the binder CMC which, despite its critical role in the capacity retention of electrodes, can not be properly detected because of the similarity of its EEL spectrum with the other organic species. Furthermore, our effort to anticipate all components naturally leads to the consideration of surface plasmons, which show significantly different shapes than their volume counterparts (see part II.2). However at a spatial resolution of 5 nm and for the large thicknesses we are probing, these have a negligible impact on the phase morphologies that are under investigation, and needn't be included in our MLLS input.

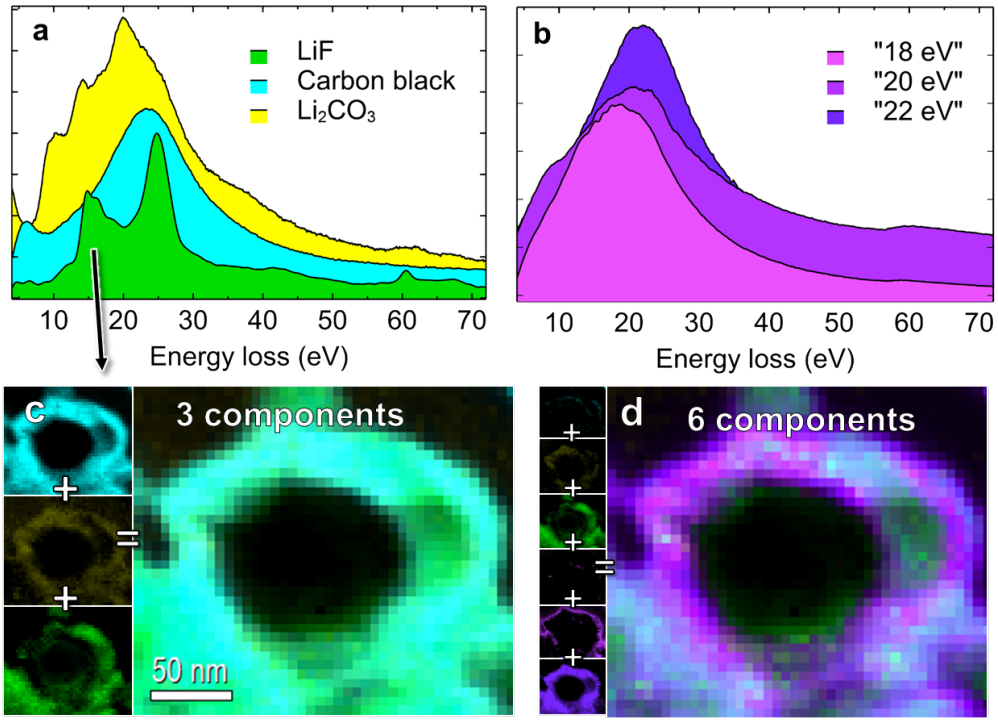

Fig. III.15: Individual and composite phase maps obtained by MLLS decomposition. a,c) Including those 3 spectra only. The "organic" phase is misinterpreted as the inactive phase carbon black. Errors are $\approx$ 18% higher than in the following case. b,d) Including an additional 3 experimental spectra it is accurately portrayed. All maps were set to the same arbitrary contrast limit.

Building our reference database

Our database is the sum of low-loss spectra taken on pure compounds as well as spectra extracted from data on cycled electrodes. For Li-Si alloys, we first used data from D. Robert [37] who analyzed the Li-Si alloys of known stoichiometry $Li_{2.33}Si$ and $Li_{3.75}Si$. Those spectra were advantageously replaced - using the quantification method detailed in next section III.3 - by those identified as Li_1Si, Li_2Si and Li_3Si in lithiated electrodes. Regarding the SEI, reference spectra were acquired on pure LiF, Li_2CO_3 and Li_2O while spectra associated with the "organic" phase were taken from actual SEIs in lithiated electrodes. Likewise, Si and *carbon black* components were obtained from pristine electrodes. It is also worth noting that experimental conditions, and most importantly the areal electron dose, were kept unchanged while acquired references and during actual electrode analysis in order to anticipate irradiation damage in our reference spectra. All things considered, no less than 11 spectra were used in MLLS decompositions. Those are summarized table III.5. Throughout this thesis that set remained the same for all analysis in order to be able to compare the weight of any given component from one spectrum image to the next.

Table III.5: The 11 reference spectra used in MLLS decomposition.

Component	Original sample
Silicon	Pristine electrode
Carbon black	Pristine electrode
Lithium	Damaged Li_xSi alloy
Li_1Si to Li_3Si	Lithiated electrode
LiF	LiF powder
Li_2CO_3	Li_2CO_3 powder
"Carb./org." spectra	Cycled electrodes (up to 100^{th} cycle)

III.2.3 Electrode scale thickness quantification

Equation III.16 defines a simple relationship between the scattered intensities recorded in EELS, absolute thicknesses, and the inelastic scattering electron mean-free path λ. Using estimates of λ for each component can enable us to put forward quantitative thickness maps and not only to reliably compare the thickness of a given component to others, but also the total thicknesses from one acquisition to another and from one sample to another. Doing so requires the total thicknesses of individual components to be averaged over many acquisitions and samples prepared from the same electrode. Results of statistical significance can thus be proposed on the electrode scale, allowing us to circumvent the large variance there is from one measurement to another due to the local scope of the STEM-EELS technique and the heterogeneity of battery electrodes. Quantitative values and trends can then be used to study electrode aging and can be compared to the literature, most interestingly on SEI accumulation and the related "breathing" effect.

Calculations of the mean free-paths λ_i

Several models have been put forward to provide estimations of the electron mean-free path. The simplest was proposed by Malis et al. [175] and describes λ as a function of the mean atomic number Z and the accelerating voltage E_0, but doesn't account for the fact the both inelastic and elastic scattered intensity are only partially recorded because of the limited collection half-angle β. A more recent model from Iakoubovskii et al. [174] does include this correction, estimating λ_i from α, β, E_0 and the specimen density ρ_i. Both models were benchmarked by Zhang et al. [22] who predicts a slightly lesser error of $\approx 5\%$ in thickness measurements using Iaboukovskii's formula (fig. III.16), which we've elected to use as a result. Calculated λ_i estimates of each components used in MLLS are reported table III.6. In all cases an interval is provided to account for the little variations in the α and β angles that were made throughout this work.

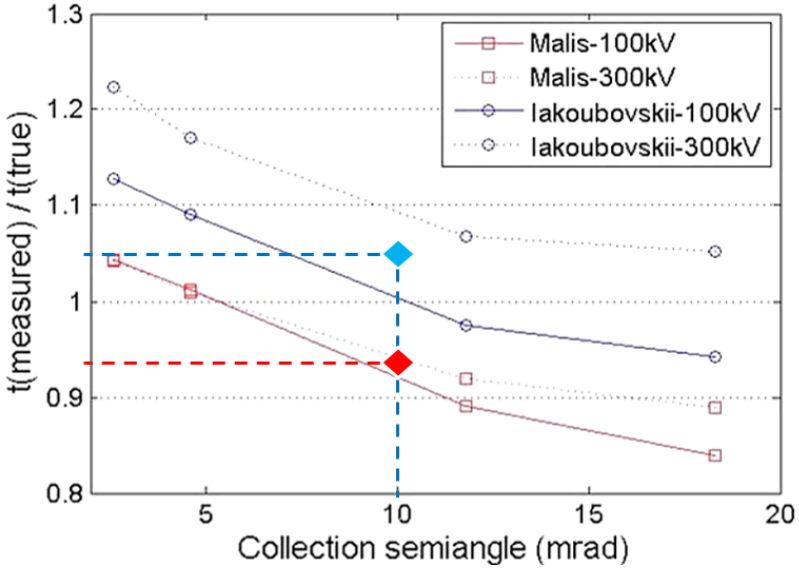

Fig. III.16: Comparison of Iakoubovskii's and Malis models to perform t/λ thickness calculations. The red and blue diamonds represent our situation (200 kV) for respective models. Iakoubovskii's introduces a slightly lower error of $\approx 5\%$. Edited from [22].

Table III.6: Inelastic mean free-path of each MLLS component calculated from the Iaboukovskii model.

Component	Density (g.cm^{-3})	λ_i (nm)
Silicon	2.33	187.5 ± 8.5
Carbon black	2 ± 0.1	196.1 ± 12.4
Lithium	0.53	267 ± 11
Li_1Si to Li_3Si	1.72; 1.42; 1.22 [162]	$202; 211; 219 \pm 9$
LiF	2.64	182.5 ± 8.5
Li_2CO_3	2.11	194 ± 6.5
org phase	1.21 (PEO) - 1.41 (FEC)	215.5 ± 13.5

Implementation and electrode scale quantification

Applying eq. III.16 to experimental spectrum images is not straightforward as no inclusive software solutions are available. Therefore scripts were developed to extract I_0 from the zero-loss peak, calculate the intensities I_1^i of each component by MLLS decomposition and use the corresponding tabulated λ_i values to perform the t/λ calculation automatically on the 197 spectrum images included in the study of cycled electrodes during this thesis. Pixels with weak signals that correspond to overly thick areas are not suited for thickness calculations and were filtered on the criterion $I_{1,tot}/I_0 > 3$. Two outputs are provided: (i) absolute thickness maps of individual components and (ii) total thicknesses $t_{i,tot}$ summed over each spectrum image. One should however be mindful that this overall thickness will depend on the total size of the spectrum image and the comparison of this quantity from one spectrum image to the next will be of little practical relevance. Better interpretations can be reached by calculating for each component i the ratio t_i/t_{Si}, which

effectively stands for the amount of compound *i per* amount of active material (silicon). Those ratios are ideal to compare amounts of a given compound regardless of spectrum image size. Thickness ratios are equivalent to volumetric ones and latter will often be used instead.

$$\frac{t_i}{t_{Si}}|_{SI} = \frac{\sum\limits_{\text{all pixels}} t_i(x,y)}{\sum\limits_{\text{all pixels}} t_{Si}(x,y)} \tag{III.17}$$

In the 2 examples reported figure III.17, the total LiF volume of the second SI is more than 3 times larger than the first, but ratios present just the opposite picture, reflecting a much larger proportion of LiF in the first spectrum image. Now, as mentioned previously, the summation of many spectrum images can give us a reliable characterization of a given electrode. Doing so allows us to calculate an overall ratio for the electrode which can subsequently be compared to other ratios from electrodes cycled in different conditions. This is illustrated fig. III.18, where the ratios LiF/Si and CB/Si (carbon black over silicon) were plotted for electrodes at different stages of cycling. We see that despite the large standard deviation there is in the dataset, a smooth trend can be revealed by summing enough measurements. Those plots reveal two significant, quantitative result: (i) there is an accumulation of LiF along cycling and (ii) the quantity of carbon black (CB), an inactive component of our electrodes, is measured to be constant as expected. This last result provides an indication of the accuracy of the method. We measure a volumic ratio $V_{CB}/V_{Si} = 0.25$, which translates to $m_{CB}/m_{Si} = 0.19$, whereas the electrode formulation stipulates 0.15.

$$\frac{t_i}{t_{Si}}|_{electrode} = \frac{\sum\limits_{\text{all SI}} t_{i,tot}}{\sum\limits_{\text{all SI}} t_{Si,tot}} \tag{III.18}$$

Detection limits and error estimation

Interpretations of the MLLS output must mind the limits of the method. Unlike core-loss EELS, through which elements can be detected in trace amounts as low as 0.1%, low-loss EELS will suffer from much higher detection limits. As a result minor contributions whose intensities are dwarfed by those of compounds present in overwhelming amounts will not stand out significantly enough to be picked up by MLLS. This is of particular importance in our case of thin SEI layers covering much thicker silicon particles. Our inability to detect the SEI in areas where large amounts of silicon or Li_xSi are present gives our SEI maps the appearance of cross-sections rather than TEM projections (fig. III.15) i.e. a ring morphology rather than a shell. Although this does not impair our capacity to measure SEI thicknesses, as they appear around the particle, and extrapolate, this geometry must be corrected for in quantification. Our focus is set especially on the *org* phase as its conformal morphology is most affected by the effect aforementioned.

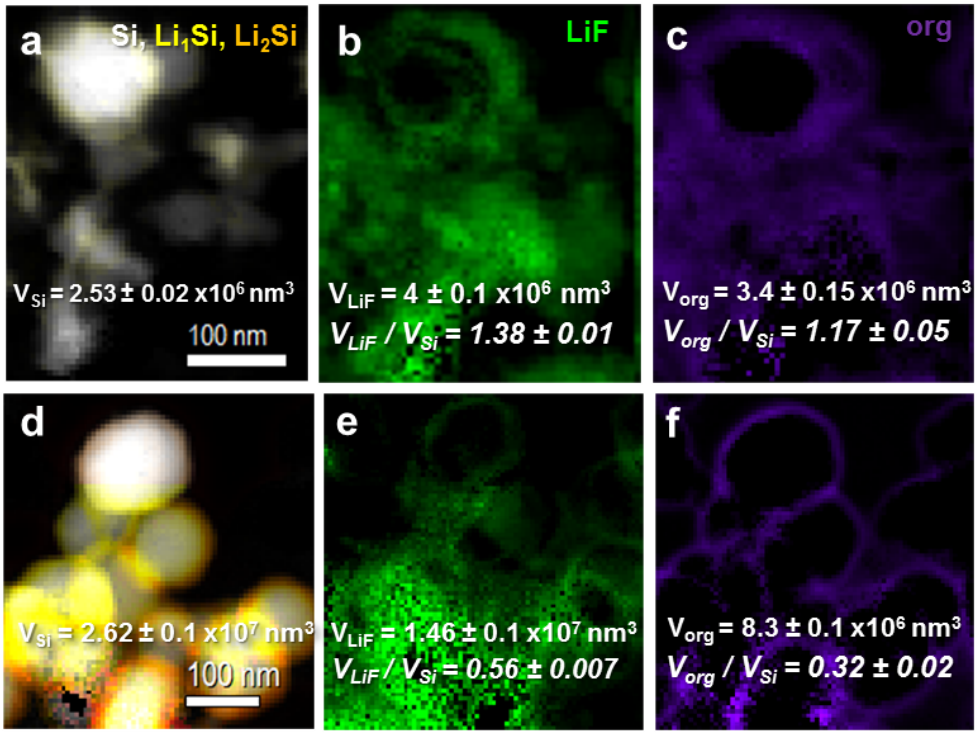

Fig. III.17: Thickness maps of the Li_xSi, LiF and *org* phases obtained by t/λ calculations on MLLS decompositions of on two spectrum images. a-c) The LiF and *org* phases are present in high proportions despite their low absolute quantity. d-f) These same species are in small relative amounts. The intensities of all maps is scaled from 0 nm (black) to 100 nm.

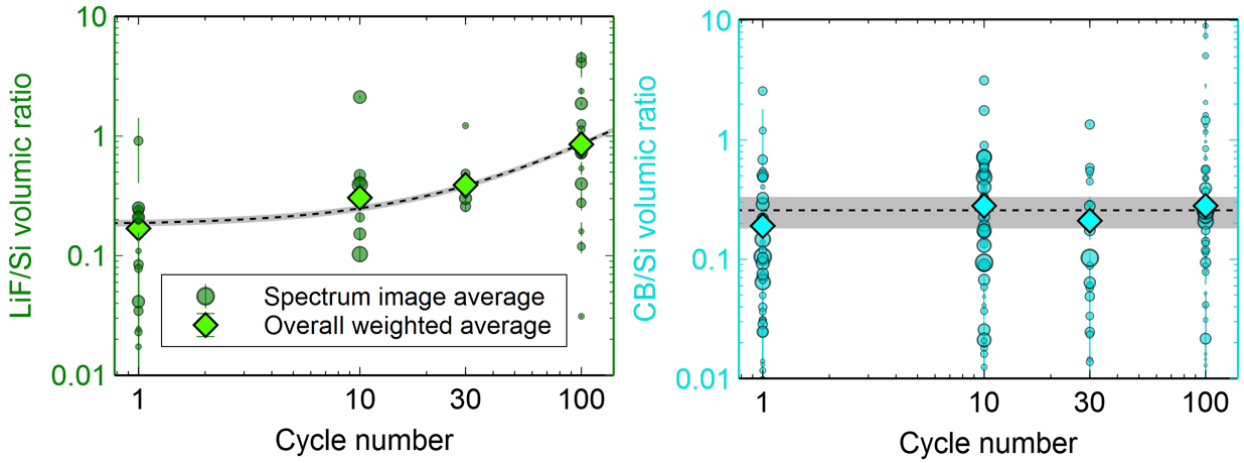

Fig. III.18: Volumetric ratios LiF/Si and CB/Si averaged over spectrum images (circles) and over all electrodes stopped at their 1st, 10th, 30th and 100th cycle respectively.

To estimate corrections, detection limits were assessed by comparing experimental data to predictions based on a core-shell configuration. Thickness profiles obtained by MLLS thickness mapping on a representative nanoparticle of radius $R \approx 75$ nm engulfed in SEI (fig. III.19.a) reveal a layer of thickness $T \approx 15$ nm but which is lost on the MLLS decomposition in the center of the particle. Under the assumption that the SEI has a conformal morphology, calculating the true

Table III.7: Contributions to the total standard deviation in thickness calculations.

Source	Fractional error
λ_i	$\approx 5\%$
Iaboukovskii formula	$\approx 5\%$ [22]
MLLS processing (errors on I_1^i)	5-10%
Detection limit correction (org.)	20%
Total thickness	30-35% (org), 10-15% (others)
Total t_i/t_{Si}	ratio <5% (org.), <2% (others)

thickness of the layer t_{org}^{true} then allows us to put forward the dependence of the measured t_{org}^{MLLS} on the ratio of SEI to total thickness. This outlines a threshold ratio of 0.2 under which MLLS returns null values (fig. III.19.d). Once more, a detection limit as high as 20% hints at how off-target quantification could be lest MLLS limits are corrected for. With this in mind, we propose an overall correction factor $A(R,T)$ as the ratio of the thicknesses t_{org}^{true} and t_{org}^{MLLS} integrated over the whole sphere. $A(R,T)$ can be developed further using a function f which fits the logarithm dependence outlined fig. III.19.d:

$$A(R,T) = \frac{\int_0^{R+T} 2\pi t_{org}^{true}(r) r dr}{\int_0^{R+T} 2\pi t_{org}^{MLLS}(r) r dr} = \frac{\int_{R_a}^{R+T} t_{org}^{true}(r) r dr}{\int_0^{R+T} f(\frac{t_{SEI}}{t_{org}}|_r) t_{org}^{true}(r) r dr} \tag{III.19}$$

Values of this correction factor for a range of *org* phase thicknesses T and SiNP radii R are reported fig. III.19.d. Results are telling of large underestimations of the total thicknesses, with more than half the layer unaccounted for if we consider thin, $T = 10\,\text{nm}$ layers on large nanoparticles. This is especially relevant given the expansion that comes along the lithiation of these particles. In practice, the distribution of particle sizes R and *org* thickness T is not precisely known and our ability to calculate it from spectrum images is limited. Therefore implementation requires calculating a value $\langle A \rangle = +50\%$ averaged over the thickness gain this methodology provides, although a sizable error is bound to be introduced by using a single standardized constant.

In a bid to asses this deviation and the accuracy of our claims, error estimation was also implemented to our MLLS scripts. Contributions from the standard deviations $\Delta\lambda_i$, fitting errors $\Delta I1^i$ as well as the systematic errors induced by the t/λ method were included in addition to the previous geometrical considerations. Overall, fractional errors are kept within reasonable limits are reported table III.7. Errors from the MLLS decomposition can be large in thin area that yield low signal counts, but these represent a small fraction of the total thickness. As a result errors on the total thickness do not add up to more than 15% and even less so if we calculate ratios.

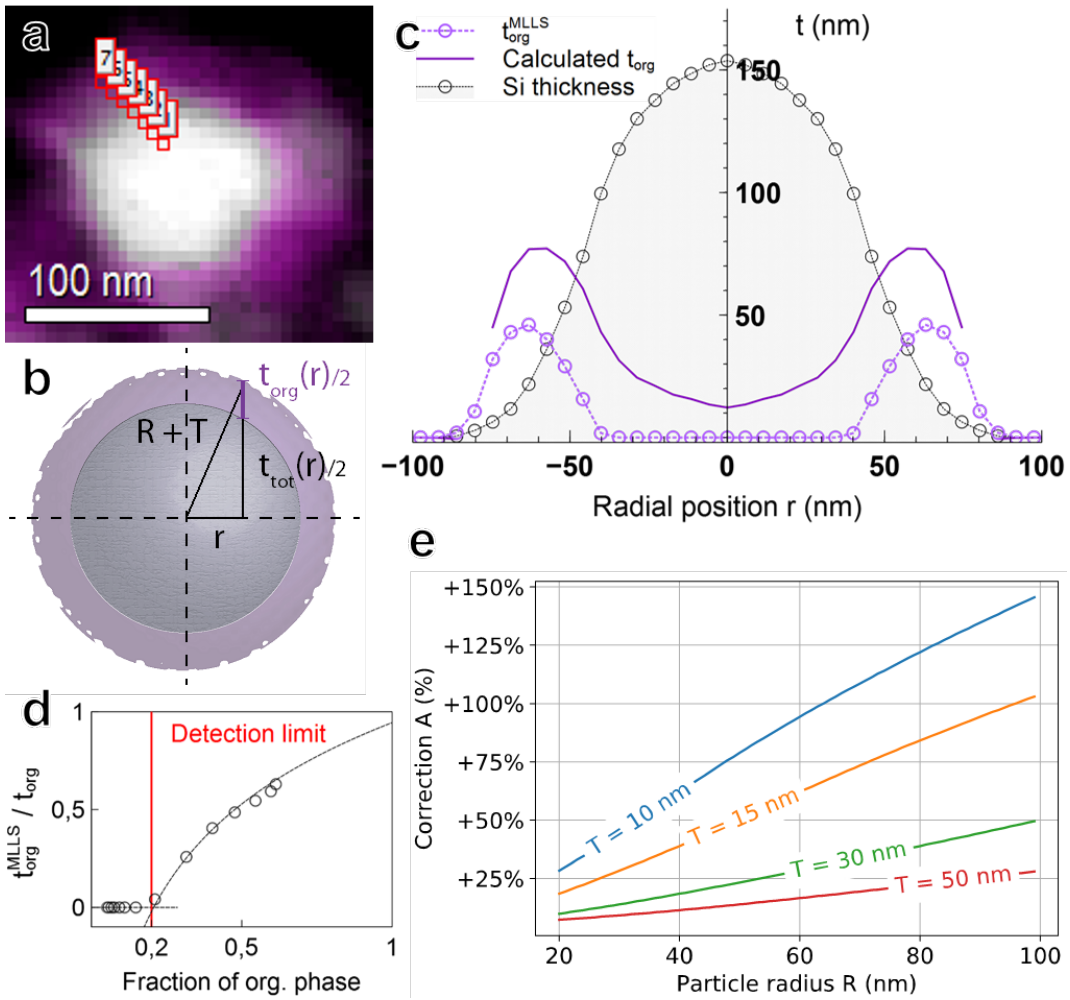

Fig. III.19: a) Thickness maps of a SEI-covered particle from which the *org* and Si profiles of c were extracted. b) Diagram of the quantities R, T and r used in III.19. c) Experimental thickness profiles and calculation of a t_org profile based on a core-shell geometry. d) Ratio of the thickness measured by MLLS to the true thickness for the *org* phase as a function of the proportion of the *org* thickness. The phase is not detected if doesn't represent more than 20% of the total. e) Correction factors calculated as functions of SEI thicknesses T and SiNP radii R.

Summary

In conclusion, individual phases can be mapped from spectrum images using the MLLS procedure. These are maps of the total inelastic intensities I_1^i which are proportional to the thickness t_i and can easily be interpreted visually for the morphology of each phase. The accuracy of outcomes however strongly depend on the reference spectra that are input to the algorithm, and this needs to be considered carefully. Previous knowledge of the species present is required to put together an all-inclusive set of spectra and obtain reliable data on our cycled electrodes. It is especially important in the case of organic SEI compounds which cannot be isolated for reference experiments and whose spectra were extracted from cycled electrodes samples. Absolute thicknesses can subsequently be calculated for each phase, provided the mean free-paths λ_i are estimated with the formula developed

by Iaboukovskii et al. Once this process is optimized at the spectrum image level, thicknesses can be summed, averaged, and compared to reach an assessment of the relative amount of each phase in a given electrode. Doing so allows us to provide electrode-scale characterization from our local STEM-EELS measurement, and carry out a quantitative aging study of silicon electrodes.

III.3 Fitting the Drude model to plasmons

MLLS was developed into a powerful tool to reveal the distribution of compounds, but cannot give more than the reference spectra input to it. MLLS results are about the morphology of known phases, but do not provide insight regarding the chemistry of these phase. Our prior knowledge of the SEI tells us however that a variety of compounds are in fact present amidst the phase we nicknamed *org*. Similarly, the lithium content of Li-Si alloys can take any value between 0 and 3.75. Fortunately, a plasmon's unique shape and position does contain valuable chemical information which can help us narrow down the chemistry of these phases. While the application is obvious in the case of Li_xSi alloys, whose plasmon energies can be directly associated to lithium contents x, as demonstrated by J.Danet [35], an application to the elusive *org* phase is also possible.

To exploit this, characteristic parameters need to be extracted of experimental spectra. This can be achieved by fitting the Drude model, described part II.2.2 and rewritten eq. III.20, to obtain the plasmon energy E_p. On both SEI compounds and Li_xSialloys, E_p values can then be interpreted according to empirical trends that are investigated in this section. The final procedure involves a combination of both MLLS algorithm and Drude model fitting to propose a local chemical characterization even when several phases coexist.

$$Im\left[\frac{1}{\varepsilon(E)}\right] = \frac{E\Delta E E_p^2}{(E^2-E_p^2)^2+(E\Delta E)^2} \tag{III.20}$$

III.3.1 Analysis of the Li_xSi phase

Quantification of the Li content in alloys

The plasmon energy E_p of binary metallic alloys will evolve monotonously with their stoichiometry, and Li-Si alloys verify that rule. As such, their composition can be quantified from E_p provided a relationship $x = f(E_p)$ (with $x \in [0, 3.75]$) is extrapolated from experimental or simulated data. Three such relationships have been proposed: (i) a second-order polynomial function from J.Danet [122], (ii) a linear function from D. Robert [37] and M. Gauthier [176] as well as (iii) an inverse function from G. Donval [177] who combined computed E_p values with the experimental datapoints of Danet. The latter is to us the more sophisticated description thanks to its joint simulation-experiment approach, and the higher number of datapoints fitted. Unlike other descriptions, Donval's also does verify the boundary $\lim_{x\to\infty} E_p = E_p^{Li}$ which is indicative of the physical significance of the model chosen.

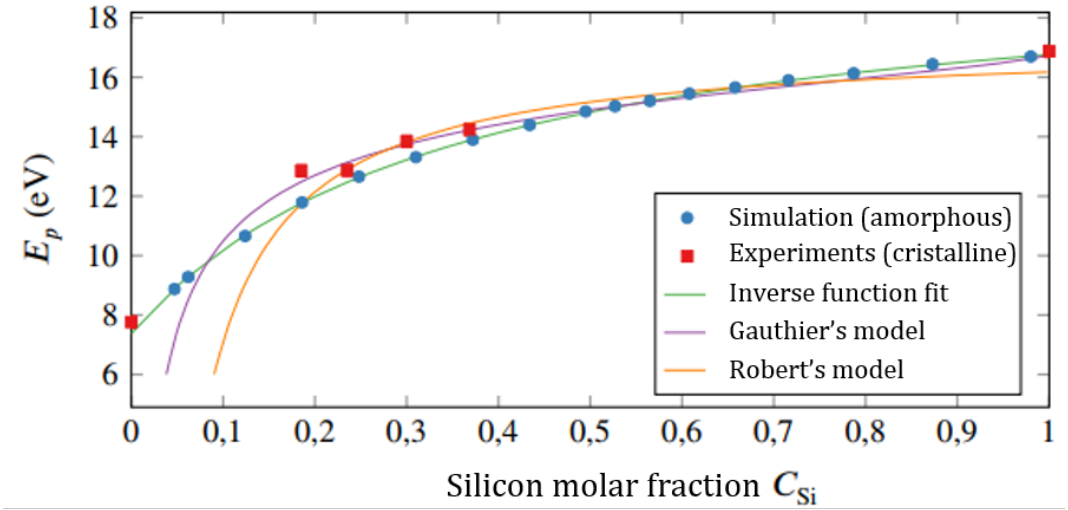

Fig. III.20: Comparison of phenomenological models used to describe Li-Si alloy composition from the plasmon energy E_p. Edited from [177].

We've built upon this by gathering the datapoints from all these works, in addition to our own, to minimize fitting errors and fit an improved and more comprehensive model $x(E_p)$ re-arranged from Donval's expression $E_p(C_{Si})$.

$$x(E_p) = \frac{a - bE_p}{E_p - c} \quad \text{with} \begin{cases} a = & 77.97 \pm 5.82 \\ b = & 4.65 \pm 0.43 \\ c = & \lim_{x\to\infty} E_p = 7.5\,\text{eV} \\ R^2 = & 0.94 \end{cases} \tag{III.21}$$

The fitting process is presented fig. III.21.a and yields a function which can now be applied to calculate the lithium content from any unknown Li_xSi specimen. With spectrum imaging, this means that lithium content maps can be calculated from the E_p maps obtained by fitting the Drude model on every pixel of our spectrum images (fig. III.21.c). Spatial resolutions match our step size of 5 nm (fig. III.21.e) and reveal local inhomogeneities and lithiation gradients, making the method a valuable tool to study, for example, the kinetics of lithiation at the level of a single SiNP, as we do chapter V.

Mitigating thickness effects: the E_{max} parameter

Composition maps calculated using $x(E_p)$ exhibit several artifacts. Alloys appear surprisingly lithium-poor in addition to edges being fitted to unrealistically high E_p values. Upon closer inspection, a mismatch between the position of the peak and E_p appears in cases where the plasmon peak is broadened by its convolution with other spectra or by the thickness itself, as outlined

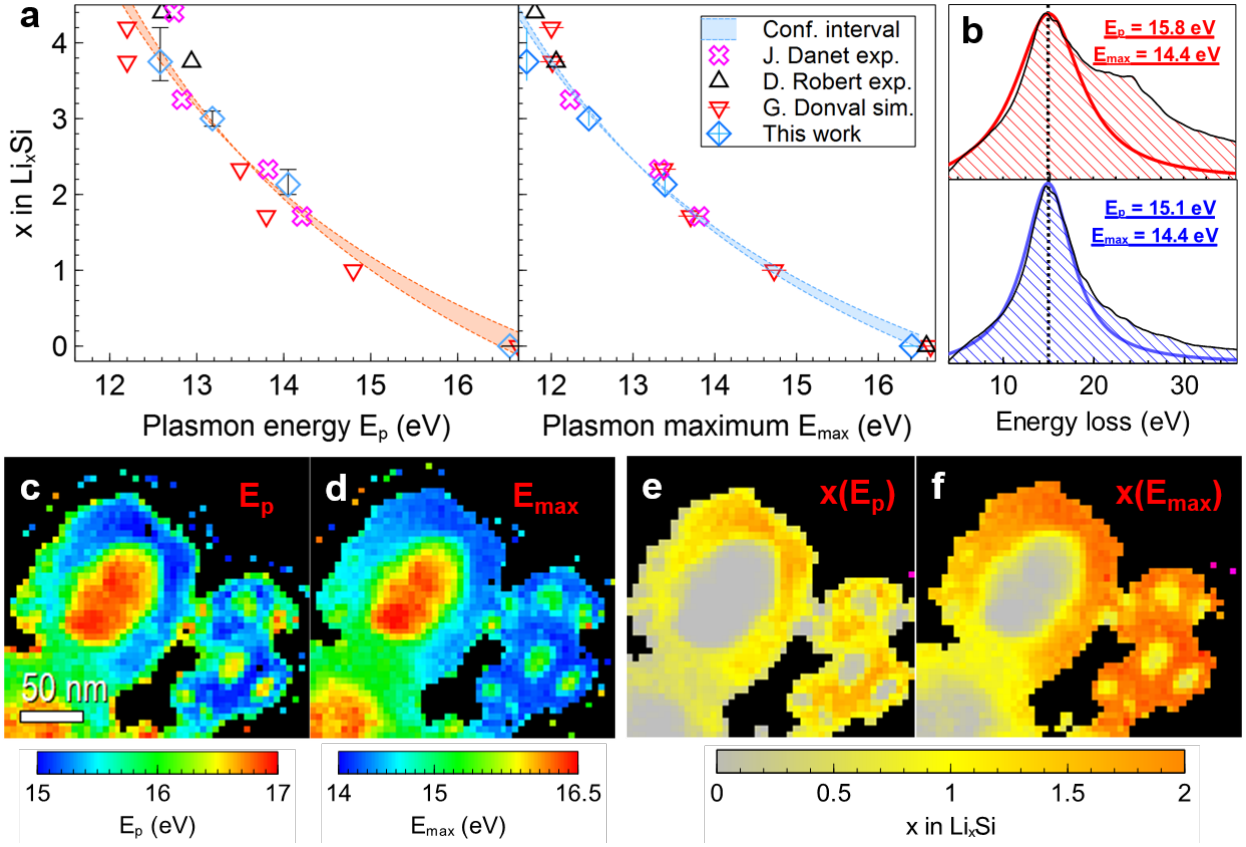

Fig. III.21: a) Fit of the E_p and E_{max} parameters obtained by Drude model fitting on reference Li_xSi samples and simulated spectra. Experimental datapoints from this work were used with a composition x based on assumptions from the litterature: x = 2.2 ± 0.1 for an electrode on its first charge to 30% [33], x = 3 ± 0.1 in subsequent charging to 60% [41, 43] and x = 3.75 ± 0.25 for a fully charged electrode. b) The measured E_p is shifted when the Li_xSi is broadened by a SEI contribution. E_{max} remains constant. c-d) Maps of parameters obtained by Drude model fitting on a spectrum image of lithiated SiNPs. Higher E_p values on edges. e-f) Corresponding lithium content maps. Edge artifacts and thickness effects are negated with E_{max}.

(fig. III.21.b). A phenomenon already commented by G. Donval [177]. Wider peaks mean a larger ΔE which in fact offsets E_p to higher values. These will inaccurately reflect lower lithium contents. Moreover E_p is often measured above E_p^{Si}, a clear indication that this phenomena is detrimental to phase identification. To remedy that, a quantity E_{max} is calculated from both E_p and ΔE. E_{max} is the plasmon maximum as described by Egerton [157], and can advantageously be used in lieu of E_p for lithium content mapping by fitting once again a function $x(E_{max})$. The confidence interval can be seen to be about 15% lower than in the E_p case thanks to the lower variance of the E_{max} dataset. This is once again linked to the compensation of the influence of thickness in measurements with E_{max}.

$$E_{max} = \sqrt{E_p^2 - \frac{\Delta E^2}{2}} \tag{III.22}$$

$$x(E_{max}) = \frac{a - bE_{max}}{E_{max} - c} \quad \text{with} \begin{cases} a = & 68.95 \pm 3.13 \\ b = & 4.14 \pm 0.24 \\ c = & \lim_{x\to\infty} E_{max} = 6.8\,\text{eV} \\ R^2 = & 0.98 \end{cases} \tag{III.23}$$

Estimating the ordering of Silicon

Besides their usefulness to quantify the lithium content in Li_xSi in lithiated electrodes, maps of E_p are also valuable to the analysis of delithiated particles. Since a small energy shift of 0.15 eV exists between the plasmons of crystalline and amorphous silicon [178], E_p maps contain an indication of the crystallinity of silicon. Here E_p can once more advantageously be replaced by E_{max}, for which the aforementioned energy shift is compounded by the slightly larger ΔE of amorphous silicon (see eq. III.22.) [173]. Now, given that our particles are initially crystalline, amorphous areas are characteristic of successive lithiation and delithiation and these maps reveal which areas have cycled and which haven't. Moreover, the plasmon energy scales with the free-electron density, which goes down with the density of directly bonded Si-Si pairs. As solid-state NMR measurements pointed out, this Si-Si ordering is itself linked to the depth of previous lithiations [36, 179]. This means that areas of lower E_{max} have hosted richer Li_xSi compositions. Thus, mere silicon plasmons can tell us not only if a particle was lithiated or not, but also to what extent, effectively making delithiated samples as valuable to analyze as lithiated ones. In fig. III.22.c, crystalline-amorphous core-shell structures are outlined through this methodology.

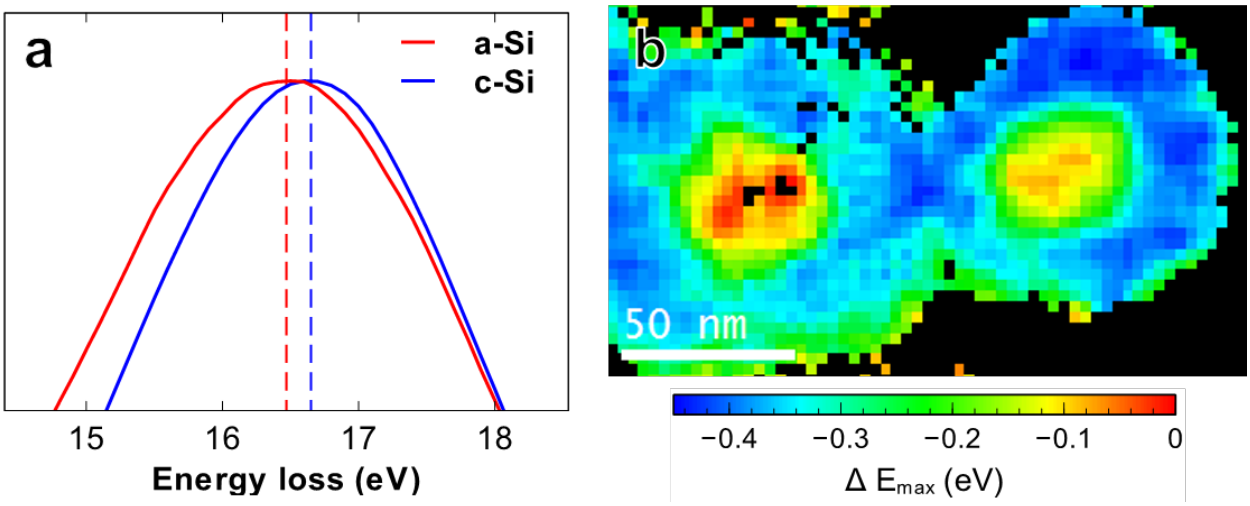

Fig. III.22: a) Energy shift between amorphous and crystalline silicon EEL spectra. b) Example of a-Si/c-Si mapping on a delithiated electrode showing a core-shell structure. Spectrum images were recorded with a step size of 3 nm as dose is not an issue for the observation of pure silicon.

III.3.2 SEI analysis refinements

Just like the plasmons of Li_xSi alloys, experimental organic and semi-organic SEI spectra can be fitted with the Drude model, but with the notable difference that no empirical model is there to interpret their plasmon energy E_p, typically in the range of 20 eV to 24 eV. Understanding what lies at both end of that range can however help us build a scale to which experimental values can be compared. Li_xSi alloys are a binary class of compounds, and quantifying x is equivalent to evaluating the closeness to either pure Li or pure Si. Similarly, the semi-organic and organic SEI compounds we have prior knowledge of - detailed part I.3. - can be roughly classified in two categories: (i) alkyl carbonates, typically lithium ethylene dicarbonate (LEDC) and poly-fluoroethylene carbonate (poly(FEC)) as well as (ii) oligomers such as polyethylene oxide (PEO). If standard E_p values can be identified for each of these representative species, experimental E_p trends could be readily interpreted, be it evolutions at the electrode scale or morphology at the particle level. It is however not a forthright endeavor. While PEO is readily available, molecules such as LEDC and poly(FEC) are hard to come by in a standalone form and we must rely on theoretical predictions. Drude theory predicts a dependence of E_p to the square root of the free-electron density n_e, but is inaccurate in the case of these insulating compounds because it assumes a metal-like behavior. This discrepancy can be accounted for by introducing a electron binding energy E_G [157, 180]. The measured plasmon energy can now be expressed as:

$$E_p^2 = E_{p,0}^2 + E_G^2 \tag{III.24}$$

Where $E_{p,0}$ is the *free electron plasmon energy*, a function of n_e according to the Drude model. LEDC and poly(FEC) electron densities were approximated from the molecules' structure and the densities of electrolyte solvents EC and FEC respectively. Regarding the E_G term, it roughly follows the expression $\varepsilon = 1 + (E_{p,0}/E_g)^2$ according to Penn [181], where ε is the permittivity of a material. Taking estimates from tabulated values of polycarbonate glasses and PEO respectively [182, 183] we calculate estimated standard E_p values for LEDC, poly(FEC) and PEO, which are reported table III.8.

These values are in agreement with experiments performed on polyethylene oxide thin films and are comparable to plasmon energies measured on experimental SEI plasmons that are, as previously mentioned, in the 20 eV to 24 eV range. According to the "carbonate-like"/"oligomer-like" dichotomy enunciated above, E_p values toward the higher bound of that interval can now be associated to PEO-like compounds, while lower values can reasonably be interpreted as alkyl carbonates such as LEDC. This is demonstrated figure III.23, where the distribution of E_p values reveals chemical gradients that cannot be identified by MLLS. Interpretations of the morphologies outlined this way are discussed in part V.3.

Table III.8: Contributions $E_{p,0}$ and E_G as well as the expected plasmon energy E_p of species representative of the organic SEI.

Compound	$E_{p,0}$ (eV)	E_G (eV)	E_p (eV)
LEDC (th.)	15.19	12.42	19.62
poly(FEC) (th.)	15.19	12.97	20.5
PEO (th.)	17.11	16.74	23.94
Reference spectrum "18 eV" (measured)			21.1
Reference spectrum "20 eV" (measured)			22.4
Reference spectrum "22 eV" (measured)			23.67
PEO (measured)			24.2

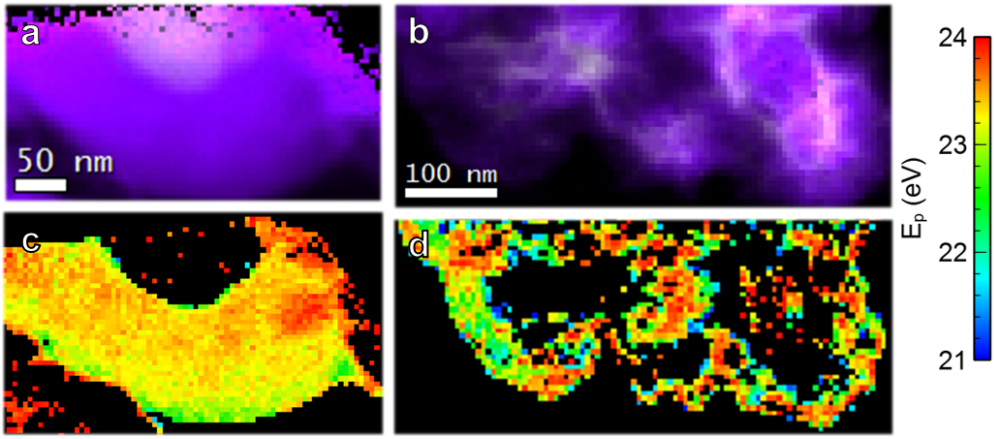

Fig. III.23: a-b) Thickness maps of the *org* phase obtained by MLLS. c-d) E_p maps from Drude model fitting. The distribution of E_p reveals sub-domains that are not visible on MLLS results.

III.3.3 Practical implementation of E_p measurements

Effectively using these empirical and theoretical frameworks for the interpretation of plasmon energy requires precise measurements which are not easy to set up in the highly heterogeneous samples we are considering.

Direct fitting of experimental spectra

Fits can be performed directly on experimental spectra, but several challenges need to be overcome. (i) Spectra include contributions that lie outside the valence excitation described by the model - i.e. interband transitions - and (ii) experimental spectra are often the sum of many components and cannot be fitted by a single Drude component. Attempting to do so can meet the fitness criterion - $R^2 > 0.9$ used in this work - but the physical significance of E_p values determined this way is dubious as it describes an overlap of several plasmons. These two issues can be addressed by limiting the fit to an energy window around the maximum intensity of the spectrum (typically

the top 30%) in order to fit solely the most intense feature of the low-loss spectrum, which is the plasmon peak of the majority compound. Figure III.24.a illustrates this procedure on a Li-Si alloy of unknown composition and an experimental SEI spectrum.

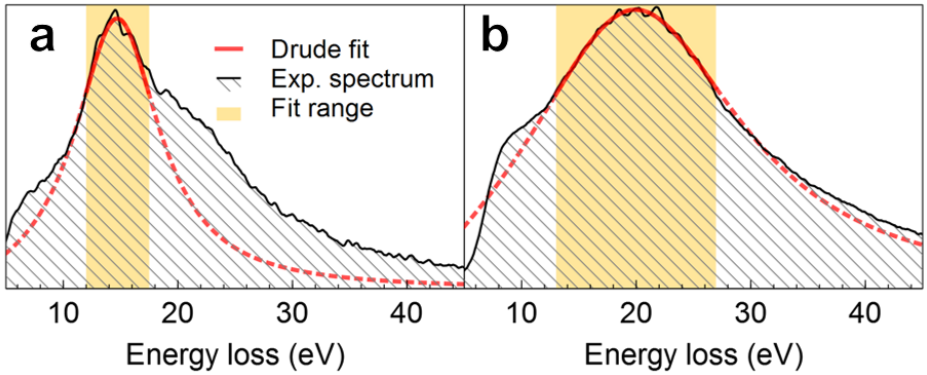

Fig. III.24: Drude model fits over limited energy ranges. a) On an experimental composite Li_xSi/organic SEI spectrum. b) On an experimental SEI spectrum.

Using only the most intense component yields valuable insight but has the adverse effect of truncating possibly large side contributions. Maps obtained this way are consequently biased in areas where numerous species are present. The situation worsens if contributions to the spectra are of similar peak intensity. Typical cases include the superposition of an organic SEI component and LiF in the 20 eV to 25 eV range, where the sharp plasmon peak of LiF (see ref. sprectrum fig. III.15) at 24 eV will drag E_p to higher values, leading to an inaccurate depiction of chemical gradients in the *org* phase (fig. III.25). Likewise the overlapping of Li_xSi alloys of different compositions cannot be properly assessed, as only fitting will only reflect the overwhelming component. In other words, E_p values gotten from direct Drude model fitting are only relevant when they come from spectra that reflect a single phase, and on cycled electrodes it is more an exception than the norm.

MLLS-Drude assisted calculation

A reliable and balanced assessment of the chemistry of each phase thus can only be reached if E_p or E_{max} values can be measured on separate *org* or Li_xSi contributions. This can be approached by performing MLLS decomposition and calculating an average E_p^{av} as a linear combination of E_p^{ref} values obtained on the reference spectra input to MLLS. The individual inelastic scattering intensities I_1^i are used as weights. For the *org* phase, accuracy can be further improved by letting the MLLS algorithm slightly adjust plasmon energy during decomposition, yielding small energy shifts δE^i we can insert in our calculations:

$$E_p^{av} = \frac{\sum_i I_1^i (E_p^{ref,i} + \delta E^i)}{\sum_i I_1^i} \tag{III.25}$$

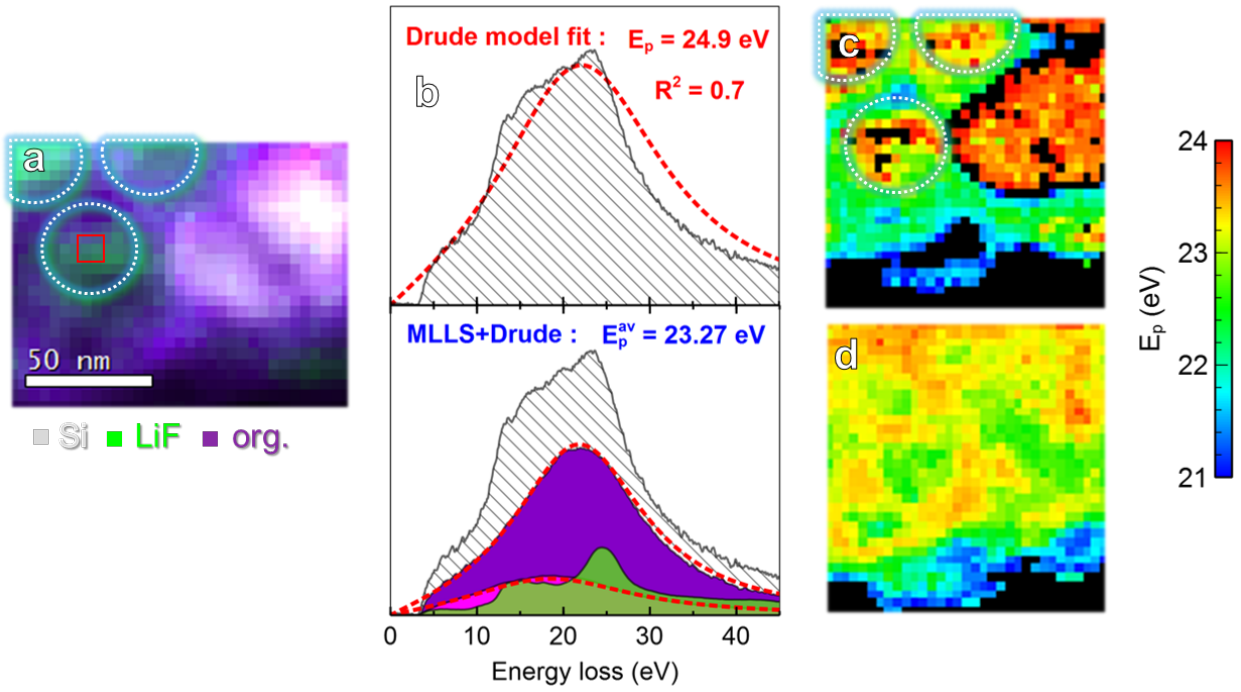

Fig. III.25: a) Thickness maps of a cycled electrode, LiF patches are covered in *org* SEI. b) Illustration of the advantage of the MLLS+Drude fitting method. The calculated E_p^{av} values solely reflects the extracted *org* components. c) E_p map obtained by direct Drude model fitting showing inaccurate higher values in LiF and Si containing areas. d) These issues are avoided when using MLLS-assisted average E_p values.

As shown figure III.25, combining both MLLS and Drude model fitting leads to a noticeable improvement. For the SEI, suppressing the contribution of LiF greatly improves the reliability of our results. As mentioned earlier, the LiF low-loss spectrum indeed has a sharp plasmon at 25 eV which throws off direct fitting of the *org* SEI when the two are overlapped. This is demonstrated figure III.25. On Li_xSi alloys, E_p values obtained from this method are averages over the entire sample thickness, thus maps are truly a 2D projection rather the "slice" we obtain with direct fitting. These more accurate results can furthermore be used to calculate weighted averages at the spectrum image and electrode scale, akin to the protocol detailed section III.2.2.

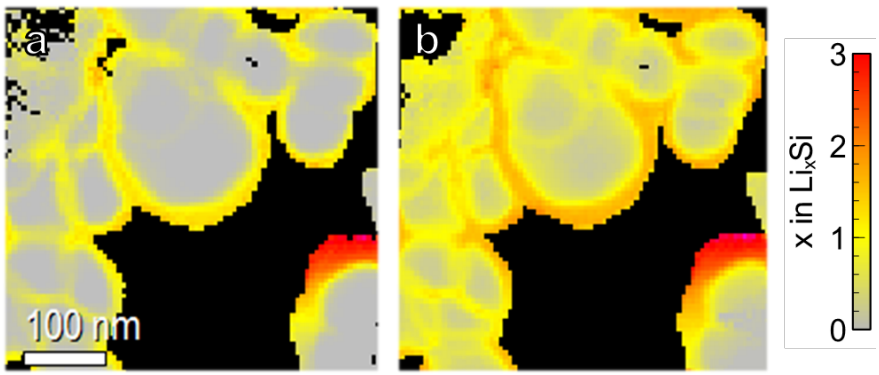

Fig. III.26: Lithium content maps of Li-Si alloys calculated from E_p maps, themselves obtained by a) direct fitting on the top 30% of spectra and b) MLLS-assisted average of reference alloys.

Summary

We show in this section that besides the morphology of phases, low-loss STEM-EELS can also help us elucidate decisively their chemistry. To do so we rely on the interpretations of plasmon energies E_p to distinguish compounds whose spectra are too similar for MLLS. Two frameworks for interpreting these values are presented for Li-Si alloys and the SEI respectively. For the former, we took advantage of the tremendous experimental and modeling work already done to propose a reliable empirical model. Additionally, E_p can advantageously be switched for the plasmon maximum E_max to suppress artifacts introduced by thickness gradients. Drude model fitting can also be shown to be an efficient tool to map the crystallinity of silicon - an asset to analyze delithiated electrodes. In regards to the SEI, we establish clear guidelines to translate E_p into chemical trends while being wary of over-interpretation. This is achieved by calculating theoretical E_p values for the SEI compounds we anticipate to which experimental values can be compared.

Performing either interpretations requires reliable measurements of E_p but the heterogeneity of our sample does not make it straightforward. Direct fitting leads to misrepresentations. To address this a hybrid analysis protocol is proposed to calculate E_p values for both the $\mathrm{Li_xSi}$ and *org* phase independently regardless of their overlapping to other components. Doing to so allows us to reveal chemical sub-domains and gradients, a particularly valuable tool to study cycled electrodes at the particle level.

Chapter IV

Lithiation of a single Silicon nanowire: towards a dynamic measurement

Understanding the degradation of silicon electrodes poses the additional challenge that they are in essence dynamic, and *post mortem* analysis might elude key nanoscale phenomena. Thus, following up on the technique development effort undergone in chapter III, we propose here to design a custom *in situ* experiment that could allow us to witness and study both the initial formation of the SEI on a silicon nanowire (SiNW) and the destabilizing effect of the volume expansion of the $\mathrm{Li_xSi}$ phase. Our attempt aims to fill a gap in the body of existing *in situ* work, and pursues our objective to develop novel characterization techniques for silicon electrode systems. Preliminary *ex situ* tests of our design are then reported. We demonstrate an ability to measure the cyclic voltammetry response of a single silicon nanowire (SiNW) in a liquid electrolyte (carbonate or ionic liquid) and reveal extreme anisotropic swelling and fracture of lithiated nanowires. Moving on to actual *in situ* experiments, results are limited in scope but a proof of concept is there.

IV.1 Designing our nanobattery device

IV.1.1 Framework and existing *in situ* cells

The lithiation of silicon electrodes has been followed *in situ* at the electrode scale early on through through techniques such as AFM [184], Raman spectroscopy [185] and XRD [42, 186], as these techniques can accommodate large samples and require little adaptation of the battery system. *Operando* TEM experiments, however, require a complete overhaul of batteries and the design of model systems from scratch. Two major experimental challenges have to be addressed: (i) downsizing the system to meet the size of the TEM chamber as well as (ii) using an electrolyte compatible with the ultrahigh vacuum environment. Research groups and instrument manufacturers have proposed two distinct strategies to address this last point. The first is to step away from liquid electrolytes altogether and use an electrolyte that can withstand vacuum. This is either a solid one, often the Li_2O layer formed natively when a lithium counter-electrode is exposed to ambient conditions, or a drop of an ionic liquid (IL) whose vapor saturation pressure P_{sat} is sufficiently low. Such an *open* cell is illustrated figure IV.1 in its 2 declinations. In the second, using an IL drop enables the use of positive electrode materials relevant to Li-ion battery systems such as $LiCoO_2$.

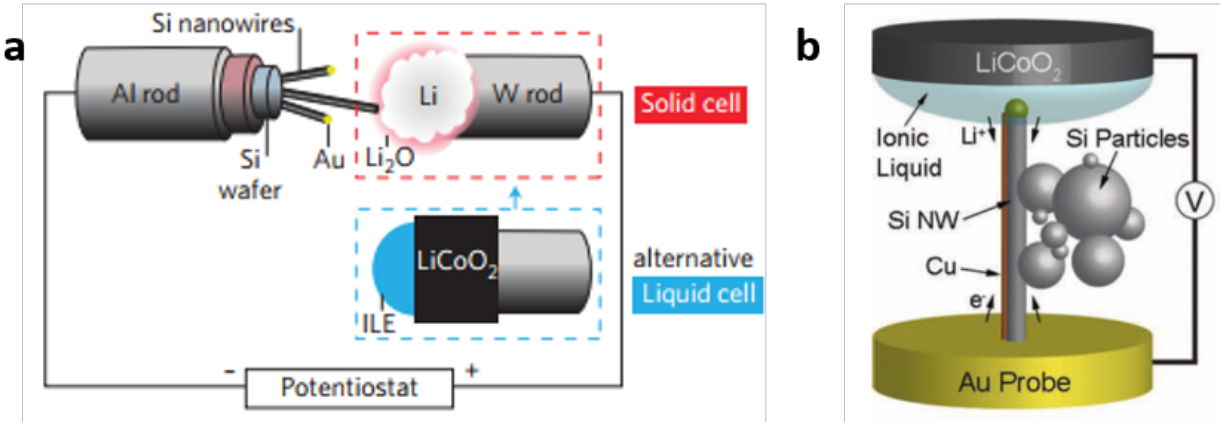

Fig. IV.1: Schematic of open *in situ* cells. a) solid electrolyte and IL-based versions of open cells. Edited from [187]. b) Open liquid cell used by McDowell et all to study the lithiation of nanoparticles [52].

The development of these systems and the most important results achieved with them on silicon can largely be attributed to the work of Xiao Hua Liu and coworkers [54, 187–189]. Those are illustrated figure IV.2. Applications to other battery material systems are covered in a recent review from Yuan et al. [190].

Those impressive results have shed light on mechanisms intrinsic to silicon. The identification of a critical particle size for pulverization, for example, has been determinant to engineer better formulations for SiNP-based electrodes. Likewise, these *in situ* observations revealed the role of stress in the self-limiting behavior that accompanies the core-shell morphology, providing yet

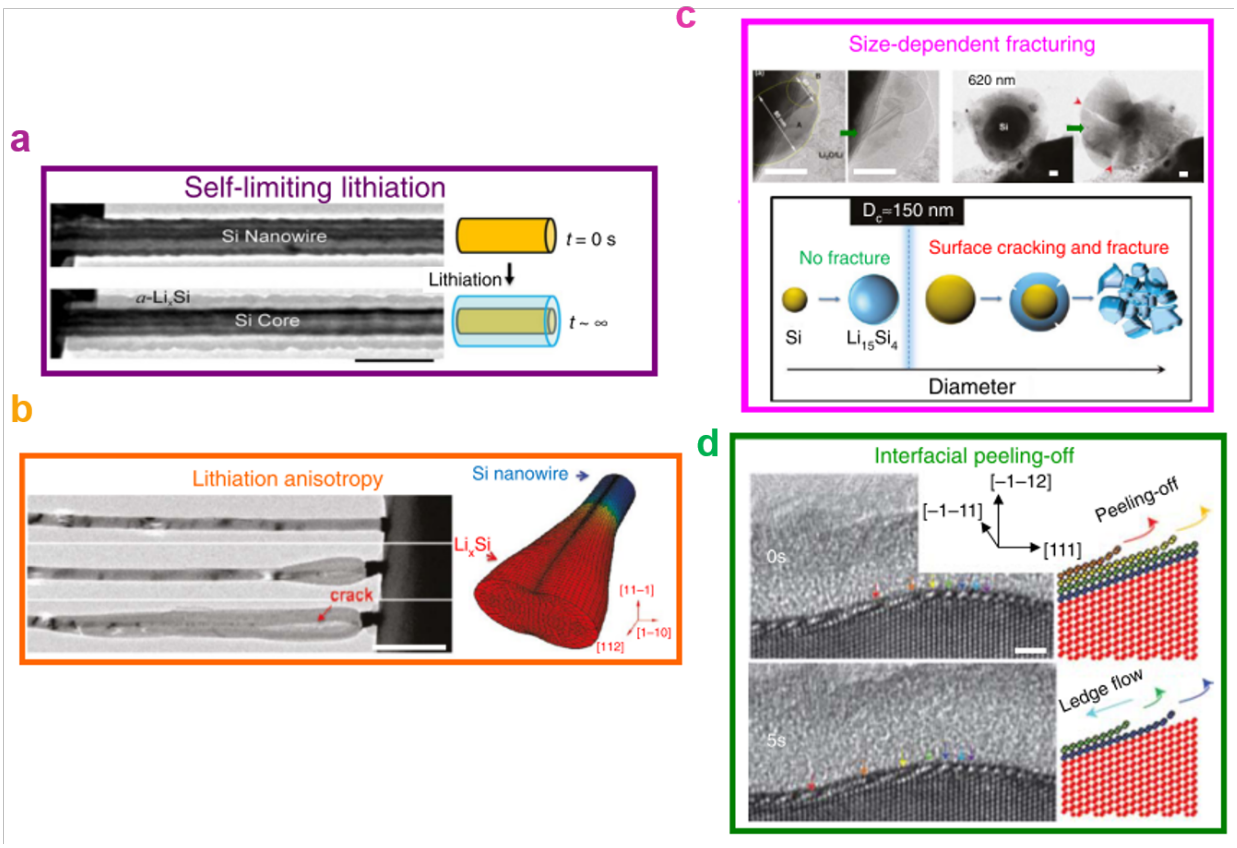

Fig. IV.2: Excerpt of *in situ* TEM results obtained with open cells on silicon nano-objects, showing (a) self-limiting lithiation [189], (b) swelling anisotropy [187], (c) the size dependent fracture of silicon nanoparticles [54] and (d) an atomic scale observation of solid state amorphization [188]. Reproduced from the review of Yuan et al. [190].

another motivation for cycling at limited capacities in actual Li-ion cells. However, the operating conditions of the model systems used in these experiments differ enormously from actual battery cycling. Kinetics especially cannot bear any comparison. Since large ohmic drops have to be overcome in open cells, lithiation proceeds in potentiostatic mode with a negative bias (down to -2 V vs Li/Li^+ [188]) being applied between silicon and the counter electrode. In addition lithium transport is unidirectional as it comes from the tip of the nanowire (even when a drop of IL are used), rather than from all directions when particles are immersed in the electrolyte in Li-ion cells. To address this last point, researchers have put forward designs referred to as *liquid* cells, in which classical carbonate electrolytes are sealed between two chips and protected from the vacuum environment of the TEM. Such a design is illustrated figure IV.3.a.

The main drawback of this design is that a sealed window is naturally quite thick relative to what TEM allows, especially given the swelling due to the pressure differential between the ambient conditions inside and the ultra high vacuum of the chamber (see fig. IV.3.d). As a result achievable resolutions are limited with liquid cells and for silicon they have scarcely been used [190].

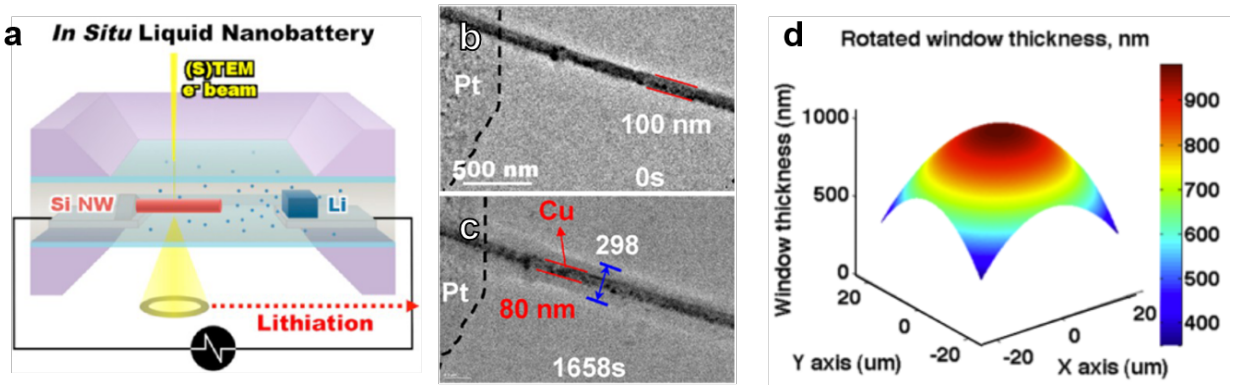

Fig. IV.3: a) Schematic of a liquid cell from Gu et al. [191]. b-c) Low-resolution *in situ* TEM observation of the lithiation of a SiNW in this cell. d) Simulation of the swelling of the membrane of a liquid cell due to the pressure differential, Edited from [192].

IV.1.2 Objectives and presentation of our design

With the qualities and drawbacks of both liquid and solid cell designs in mind, we put forward here a hybrid design that aims to combine a limited sample thickness with the "immersed" geometry we have previously mentioned. In other words our nanobattery shall be an open cell, but with a substrate for the deposition of an electrolyte on a silicon nanowire. An additional objective is that *operando* experiments should proceed *via* voltammetry, as done by Holtz et al. for $LiFePO_4$ in a liquid cell, rather than simple biasing as is usually done in solid cells [190]. We notably base ourselves on the design from Mai et al. reported in their paper *Single nanowire electrochemical devices* and illustrated figure IV.4.

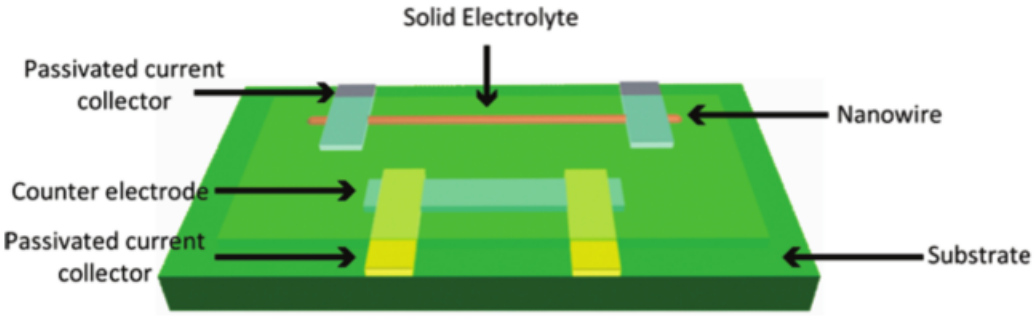

Fig. IV.4: Schematic diagram of a single nanowire electrode device design. A single Si nanowire is the work electrode, and a $LiCoO_2$ nanofilm the counter electrode in a PEO-$LiClO_4$-PC-EC polymer electrolyte. Reproduced from [185].

We propose to revamp this design to adapt it to the constraints of a TEM experiment by integrating two major improvements. First, the SiNW should be deposited on an electron-transparent substrate. To this effect, we use a silicon wafer with a 40 nm Si_3N_4 coat on both sides as substrate, in which a 100 µm-wide "window" is opened after silicon is selectively *wet* etched in KOH. This is notably inspired by the technology developed by Martien Den Hertog [193] for *in situ* heating experiments.

Regarding the electrolyte, we have defined an objective of having our SiNW immersed in a liquid electrolyte and ionic liquids are ideally suited, especially since they have recently attracted attention for actual battery systems [194] thanks to their non-flammability, high thermal and electrochemical stability. We do however need to shape our electrolyte layer in a thin film to limit the thickness of the device. This was achieved by Ferrari et al. who demonstrated ionic conductivities above 0.25 mS/cm for 70:30 blends of 1M LiTFSI in PYR13TFSI and the PVdF-HFP polymer [195]. This electrolyte system dissolved in acetone can be drop-casted onto our substrate and adopts a 100 nm thin film morphology as the solvent dries. This was verified through AFM measurements. We obtain a design that combines the capability for "on-chip" electrochemistry experiments of Mai et al. [185] with a compatibility with TEM experiments. Fabrication steps are illustrated figure IV.5. The initial design of our device and its fabrication protocol can be credited to Julien Danet.

We rely on lithography and physical vapor deposition processes from microelectronics technology. To deposit a single SiNW onto the Si_3N_4 window for example, a resin mask is used to protect the substrate while a dilute water solution of SiNW is drop casted onto the entire sample. Nanowires deposited outside the window are then removed during lift-off. Contacts are then manually aligned on a single nanowire by optical lithography, and the native SiO_2 is etched prior to a 250 nm Cu deposit to ensure a better copper on silicon contact. Regarding the electrode themselves, we have opted for 100 nm to 150 nm thick monocrystalline nanowires that are n-doped (10^{19} at./cm^3) to improve their electrical conductivity. Doping has been shown to improve the first lithiation kinetics [196] and we hope to reduce the potential drop our *in situ* experiment will inevitably deal with.

Fabrication was carried out in the cleanroom on 14 mm $\times$ 14 mm Si_3N_4-coated, 300 m-thick monocrystalline silicon substrates. Photolithography masks were designed to accommodate the fabrication of 16 devices per substrate. $LiCoO_2$ films were deposited by Christophe Secouard and Sophie Tintignac [197], and nanowires grown by Pascale Gentile [198]. To collect individual devices, substrates were then either micro-cleaved or sawed after the application of protective resin film. In total, the development of the fabrication protocol and the preliminary tests reported in the next section required the fabrication of more than 500 devices.

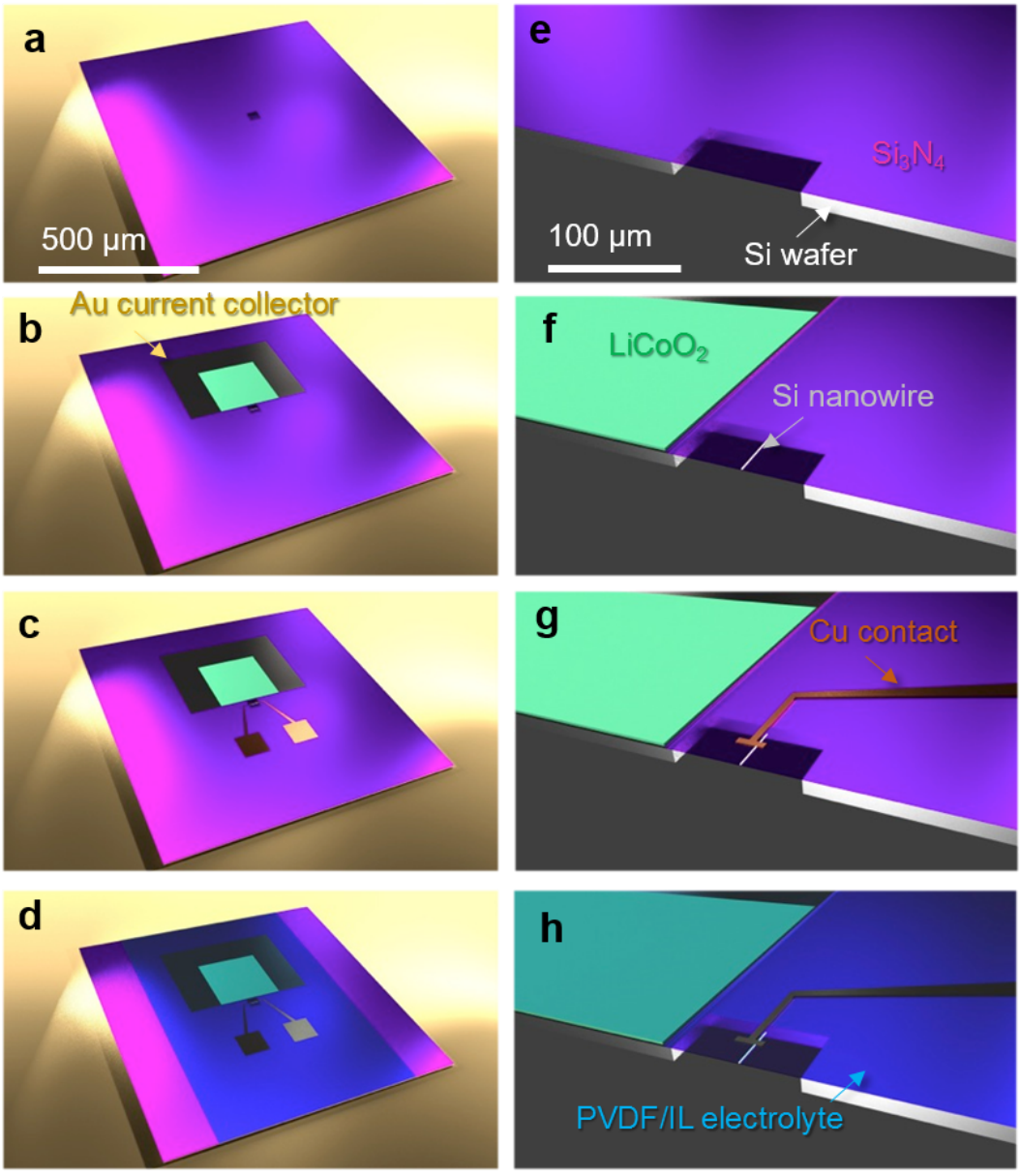

Fig. IV.5: Step-by-step fabrication of our 2 mm × 2 mm nanobattery. a,e) Etching of an electron transparent window. b,f) Deposition of a 200 nm-thick $LiCoO_2$ thin film on a gold current collector (2 physical vapor deposition steps). A silicon nanowire is deposited by drop casting. c,g) Copper contacts are deposited onto the SiNW. d,f) The polymer/IL blended electrolyte is drop casted onto the nanobattery and forms a thin film. The large current collector "pads" are there to facilitate wire bonding to the TEM holder.

IV.2 Single-nanowire electrochemistry

Prior to the *in situ* experiments going live, the ability of our device for electrochemical measurements has to be checked independently. To this effect, a cell was specially designed to accommodate a modified version of our nanobattery chip. In addition, the fabrication protocol was altered in order to allow for the mounting of half-cells in order to test electrodes one by one.

IV.2.1 SiNW-half cells and preliminary cyclic voltammetric study

A schematic of this cell is presented figure IV.6. Moreover, we have modified the cell dimensions as well as the copper collector geometry so as to take contact on several nanowires at once and facilitate our preliminary experiments. The electrode in the new configuration is a 400 µm copper "comb" that covers several nanowires as represented in the insert of figure IV.6.a and the SEM observation of figure IV.7.c. Half cells are then mounted by fixing the chip in a teflon clamp and stacking an electrolyte-soaked Whatman separator and a piece of metallic lithium ribbon onto the nanowire window. Current collectors of both electrodes are connected to the cell *via* wire bonding. The novel rectangular dimension of the chip is a development introduced in later stages of this work. It enables the use of gold rather than copper as a current collector, which helps with wire bonding. It is also worth noting that measures were taken to ensure currents as small as a few picoamperes could be measured, as we would expect from the voltammetric response of a single nanowire. A BioLogic SP-300 potentiostat is used with a its low-current option, and either the glovebox or the TEM will act as Faraday cage.

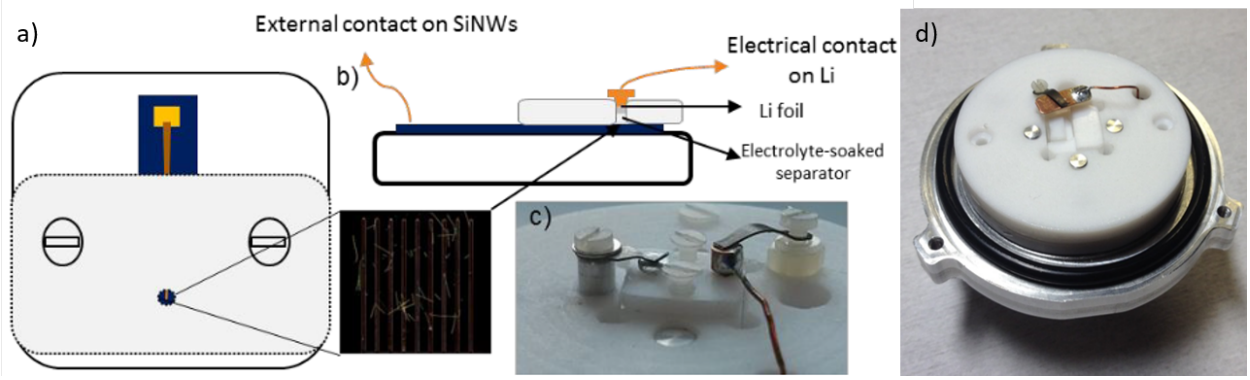

Fig. IV.6: a) Schematic of our modified nanobattery chip fixed in a teflon clamp. A 1 mm-diameter circular window is opened to mount half cells onto the nanowires represented in the insert. b) Side view of the half cell configuration. A toroidal joint placed under the teflon cap seals the cell. c) Photography of the mounted half cell. d) Photograph of the entire test cell.

In this configuration we were able to follow the lithiation of nanowires by cyclic voltammetry between 1 V and 10 mV vs. Li/Li^+. Two of such voltammograms and corresponding *post mortem* SEM observations are reported figure IV.7. The two experiments presented here reflect a successful

scaling down of the system. Indeed, lithiation reduction peaks could be measured in 5 consecutive cycles with currents as low as 1 nA accurately picked up (figure IV.7.e). This confirms that our on-chip design is suited to perform lithiation cycles on a few nanowires and accurately record their voltammetric response. This gives us the go ahead for *in situ* experiments on a single one.

Besides the proof of concept they represent, those two voltammograms contain noteworthy results themselves. We first note that in both experiments the integrated area of delithiation oxidation peaks *b* is about 5 times lower than that of the lithiation reduction peaks *a*. This indicates that most of the lithium inserted in silicon upon alloying is trapped and does not cycle reversibly. That could be owed to the loss of electrical contact as observed with the delamination of the copper layer in the insert of figure IV.7.c. It prompted us to reduce the size of our nanowires from 150 nm to 100 nm. In the 2nd experiment of figure IV.7.e however, we see 2 delithiation peaks, one sharp (*b*) at about 0.5 V vs. Li/Li^+ and the other broader (b^*) at a lower potential. This indicates a significant discrepancy in the phases formed in both experiments. The *b* peak is indeed associated with the dealloying of crystalline $Li_{15}Si_4$ into Li_2Si [43], whereas b^* suggests the dealloying of amorphous Li-Si alloys. Given the different sweep rates used in both voltammetries, it suggests that higher lithiation rates foster the formation of c-$Li_{15}Si_4$, in line with the *in situ* NMR results of Ogata et al. [45]. Besides the Li (de)alloying reactions, peaks that correspond to the SEI formation are also measured in the voltammogram of IV.7.e as *c* and *d*. This oxidation peak does not come as a surprise, as the organic part of the SEI is known to oxidize upon electrode discharge in what is referred to as SEI *breathing* [121].

IV.2.2 *Post mortem* characterization of lithiated SiNW

The morphology of those lithiated SiNWs stands out. With a sweep rate of 1 mV/s, nanowire also undergo tremendous plastic deformations in the direction normal to their growth, going as for a making complete loops as illustrated figure IV.7. Furthermore, we witness their evolution from a cylindrical geometry (fig. IV.7.f) to a ribbon-like configuration (fig. IV.8). A longitudinal fracture appears along the growth axis of the nanowire, and a dumbbell shape emerges. Such morphologies were also reported by Liu and coworkers in their *in situ* experiments [187]. Subsequent studies by Lee, McDowell et al. [199] showed that this structure heavily depends on the SiNW growth axis as lithiation does not proceed isotropically. Longitudinal fractures are typical of <112>. Understanding the stresses involved in such extreme plastic deformations is of practical interest, and several authors have simulated stress profiles and morphologies for <111>, <110> and <112> nanowires, as reported in a recent review from An et al. [200].

To distinguish the morphology of nanowires and of their SEI, we have extracted lithiated SiNWs from the chips in the FIB and prepared them on half-grids to carry on TEM analyses. This is illustrated figure IV.9. Since no vacuum transfer protocol from the SEM existed at the time of

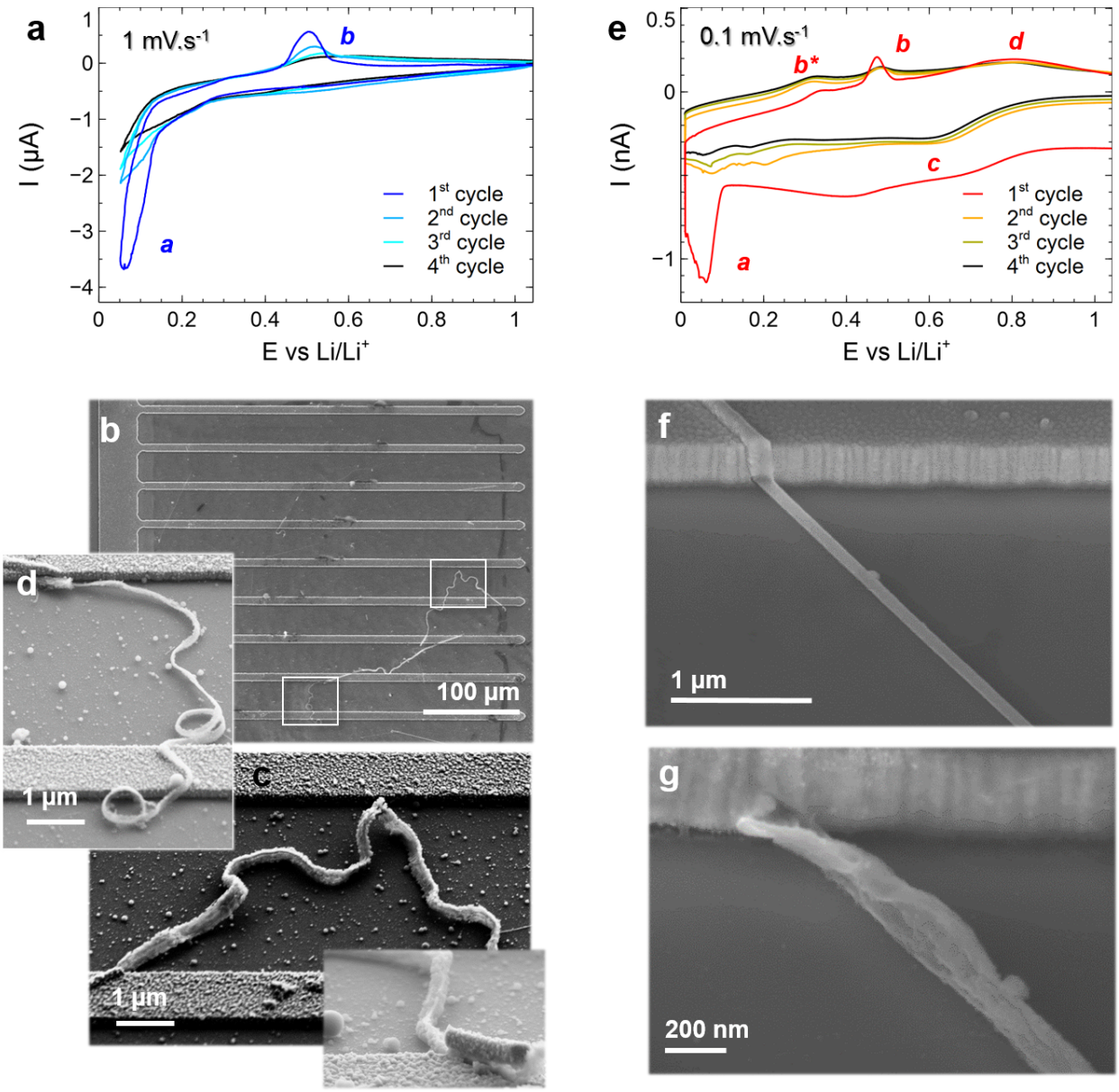

Fig. IV.7: (a,e) Voltammograms between 1 V and 10 mV vs. Li/Li^+ for SiNW half cells at sweep rates of (a) 1 mV/s and (e) 0.1 mV/s. In the latter the potential was held at 10 mV vs. Li/Li^+ for 5 minutes. (b-d) *Post mortem* SEM observations of 2 SiNWs of the electrode corresponding to the voltammogram of (a). The fast potential sweep rate is associated with larger plastic deformations and delamination from the current collector as represented in the insert of (c). (f-g) Before and after SEM observation of one SiNW that cycled in the experiment reported in (e).

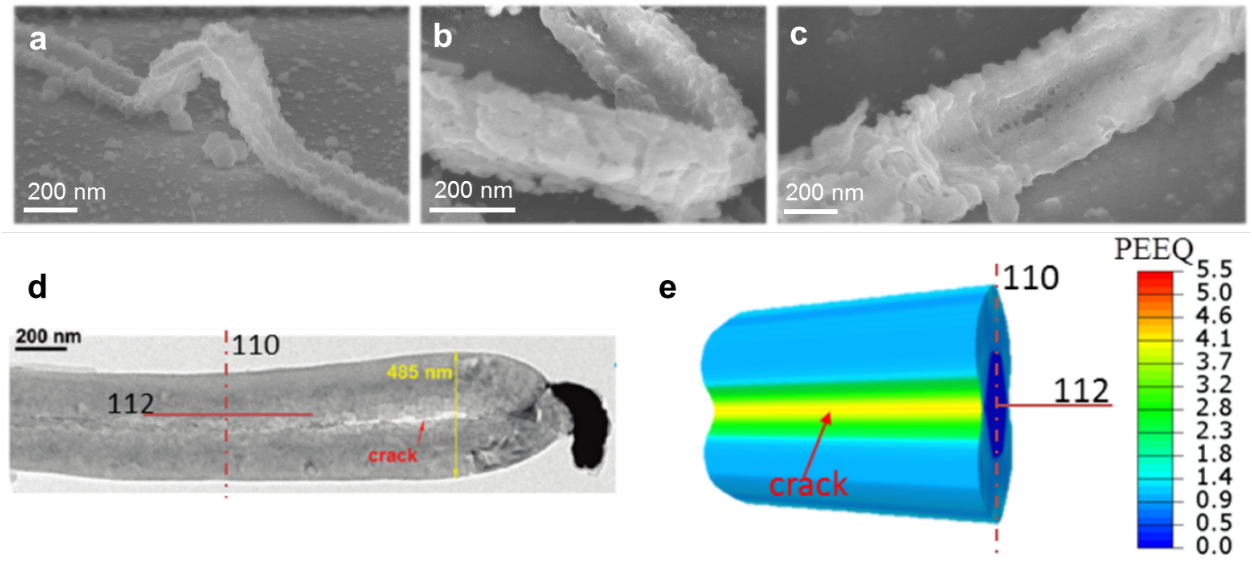

Fig. IV.8: a-c) SEM observations of lithiated <112> silicon nanowires. d) TEM micrograph of a fractured SiNW after *in situ* lithiation [187]. e) Simulated map of the equivalent plastic strain (PEEQ) that develops in a <112> silicon nanowire upon lithiation.

the experiment, samples were exposed to ambient oxygen and water. Lithiated silicon cannot be directly observed as a result. Lithium most likely reacted into LiOH and Li_2O, now part of the layer represented as purple. However, the shape of the corresponding EEL spectrum indicate that carbonated compounds are prevalent in the layer. We see here that after only 5 cycles, the SEI has accumulated to a layer that is almost 100 nm-thick. This is likely related to the tremendous stresses applied to the SEI as the nanowire deforms and twists. This is supported by TEM observations of a second lithiated nanowire, figure IV.9.d-e, which feature the apparition of cracks in the SEI. Fresh surfaces are thus exposed to electrolyte reductions cycle after cycle. In figure IV.9, the cross section of a 3rd nanowire is extracted rather than its full length. We observe a crescent-like shape fractured in its center, as we would expect from the dumbbell morphology outlined earlier for <112> nanowires.

It can be argued that these characterization results are not critical to the understanding of the system at hand. we feel however that they are a testament to experimental capabilities we have developed to accompany single-nanowire electrochemistry, and as such are an integral part of this development work.

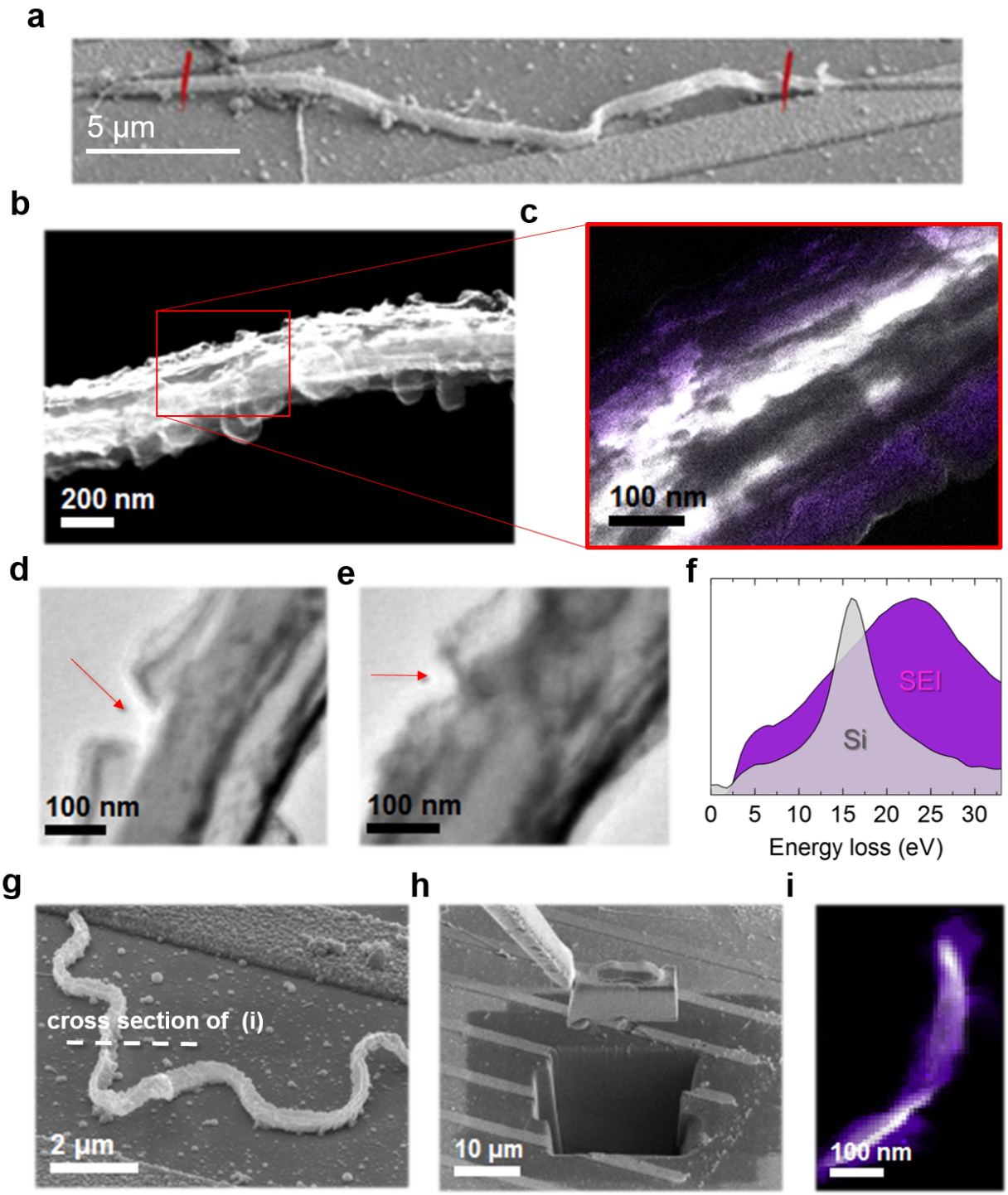

Fig. IV.9: TEM analysis of lithiated SiNWs. a) SEM observation prior to FIB extraction for (b-c). Red lines indicate where the nanowire was cut. b) HAADF STEM observation. c) Composite color map of silicon (16.5 eV, white) and the SEI (23 eV, purple) from an EFTEM experiment. The 2 EEL spectra this corresponds to are represent in (f). d-e) SEI cracking along another SiNW extracted through the same process. g-h) SEM observations prior to the extraction of a 3rd nanowire. i) Composite color map from EFTEM observations of the cross section of the nanowire illustrated in (a).

IV.2.3 *Ex situ* testing of the complete device

Our re-purposed on-chip half cells have proven their capacity to perform voltammetries on SiNWs, and preliminary tests continue on other individual components of the full device. The crystallinity and electrochemical performances of the $LiCoO_2$ layer were successfully demonstrated (not reported here), and we move on to a critical constituent of our system: the electrolyte. The matter of its thickness first requires fine tuning of the fabrication protocol, as an overly thick layer would be detrimental to our TEM observation capabilities. Our polymer/IL blend is dissolved in acetone and drop-casted onto the chip. Subsequent AFM measurements indicate that the thickness of the layer will strongly depend on how dilute our solution is. A factor of 12 yields 100 nm-thick layers that immerse our nanowire as designed.

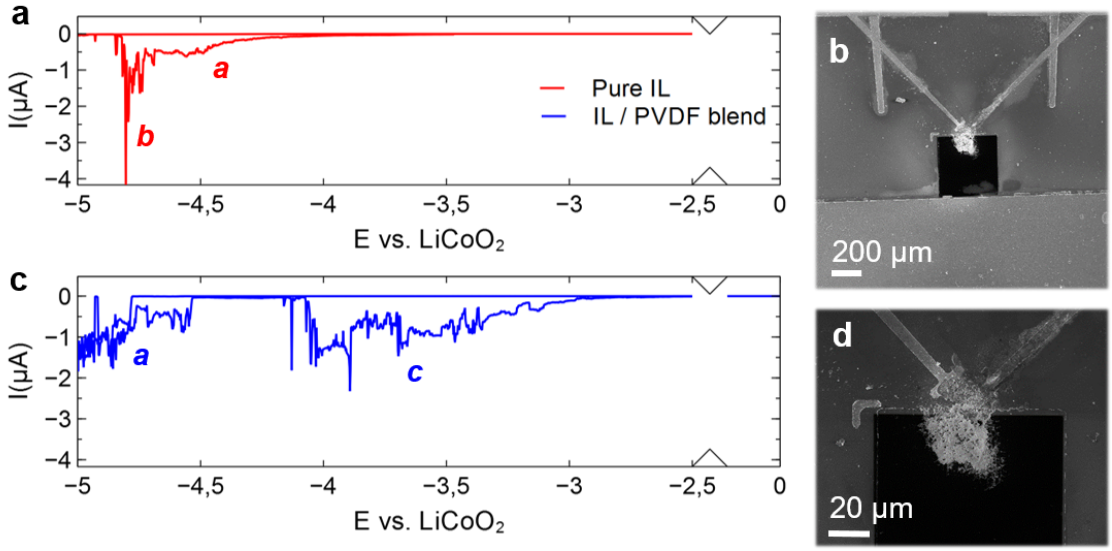

Fig. IV.10: Preliminary *ex situ* cyclic voltammetry tests at 0.1 mV/s of the complete nanobattery device with a single nanowire electrode. a) With a pure PYR13TFSI/1M LiTFSI ionic liquid electrolyte. c) With the final 70:30 IL/polymer thin film electrolyte. b,d) SEM observation of the electrode used in (a) after rinsing. Lithium was electro-deposited in a dendrite morphology.

With the full device fabricated, we carry on cyclic voltammetry between a single SiNW and $LiCoO_2$. Since a large overpotential is expected from the impedance added by the connection of $LiCoO_2$ by wire bonding, potentials were swept down to -5 V vs. $LiCoO_2$. Two of such experiments are reported in figure IV.10. Using a pure IL electrolyte first (fig. IV.10.a) we see that peaks are indeed significantly offset. *b* corresponds to the electro-deposition of lithium as seen in the SEM observations (fig. IV.10.b,d). Given that in our 2-electrodes setup $LiCoO_2$ is in a large excess and should be at a fixed potential between 4 and 4.2 V vs. Li/Li^+ [197], peak *b* is measured at -4.9 V vs. Li/Li^+ thus offset by about 800 mV. This is even more pronounced with the polymer/IL blend (fig. IV.10.c). The pseudo-plateau *a*, which likely corresponds to SEI formation given its shape, is offset by an extra approximate 300 mV. A new feature *c* also stands out but could not be identified.

Those results are telling of the very high internal impedance intrinsic to our device (estimated at 10^{10} Ω by Mai et al. [185]), and show that the potential should be swept down to -6 V vs. $LiCoO_2$ to ensure potentials drops are overcome.

IV.3 Towards *operando* TEM experiments

IV.3.1 In-house biasing holder development

With the device fabricated and its components tested individually *ex situ*, we now get to the TEM holder itself. We have adapted an *in situ* biasing holder already developed in-house for the JEOL 3010 microscope. As shown figure IV.11.a-b, its "head" is modular and can be replaced by one adapted to the dimension of our nanobattery chip. A new design was conceived and fabricated with the help of Nicolas Mollard. For *operando* experiments, devices can be mechanically fixed in the socket of the head, with the Si_3N_4 window facing the opening made for that purpose.

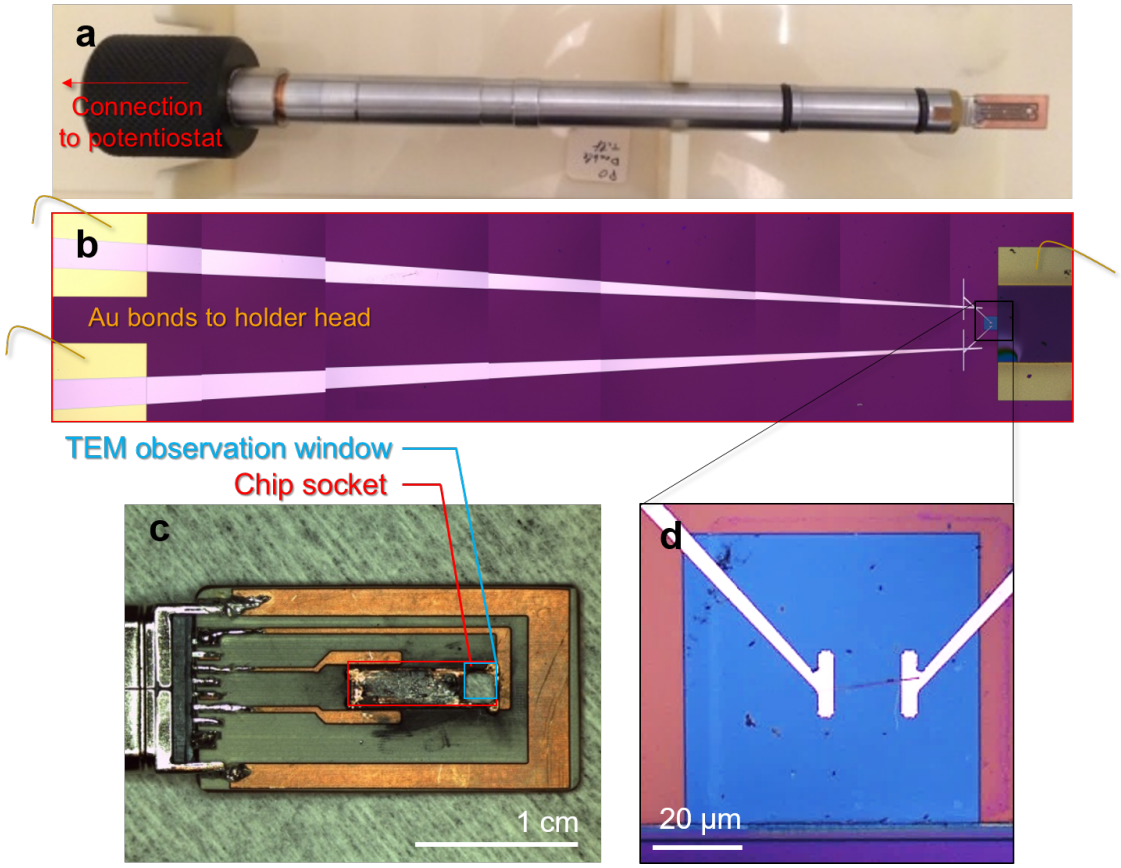

Fig. IV.11: Photographs of the *in situ* experiment apparatus. a) Biasing holder for the JEOL 3010. b) On-chip nanobattery. c) TEM holder "head". d) Single SiNW with copper contacts on the electron transparent Si_3N_4 window.

IV.3.2 *In situ* nanobattery operation & results

Performing voltammetry in the TEM poses several challenges. At 0.1 mV/s, cycling from -1.5 V to -5 V takes 10 hours. Given the sensitivity of lithiated species and polymers to the electron beam, exposure to the electron beam cannot be continuous. Otherwise our electrolyte would be destroyed by irradiation before lithiation has had a chance to proceed. Such extensive damage on the polymer/IL electrolyte is illustrated on figure IV.12.

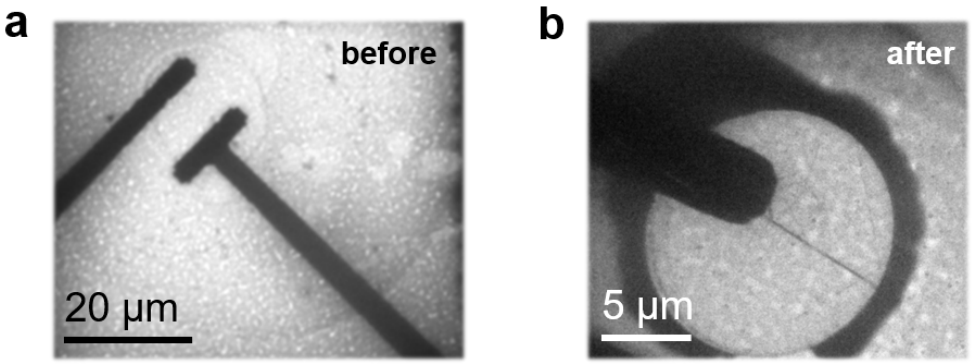

Fig. IV.12: Low magnification TEM micrographs of the electrolyte before and after an *in situ* experiment.

Consequently, TEM acquisition should be intermittent and happen automatically at fixed intervals, with the electron beam being blanked in between. To do so, scripts were developed for the JEOL 3010 so that the TEM only acquired every 10 s when the potential passed below -4.5 V vs. Li/Li^+. Unfortunately, most devices presented either short-circuits or faulty electrical contacts. Few experiments could actually be carried on as screening through samples proved laborious. We attribute this to the unreliability of manual bonding, especially given how thin the protective layers of Si_3N_4 is. Nonetheless, experiments that could be performed in practice are akin to that reported figure IV.13.b, which closely resembles the voltammetric response of figure IV.10.b recorded *ex situ* with the dedicated cell. Comparing the two shows that an additional large impedance tilts the response, which we attribute to even poorer contacts in the TEM holder compared to the *ex situ* cell. As encouraging as this is, we were not able image the lithiation and/or SEI formation reactions that should correspond to this voltammogram in the TEM.

We were however able to perform *in situ* lithiation by condensing the beam on our SiNW for a few seconds. Such beam-induced reactions in a liquid electrolyte have been used purposefully in the past to study the lithiation of silicon [201] in the TEM. As shown by Abellan and coworkers [202], salts such as LiTFSI can be decomposed into Li^+ and further react with free electrons under the beam. This process is exemplified figure IV.15. We see here that after such a brief time interval, the classical core-shell morphology has already developed in our nanowire. However it was not lithiated homogeneously. The area directly under the condensed beam, figure IV.14.c, exhibits a larger shell and a thinner core than the other end of the nanowire illustrated figure IV.14.b. Moreover darker

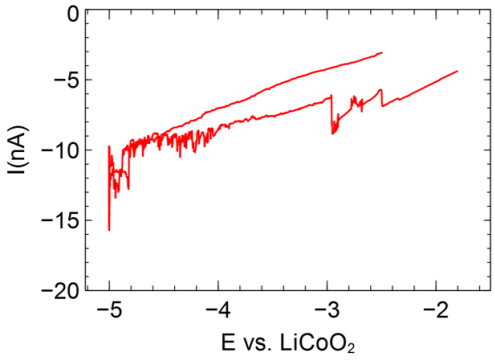

Fig. IV.13: Cyclic voltammetries from -1.5 V to -5 V at 0.1 mV/s from the *in situ* operation of our nanobattery.

contrasts at the surface of our nanowire suggests the formation of a SEI approximately 15 nm to 20 nm thick.

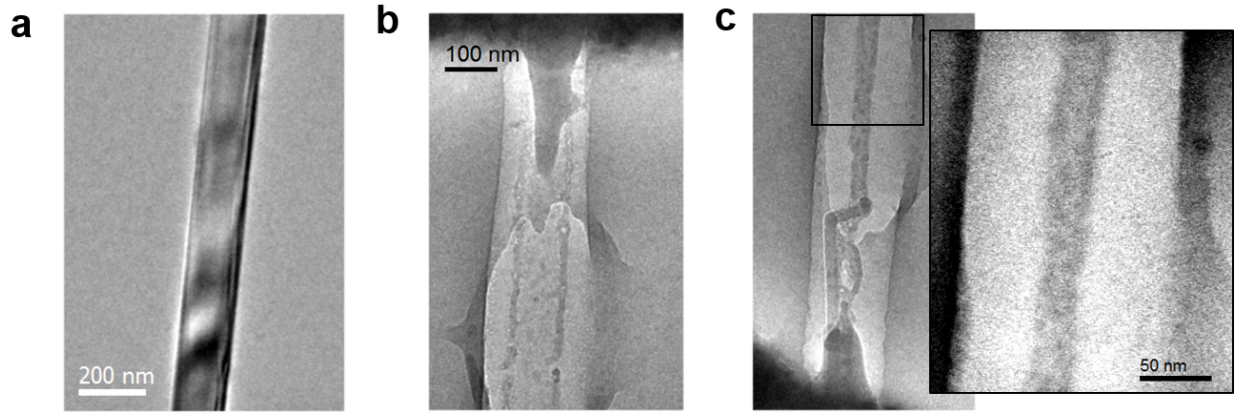

Fig. IV.14: TEM micrographs of a SiNW that underwent beam-induced lithiation *in situ*. a) Observation of the nanowire prior to extensive exposure. b-c) After the electron beam was condensed on the nanowire for a few seconds.

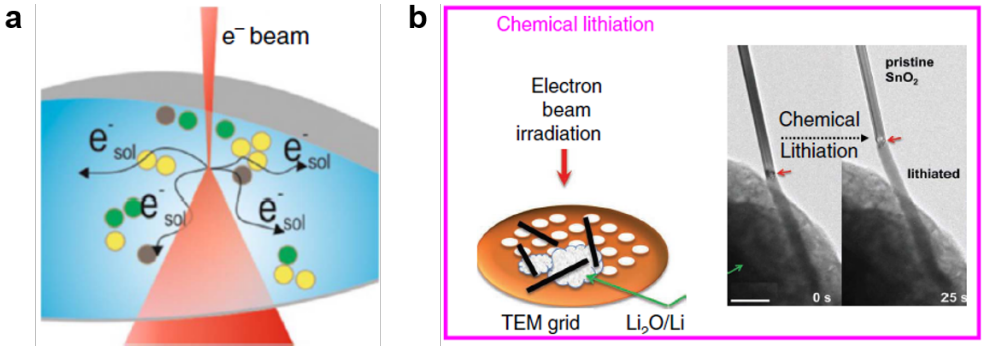

Fig. IV.15: a) Schematics of beam-induced electrolyte decomposition [202]. b) Lithiation of a SnO_2 nanowire driven by beam-induced Li_2O decomposition. The scale bar is 500 nm. [203]

IV.3.3 Conclusion and perspectives of further development

The development of the in-house *in situ* TEM experiment reported in this chapter has been an ongoing effort throughout this thesis work. We have demonstrated that microelectronics fabrication techniques can be harnessed to produce specifically purposed on-chip cells for the electrochemical study of individual nano-objects. Thanks to contributions from solid state battery technology (crystalline $LiCoO_2$ thin films and polymer electrolyte) and cleanroom protocols (custom Si_3N_4 electron-transparent windows) on one side and TEM on the other, we place ourselves at a crossroads of instrumentation and characterization. The shortcomings of the approach, especially regarding electrical contacts, have motivated continuous improvements and a new design is proposed to address the issues we have faced by removing bonding altogether. We believe that using standardized contacts in a 4 or 6-point biasing holder would provide superior reliability. A new chip design adapted to such a holder from DENS is proposed and fabricated, although *in situ* operation could not be achieved with the thesis time frame. It is presented figure IV.16. Nevertheless, *ex situ* results prove electrochemistry can be performed on few to single silicon nanowires and correlated to morphological characterizations. Direct evidence was notably gathered for current collector delamination and the detrimental effect of the rate of lithiation on capacity retention. Those two local phenomena are thought to be intrinsic to silicon and will play a role in the discussion on aging presented chapter VI.

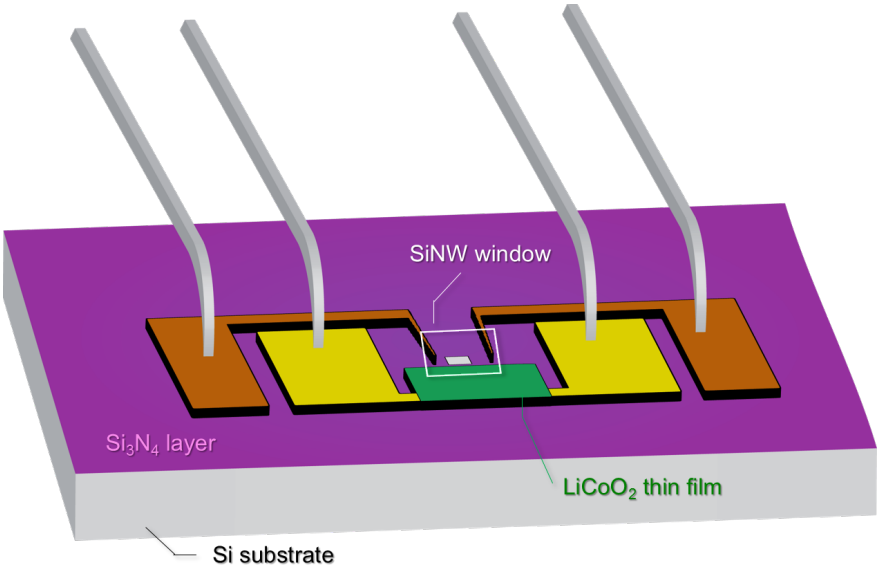

Fig. IV.16: Schematic of the new chip design to bypass problems associated with manual wire bonding. The 4 point probes of the commercial *in situ* holder are represented.

Chapter V

First cycles and particle-scale reaction mechanisms

The STEM-EELS methodology described in chapter III allows simultaneous observations of the chemistry and morphology of nanoparticles and the SEI. In this chapter, we take advantage of this capacity to first study the lithiation process itself in nanoparticles. Insight is gathered on how the core-shell structure and the lithium content of nanoparticles evolve with the state of charge (SoC) in the first cycle, and outline a process in stark contrast with the biphasic one identified for microparticles. To further investigates the driving forces behind this mechanism, a model is then proposed based on the strain mediation effect put forward by Zhao [204], McDowell [52] and others with the additional input of our own strain measurements. Emphasis is then put on the SEI morphology. The mosaic model (see chapter I.2) is confronted to experiments, and the SEI's internal structure is described qualitatively.

V.1 Challenging the biphasic lithiation process in nanoparticles

V.1.1 Effect of the particle size and context

As described part I.2., the lithiation of crystalline silicon proceeds through solid-state amorphization. A reaction front progresses inward, creating a core-shell structure when nanoparticles are used. This reaction is reported to be a biphasic process from the pseudo-plateau seen in galvanostatic electrochemical data [33, 186], with the newly created amorphous phase having a fixed lithium content x. However a wide array of values were reported for x, ranging from around 1 to 3.5 Li/Si at. ratio. An overview of this spread of values is given table V.1. Two groups of results stand out : (i) at the lower end, measures taken on nanoparticles with compositions Li_1Si-Li_2Si, and (ii) higher values from larger micrometric particles.

Li to Si ratios in this last set concentrate near $x = 3.2 \pm 0.3$, regardless of the state of charge (SoC). Given that the maximum ratio is known to be $x = 3.75$ in fully lithiated silicon [205], those values suggest that in micrometric particles the first lithiation is indeed biphasic. This behavior is however quite different for nanoparticles. There, measured Li/Si ratios lie between $x = 1$ and $x = 2.5$. The most comprehensive set of results comes from the thesis work of D. Robert [37], who reports Li/Si ratio distributions heavily dependent on the SoC (fig. V.1).

Table V.1: Overview of Li_xSi lithium contents for the first lithiation of silicon electrodes reported in the literature. The "XRD" method refers to an indirect determination of the lithium content from the intensity of the diffraction peak of crystalline Si and the electrochemical data.

Ref.	Particle size	SoC	Method	Li/Si at. ratio
Limthongkul et al. [33]	1-5 µm	30%	XRD	2.17
Li et al. [206]	1-5 µm	30-100%	XRD	3.5
Hatchard et al. [186]	1-5 µm		XRD	3.5
Key et al [207]	1-5 µm		NMR	3.4 ± 0.2
Danet et al. [35]	1-5 µm	30-50%	EELS	2.9
Robert et al. [37]	1-5 µm	40%, 100%	EELS	3.3, 3.5
Bordes et al. [208]	5-10 µm	25%	AES/ToF-SIMS	3.1
Gauthier et al. [209]	50 nm	90%	EELS	1.4-1.9
Radvanyii et al. [41]	100 nm	30%	AES	1-2
Trill et al. [210]	100-200 nm	15-50%	NMR	1.7-2.3
Robert et al. [37]	100 nm	40%, 100%	EELS	1.7 ± 0.4, 2.5 ± 0.5

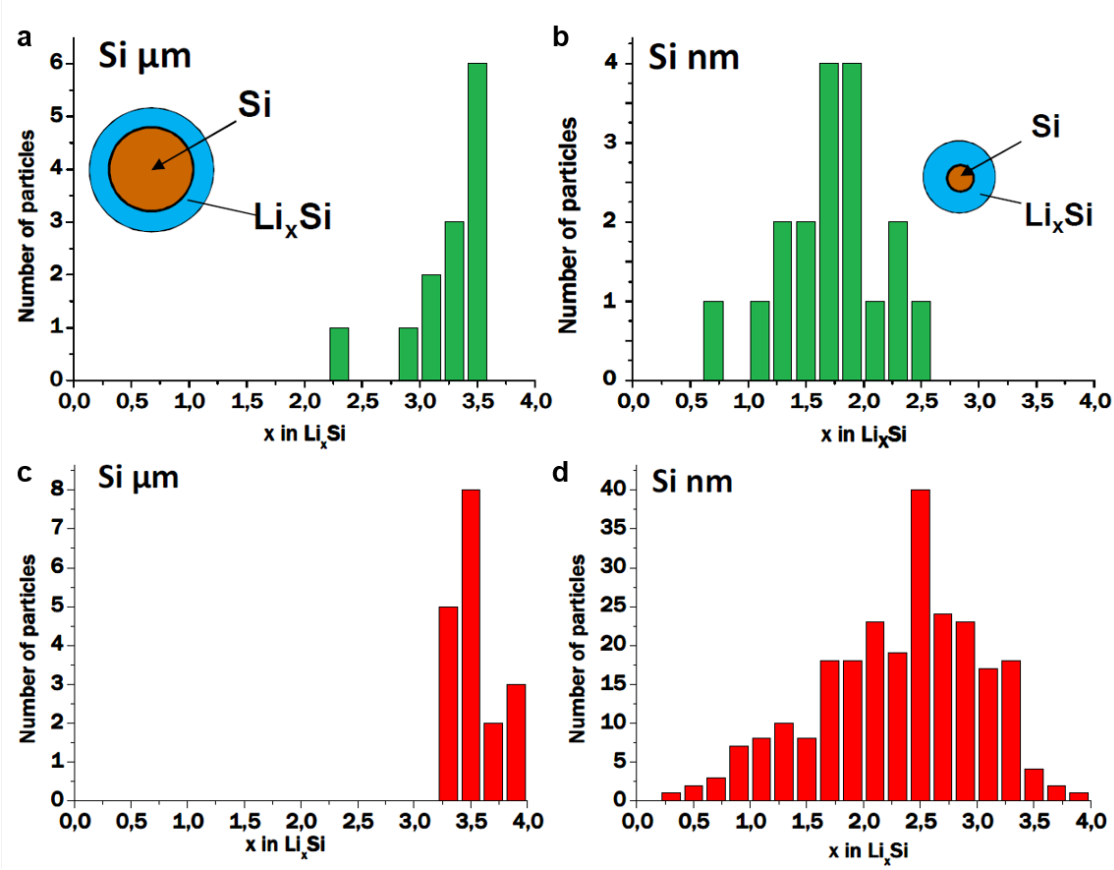

Fig. V.1: Li/Si atomic ratios measured by STEM-EELS in silicon microparticles and nanoparticles at (a,b) 40% partial lithiation and (c,d) full lithiation. Edited from D. Robert's PhD [37].

Concurrent amorphization and solid-solution processes

This discrepancy puts the microparticle result in a new light. The presence of $\mathrm{Li}_{3.2\pm0.3}\mathrm{Si}$ is likely not the product of a single biphasic electrochemical reaction c-Si/$\mathrm{Li_xSi}$. If it were, similar compositions would be found across all particle sizes and SoCs. Besides, simulations [33, 211] indicate that $\mathrm{Li_2Si}$ would be thermodynamically favored in a standalone two-phase process. Since this value, or any other, is not consistently measured, Li/Si ratios are more likely the result of further lithiation of the amorphous shell through the solid solution process previously described part I.2.2. It follows that the variety of Li/Si ratios measured corresponds to a range of different outcomes in the competition of the amorphization and the solid-solution processes. In an effort to understand how this competition is mediated by particle size, we put forward the hypothesis below.

The amorphization reaction proceeds along a extremely thin boundary of 1 nm to 2 nm according to the *in situ* TEM experiment from Liu et al. [212]. Since it can safely be understood to be an interfacial reaction, we see now the kinetics of amorphization depend of the specific surface of a particle, which itself scales as $1/r$. It follows that in microparticles, a lower driving force for amorphization will result in the solid solution process to be favored, and a lithium-rich shell

will develop. In contrast, the higher specific surface of nanoparticles will result in a different balance. With a higher driving force for amorphization, lithiation can proceed with lower lithium concentrations in the shell. An explanation is however still needed for the fact that x will depend on the state of charge in nanoparticles and not solely on particle size.

Stress contributions

We now look towards published chemo-mechanical models of lithiation [211, 213, 214]. In those, emphasis is put on the mediating role of the stresses that develop in the core-shell structure on the kinetics of lithiation. Understanding how and where stresses develop during lithiation is key to understand the driving forces for the two reactions and further elucidate this size effect.

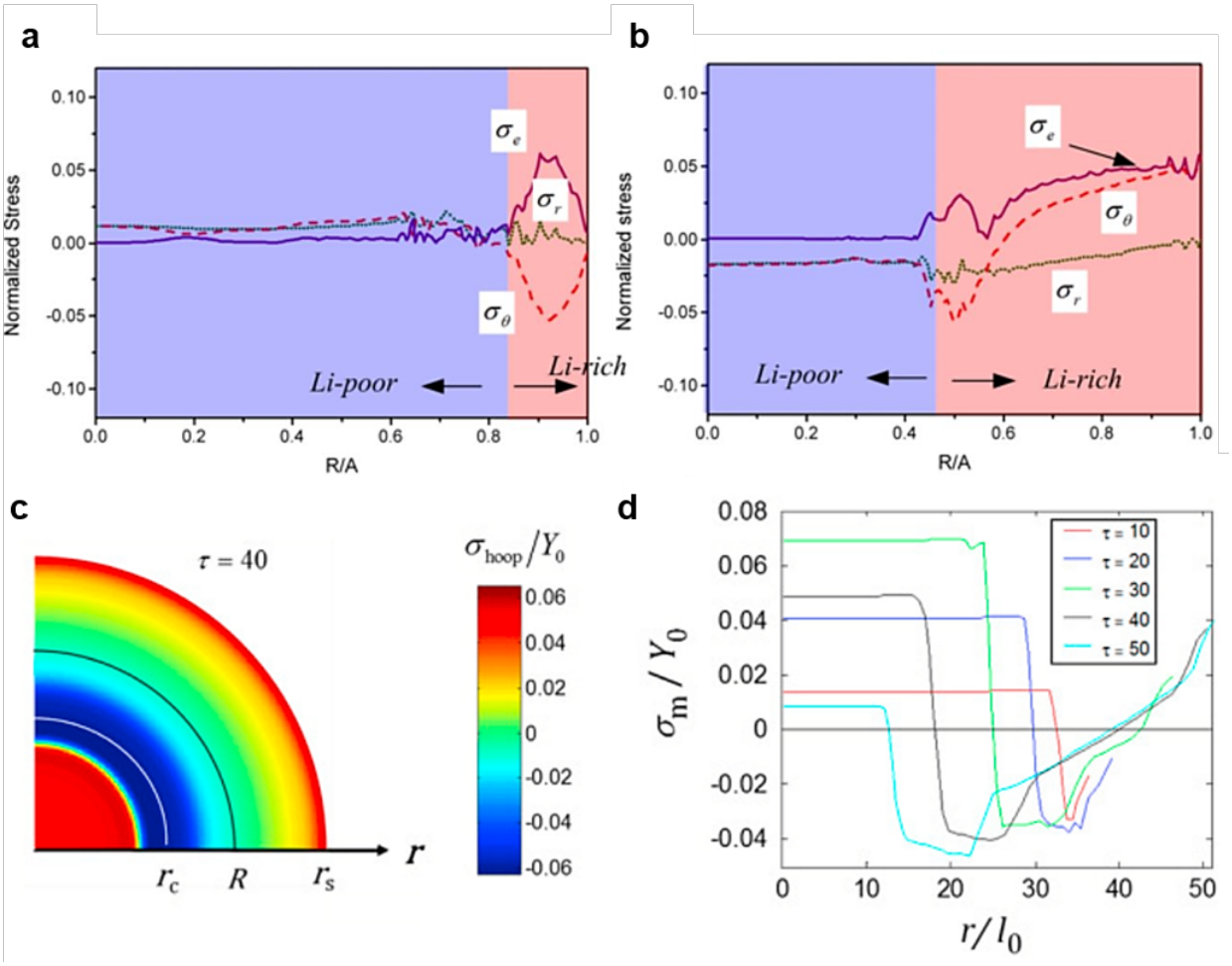

Fig. V.2: (a,b) Comparison of radial distributions of the von Mises effective stress, σ_e, radial stress, σ_r and hoop stress σ_θ obtained by the phase-field model with the phase boundary located approximately at (a) a/b = 0.85 and (b) a/b = 0.5. Where a is the core radius and b the total particle radius. Reproduced from [213]. (c,d) Distribution of the hoop and mean stress in a nanoparticle at intermediate stages of lithiation. Reproduced from [214].

Models converge towards the following scenario: (i) Initially a thin layer of c-Si is amorphized, and compressive hoop stress builds up in this lithiated shell (see fig. V.2.a). (ii) As the reaction front progresses inward, this compressive stresses becomes tensile and effectively promotes further lithiation of the amorphous phase (see fig. V.2.b,d). (iii) Meanwhile, the crystalline core (and especially the crystalline/amorphous boundary) is increasingly compressed by the growing shell. This compression balances the electrochemical driving force and causes a slowdown of the reaction front. (iv) Compression eventually overcomes the electrochemical driving force for amorphization and the reaction front halts, leaving the core shrunk to a critical radius r_c. Solid solution behavior takes over and particle lithiation continues by further lithiation of the shell.

We see here that our two concurrent reactions are mediated by stresses that evolve very differently throughout lithiation. While the mean stress at the crystalline/amorphous phase boundary varies weakly in the early stages of lithiation (fig. V.2.b,d), stresses in the shell's outer part switch from compressive to tensile. Those predicted trends show good agreement with *in situ* stress measurements *via* Raman spectroscopy from Zeng et al. [215]. Now, compressive stresses have a tendency to slow down reactions while tensile stresses promote them [69, 70]. This means that while the driving force for amorphization remains relatively unchanged at first, further lithiation of the amorphous phase becomes energetically favored as the shell grows, which explains the progressive enrichment D. Robert observes.

V.1.2 Elucidating the first lithiation of SiNP with STEM-EELS

To verify the lithiation mechanisms we have postulated, we analyzed 85 lithiated nanoparticles from 32 spectrum images acquired from Li-Si half-cells lithiated at 1200 mAh/g, 2400 mAh/g and 3000 mAh/g, which correspond to 30%, 60% and 100% theoretical SoC respectively. The methodology detailed chapter III allows us to simultaneously measure reliable lithium contents x as well as the size of the shell and core of a given particle by drawing radial profiles as described fig. V.3.

Iterating this analysis yielded an array of points (x, core/shell ratio), each of which correspond to an "effective" SoC that stems from these two parameters. Calculating the SoC of each individual particle allows us to paint a more precise picture that simply relying on the limited capacity since, as the EELS measurements from Robert [37] and Gauthier [176] pointed out, SiNPs are heterogeneously lithiated in the electrode.

$$SoC_{particle} = \frac{n_{Li}}{3.75 n_{Si}} = \frac{x\, n_{Li_xSi}}{3.75(n_{Si,core} + n_{Li_xSi})} \tag{V.1}$$

This expression can be developed into a function of x and the core-shell ratio a/b, using the densities ρ_{Li_xSi} [162] and the molar masses M_{Li_xSi}.

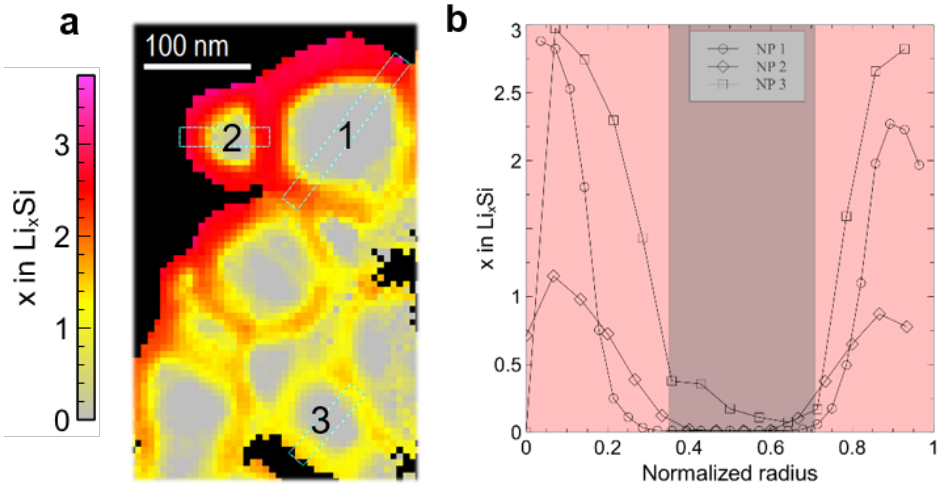

Fig. V.3: a) Lithium content map calculated from STEM-EELS measurements on lithiated silicon nanoparticles. b) Profiles of the nanoparticles marked in (a). Core and shell thicknesses can easily be measured in these profiles to yield to core/shell ratio a/b.

$$SoC_{particle}(x, a/b) = \frac{x}{3.75}\left[1 + \frac{(a/b)^3 \rho_{Si}/M_{Si}}{(1-a/b)^3 \rho_{Li_xSi}/M_{Li_xSi}}\right]^{-1} \tag{V.2}$$

Eq. V.2 now makes it possible to follow how x and a/b evolve with the SoC i.e. as lithiation progresses and verify the mechanism we postulate in the previous subsection. Results are reported fig. V.4. The volume expansion of lithiated silicon was accounted for in the calculation of the normalized core radius.

A selection of lithium content maps obtained by STEM-EELS is provided as visual cues to follow lithiation as its different stages (fig. V.6.a-f). At a glance our data is in agreement with the self-limiting behavior we mentioned. A two-step process appears clearly. In the first region, for SoCs below 0.5, the core shrinks while x increases incrementally from around 0.9 to about 1.9, in line with the scenario detailed before. Around this point amorphization stops and further particle lithiation solely relies on the enrichment of the shell through the solid solution process up to $x = 3.75$. These values are coherent with those of previous reports summarized table V.1, which feature x values below 2 at low SoCs [41, 210]. Those measured *via* EELS at high SoCs by Gauthier et al. [176] seem however surprisingly low. Since it is the most local method of the lot and that only two particles contribute to the value reported, we attribute this to the heterogeneity of the electrode. Another representation of the data is found figure V.5. Logically, the lithium content of the shell follows a trend opposite to the core radius, slowly increasing at first before it picks up once amorphization comes to a halt at $SoC \approx 0.5$.

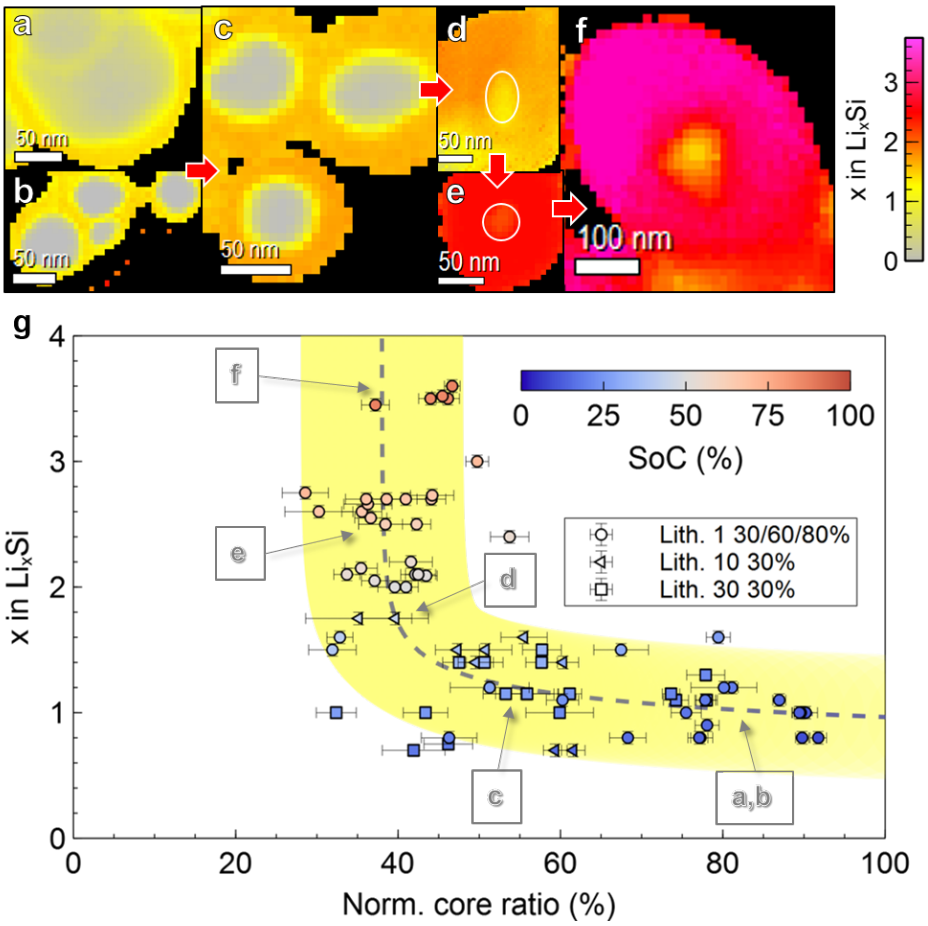

Fig. V.4: a-f) Lithiated SiNPs at consecutive stages of lithiation marked by their respective legends in (g). g) Lithium content x plotted as a function of the normalized core radius. The calculated SoC is represented in a heatmap. Additional points from electrodes at their 10th and 30th partial lithiation help us obtain a more precise fit.

The critical core/shell ratio r_c

The core-shell ratio a/b reaches a bottom threshold that we call the critical core-shell ratio r_c. This marks a transition between two regimes that are perhaps more easily distinguished figure V.6.h, where the normalized core ratio is plotted directly against the state of charge. Interestingly, a significant amount of particles (circled in black) stand out from the lithiation path highlighted. Those correspond exclusively to nanoparticles observed in electrodes at their 30th to 100th lithiation and whose shells are surprisingly large given their low lithium content. Since particles of the same size are expected to consistently exhibit the same behavior throughout lithiation, this means that those large shells can only originate from a deep lithiation in the previous cycles of those electrodes. This indicates that a given particle can be lithiated to different extents along an electrode's lifetime, which hints at aging mechanisms discussed chapter VI.

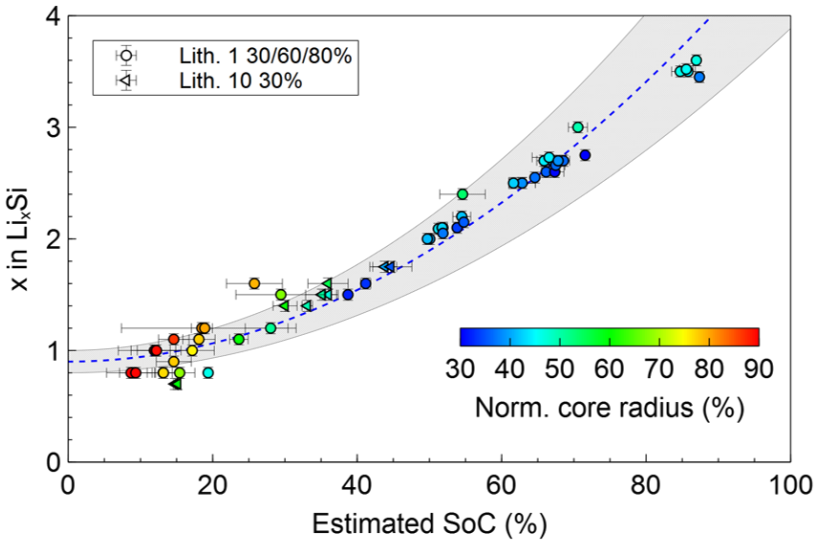

Fig. V.5: Lithium content x plotted as a function of the SoC in lithiated silicon nanoparticles at their first lithiation.

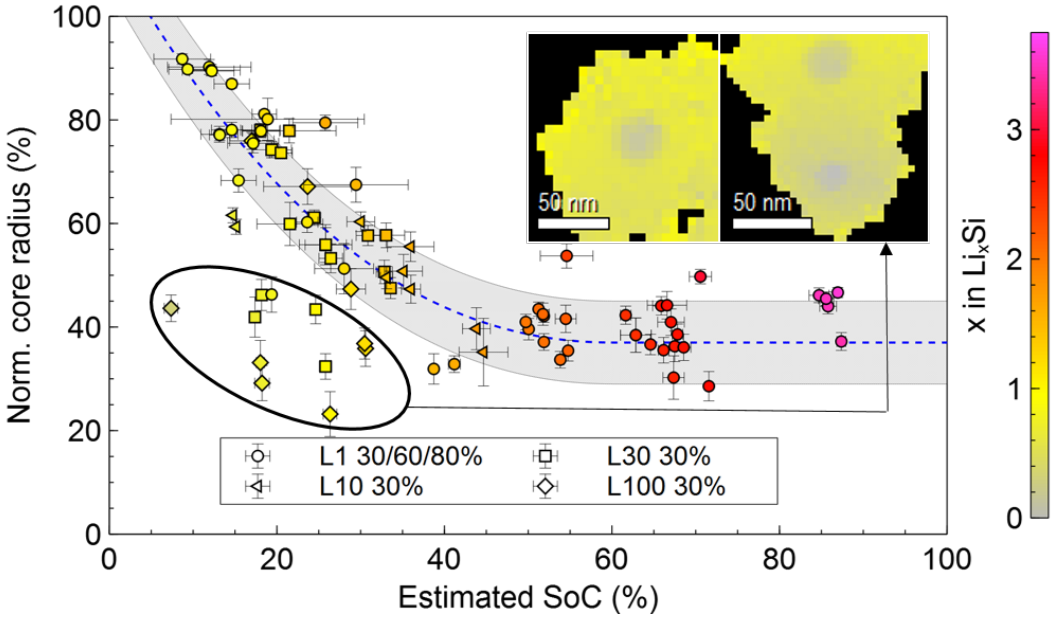

Fig. V.6: Evolution of the normalized core radius with the state of charge in lithiated silicon nanoparticles. Two regimes are easily distinguishable, with a critical core-shell ratio at $r_c \approx 0.35$ standing out. Points circled in black are outside those regimes and were not included in the fit. They correspond to the large but lithium-poor shells observed in nanoparticles from an electrode at its 100th lithiation. Two of those are represented in insert.

We identify a critical core-shell ratio at $r_c \approx 0.4 \pm 0.05$, roughly in line with the experimental conclusions of McDowell et al. [52] who measured r_c values between approximately 0.2 and 0.4 *via in situ* TEM experiments. Interestingly, those show a significant correlation with the initial size of SiNPs. Larger relative core radii are observed as particle size increases. While this

phenomenon is not commented on in the original paper, this fits the mechanism we hypothesized in the previous section. The higher specific surface of smaller particles provides a greater driving force for amorphization. As a result the reaction front can continue further inward before it stops.

Simulations from Drozdov et al. [216] put forward a complementary explanation. The authors show that varying the elastic properties of the shell results in significantly different r_c values. In this scenario, the existing size effect would be compounded by the variation of the mechanical properties of the Li_xSi shell on the lithium concentration. More particularly, a "softer" shell is associated with larger cores. Now, given that the Young's modulus E and Poisson ratio ν go down as x increases according to simulations from Shenoy et al. [66] and experiments from Bucci et al. [64], we can deduce that the lithium-poor, harder shells of smaller nanoparticles are associated with smaller cores. This hypothesis fits well our own observations of a logarithmic dependence of r_c to particle diameter V.7. The discrepancy observed with datapoints from McDowell et al. does not come as a surprise, given that lithiation occurs at a fixed potential around 0 $V_{Li^+/Li}$ in the *in situ* TEM experiment rather than along the slopping voltage profile of our galvanostatic experiments. In the former case, strain retardation is more easily overcome which expectedly results in smaller cores. The fact that our post-mortem experiments yield results comparable to *in situ* measurements is itself of great interest. It speaks to the stability of the system in time, and validates our approach and the pertinence of its results.

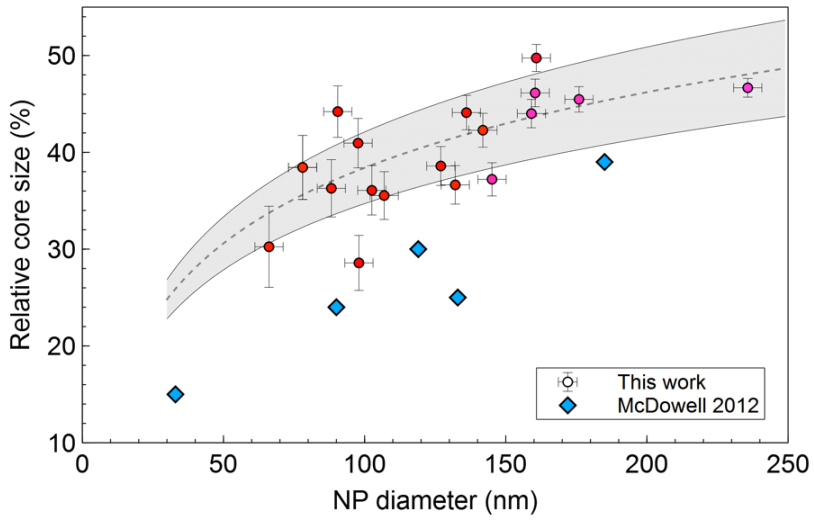

Fig. V.7: Critical normalized core radius as a function of particle diameter. Data is plotted alongside *in situ* TEM observations from McDowell et al. Red to magenta marker colors follow the same color scheme as fig. V.4 to fig. V.6, indicating a lithium content of $x \approx 3$.

V.1.3 Simulated voltage profiles and strain measurements

A simplified chemo-mechanical model

In an effort to provide further validation of the lithiation mechanism investigated in this section and to challenge the models developed in the literature, we calculated voltage profiles using our experimental data (x, core-shell ratio a/b) as input to the simplified two-phase lithiation model from Zhao et al. [217]. This approach, notably relayed in several *in situ* works [52, 218, 219], postulates a stress contribution to the Gibbs free energy of the amorphization reaction that can be expressed by the following formula:

$$\Delta G_{stress}(c-Si/Li_xSi) = \frac{2\sigma_Y \Omega_{Si}}{x}\left[\sigma_m^{Si} - \sigma_m^{Li_xSi}\right] \tag{V.3}$$

Where $\beta = \Omega_{Li_xSi}/\Omega_{Si}$ is the volumetric expansion coefficient of the $\mathrm{Li_xSi}$ phase, and $\sigma_m^{Li_xSi}$, σ_m^{Si} are the mean stresses at the lithiation front and in the crystalline core respectively. Now, Zhao et al. estimate those quantities by:

$$\sigma_m^{Si} = 2\sigma_Y\, ln(a/b) \quad \text{and} \quad \sigma_m^{Li_xSi} = 2\sigma_Y(ln(a/b) - 1/3) \tag{V.4}$$

Substituting eq. V.4 in eq. V.3 now yields:

$$\Delta G_{stress}(c-Si/Li_xSi) = \frac{2\sigma_Y(x)\Omega_{Si}}{x}\left[0.4(1-\beta(x))\, ln(a/b) + \frac{\beta(x)}{3}\right] \tag{V.5}$$

$$E_{calc}(x,a/b) = \frac{-1}{xF}\left[\Delta G_{stress}(c-Si/Li_xSi)(x,a/b) + \Delta G_r(Li_xSi)\right] \tag{V.6}$$

Estimating the stress contribution

Here σ_Y is the yield stress of the lithiated amorphous shell. This quantity naturally depends on the lithium concentration x [66, 162]. If we now rely on the empirical relation derived from Bucci et al. [64] $\sigma_Y(x) = (0.49 + 0.07x)$ GPa, we see that eq. V.4 yields impressive compressions in the crystalline silicon core, in excess of -3 GPa, when the core/shell ratio a/b reaches the critical radius r_c. Now, this prediction has seldom been challenged experimentally in nanoparticles. With that in mind, we carried on *in situ* Raman and XRD results in collaboration with Tardif, Pavlenko et al. [220], on the same composite silicon electrodes. There, stresses are measured around 0.3 GPa, in agreement with a similar experiment from Zeng et al. [215].

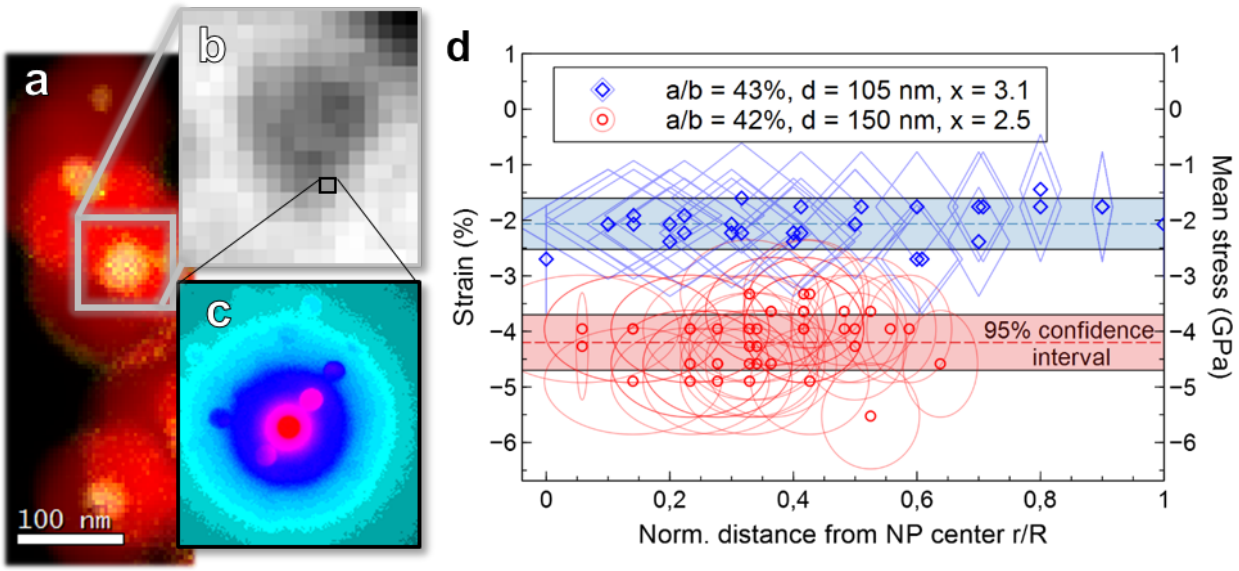

Fig. V.8: Local stress measurements in the crystalline core of lithiated nanoparticles by NPED. a) Composite thickness map of Li_xSi alloys obtained by STEM-EELS prior to NPED. Li_3Si scale: 0-300 nm. Si scale: 0-100 nm. b) Virtual bright field image reconstructed from the NPED 4D dataset. c) Typical diffraction pattern represented in "exponential" color scale. d) Calculated strain values as a function of the normalized distance to the particle's center for two lithiated SiNPs. The large blue diamonds and red circles around markers represent uncertainties.

This was compared to our own local stress measurements however, obtained by nanobeam precession electron diffraction (NPED) with the help of J.L. Rouvière who pioneered the technique [221](fig. V.8). Results indicate compressions that are almost an order of magnitude higher than the macroscopic XRD result. More accurately, the core of 2 SiNPs analyzed here appears to be subject to a relatively homogeneous compression, of -2.05 ± 0.45 GPa and -4.24 ± 0.50 GPa respectively (calculated from strains using the elastic modulus of silicon for hydrostatic loads $E = 97.8$ GPa [222]). Broadly speaking, those values match those simulated by Huang et al. [59] (-2 GPa to -8 GPa) and Chen et al. [213] (-2 GPa to -5 GPa) with the notable exception that these authors report a sharp drop at the core boundary. Although we acknowledge the limited accuracy of our diffraction measurements (small crystals in random orientations, large amorphous layers on top, short acquisition times to prevent irradiation damage) and our small sample size, we are confident in the order of magnitude put forward. We cannot however comment on whether stresses are higher at the interface with the data at hand. Nonetheless this valuable proof of concept warrants further application of the technique to solve strain-related issues in nanometric battery materials.

Now, there is a dramatic discrepancy between electrode-scale measurements (*in situ* XRD) on one hand and particle-scale predictions and measurements (simulations, NPED results) on the other. A possible explanation is that in the first case, the signal is averaged over many particles that do not contribute evenly to the strain measurement, e.g. that all particles are not stressed evenly. This either

means that the electrode is not lithiated homogeneously and/or that some particles that participate to the electrode's capacity are not lithiated in the core-shell pattern and do not have compressed crystalline features. Both phenomena are investigated in the next section.

Given this novel insight on the magnitude of the core stress, we carry on calculations of a voltage profile with eq. V.6. We opt to use the formation energy ΔG_r of $Li_{0.9}Si$, since it is the composition identified by STEM-EELS at the initial stages of cycling. A choice supported by ab initio calculations by Chevrier et al. [65] and confirmed by Shenoy et al. [66], who report $\Delta G_r = -0.2\,eV$ for Li_1Si, a close match to the value of $-0.18\,eV$ determined experimentally by Limthongkul et al. [33]. Results are plotted for both the core-shell ratio and lithium content x (fig. V.9), and show good agreement with the mechanisms derived from our STEM-EELS data. Since as rule of thumb the system will follow the path of least energy i.e. lower absolute potential, we see that core-amorphization (orange line) will proceed until the Li/Si atomic ratio reaches $x = 2 \pm 0.1$, after which the solid-solution reaction takes over and x increases to 3.75. To proceed lithiation is then forced to proceed *via* further amorphization, which corresponds to a sharp drop in the potential (arrow "2" on fig. V.9).

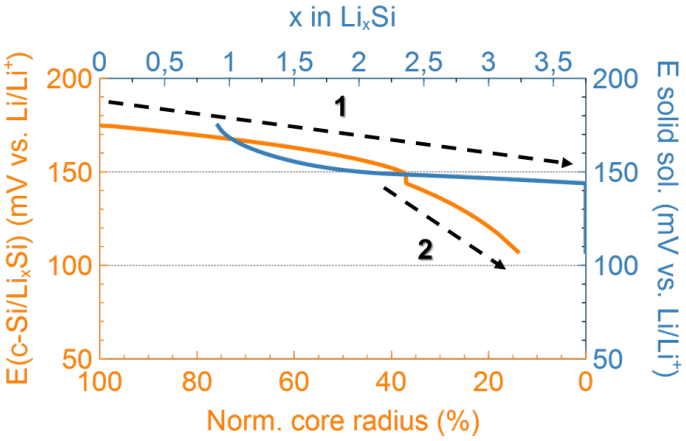

Fig. V.9: Voltage profiles calculated from eq. V.6 with our STEM-EELS data as input and represented against both the Li/Si ratio x, and the core/shell ratio a/b.

Summary

The mechanisms of the of silicon particles is heavily dependent on their size. While overwhelming evidence exists for a biphasic-like process in microparticles ($x = 3.2 \pm 0.3$), nanoparticles seem to exhibit lithium contents that typically start much lower and gradually increase as lithiation progresses. To explain this size effect, we formulate the hypothesis that amorphization and solid-solution reaction processes compete during the first lithiation. The lower specific surface of microparticles hinders amorphization which leads to lithium-rich shells even at low SoCs, while in nanoparticles the driving force for amorphization is higher. A review of modeling work in the

literature shows that the stresses building up during shell growth will favor increasingly high Li contents as lithiation progresses, which explains the gradual increase seen in NPs. To challenge this model experimentally, we take advantage of low-loss STEM-EELS which allows us to probe both the morphology (core/shell ratio) and chemistry (lithium content x) of lithiated nanoparticles at different state of charges. The data provides evidence of two lithiation steps, in line with the aforementioned hypothesis: (i) SoC < 0.5 - the core shrinks until it reaches a critical core/shell ratio r_c that shows a logarithmic dependence with the particle size. Lithium content goes from $x \approx 0.9$ to $x \approx 2$. (ii) SoC > 0.5 - Amorphization stops and lithium content increases in the shell up to $x = 3.75$. To provide further validation of this mechanism, we calculate voltage profiles with the model from Zhao et al. We adjust the stress contribution from this model to match our electron diffraction stress measurements, which themselves are in good agreement with previous modeling works. Both describe stress gradients in crystalline core, from -3 ± 1 GPa at the particle's center to -6 ± 1 GPa at the phase boundary. The mismatch there is between this ED result and one obtained from *in situ* XRD, averaged over a large electrode volume, suggests heterogeneous cycling in the electrode. This hypothesis is challenged in the next section.

V.2 The morphology of lithiated nanoparticles and clusters

Let us now consider nanoparticle clusters, which are at the scale at which STEM-EELS operates (a few micron squared). Since sample preparation is minimalist (see chapter II.1.1), those structures are understood to come unaltered from the electrode, and their observation provides qualitative insight on the local kinetics of lithiation.

V.2.1 Inhomogeneity at the cluster and electrode scales

In addition to lithium content maps for lithiated samples, E_{max} maps provide an indication of the ordering of silicon and are a convenient way to appreciate the morphology of NP clusters in delithiated samples. Both analysis are useful to obtain typical views of SiNP clusters from cycled electrodes, which we report figure V.10. Notable features stand out. Foremost is the heterogeneity of lithiation, apparent on Li content maps: particles at different state of charges cohabit, with domains made of handful of particles exhibiting different lithium contents and core/shell ratios in contact with each other (figure V.10.a-d). This notably mirrors other local chemical characterization results from E. Radvanyii [223] (AES) who also noted homogeneous Li/Si atomic ratios in individual shells, but which vary from one particle to another. This includes particles that have remained in their pristine crystalline state, as we can see figure V.10.h as well as in figure V.11, which features entire clusters that do not contribute to the electrode's capacity. Although we cannot reliably quantify the total amount of inactive silicon, it is a qualitative confirmation of the hypothesis we put forward for the mismatch between electrode-scale and local stress measurements. It also suggests that a significant amount of active matter is isolated from the electrode's percolating network from the start.

Coming back to lithiated clusters, we see that SoCs ranging from $\approx 10\%$ to $\approx 30\%$ were observed despite the electrodes being cycled to 1200 mAh/g, i.e. to 30% limited capacity. Furthermore, we note that despite the wide distribution of particle sizes, the core/shell proportions correspond to Li/Si ratios in a way that matches the mechanisms detailed in the previous section. Upon delithiation, those core-shell structures naturally remain, forming the composite crystalline-amorphous patterns evidenced fig. V.10.e-g.

A possible explanation for this local lithiation gradient would be related to the distribution of the conductive additive, carbon black, with the underlying assumption that lithiation is reaction-limited. An overview of our results, using the methodology detailed in III.2.2, make it clear however that there is no correlation whatsoever (weighted Pearson correlation coefficient of -0.04) between the relative local amount of carbon black and the average lithium content in clusters (fig. V.12). Carbon black is in fact observed to be poorly dispersed in the electrode and to clump in aggregates that do not contribute to the electrode percolating network.

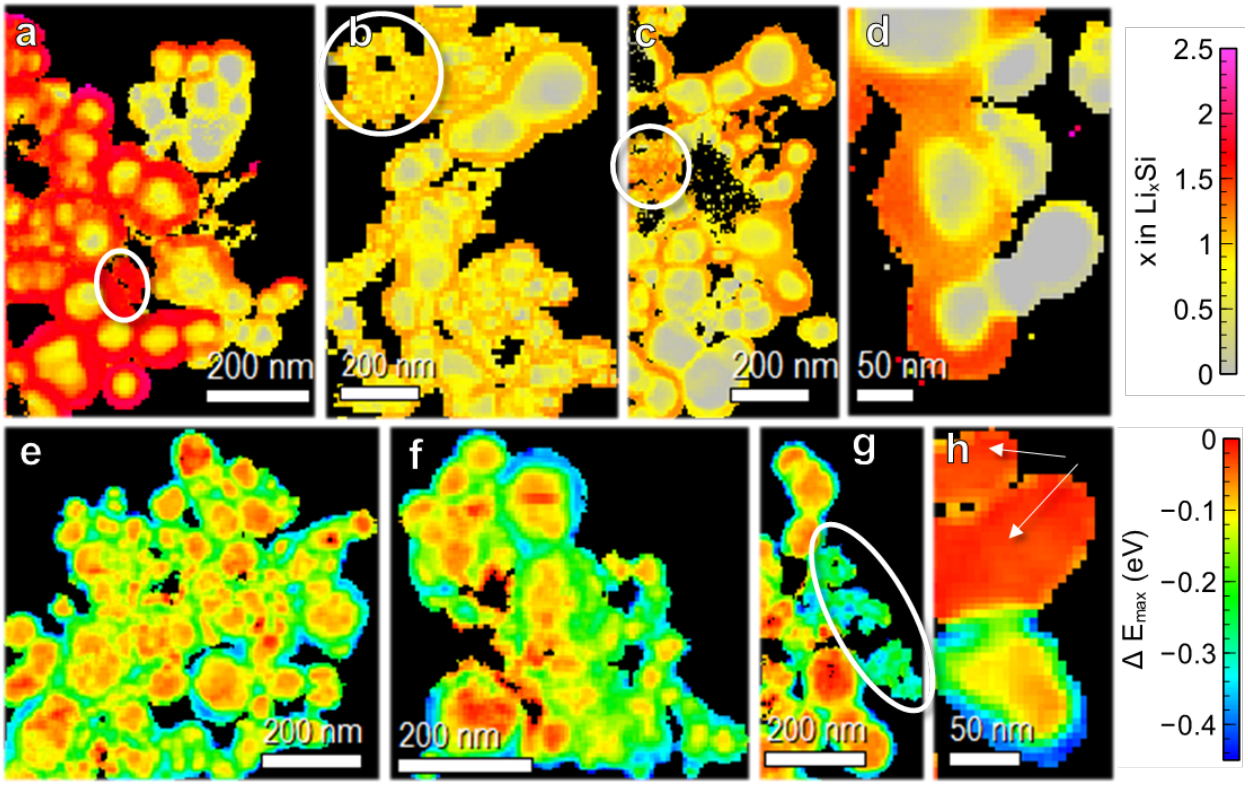

Fig. V.10: Li content maps calculated from STEM-EELS observations of SiNPs clusters from electrodes cycled to 1200 mAh/g. a-d) Lithiated particles after the 10th lithiation. Heterogeneous lithiation is observed. Peculiar, homogeneously lithiated structures are highlighted in white. e-h) E_{max} maps revealing amorphous (blue-green)/crystalline (yellow-red) silicon composite structures in SiNPs clusters after the 10th delithiation.

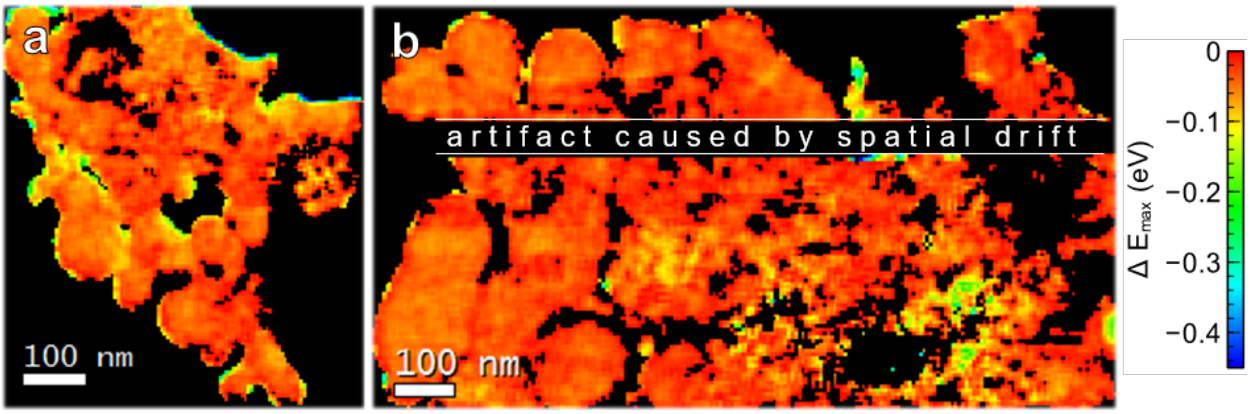

Fig. V.11: E_{max} maps calculated from STEM-EELS data, revealing crystalline (red color) SiNPs clusters after the 10th lithiation. These particles are in their pristine state and do no contribute to the electrode's capacity.

That leads us to consider a second scenario where Li^+ diffusion would be limiting. The nature of the surrounding SEI could play a role, and this is investigated in the next section. It is also worth noticing that this uneven lithium distribution persisted despite the electrode being left in the glovebox for weeks prior to observation. This means that thermodynamics alone are not sufficient to equilibrate Li content within clusters.

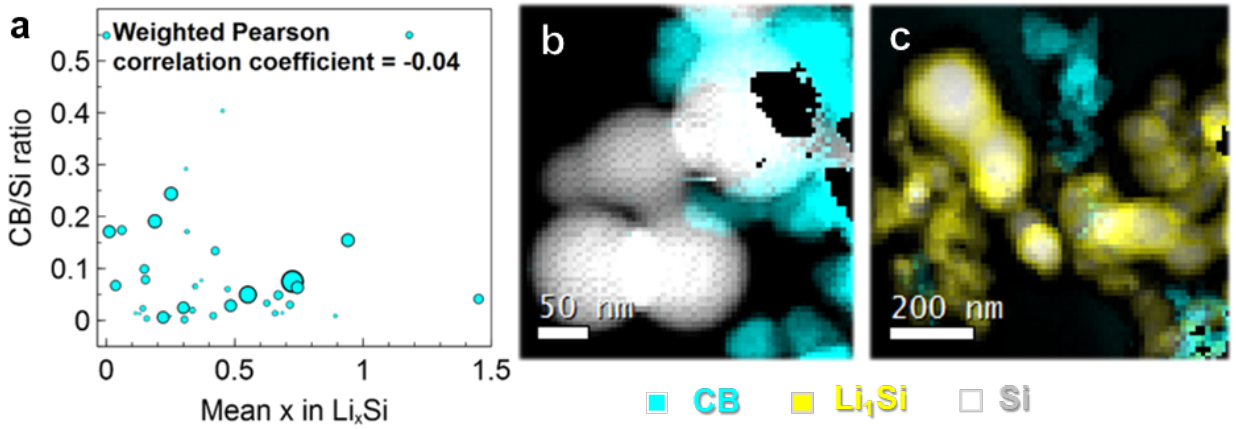

Fig. V.12: a) Scatter plot of the average Li/Si atomic ratio x against the carbon black (CB) on silicon volumic ratio for 38 spectrum images of SiNP clusters from electrodes cycled in half-cells (1st and 10th cycle) to 1200 mAh/g. Markers are sized proportionally to the volume of silicon in each spectrum image, i.e. to the weight used in the calculation of the correlation coefficient. It has a value between +1 and -1, where 1 is total positive linear correlation, 0 is no linear correlation, and -1 is total negative linear correlation. b-c) Composite thickness maps of carbon black (teal), silicon (white) and Li_1Si (yellow) showing CB agglomerates. Intensity ranges from 0 nm to 200 nm.

Moreover, most particles seem to be fused into a bulky continuous network, to an extent that is unexpected given the analysis of the pristine silicon powder (see chapter II.1). It is however unclear whether this evolution is lithiation-driven or if particles are in fact already sintered before cycling in their pristine state, although *in situ* TEM observations from Karki, Cumings et al. [224] did reveal what they have called *lithium-assisted electrochemical welding* between several silicon nanowires. Strikingly different structures, highlighted in white circles, are also observed alongside the expected core-shells. These areas appear to be lithiated in a homogeneous manner in contrast to two phases process observed everywhere else. Such structures were eventually observed in detail (fig. V.13). They consist of amorphous matrixes that contain small (< 10 nm) crystalline cores. These structures result from the consecutive lithiation and delithiation of a distinct population of smaller coalesced nanoparticles (see HRTEM observations of the pristine powder in II) that incidentally are polycrystalline and contain many defects. They typically exhibit similar Li/Si atomic ratios x than the surrounding monocrystalline SiNPs, understandably as x will depend on the local electrochemical potential in a solid solution process. Much higher state of charges are however observed. We can calculate $SoC = 40 \pm 5\%$ for both fig. V.13.a and fig. V.13.b.

V.2.2 Preferential lithiation across grain boundaries

The lithiation of the numerous grain boundaries of these particles is energetically favored over solid state amorphization, which requires breaking of the silicon lattice. This explains the higher states of charges observed. Defects will indeed act as "fast lithiation paths" and lithiation then pro-

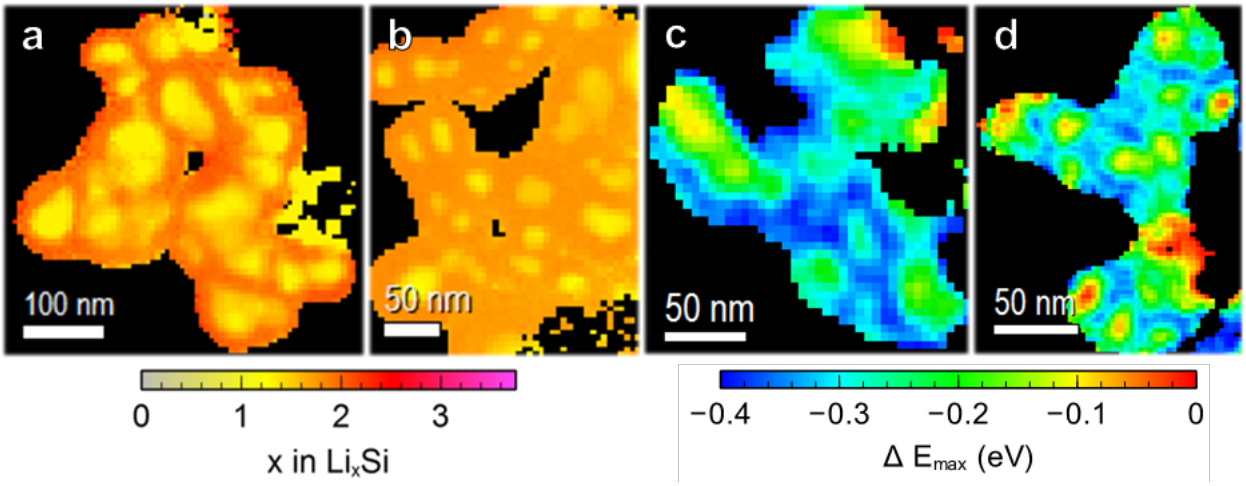

Fig. V.13: STEM-EELS observations of SiNPs from electrodes at their 10th cycle to 1200 mAh/g. a-b) Lithium content maps of lithiated smaller nanoparticles. c-d) E_{max} maps of such NPs after delithiation.

ceeds with the secondary core-shell structures created, which was easily visualized in microparticles from the FIB cross-section of lithiated electrodes by D. Robert [37] in SEM observations and A. Bordes with ToF-SIMS [208, 225] (fig. V.14.b).

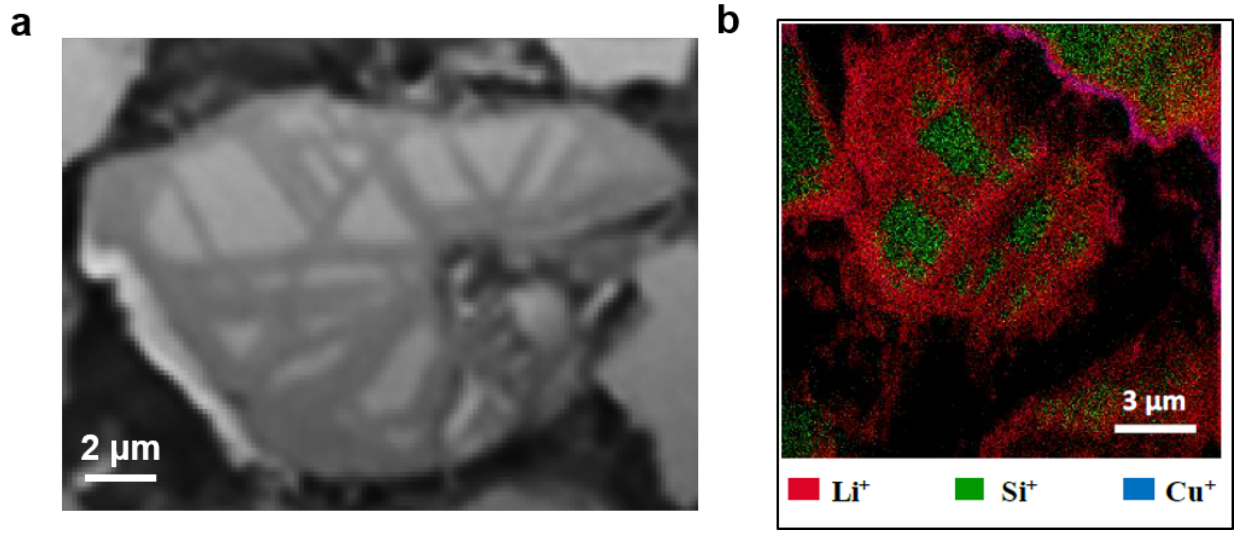

Fig. V.14: Observations of FIB cross-sections of partially lithiated silicon electrodes made of microparticles. a) SEM measurement after the 1st lithiation to 1800 mAh/g. Reproduced from [37]. b) ToF-SIMS measurement after 3 cycles at 1000 mAh/g. Reproduced from [225].

We show here that the same is true in nanoparticles. While the high density of defects in the highly polycrystalline NP population yields the homogeneously lithiated smaller structures highlighted fig. V.10), the few grain boundaries of in our larger particles result in secondary core-shell structures that provide ample evidence of this phenomenon. In both lithiated and delithiated samples, lithiated defects can indeed be observed to split particles, thus multiplying the surface of the reaction front for amorphization. This should promote faster local lithiation kinetics and the

rate capabilities of our electrode. At the macro-scale, *in situ* XRD results from Wang et al. [226] also show that the diffracted intensity does not go down in the first part of the lithiation of silicon SiNPs, which suggests that the lithiation of disordered features indeed proceeds preferentially at the electrode scale. Our own *in situ* XRD measurements [220] confirmed this behavior with good repeatability.

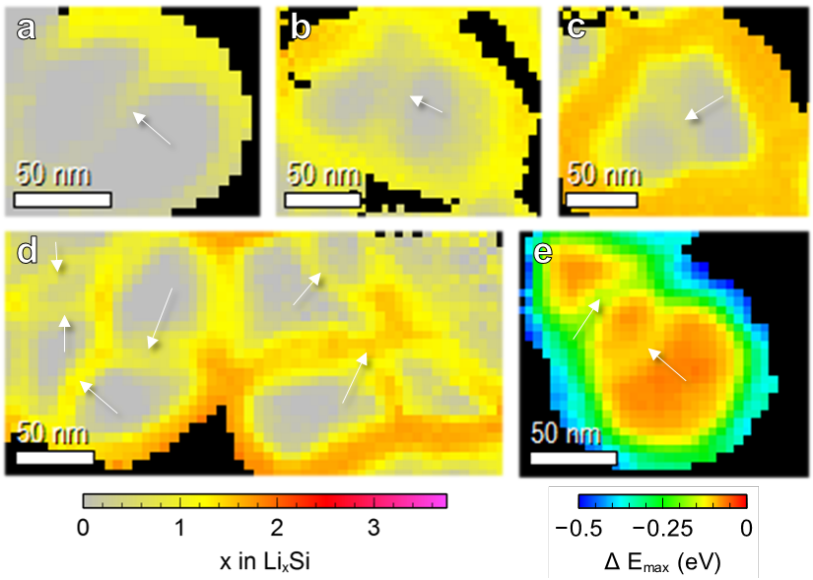

Fig. V.15: STEM-EELS observations of lithiated defects delimiting secondary core-shell structures. a-d) Li content maps obtained by Drude model fitting. e) E_{max} map showing amorphous silicon left after the delithiation of defects.

V.2.3 Further evidence of uneven lithium diffusion

Irregular core faceting

The lithiation of defects is not the sole responsible for the irregular shape of the crystalline silicon cores. While a spherical geometry is maintained in the early stages of lithiation for monocrystalline particles (see fig. V.10), low-dose STEM [227] observations also reveal faceting of these cores in SiNPs at later stages of lithiation. Sharp polygonal shapes are detected and outlined in orange dashes figure V.16. These facets are similar to those observed by Luo et al. [219] and others [52, 54] in their respective *in situ* TEM experiment and are a consequence of the anisotropic growth of the shell. At the atomic scale, lithiation involves the lateral movement of ledges on the close-packed <111> atomic planes [228, 229]. Hence the lithiation first proceeds along the preferred growth direction, which has been reported to be <110> [230]. This explain the faceting observed and should turn the crystalline silicon core into in a regular polyhedron. However, many other projected shapes were observed across particles, some even irregular. It is unlikely that these are different projections of the same polyhedron since, again, a regular shape is expected. Those more probably

arise from an uneven lithium transport that will depend on the configuration of each particle to porosities and the SEI. It is yet another suggestion that lithiation at the particle scale is essentially diffusion-controlled.

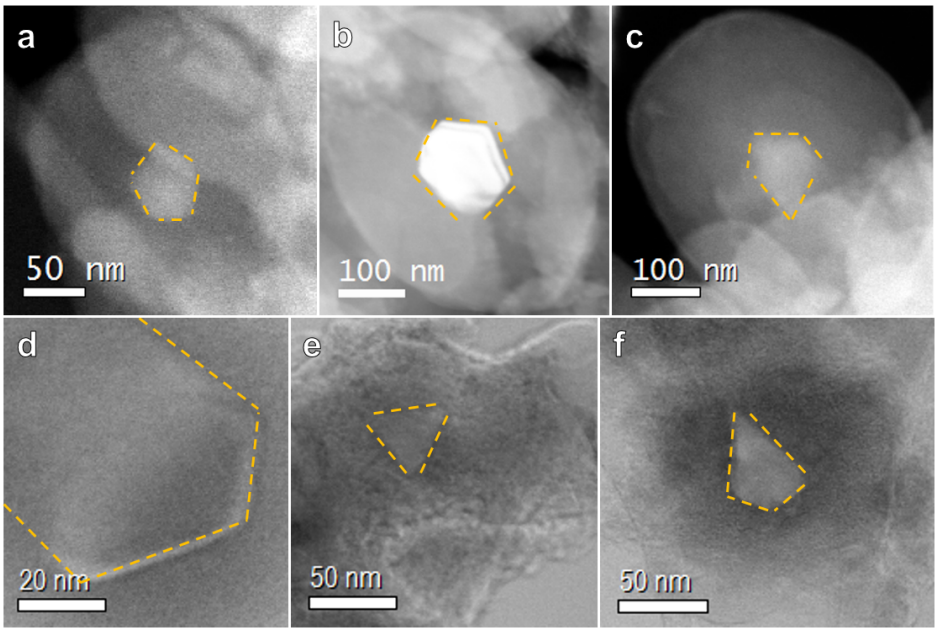

Fig. V.16: (a-c) Annular dark field and (d-f) annular bright field STEM observations of lithiated SiNPs from an electrode at its 1st lithiation to 3000 mAh/g (80% theoretical capacity). Crystalline cores stand out by their diffraction contrast and exhibit polygonal shapes as a result of anisotropic lithium diffusion in silicon.

Incomplete delithiation and trapped Li^+ ions

Inspecting delithiated samples provides an additional proof that particles are unevenly solicited in particle clusters. Just like lithiation, delithiation will proceed in a heterogeneous manner. E_{max} maps indeed reveal significant local gradients, with unlithiated particles (red color in fig. V.17.a) adjacent to values largely under the 16.15 eV to 16.3 eV interval we associate with amorphous silicon (blue color in fig. V.17.a). It is indicative of trapped lithium atoms, which are even observed in alloy-like concentrations up to around Li_1Si (fig. V.17.b-e). This echoes recent publications [40, 179, 231] where observations of $Li_{1.1-1.2}Si$ are also reported as a result of fast delithiations [40, 179, 231]. Once again, this hints at significant local differences in lithium transport, with NPs in close proximity showing different concentrations of trapped atoms. Whether this phenomenon emerges as electrodes age or is intrinsic to cycling will be explored in chapter VI.

Summary

The low-dose STEM-EELS capabilities we developed allows for large field-of-view observations. Taking advantage of this, we observe striking heterogeneity in nanoparticle clusters, both in lithiated

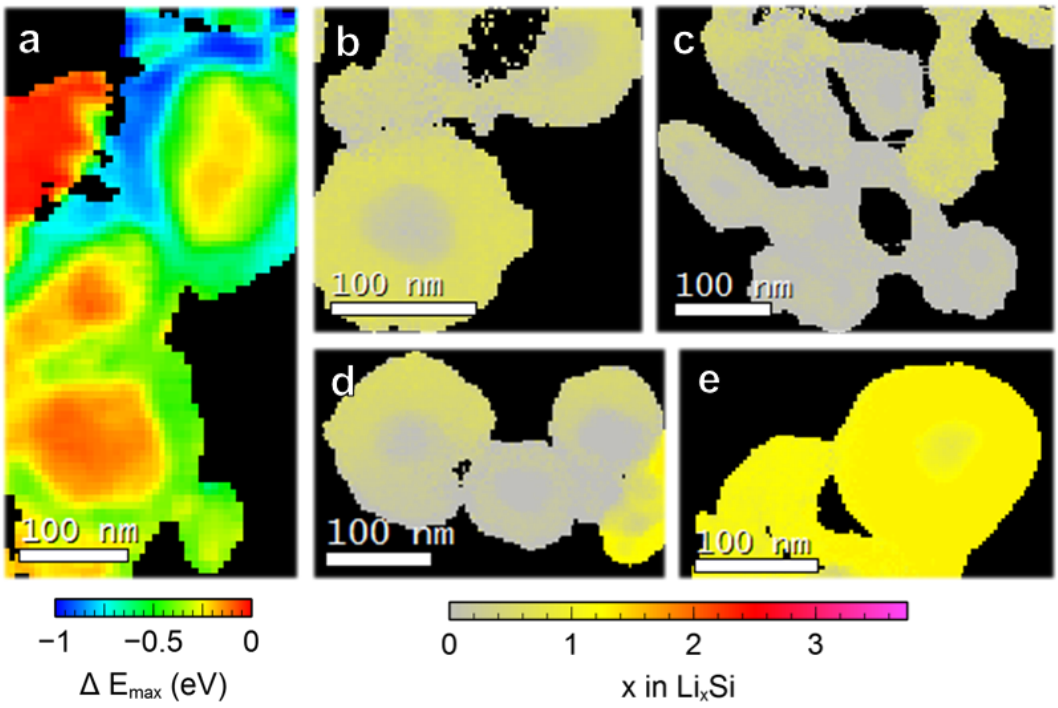

Fig. V.17: STEM-EELS analysis of SiNPs from an electrode at its 30th delithiation. a) E_{max} map. The values observed in the top particle are well below those expected for a-Si. This results from an incomplete delithiation and is characteristic of trapped Li atoms. b-e) Li content maps showing the presence of alloys as rich as Li_1Si.

and delithiated electrodes, which matches predictions from the diffraction measurements detailed in the previous section. Even at this local scale, different lithium contents are detected from one particle to another which is a telltale of local variations of lithiation kinetics. Since the distribution of the conducting additive carbon black seems to show little correlation with these chemical gradients, we conclude that this is the result of uneven lithium transport in a diffusion-limited reaction. Investigation of what influences Li diffusion locally, notably the SEI, is continued in the rest of the manuscript. Morphologically, different structures appear besides the expected core-shells. This is related to the particles' structures itself. As expected from observations of silicon microparticles, defects will in fact act as fast lithiation paths which forms secondary core-shells for which we present ample evidence. This multiplies the surface of the amorphization front and speeds up lithiation.

V.3 Local chemistry and morphology of the SEI

The formation and subsequent evolution of the SEI, a layer that is very heterogeneous chemically and whose morphology has stayed elusive despite intense scrutiny, is thought to be instrumental to the cyclability of electrodes. Although extensive information has been provided on the overall composition of the SEI, conclusive evidence has not been presented for how its compounds are distributed in the *mosaic model* (see chapter I.3), and local characterizations are needed. For this reason the potential for phase mapping of low-dose STEM-EELS is especially relevant here and provides a unique opportunity to describe the layer's morphology. To this effect, thickness maps for a number of compounds have been calculated using the MLLS methodology detailed in chapter III.2. Naturally, our choice of reference low-loss spectra of standard SEI compounds is critical to the robustness of the method. References have to reflect the diverse chemistry of the layer. We have focused on the following species:

- Organic/carbonate components. Compounds in this loose array, from lithiated alkyl-carbonates to polymeric species, were mapped as a single phase due to the similarity of their low-loss EEL spectra.
- LiF. Lithium fluoride is a major SEI component which results from the decomposition of both the $LiPF_6$ salt and the FEC solvent.
- Li_2CO_3. Alternatively reported to be a major SEI component or to only be present in trace amounts.
- Li_4SiO_4 and Li_2O. Both are expected as a result of the lithiation of the native oxide SiO_2 and should be observed to coat lithiated nanoparticles.

V.3.1 Analysis of the SEI's inorganic components

Lithiated silica: Li_4SiO_4

Although Li_4SiO_4 has been reported as a product of the lithiation of the native oxide SiO_2 [98, 99, 118], we have not found consistent evidence for the presence of either on the surface of lithiated SiNPs in our STEM-EELS datasets. This surface layer is expected to be present in amounts that should be easily detectable. Zhang et al. [100] indeed report volumetric expansions of about 200% for Li_4SiO_4 relative to SiO_2, which should result in layers 4.5 ± 1.5 nm thick for a native oxide layer of 1.5 ± 0.5 nm. Exploring the surface of lithiated nanoparticles did not reveal EEL spectra close to our Li_4SiO_4 standard however, but that are rather similar to that of references of the *org* phases. This analysis is reported figure V.18. Thus a strong case can be made for the absence of

Li_4SiO_4 from the system, especially in light of other reports. Meng et al. [111] have indeed reported that the formation of a Li_xSiO_y layer was eliminated when FEC was used.

However detecting this species *via* STEM-EELS is arduous, and the robustness of the STEM-EELS analysis can be debated here. Limiting factors include (i) the great sensitivity of Li_4SiO_4 to electron irradiation, (ii) the similarity of its low-loss spectrum to other references which degrades the performance of the MLLS decomposition, (iii) its overlapping with surface plasmons, as well as (iv) the weak signal of such thin layers.

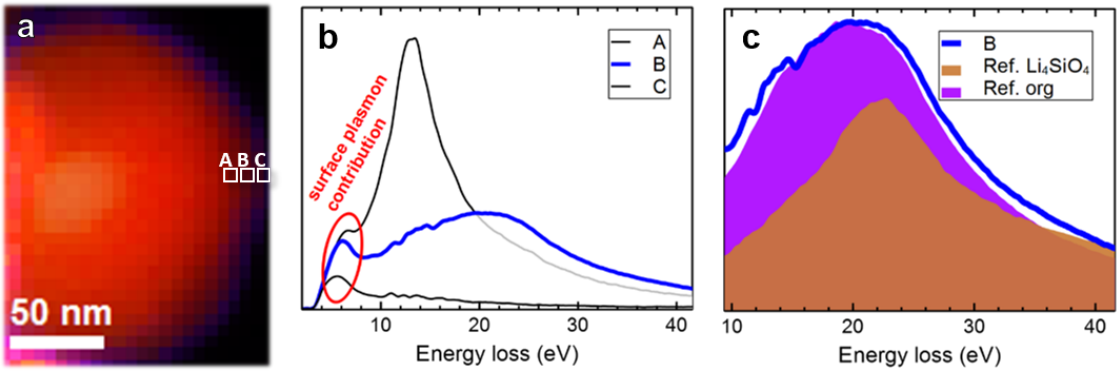

Fig. V.18: STEM-EELS profile of the surface spectra of a lithiated silicon nanoparticle. a) Composite thickness map of Li_3Si (red), Si (white), and the *org* phase (purple). b) Experimental EEL spectra extracted from the areas highlighted in (a). c) Comparison of spectrum B with the reference spectra of standard compounds.

Trace inorganics: Li_2O and Li_2CO_3

Regarding the inorganics Li_2O and Li_2CO_3, we observe no more than trace amounts which we associate with occasional contamination, in agreement with conclusions from Aurbach [83] and Edström [88, 232]. Excessive irradiation could also lead to Li_2O formation as shown experimentally (see III.1). Besides, XPS and NMR experiments performed on the same samples [118] detect neither in significant amounts and come independently to the same conclusion. We do not however exclude the possibility that Li_2O is present in trace amounts that we cannot decisively detect. It is nonetheless clear that neither Li_2O nor Li_2CO_3 are significant SEI compounds in our samples.

To summarize our findings on these compounds, we can only conclude on their limited contribution compared to, as we will see, the overwhelming amounts of LiF, carbonates and other organics in the SEI. The presence of Li_2O, Li_4SiO_4 and Li_2CO_3 in domains smaller than a few nanometers cannot be excluded. XPS studies are more suited to this analysis.

Lithium fluoride and its nanocrystals

Inorganics are nevertheless far from absent in the SEI, and LiF is known to be one of its major component. Thanks to the peculiar shape of the low-loss spectrum of LiF (see III.2.2), it is easily separated from other components by the MLLS procedure. As a result the morphology of the LiF phase can be probed with great accuracy. Two distinct layouts can be distinguished. The first is the presence of LiF in segregated domains or particle-like "chunks" (fig. V.19) that can be as wide as 100 nm. This particular geometry has already been hypothesized from XPS observations by Edström et al. on graphite [88]. Furthermore, thickness calculations allow us to get a sense of the 3D morphology of these formations and outline either flakes or spherical shapes, although it is difficult to identify clear trends. Likewise, the disposition of these domains across SiNPs is seemingly random and does not show significant correlations with lithium contents or the presence of carbon black. It is the predominant morphology we observe in SiNPs from electrodes stopped at their 1st and 10th cycle.

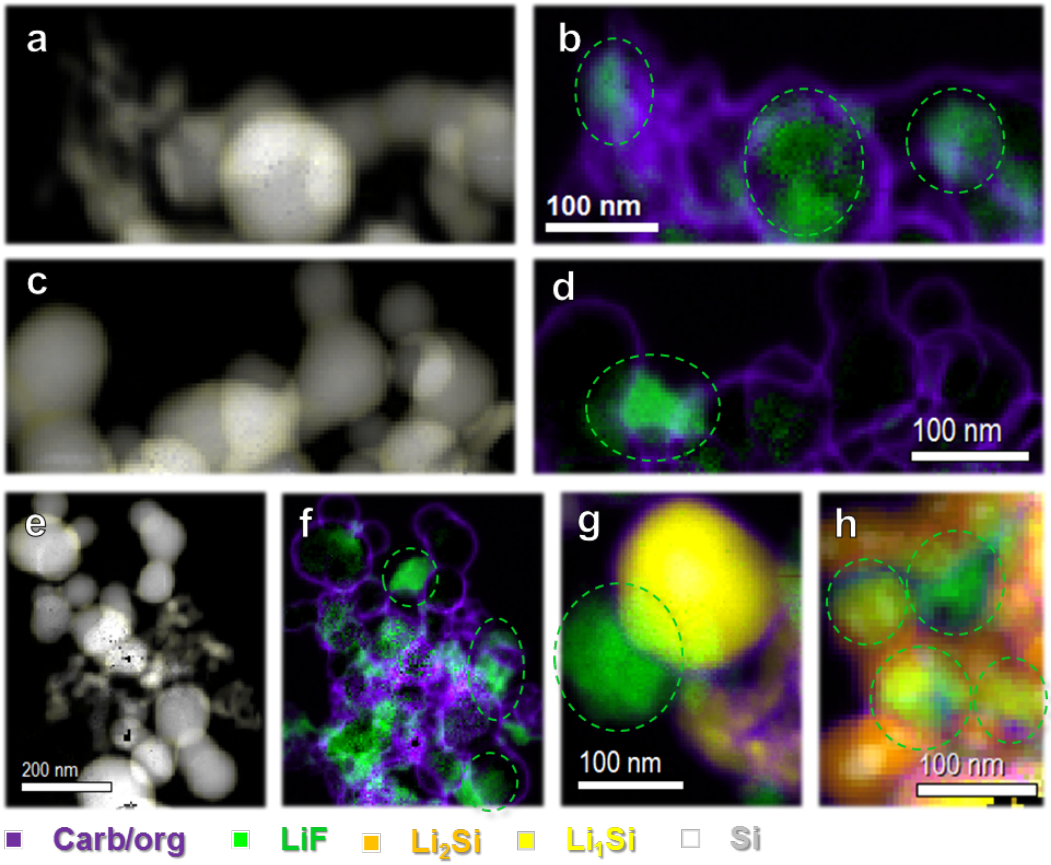

Fig. V.19: Composite thickness maps of SEI components and Li-Si alloys obtained from STEM-EELS observations of SiNPs clusters from electrodes cycled to 1200 mAh/g at their 1st and 10th cycle. LiF is observed in discrete and large domains. a-f) 10th delithiation. Intensity maximum at 200 nm. g-h) 10th lithiation. Intensity maximum at 150 nm of thickness.

LiF is also observed in the form of continuous layers surrounding our nanoparticles (fig. V.20). Unlike the large domains described above however, this conformal morphology is scarcely seen in the early stages of cycling - 1st and 10th cycles. Rather, it is more often observed in electrodes at their 30th and 100th cycles. This suggests that these two morphologies have two corresponding formation mechanisms, one occurring continuously across the lifetime of the electrode (layers) and the other forming the chunks we mentioned, most likely during the first few cycles. Moreover, we know that two reaction pathways have been proposed for the formation of LiF. The first and most commonly described is the degradation of the $LiPF_6$ salt [233]. The second is the reduction of the FEC solvent [234–236]. Since FEC reduction is known to be ongoing cycle after cycle [104], we can speculate that the layer-like morphology mostly comes from FEC and the particle-like domains mostly from $LiPF_6$.

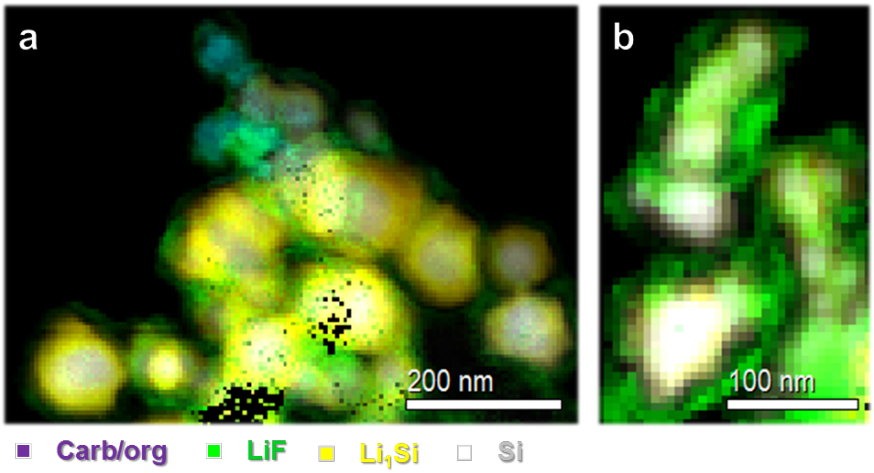

Fig. V.20: Layer-like LiF deposits seen in composite thickness maps of SEI components and Li-Si alloys obtained from STEM-EELS observations of SiNPs clusters from electrodes cycled in half cells at their 30th lithiation to 1200 mAh/g. a) Intensity maximum at 150 nm. b) Intensity maximum at 100 nm of thickness.

Another clue comes from STEM observations of both formations (fig. V.21). Diffraction contrast reveals $\approx 10 \pm 5$ nm wide crystals in the LiF phase. This is in line with HRTEM observations from Chattopadhyay [93] who describes growing LiF crystals in an amorphous matrix. In the particle-like LiF however, no such contrast is observed. Closer inspection also reveals that the two structures exhibit different spectral signatures. While the first experimental EEL spectrum resembles closely our pure LiF reference, the second shows, roughly, an additional contribution centered at 20 eV, which corresponds to organic SEI products. These findings superpose well with recent simulation works, which predict the formation of LiF nanocrystals in an amorphous alkyl carbonate matrix [237, 238]. Therefore we speculate that FEC reduction results in this composite phase. Its morphology especially stands out in STEM observations of electrode cross-sections prepared by FIB (fig. V.22). This aligns well with the study from L. Giebeler et al. [239], who also noted that, with FEC, additional LiF nanocrystals were embedded within the surface film.

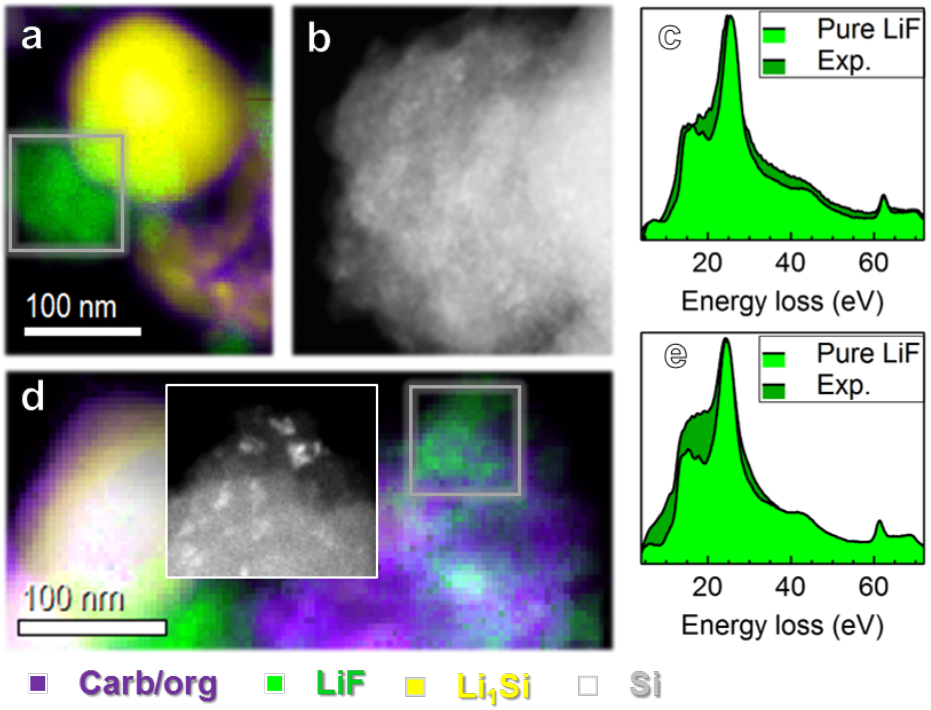

Fig. V.21: STEM-EELS phase mapping, annular dark field STEM, and EEL spectrum of the two LiF formations. (a-c) Particle-like LiF. (d-e) Layer-like LiF.

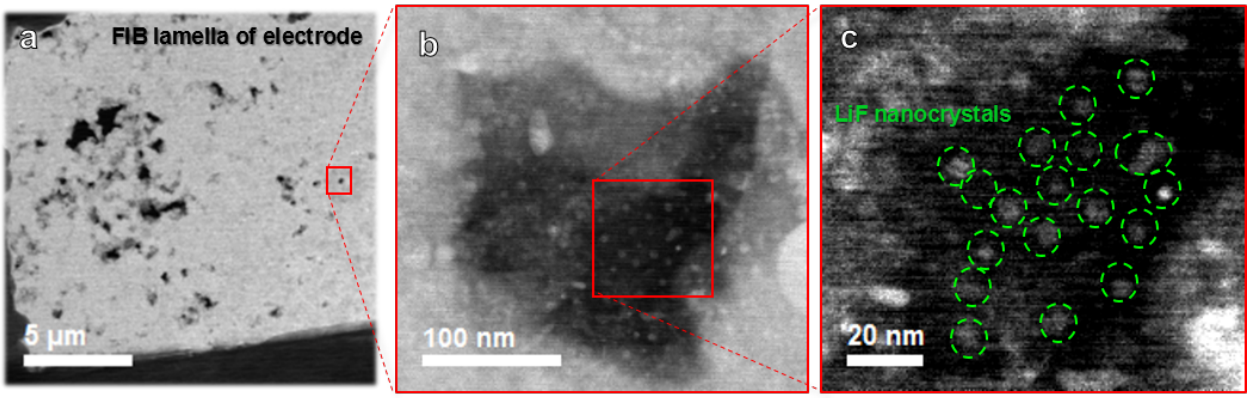

Fig. V.22: Annular dark field STEM observations of a FIB cross section of an electrode at its 10th lithiation. Diffraction contract reveals what is likely to be LiF nanocrystals in porosities.

Qualitatively, the overall amount of lithium fluoride we detect is noteworthy in itself. Extremely large domains are observed at all stages of cycling, which contradicts other reports that conclude on a limited contribution from LiF to the silicon SEI [94, 117, 240]. Although higher quantities are expected when using the FEC additive [110, 111], the result remains surprising. A possible explanation comes from the presence of unwashed $LiPF_6$, but reference STEM-EELS experiments on pure $LiPF_6$ in the same experimental conditions did not lead to similar observations. $LiPF_6$ shows a distinct EEL spectrum and does not turn to LiF at the electron dose ($200\,e\,\text{Å}^{-2}$, see III.1) used for the analysis we report.

V.3.2 The carbonate-organic phase

We now turn our attention to what we have called the *carbonate-organic* phase. As mentioned above, this seemingly homogeneous phase hides a mosaic of compounds [75]. Among those, lithium ethylene dicarbonate (LEDC), for example, could not be obtained in pure form and MLLS decomposition was carried out with 3 reference spectra that are directly extracted from cycled electrodes (see III.2). Since the nature of the compounds cannot be directly inferred from their low-loss spectra, we are initially limited to the morphology of this phase. We can however determine the position of each individual spectrum to reveal chemical gradients. Moreover, looking at the intensity of the Li-K edge at $\approx 60\,\text{eV}$, which is acquired simultaneously to the low-loss spectrum, can yield complementary information. From the prior knowledge we have of the compounds present, we can then provide a rough assessment of how those are distributed. We subsequently rely on this depiction to quantitatively describe aging in the next chapter.

An ubiquitous and conformal layer

If we put aside the chemical complexity of the layer, an overview of its morphology can easily be obtained by summing the 3 contributions output by the MLLS decomposition. As we already saw in fig. V.19, the "carb-org" phase adopts a conformal morphology, and layers of thickness 5 nm to 20 nm are seen engulfing particles from the first cycle and on (fig. V.23). Moreover smaller particles naturally appear to be covered in proportionally thicker layers due to their higher specific surface (fig. V.23.b). The presence of this layer was observed almost systematically, even on most of the significant number of SiNPs that do not contribute to the electrode's capacity (fig. V.23.c,e). Although this is expected given that solvent reduction occurs at potentials above those needed for the lithiation of silicon (FEC: 1 $V_{Li^+/Li}$, EC: 0.6 $V_{Li^+/Li}$ [234]), it suggests that particles that are electrochemically active and grow SEIs do not get subsequently lithiated. It follows that, in addition to the inhomogeneities we observe at the cluster scale (see V.2), chemical gradients exist at the electrode scale and SiNPs are not solicited evenly. Further investigation of this can be found in VI.1.

To compare our results to those of other published works and provide qualitative result on the thickness of this phase, we have gathered measurements on particles from electrodes at their 1st lithiation (74 particles) and delithiation (86 particles). Results are reported figure V.24. Interestingly, delithiated samples appear to show measurably thinner layers, with averages going down from approximately 14.7 nm to 11.9 nm from the 1st lithiation to the 1st delithiation.This trend is also qualitatively picked up on by XPS and NMR measurements [118] on the same samples at the electrode scale. It is worth noting that this matches other reports [94, 119], most notably from Fears and al. [120] in their *in situ* neutron reflectometry experiment.

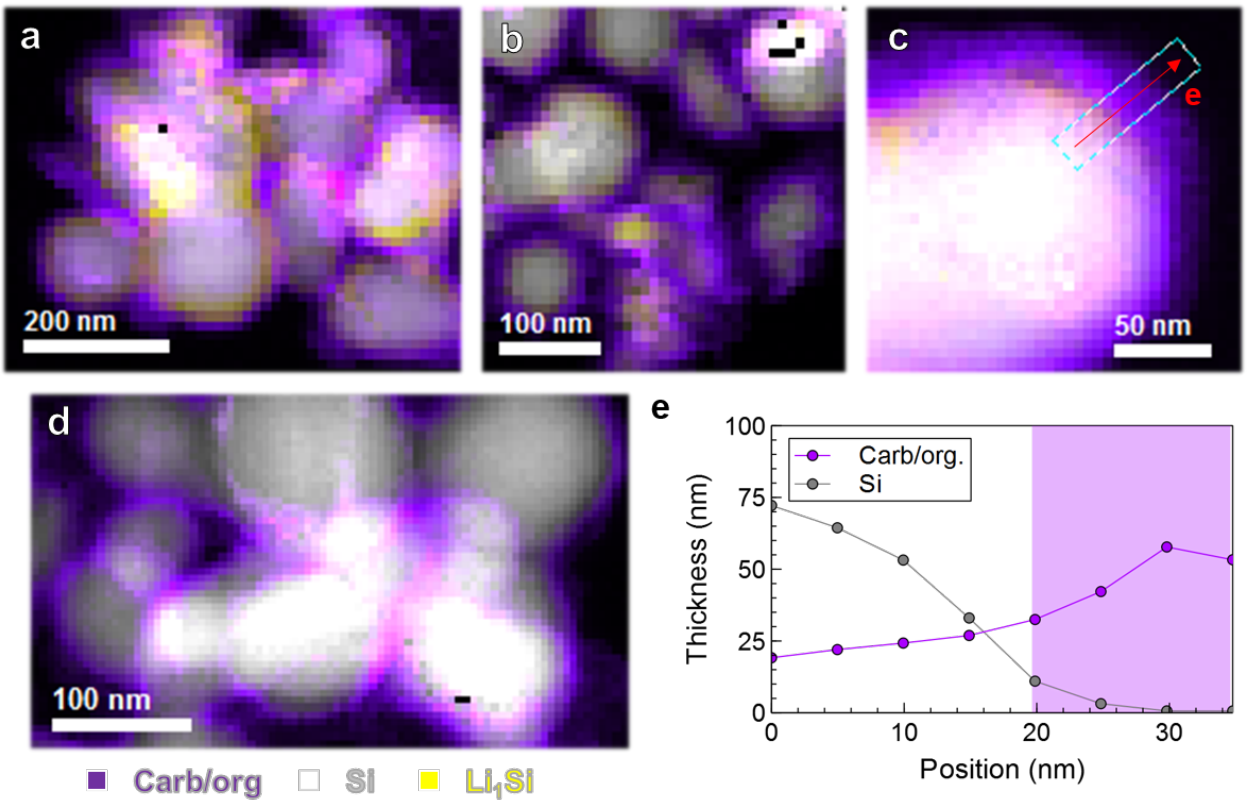

Fig. V.23: Composite thickness maps obtained by STEM-EELS. To favor a clearer overview of the overall morphology of the layer, Li_xSi compounds and carb/org species were represented with two scales of 0 nm to 200 nm and 0 nm to 100 nm respectively. The LiF contribution was not represented. a-e) SiNPs from an electrode at its 1st lithiation. f) Overlapped thickness profiles from the area drawn in (e), allowing us to measure layer thicknesses.

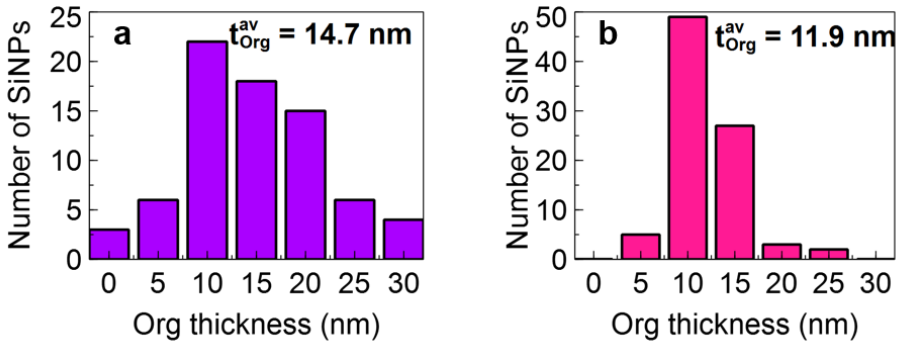

Fig. V.24: Histograms of the thickness measured for the carb/org layer based following the example given in fig. V.23.e. a) After the 1st lithiation. b) After the 1st delithiation.

Highlighting chemical gradients

With this in mind on the overall morphology of the layer, we now take a closer look at its chemistry. As previously mentioned, the phase is in fact made of a diverse array of oligomers, alkyl-carbonates and semi-carbonates. The diversity of experimental spectra we regroup in our "carb-org"

phase is itself an indication of this variety. The quantity E_{max} for the plasmon peaks of *org* spectra lays in the 14 eV to 20 eV interval, but E_{max} values cannot in themselves be directly attributed to particular chemistries. However, by combining calculations and empirical EELS measurements of PEO films (see III.3.2), we have extrapolated that the end of that energy range likely corresponds to oligomer-like compounds, while lower plasmon energies are associated with carbonates such as LEDC. Now, we can get a sense of how these two sets of compounds are distributed in the SEI by representing our 3 reference components as individual phases rather than grouping them. This is done on a SiNP cluster from an electrode at its 1st delithiation in fig. V.25.a. An alternative way to outline the chemical gradients in question is to carry out direct fitting of the plasmon positions (fig. V.25.b). This offers a finer sensitivity that can be especially relevant to highlight small domains in thick layers - such as those found after extensive cycling, see VI.2.

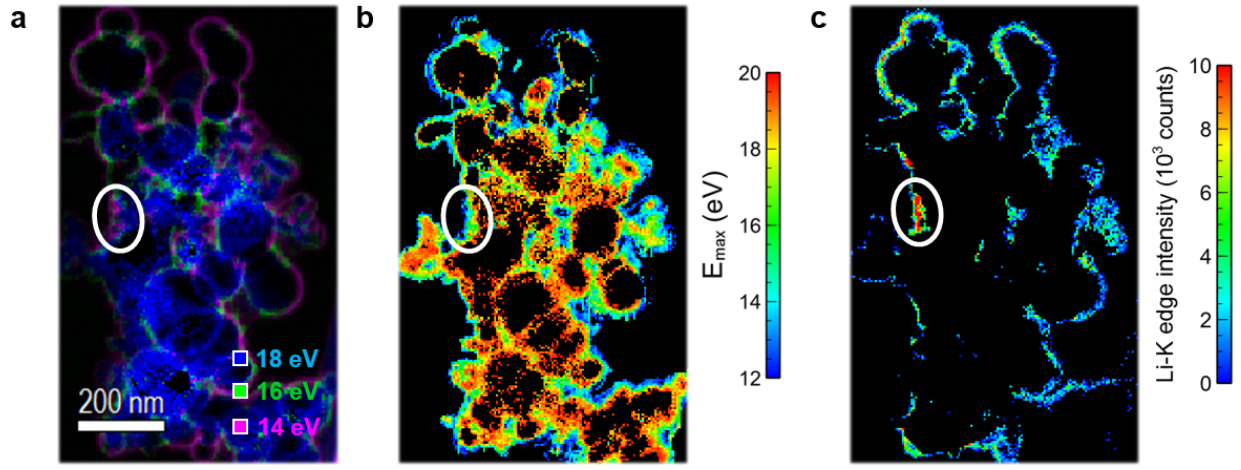

Fig. V.25: a) Composite thickness map obtained by quantification of the MLLS decomposition of STEM-EELS measurements of SiNPs from an electrode at its 1st delithiation. Intensities range from 0 nm to 100 nm. b) E_{max} map of the "carb-org" layer obtained by the method detailed in III.3. c) Li-K intensity map of the "carb-org" layer.

A look at the composite thickness maps shows that, behind the conformal aspect highlighted earlier, our three sub-phases adopt distinct morphologies. While compounds corresponding to lower E_{max} values ("14 eV", magenta) do seem to coat nanoparticles uniformly, those represented by the "16 eV" spectrum, in green, form segregated domains rather than layers. The "18 eV" component is itself rather clumped towards the inside as well as the left-hand side of the SiNPs cluster studied here. The fact that this trend could be an artifact of the fitting process was also checked for, by looking for a possible correlation between thickness and the plasmon energy E_{max}. This is done by plotting a bivariate histogram of the two quantities (fig. V.26) for 13 spectrum images from the same sample as the one analyzed in fig. V.25. No correlation is observed and the morphologies outlined are reliable.

In addition to the plasmon energy, the lithium K edge, at 60 eV, can moreover be exploited to provide an additional characterization of the layer. Although technically not a part of the low-loss

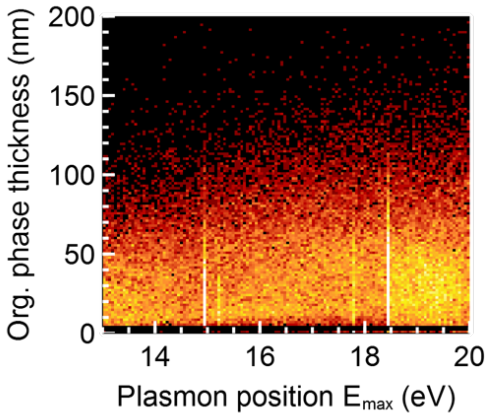

Fig. V.26: Bivariate histogram of the plasmon energy E_{max} and the Org. phase thickness for 13 spectrum images from an electrode at its 1st delithiation to 1200 mAh/g. No correlation is observed.

spectrum, the Li-K edge is acquired simultaneously to the plasmons used for phase mapping and can thus be advantageously correlated to the plasmon energy. A glance at the two maps side by side shows that low-E_{max} compounds appear to correspond to higher Li-K intensities, with the area highlighted in white providing a clear example. This qualitative trend can be confirmed by plotting a bivariate histogram of these two quantities (fig. V.27.a). Here, we see that higher E_{max} compounds have indeed a tendency to be Li-poor. With figure V.27.b, we look at spectra whose Li-K intensity is null to reveal that, once more, their plasmons energies are visibly concentrated towards the end of the energy range. Coming back to the rule of thumb defined in III.3.2, we see that low E_{max}, carbonate-like compounds tend to contain lithium while high E_{max} oligomer-like species do not. This is coherent with our initial assumption of the presence of poly(FEC), thought to be the major lithium-containing organic SEI compound [103, 109].

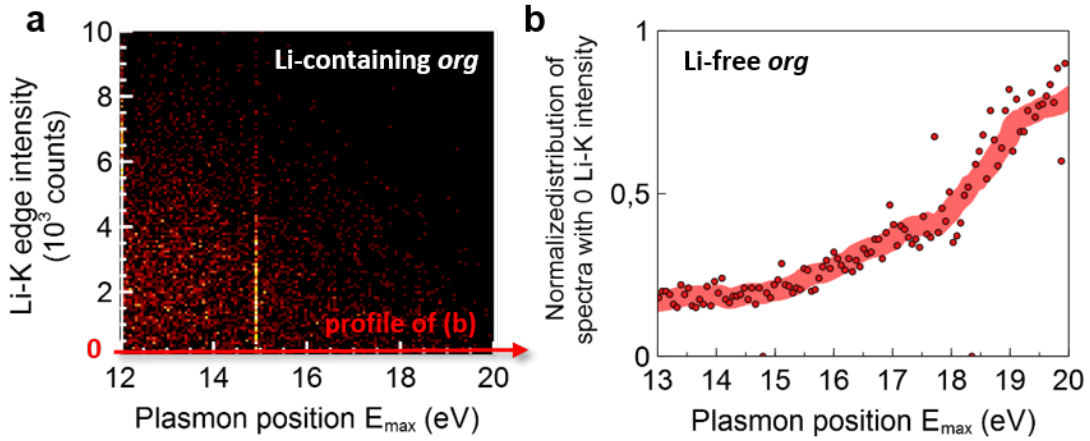

Fig. V.27: a) Bivariate histogram of the Li-K intensity and E_{max} parameter. b) Normalized distribution of the E_{max} parameter for "carb-org" compounds that do not contain lithium.

Chapter summary

In this chapter, we have taken advantage of the versatility of the low-loss STEM-EELS methodology developed in III to study the first cycle of silicon electrodes at the particle scale. Thanks to the spatial resolution and chemical sensitivity of the technique, extensive insight is gathered on the reaction mechanism of the first lithiation. A model is proposed where solid-state amorphization and solid-solution processes proceed concurrently, in a balance mediated by the particle sizes and the stresses that builds up in the particle's crystalline core. Results also match remarkably well with *in situ* works, from the self-limiting behavior identified by McDowell [52], to the gradual increase in the lithium content of the amorphous phase Li_xSi exposed through *in situ* NMR by Ogata et al. This is of merit to show the relevance of the low-loss STEM-EELS methodology, especially for *post mortem* observations. Furthermore, local electron diffraction measurement provide complementary insight, and offer the first experimental validation of the numerous simulations found in the literature. A comparison with *in situ* XRD measurements suggests that SiNP-based electrodes cycle with significant heterogeneity. This is confirmed by the STEM-EELS observation of large SiNP clusters, which reveals that lithiation is uneven at both the cluster-scale (local Li distribution gradients) and electrode scale (entire clusters are in their pristine state). A distinct NP population also exhibits morphologies that stray away from the core-shell pattern due to their numerous defects that act as fast Li diffusion paths. This compounds the drowning out of the average stress measured at the electrode scale by XRD.

We then turn our focus to the SEI, for which the MLLS-enabled phase mapping capabilities of STEM-EELS are used to their fullest. Regarding the inorganic components Li_2O, Li_4SiO_4 and Li_2CO_3, no conclusive evidence is found besides the fact that they are not a significant part of the SEI we observe. LiF is by far the main inorganic SEI component, and is present either in large segregated domains or in layers. We attribute these two structures to the two LiF formation pathways identified in the literature, from $LiPF_6$ and FEC reduction respectively. LiF nanocrystals were also identified as telltales of FEC reduction. The plethora of alkyl carbonates, oligomers and others that compose the rest of the SEI, are mapped jointly under the name *org* phase. An overall conformal morphology is outlined, and the analysis of 160 particles reveals an average thickness of 14.7 nm after the 1st lithiation, down to 11.9 nm after delithiation, in line with previous reports of a so-called *breathing* of this phase. Among its diverse chemistry, we then show that, despite the limited chemical sensitivity of low-loss STEM-EELS, not only can we effectively identify chemical gradients, but also offer reasonable interpretations. This is achieved by taking advantage of the plurality of data contained in the low-loss spectrum.

Chapter VI

Electrode aging in half and full cells

This last chapter is dedicated to the study of electrode aging. Electrode formulations and cycling conditions are reported in chapter II. Although they have a significant influence on the extent of the aging phenomena of interest, we aim to shed light on mechanisms intrinsic to Li-Si alloys as well as the SEI, and that apply to all Si-based electrodes. To this effect, we build on the local morphological and chemical description of the functioning electrode detailed in chapter V, to highlight how these structures and patterns evolve during the electrode's prolonged cycling in both full and half cells. For this, we rely once more on the STEM-EELS developments detailed in chapter III, but with an emphasis on the summation methods detailed in III.2.3 to outline quantitative trends. This is achieved through a careful systematic analysis of 197 spectrum images gathered at all stages of the electrode's lifetime on over 1100 silicon nanoparticles.

Our aim is not to identify the root causes of the capacity decay of silicon-based electrodes, which have already been well established in previous reports [27, 28], but rather to challenge them *via* local STEM-EELS observations.

VI.1 Disconnection of particles and over-lithiation

This section details the evolution of the silicon active matter upon successive lithiation/delithiation cycles. STEM-EELS gives us the opportunity to confront mechanisms that have been proposed to justify the capacity decay of silicon electrodes to direct local observations at both the particle and cluster scale. In particular, the analysis of FIB-cross sections allows us to reveal gradients in the depth of electrodes, notably through quantification as mentioned above.

VI.1.1 Cluster pulverization and Li trapping

Evidence of cluster pulverization

The poor capacity retention of silicon electrodes has been notoriously attributed to the disconnection of a significant portion of the active matter from the percolating network [11, 13]. STEM-EELS observations of delithiated SiNPs clusters from lithiated electrodes at their 10th cycle already yields insight on the matter. In large field of view observations, scattered silicon particles can indeed be spotted as dispersed in thick SEI matrices (fig. VI.1), as if clusters were shattered by the stresses that build up with volumes changes along lithiation. Remarkably, some of these particles also exhibit the composite amorphous/crystalline patterns that we identified as typical of a previous lithiation. This suggests that these SiNPs have indeed previously contributed to the electrode's capacity but that this has stopped through a disconnection of the percolating network. Moreover a significant part of the SiNPs has remained in its pristine state, which is further confirmation of the inhomogeneous lithiation we've observed in part V.2.

Trapped Li atoms in delithiated electrodes

Another symptom of the progressive disconnection of nanoparticles can be observed in delithiated electrodes in the form of trapped Li atoms. This phenomena, also the focus of recent papers from Lee et al. [241, 242], is directly illustrated *via* STEM-EELS measurements in V.2.3. Now, the accumulation of STEM-EELS datasets puts us in a position where data on thousands of particles can be averaged and compared, *via* the methodology detailed in III.2.3. Doing so allows us to quantify how Li trapping evolves as silicon electrodes cycle (fig. VI.2.a) in half cells, from a multitude of local STEM-EELS observations such as those reported fig. VI.2.b-c. Indeed, looking at the overall Li/Si atomic ratio in delithiated electrodes at their 1st, 10th and 30th cycles shows a significant increase throughout aging - data for the 100th cycle was not available. A similar assessment can be made for lithiation (red markers) and we are reminded of the potential-composition curves reported in II.1: a significant quantity of lithium is inserted irreversibly in silicon.

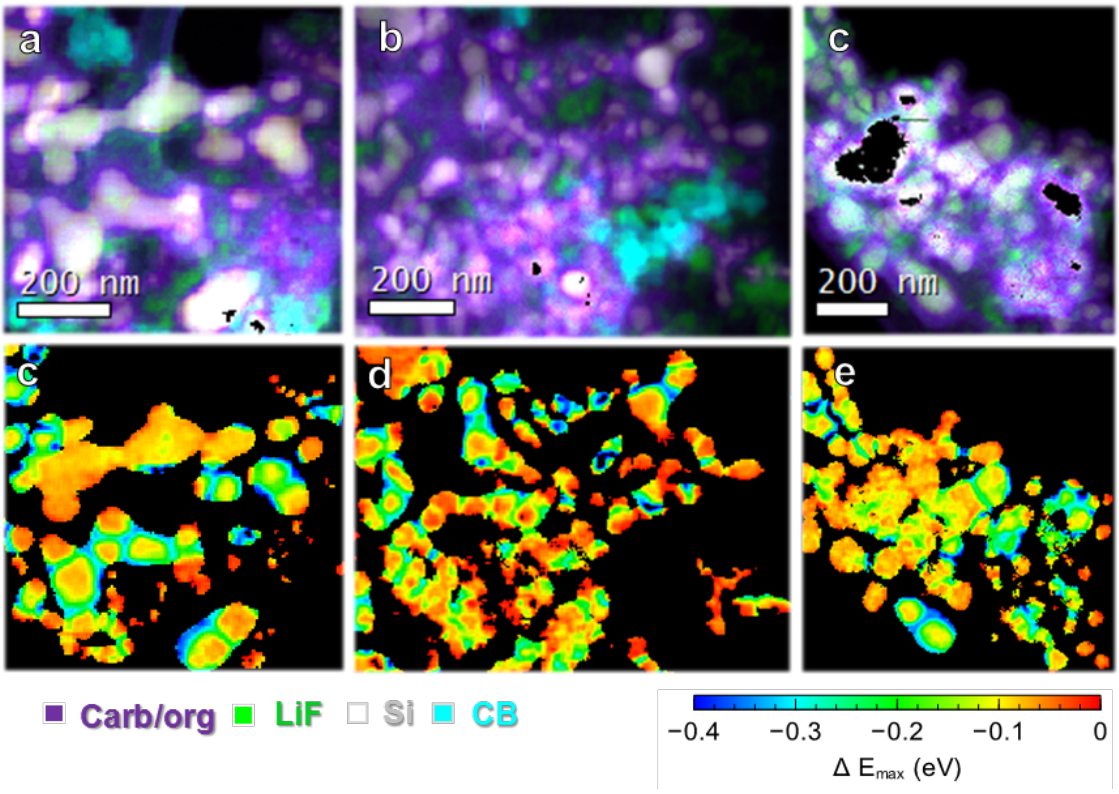

Fig. VI.1: a-c) Composite thickness maps of SiNP clusters from STEM-EELS observations of electrodes at their 10th lithiation. d-e) E_{max} maps of the silicon spectra of these same clusters obtained by Drude model fitting (see III.3.1). Delithiated and pristine particles are observed in lithiated electrodes.

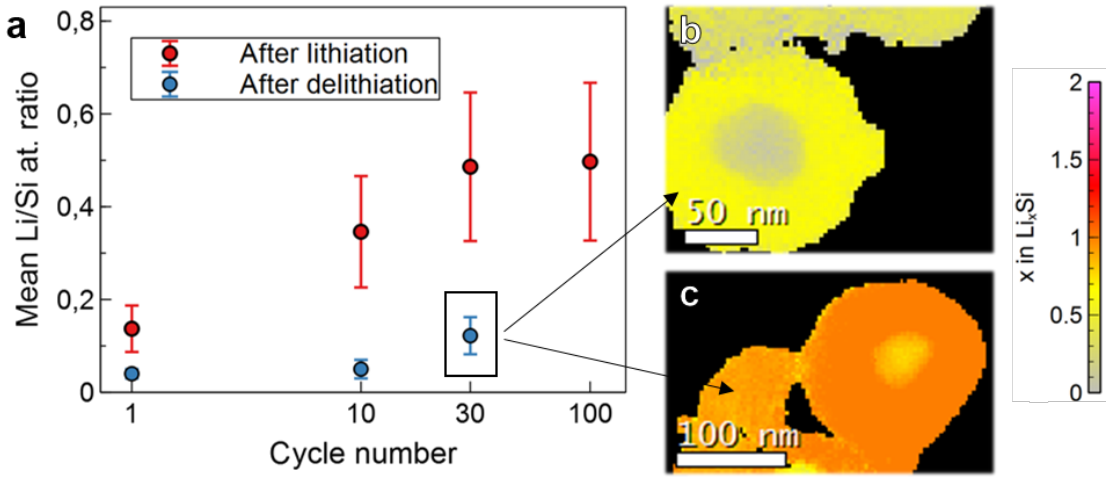

Fig. VI.2: Lithium trapping in aged silicon electrodes after lithiation and delithiation in half-cells. a) Li/Si atomic ratio calculated from the thicknesses of the Li_xSi phases from STEM-EELS analyses, averaged over all observations of electrodes cycled to their 1st, 10th, 30th and 100th cycle respectively. b-c) Lithium content maps calculated from STEM-EELS datasets showing the presence of lithiated particles in delithiated electrodes.

VI.1.2 *Over*-lithiation of nanoparticles in aged electrodes

Nanoparticle morphological evolution upon extensive cycling

The active matter itself undergoes tremendous morphological changes further down an electrode's lifetime. This is first illustrated in E_{max} maps from STEM-EELS observations of an electrode cycled in full cell configuration to its 100th delithiation, as reported in figure VI.3. Here, the shells of extensively cycled nanoparticles exhibit a spiky aspect, akin to dendrite deposition. Remarkably, severely damaged particles can once more be observed adjacent to SiNPs in their pristine state (fig. VI.3.c), which again testifies of local heterogeneities in lithiation that was have attributed to gradients in Li^+ transport.

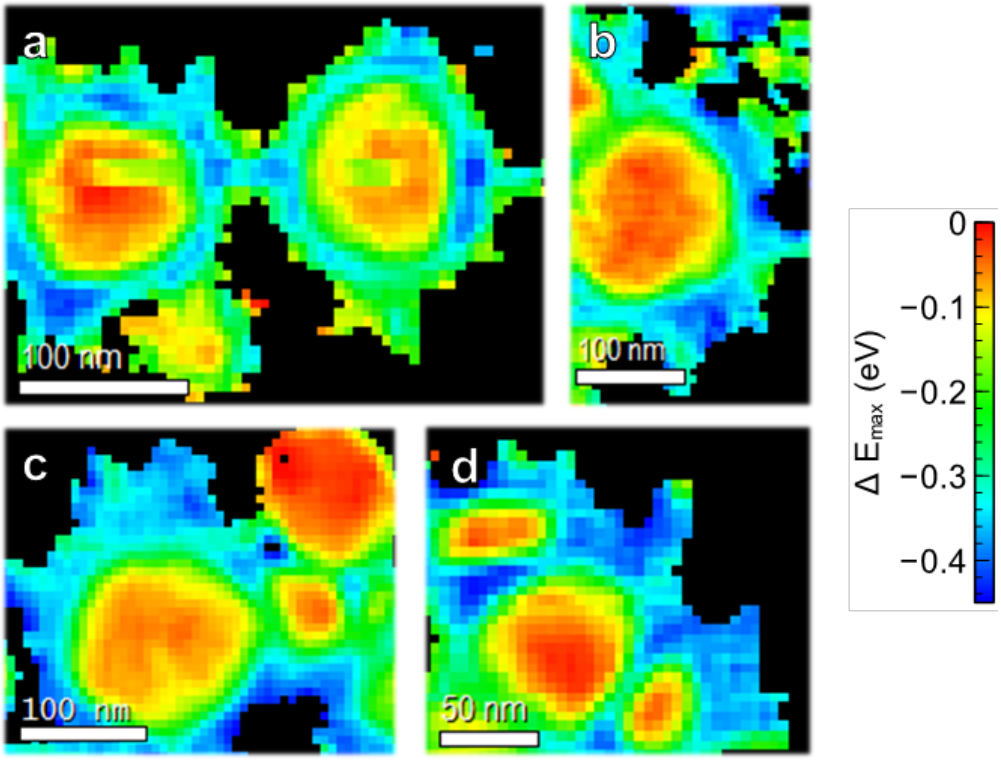

Fig. VI.3: a-d) E_{max} maps of SiNPs from an electrode cycled in a full cell configuration at its 100th delithiation obtained by Drude model fitting of STEM-EELS datasets. Amorphous silicon dendrites are observed.

Further analysis, this time of the electrode "Half cell L100" which has developed an extreme irreversible capacity, provides evidence that the nanoparticle morphology can in fact be rearranged to give way to a continuous amorphous silicon network whose "filaments" can be as thin as 10 nm. Thicker areas likely correspond to the remnants of what were crystalline cores. This extreme modification was detected in 15 individual spectrum images taken on 2 different samples, showing that it is not an isolated phenomenon, but rather a systematic evolution in damaged electrodes whose physical origin is puzzling. An excerpt of these observations is provided figure VI.4 in the form of

composite thickness maps calculated from our STEM-EELS observations. They echo preliminary findings from D.Robert [37] who also demonstrated the existence of these networks after 50 cycles in electrodes cycled to their full theoretical capacity in half cells. Additionally we confirm here the amorphous nature of those filaments since lithium content maps (fig. VI.5) indicate compositions around $Li_{0.5}Si$. Results also show a consistent association of this filament structure with dramatic SEI agglomerates. This is likely owed to the increased specific surface of the network compared to spherical particles, and is evidence of yet another negative synergistic effect between the lithiation of silicon and the continuous growth of the SEI.

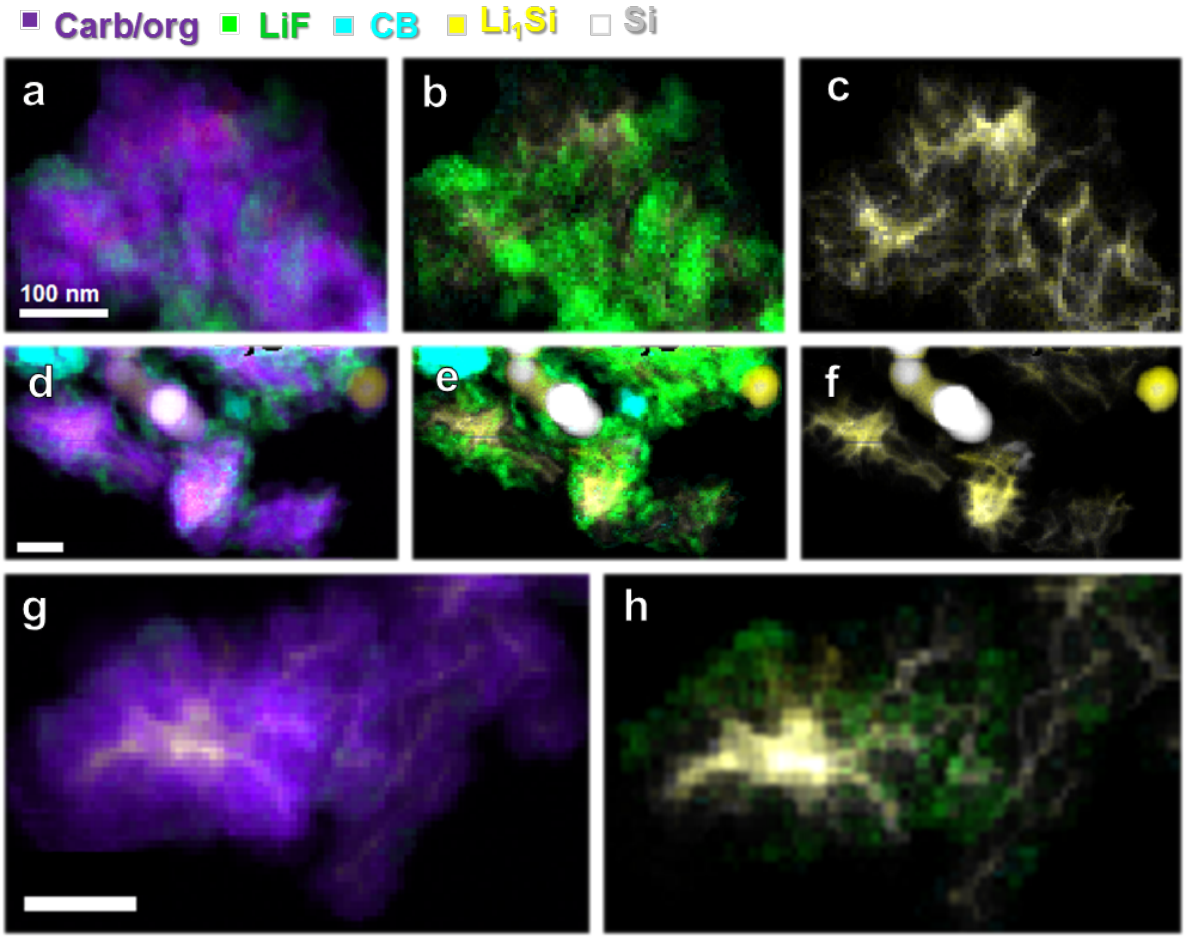

Fig. VI.4: Composite thickness maps of a silicon network observed in 2 electrodes cycled in half cells to their 100th lithiation by STEM-EELS. Colossal SEI accumulation can be observed. a,d,g) All thickness maps are superposed. b,e,h) LiF and Li_xSi only. c,f) Li_xSi only. All scale bars represent 100 nm.

The formation of such a bicontinuous network in fact appears to be an intrinsic properties of alloying materials. Chen, Sieradzki et al. [243] indeed showed a similar evolution in amorphous Sn microparticles (fig. VI.6.a), a material analogous to Si regarding its reaction with lithium. Through a systematic study of the influence of the particle size, the alloy composition and the applied delithiation rate (i.e. applied current per active matter mass), the authors propose that this structure will evolve spontaneously when the dissolution rate of lithium outruns surface diffusion

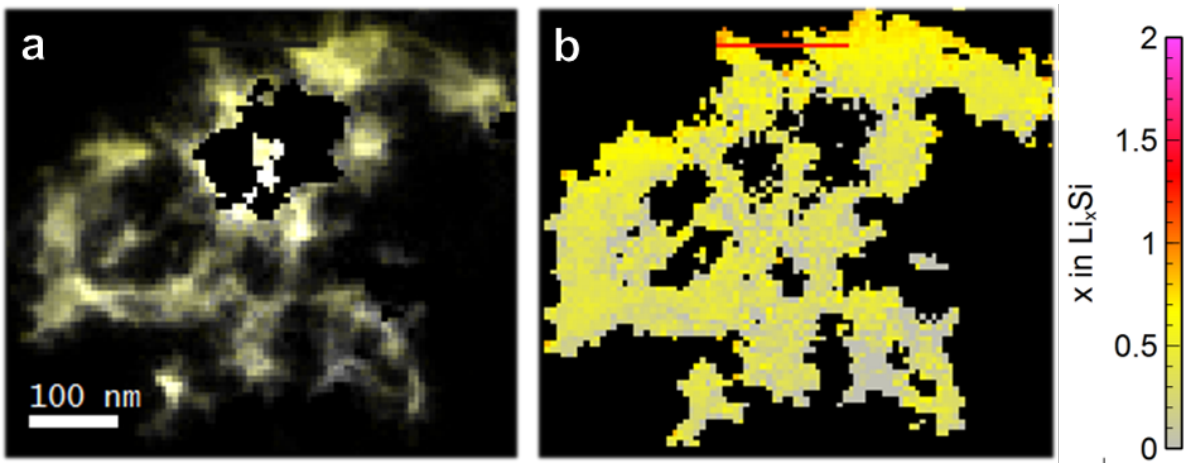

Fig. VI.5: a) Composite thickness maps of an amorphous silicon network observed in 2 electrodes cycled in half cells to their 100th lithiation by STEM-EELS. b) Lithium content map calculated from the same STEM-EELS dataset.

during delithiation. They show that high lithium concentrations and rates promote the formation of networks, while small particle sizes hinder it. Sn particles of diameters below 300 nm stay stable upon dealloying, even for compositions of ≈75 at.% Li. Since we are dealing with even smaller nanoparticles, this suggests that their evolution into networks was caused by extreme local cycling conditions: (i) prior to their transformation, particles were *over*-lithiated, at state of charges clearly above the 30% theoretical capacity limit we have fixed. The absence of crystalline features shows that particles were most likely lithiated entirely to $Li_{3.75}Si$. (ii) They were subject to tremendous delithiation rates. Chen and Sieradzki report that filament thickness diminishes with increasing delithiation rate (see fig. VI.6.b) and that the effect is limited for rates below C/2 (i.e. full lithiation in 2 hours). Given that our cycling conditions are calculated for ≈ C/7.5, this means that the areas represented in figure VI.4 saw currents that could be more than one order of magnitude higher than nominal. It follows that this can only happen if a significant portion of our electrode is inactive and all current in concentrated to a limited number of remaining nanoparticles, after much of the active matter has become disconnected. In fact, the electrode where these networks were observed exhibited an abnormally high irreversible capacity. More on this last point can be found in section VI.2.1.

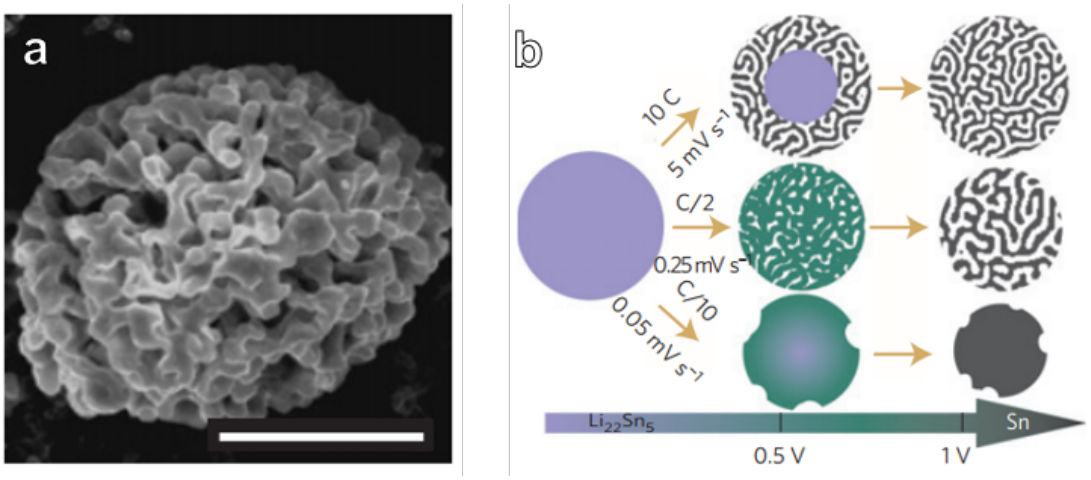

Fig. VI.6: a) SEM micrograph of a porous Sn microparticle after dealloying from $Li_{22}Sn_5$. The scalebar is 2 µm. b) Schematic of the influence of the delithiation rate on the resulting morphology. Reproduced from [243].

Evidence of a second disconnection phenomenon

The overlithiation of a limited number of particles in aged electrodes was already proposed by Oumellal et al. [151] and confirmed by local Auger electron spectroscopy measurements from E. Radvanyi [41] who observed alloy compositions around Li_1Si at the first cycle on the surface of an electrode cycled to 1200 mAh/g, whereas after 50 cycles this had jumped to Li_3Si. However, these authors propose that this evolution is the result of a second and more prominent disconnection phenomenon: the blocking of the Li+ transport network. They hypothesize that as the SEI accumulates in the bulk of the electrode cycle after cycle, ionic transport is hindered. Lithiation consequently becomes a diffusion-limited reaction and a gradient develops across the depth of the electrode, with an *overlithiation* of the surface layer, and particles closer to the current collector rendered inactive. This scenario is illustrated fig. VI.7.

In our case, the evidence for overlithiation is circumstantial and it is difficult to comment on Oumellal's hypothesis. Although the observation of the amorphous silicon networks detailed above is conclusive, it is unclear whether it was caused by the disconnection of other particles from the percolating network or the blocking of ionic transport channels in the electrode. Some of the lithiated particles found in electrode at their 100th lithiation provide insight on the matter however. Their observation is reported fig. VI.8. We see that nanoparticles can exhibit combinations of core-shell ratios and lithium contents that are incompatible with the expected lithiation mechanism, outlined in V.1 and drawn here in grey. According to our model, their surprisingly large amorphous shells (core-shell ratios around 30%) could only have formed for local state of charges above 50%, despite our capacity limit being set to 30%. This suggests that those particles were indeed *overlithiated* at a given point, hence their relatively thick shells and, in some cases, the roughening

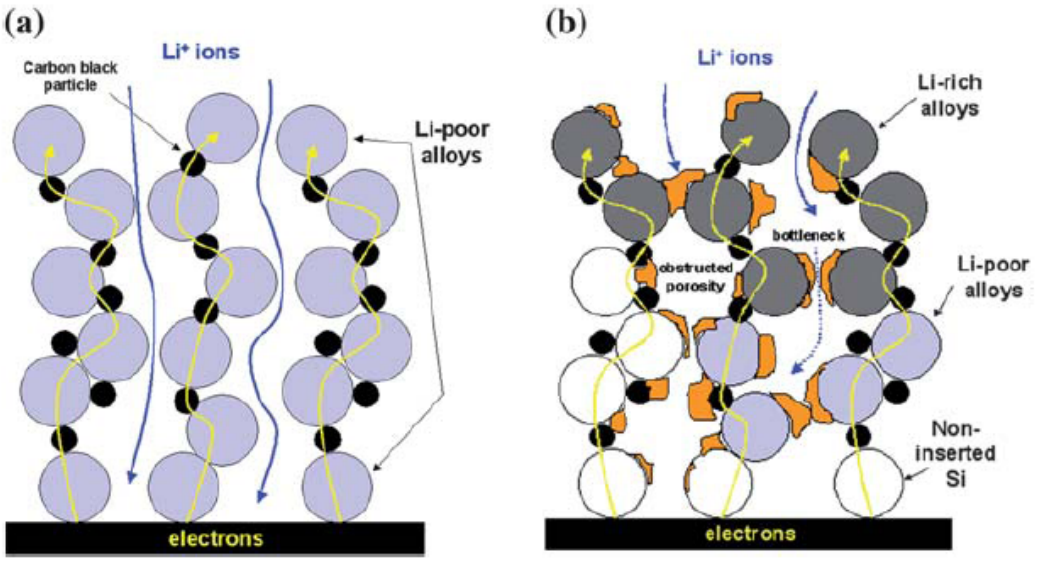

Fig. VI.7: Sketch of the non homogeneous lithium insertion into the composite electrode at the end of discharge, in the fresh state (a) and in the aged state (b).Reproduced from [151].

of their surface and the presence of amorphous filaments (fig. VI.8.b). However upon subsequent cycles those particles did not come back to this overlithiated state, since lithium contents presently do not exceed $Li_{1.5}Si$. Such changing kinetics are evidence of a shifting chemical environment around these particles, and give credit to the idea of increasingly difficult lithium transport in the electrode most likely because of SEI accumulation.

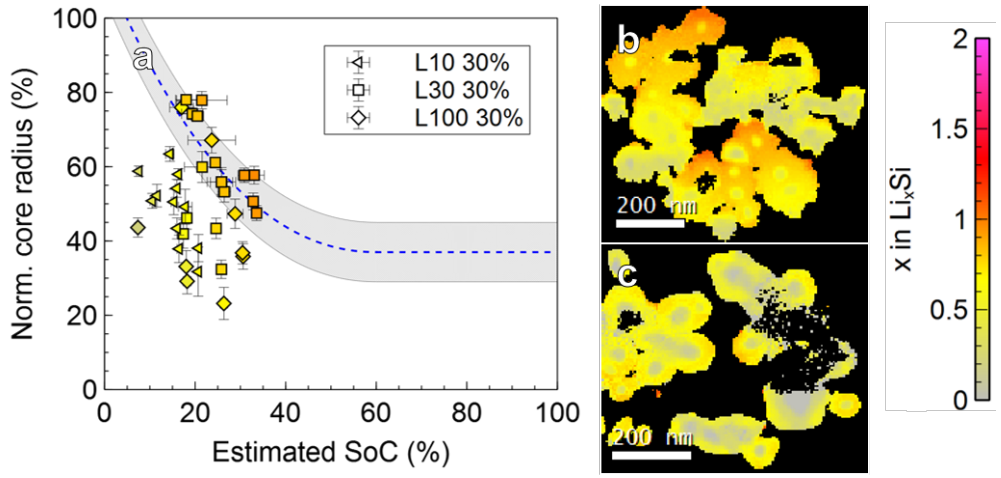

Fig. VI.8: Evidence of overlithiation in electrodes stopped at their 100th lithiation in half-cells. a) Normalized core radius (or core/shell ratio) versus state of charge of lithiated silicon nanoparticles. The grey area represents our model of the 1st lithiation outlined in V.1. After extended cycling a significant amount of particles do not follow that mechanism. b-c) Li/Si atomic ratio maps calculated from STEM-EELS datasets.

VI.1.3 Depth profiling on FIB lamellas: searching for electrode-scale gradients

Objectives and preliminary SEM observation

As shown above, particle-scale observations of aged electrodes reveal two competing phenomena that hinder lithiation at the electrode scale: (i) the pulverization of silicon clusters, which results in a disconnection from the percolating network. (ii) the blocking of Li^+ transport channels caused by the accumulation of the SEI. Now, we have seen that Oumellal, Radvanyi and coauthors [41, 151] favor a scenario where Li^+ transport is limiting and (i) is negligible, resulting in an overlithiation of the surface of the electrode. Since the experimental evidence for this is scarce, we look to probe the depth of the electrode in order to investigate those alleged electrode-scale gradients.

This is achieved by preparing cross-sections of an electrode stopped at its 10th lithiation in half-cell configuration. The FIB preparation protocol of these cross-sections, or lamellas, is particularly difficult given the porous nature of electrodes as well as, once more, the sensitivity of the species of interest. It is detailed in part II.1. Nevertheless, a total of 3 lamellas were successfully prepared. Preliminary SEM analysis already provides a qualitative indication of significant chemical inhomogeneity, using the backscattered electron detector (EBSD). Backscattered electrons have the advantage that they are sensitive to the atomic mass of the nuclei they scatter from. As a result, heavier elements which backscatter more efficiently appear brighter than lighter elements. In figure VI.9, the EBSD intensity is notably lower near the current collector. It is indicative of a lower average atomic number e.g. a higher concentration in SEI and lithiated species relative to silicon in the depth of the electrode, whereas according to the mechanism described earlier, the opposite should be true. Further investigation is warranted.

Depth profiling of SEI species

The electrode is milled until areas that are 1 nanoparticle thick are revealed and an electron transparency conform to TEM requirements is observed in the SEM. After vacuum transfer, large field of view ($> 5\,\mu m^2$) STEM-EELS datasets can subsequently be acquired on the lamella at different depths. This is illustrated figure VI.10. In addition to the structures already identified in V.2, with the SEI featuring segregated LiF domains and a organic phase that is organized in a conformal coating around SiNPs, we find back the core-shell structures that are expected in cycled electrodes. From single STEM-EELS spectrum images, valuable insight can already be gathered as to the size of disconnected domains. The area corresponding to figure VI.10.b-c features delithiated silicon which indicates a formerly active domain, now disconnected, whereas in figure VI.10.d-e we observe an active cluster. The two are directly adjacent. Yet it is difficult to go beyond such qualitative remarks with thickness maps alone. To assess whether there is in fact an

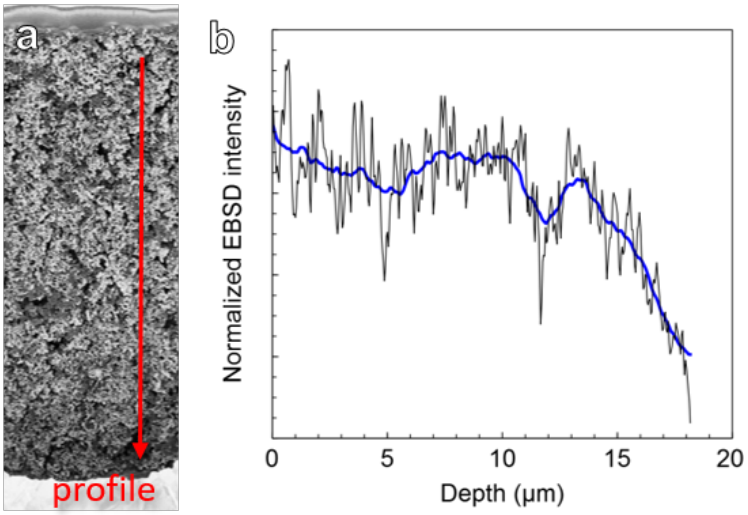

Fig. VI.9: a) SEM observation of the cross-section of an electrode prior to lamella extraction in the FIB. Using the backscattered electron (EBSD) detector allows us to obtain chemical contrast. b) Depth profile integrated over the width of (a). Darker contrasts are associated to lower mean atomic numbers.

uneven distribution of Li_xSi and SEI species across the depth of the electrode, we now look towards summing up and comparing the relative amount of each species of interest for all spectrum images. The FIB preparation preserves the electrode structure and the position of the clusters probed by each spectrum image in the electrode is known. This allows us to draw the plots reported figure VI.11.

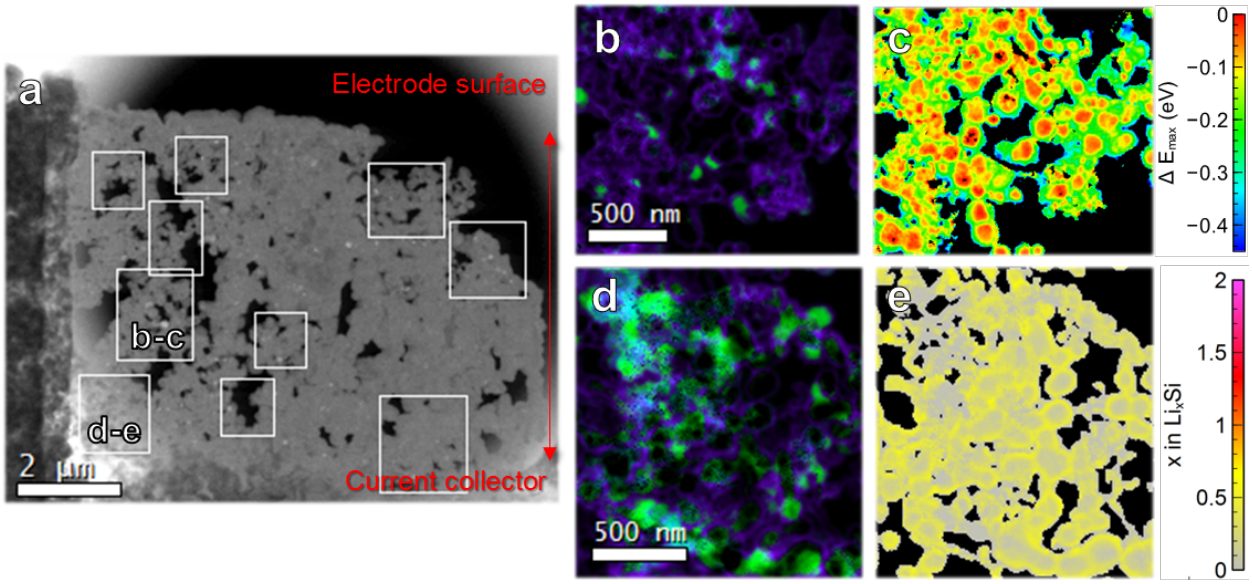

Fig. VI.10: STEM-EELS analysis of an electrode cross-section prepared by FIB. a) Large field of view HAADF STEM image of the 5 µm of the electrode. White rectangles represent STEM-EELS acquisition areas. b) Composite thickness image of LiF (green), the *org* phase (purple) as well as carbon black (teal). c) E_{max} map of that same area obtained by Drude model fitting. The presence of crystalline/amorphous core-shell structures can be observed. d) Composite thickness map. e) Corresponding Li/Si at. ratio map (i.e. x in Li_xSi).

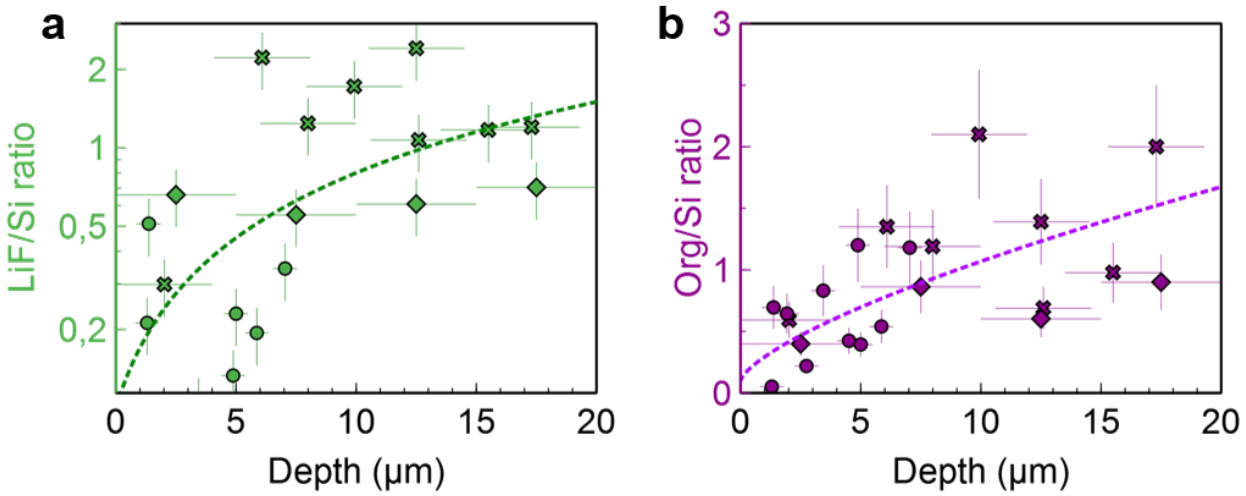

Fig. VI.11: Volumetric ratios of LiF and the *org* phase on silicon at different depth in the electrode from the electrolyte/electrode interface to the current collector. Each point represents a STEM-EELS dataset, or spectrum image. Marker shapes are used to differentiate data from the 3 lamellas we analyzed.

Semblance of trends can be read on these two plots. Despite a significant variance in our dataset, and the presence of several outliers, there appears to be an increasing amount of SEI, both from the LiF contribution and from the *org* phase (abusively named so as all non-inorganic components of the SEI, see chapter III.2) as we approach the current collector. Although the trend is drawn from a limited number of points, it is supported by an earlier SEM-EBSD observation, as well as a complementary subsequent ToF-SIMS measurement performed by A. Bordes on one of the lamellas observed by STEM-EELS. The resulting elemental maps are reported VI.12. With this additional experiment, we were able to reach the same conclusion from an independent measurement: a higher lithium concentration clearly stands out near the current collector, which supports the trend we have identified for LiF. On VI.12.c, we see that the same is true for carbonated electrolyte reduction products, if we assume the contributions of carbon black and CMC to the ToF-SIMS signal to be negligible. Better yet, the "shadowing" artifact that is commonly observed in ToF-SIMS can easily be dismissed in this planar geometry [244]. We therefore consider this result as robust since several results converge.

Yet interpretation is not straightforward. We envision two scenarios: (i) Throughout aging, particle clusters are pulverized by the swelling/contraction cycles that accompany lithiation. This causes the percolating network to break in multiple areas, and the closer particles are to the surface of the electrode, the more likely they are to be disconnected. As a result reactions at the surface of the electrode (interface with the electrolyte) become reaction limited, or electron-starved. It follows that electrolyte reduction would proceed preferentially near the current collector from which electrons flow. Larger amounts of SEI would form at the bottom of the electrode as a result. In this case the electrochemical balance is flipped compared to what Oumellal and others postulated: electron flow, rather than Li^+ diffusion, is limiting and creates the inhomogeneity that

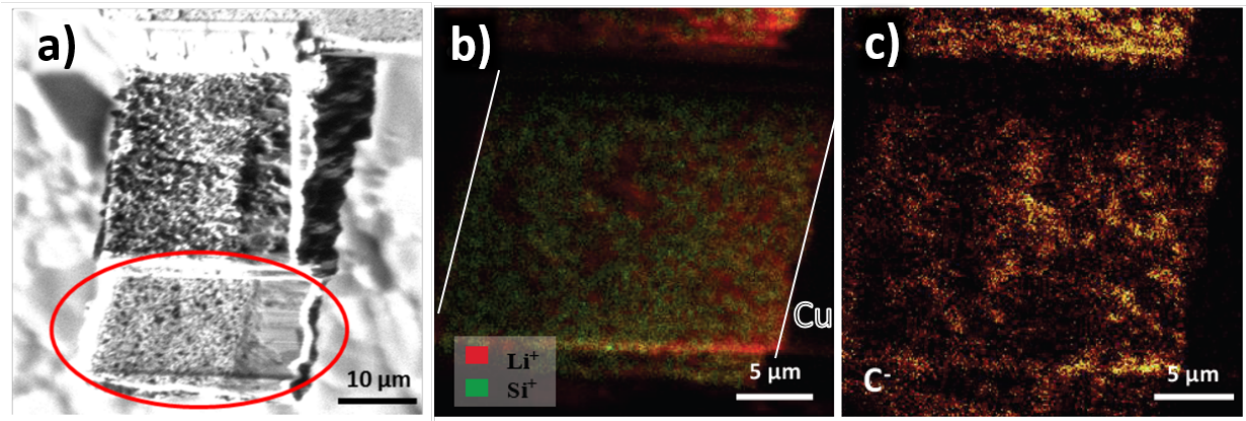

Fig. VI.12: ToF-SIMS analysis of one of the FIB-prepared lamellas **after** the STEM-EELS experiment. a) SEM observation of the lamella welded to a TEM half-grid. b-c) ToF-SIMS cartography of Li, Si and C showing a heterogeneous distribution.

we witness. The poor dispersion of the conducting additive carbon black possibly participates (see V.2.1). However another factor, considerably more trivial, could explain the gradients observed here. We know from the ^{7}Li NMR experiments performed by Delpuech et al. [27] that the electrolyte from aged cells presents additional resonances that are characteristic of soluted lithiated species. Jin et al. [245] also determined that there are soluble PEO-based compounds among FEC reduction products *via* ^{13}C NMR. This leads us to scenario (ii): those gradients could in fact be the result of the sedimentation of soluble species from the electrolyte drying during sample preparation. Rinsing was in fact purposefully avoided so as to preserve these compounds.

Although it is worth considering, the second case is arguably less likely. LiF, for example, is known to be poorly soluble in carbonate solutions [246]. Furthermore it lies on the assumption that sedimentation would result in concentrations 10 times higher at the bottom of the electrode according to the data reported figure VI.11, which is doubtful given the porous nature of the electrode and the limited timescale of the drying process. Moreover, scenario (ii) can confidently be discriminated against by looking at insoluble species. Li_xSi compounds, especially, should also be present in higher amounts near the bottom of the electrode if the electron flow is in fact the limiting factor. In addition, considering the distribution of those lithium-silicon alloys allows us to directly challenge the hypothesis from Oumellal et al.

We are however confronted to significant damage that is inherent to the FIB preparation protocol. Indeed, lithiated particles exhibit compositions that are close to $Li_{0.5}Si$, which matches the floor composition $Li_{0.4}Si$ found in alloys subject to intense irradiation damage (see III.1.1). Such extensive degradation is not unexpected given that the displacement cross-section of lithium peaks around 30 kV, which is exactly the energy of the Ga^+ ions used for FIB milling. Consequently, Li-Si alloys undergo significant damage during the preparation of each lamella and metallic lithium deposits are observed on the surface of nanoparticles, as illustrated figure VI.13.a-b. These deposits

have previously been identified as telltales of lithium depletion, and an assessment of the distribution of lithium in the electrode can still be reached provided we include the metallic lithium phase in our calculation. This is reported figure VI.13.c.

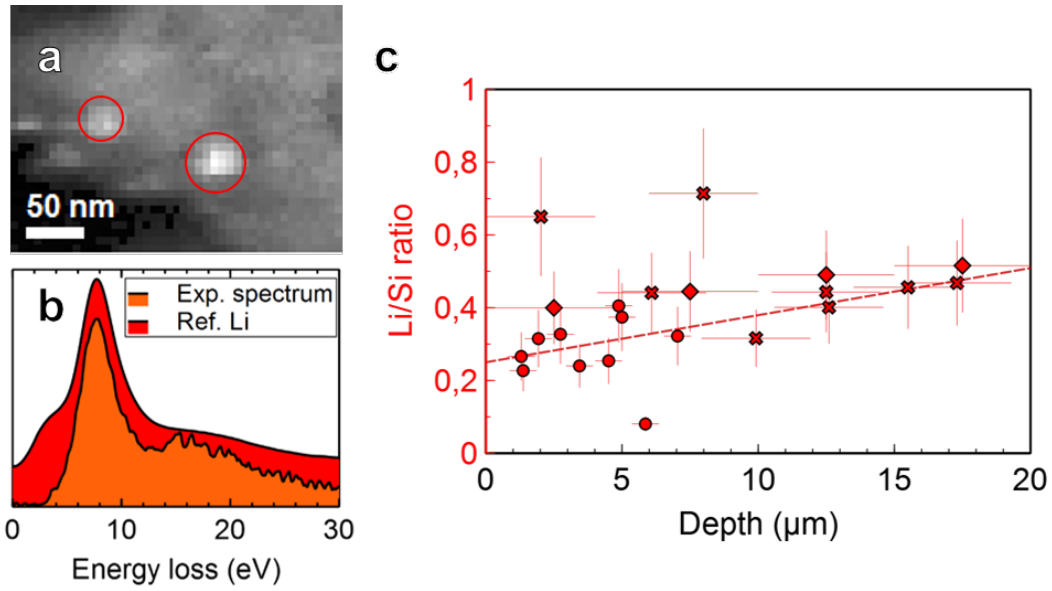

Fig. VI.13: a) Energy slice of a STEM-EELS dataset centered on 7.5 eV, the plasmon peak energy of metallic lithium. Two Li deposits are highlighted in red circles. b) Reference Li-metal EEL spectrum and experimental spectrum from the areas highlighted in red circles in (a). c) Overall Li/Si atomic ratio at different depth in the electrode. Each point represents a STEM-EELS dataset, or spectrum image. Marker shapes are used to differentiate data from the 3 lamellas we analyzed.

Once again, despite the presence of outliers in this dataset, an appreciable trend stands out. Overall, there appears to be an appreciably higher Li concentration in Li-Si alloys deeper in the electrode. Atomic ratios are observed to climb from 0.25 at the electrode's surface to 0.5 near the current collector. This matches scenario (i) detailed above, which states that lithiation kinetics are mediated by the electron flow in this electrode. We believe that this mechanism does not contradict previous findings but is rather complementary. If the mechanical strain from lithiation is mitigated by the electrode's architecture or other factors, pulverization will be limited and disconnection of the active matter will be marginal. As SEI accumulates homogeneously across the electrode, ionic transport to the depth of the electrode becomes hindered, causing *overlithiation* of the surface. This is the case outlined by Oumellal and Radvanyii.

On the contrary, if pulverization occurs to a greater extent, particles at the surface of the electrode are more likely to be disconnected from the percolating network. Both SEI reduction and lithiation reactions would then proceeds preferentially near the current collector, as shown in the present manuscript. Another factor could participate: the existence of a gradient of electrical potential in the electrode, with more reductive potentials at the electrode/current collector interface, which would naturally lead to higher overall Li contents in the Li_xSi compounds formed in the depth

of the electrode as seen here. This phenomenon was outlined by J. Gao in a recent review [247] and evidenced by the *in situ* electron holography experiments of Yamamoto et al. [248, 249]. In a nutshell, from Oumellal and Radvanyi's result in one hand and ours on the other, we see that chemical gradients will develop either way, but in opposite directions depending on the extent of the disconnection of the active matter.

VI.2 Quantifying the SEI's evolution throughout aging

In silicon-based electrodes, the tremendous volume changes that occur during cycling impose considerable stresses to the SEI. Cracks appear in the layer [15, 240, 250] and fresh Li_xSi surfaces are exposed. This fosters continuous electrolyte reduction. As a result, not only does an insulating film form between SiNPs [242], limiting lithiation kinetics, but charges are also irreversibly consumed in the process. This last point is critical in full cells, as shown by Delpuech et al. [27] with the *slippage* phenomenon (see I.1.2). For those reasons SEI accumulation has been pointed to as the prime cause of the poor capacity retention of Si-based electrodes.

In this section, we aim to provide direct observations of the evolution of the silicon electrolyte interface of aged silicon electrodes. Electrode-scale results from the literature can benefit from being challenged at a local scale *via* STEM-EELS, and the trends in overall accumulation as well as the evolution of the chemistry of the SEI throughout aging will be discussed. Furthermore, we can take advantage of our ability to analyze multiple phases simultaneously to look for correlations between the SEI's composition and local lithiation performances. Finally, we look for modifications in the SEI when the carbonate solvent is partly substituted for the ionic liquid PYR13TFSI, in a bid to mitigate the continuous SEI reduction.

VI.2.1 SEI accumulation and mass increase of electrodes

Phase mapping in aged electrodes

Several studies have followed the mass increase of an electrode through simple gravimetric methods [26, 37, 41], and others have measured a gradual decline in porosity [89] throughout aging. These measurements indisputably point to a build up of electrolyte reduction products in the bulk of the electrode, but there is no local investigation of this phenomenon to date. In figure VI.14, we show that accumulation can be directly quantified from STEM-EELS data.

After the 1st lithiation, we retrieve the overall morphology detailed in V.2. Particles are coated in a thin, ≈ 15 nm thick layer mapped as the *org* phase, while LiF is present in small "chunks". Carbon black (CB) is once more noted to form agglomerates and does not appear to be distributed well enough to contribute efficiently to the percolating network (fig. VI.14a-b). After the 30th lithiation, the *org* layer has gotten thicker and small particles especially see themselves engulfed in a thick matrix. In some cases, *org* layers were measured to be as thick as 100 nm, in line with other findings such as those from E. Peled et al. who measured 71 nm on silicon nanowires [251]. This is illustrated figure VI.15. At the 100th lithiation, significant differences can be observed between electrodes cycled in full and half cells. In half cells, overlithiated particles have turned into a continuous amorphous network whose increased effective surface has favored the growth of large

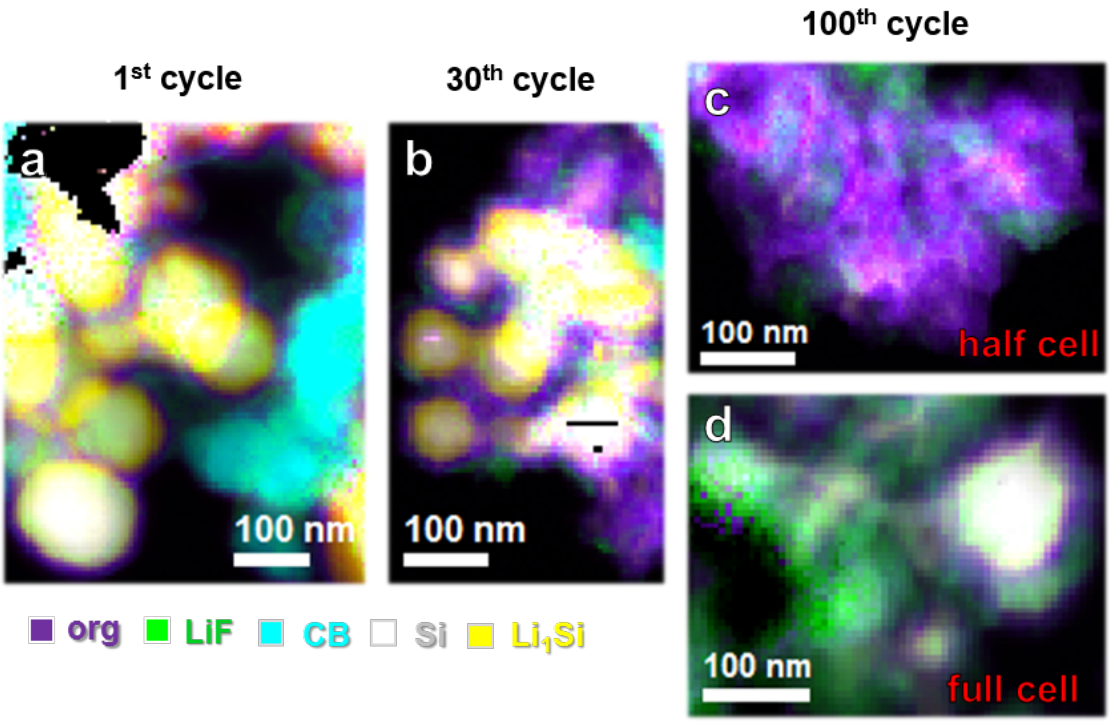

Fig. VI.14: Composite thickness maps calculated from STEM-EELS datasets through the t/λ method. All observed particles come from electrodes cycled with a limited capacity of 1200 mAh/g and stopped after lithiation. a) 1st lithiation in half cell configuration. b) 30th lithiation (half cell). c) 100th lithiation (half cell). d) 100th lithiation (full cell). Intensities range from 0 nm to 150 nm.

amounts of SEI, LiF and organic products alike. In full cells however, accrued SEI quantities can be observed, yet understandably to a lesser extent since particles do not evolve into filaments.

Quantification over all spectrum images

Quantitative trends can hardly be drawn from a few thickness maps, but multiplying STEM-EELS measurements can allow us to assess the relative amount of a given compound in each electrode. From there, one can evaluate the extent of accumulation, one phase at a time. This is reported figure VI.16.

From this representation of the data, we see once more that SEI accumulation relates to LiF as well as organic species. This has been subject to controversy. Several studies have indeed concluded that LiF formed in the first cycles and did not evolve afterwards [118]. However there is strong evidence for a continuous reduction of the FEC additive [104] (used here in a concentration of 10 w%) throughout the lifetime of the electrode, and LiF has been identified as a by-product of FEC reduction in several reports [103, 111]. This is coherent with the roughly three-fold increase measured here from the 1st to the 100th cycle, with volumetric ratios going from around 0.25 to around 0.8. Likewise the irreversible capacity increases three-fold between the 1st and 100th cycle,

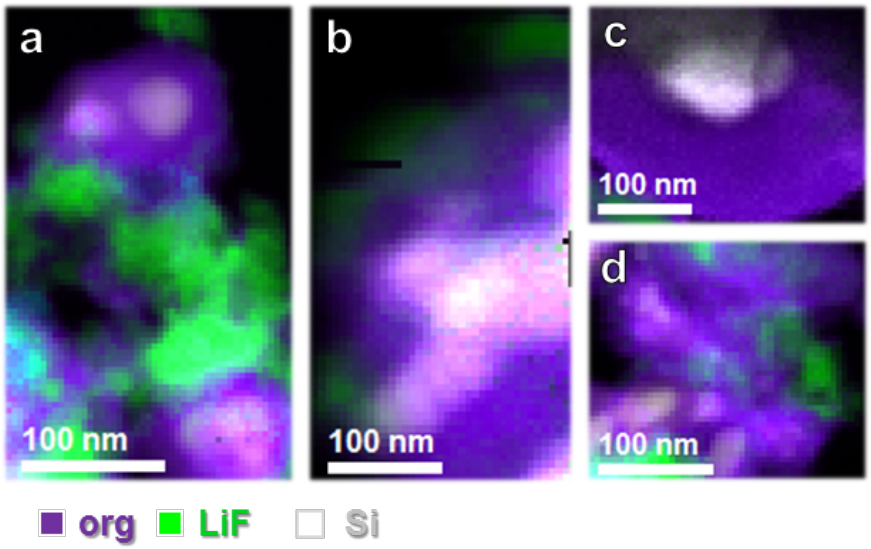

Fig. VI.15: Composite thickness maps calculated from STEM-EELS datasets through the t/λ method. All observed particles come from electrodes cycled at 1200 mAh/g in full cell configuration and stopped after lithiation. a) 10th lithiation. b-d) 100th lithiation. Intensities range from 0 nm to 300 nm for SEI components and 0 nm to 100 nm for silicon.

as illustrated figure VI.17. This correspondence supports the notion that the main react path to LiF is electrochemical. Interestingly, there is little to no difference in LiF/Si volumetric ratios between electrodes cycled in full cells and half cells, despite the much lower reversible capacities of aged full cells, e.g. the lesser strain put on the SEI. This could mean that LiF is not as dependent as other SEI components on the cracking of the layer to accumulate.

Regarding the *org* phase, accumulation trends are considerably greater. A 2.3-fold increase is observed in full cells, from 0.7 to 1.7 whereas in half cells it is over 7-fold, roughly from 0.7 to 5.1. This discrepancy can partly be explained by the known mechanism of a continuous reduction of the carbonate solvent on fresh surfaces exposed by volumes changes of the Li-Si system, which occurs continuously in half-cells while cycling practically halts after a few dozens of cycles in full-cells. However the electrode cycled to 100 cycles in half cells exhibits singular performances and should be considered separately, as shown figure VI.17. If we exclude this datapoint from the fit, we now measure a milder increase for the volumetric ratio of the *org* phase in half cells, from 0.74 to 3.06, a 4-fold increase. A summary of these values can be found table VI.1.

The volumetric ratios that correspond to delithiated electrodes can also be seen to be consistently below those of lithiated ones. This matches reports of the so-called *breathing* phenomenon, which has been associated with a oxidation of the SEI upon discharge [118]. This is not observed for LiF, which is appropriate given that the inorganic part of the SEI has not been reported to be subject to breathing [121].

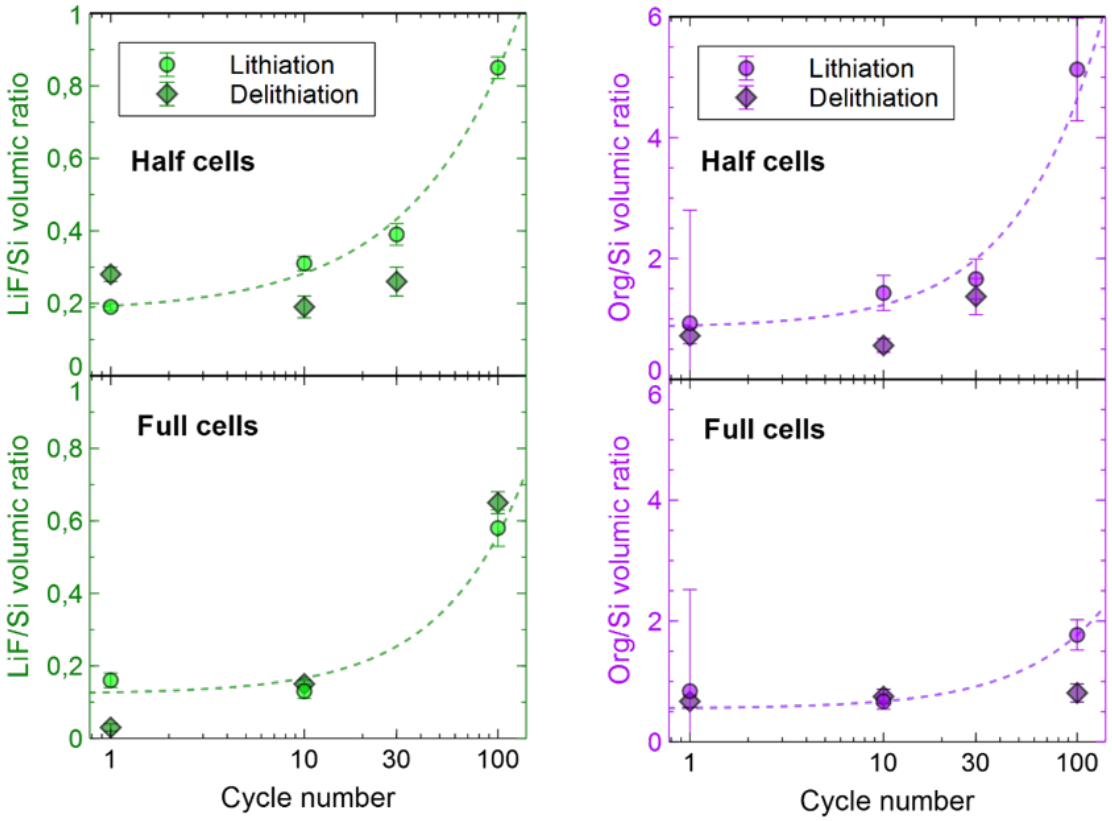

Fig. VI.16: Volumetric ratios of LiF as well as the *org* phase averaged over numerous spectrum images from several electrodes cycled in full and half cell configuration. The datapoints for the *org* phase at the first cycle were averaged together and are common to the two plots.

Relating SEI quantities to the irreversible capacity

The quantities of SEI that we measure should be directly linked to the irreversible capacity of the cells, which is the quantity of electrodes that are not retrieved upon discharge. If we now look at the irreversible capacity plot for a few of the electrodes we analyzed, we see that full and half cells alike exhibit similar profiles - if we extrapolate "Half-cell L30", thought to be representative of a "regular" half cell behavior. This is in agreement with the aging study from Delpuech et al. [27] down to the values themselves, of about 1500 mAh/g after 100 cycles. However, "Half cell L100"

Table VI.1: Summary of the volumetric ratios of SEI components calculated from STEM-EELS datasets of electrodes cycled in full and half-cells.

Data	LiF	*org* phase	LiF/*org*
1st cycle	0.18	0.74	0.24
100th cycle (linear fit on full cells)	0.62	1.71	0.36
100th cycle (linear fit on half cells)	0.66	3.06	0.22
"Half-cell L100"	0.85	5.13	0.17

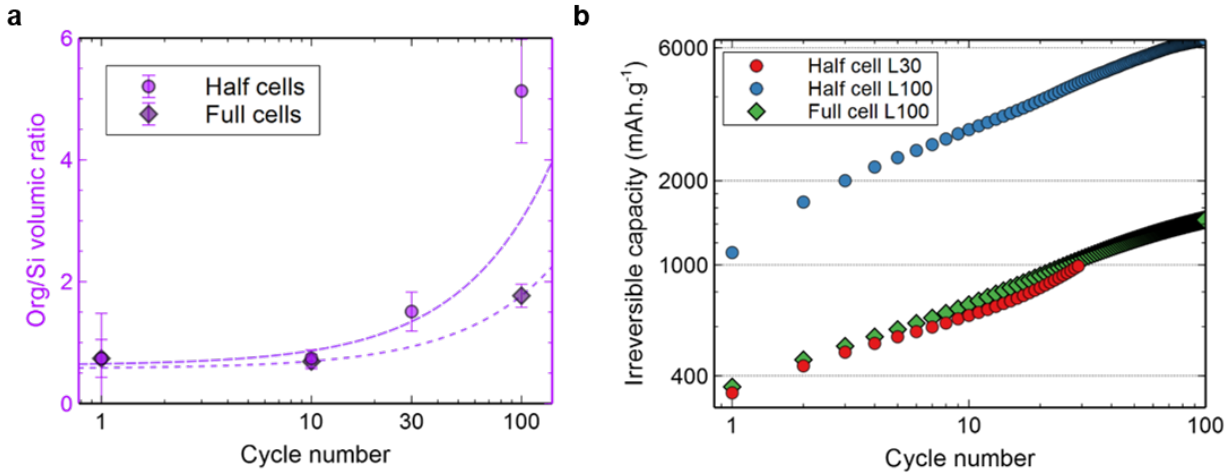

Fig. VI.17: a) Volumic ratio of the *org* phase on silicon for cells cycled in full and half cell configuration. The datapoints for lithiated and delithiated electrodes were averaged. b) Specific irreversible capacity calculated from galvanostatic cycling data. A logarithmic scale was used on the y-axis to visualize "Half cell L100" and others side by side.

shows close to 4 times the irreversible capacity of other cells. This understandably corresponds to a greater SEI accumulation but, surprisingly, the higher SEI content measured in "Half-cell L100" is not proportional to the increase in irreversible capacity. This either suggests that (i) the irreversible capacity contains more than the electrons lost in reduction reactions of the electrolyte. Electrons consumed in $\mathrm{Si} + \mathrm{xe}^- + \mathrm{xLi}^+ \rightarrow \mathrm{Li_xSi}$ could also be lost irreversibly. Therefore the disconnection of the active matter could play a significant role here. It matches the extreme *overlithiation* phenomena observed in the first section of this chapter. Or (ii): electrolyte degradation products become more dense (per mole of electrons consumed) in later cycles. This would explain while a large increase in irreversible capacity translates to a limited difference in volumetric ratios between "Half cell L100" and the rest of the fit on half-cell data.

Likewise, the discrepancy in volumetric ratios between full and half cells does not correspond to a major difference in the irreversible capacity plots. As previously stated, this could mean that denser products are formed in aged full-cells compared to half-cells.

Estimating the overall mass increase of electrodes

While the STEM-EELS analysis of this work yields the volume of each phase, other reports have rather put forward an overall mass increase of electrodes cycled in half cells across aging [26, 37, 41]. A comparison could allow us to assess the reliability of our method which admittedly relies on a very limited sample size. Indeed, a little over 10^3 nanoparticles were analyzed in his thesis work, while each electrode contains 10^{10} to 10^{11} SiNPs. Now, the mass increase that corresponds to a

given STEM-EELS measurement can simply be estimated through equation VI.1 and VI.2, where m_0 is the mass of the components present in the pristine electrode: silicon and carbon black (CB).

$$\frac{m_{aged}}{m_0} = \frac{m_{LiF} + m_{org} + m_{Si} + m_{CB}}{m_{Si} + m_{CB}} \tag{VI.1}$$

$$\text{With} \quad m_{Si} = \sum_x V_{Li_xSi} \rho_{Li_xSi} \frac{M_{Si}}{M_{Li_xSi}} \tag{VI.2}$$

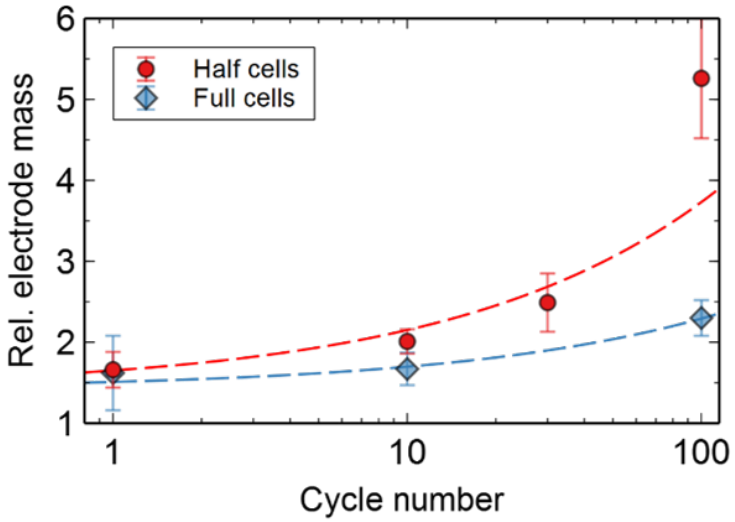

Fig. VI.18: Relative mass of aged electrodes (in units of the pristine electrode mass m_0) calculated from the volumes obtained by quantification of the STEM-EELS data.

The densities ρ_i used to calculate the masses m_i are summarized in chapter III.2.3. Applying these equations leads to figure VI.18, where once again we've distinguished the half and full cell cases. Naturally the tremendous accumulation of the *org* phase translates to a significant increase in the electrode mass in half cells - a 3.2-fold increase without "Half cell L100", 5-fold with it included, whereas in full cells it is not as severe, at a 2-fold increase. This data can now be plotted side by side with that of D. Mazouzi et al., obtained from microbalance measurements on electrodes cycled in half-cells. This is done figure VI.19.

The comparison with Mazouzi's datapoints (purple markers) is especially pertinent since their electrodes have the same formulation and loading (80:12:8 Si:CB:CMC, 1 mg cm^{-2}) and were cycled in the same conditions (1 Li in 2 hours i.e C/7.5, cycling from 1 V to 0.01 V vs Li/Li$^+$) in an identical electrolyte, with the exception of the 2% VC added in their case. In addition, irreversible capacities were measured to be similar to our work. Robert's (yellow markers) reflects an electrode that was cycled to its full theoretical capacity of 3600 mAh g. Full lithiation cycles will understandably subject particles and their SEI to dramatic stresses, so that the electrode's mass understandably reaches $5\,m_0$ after only 50 cycles. As to Radvanyi's (green markers), the formulation

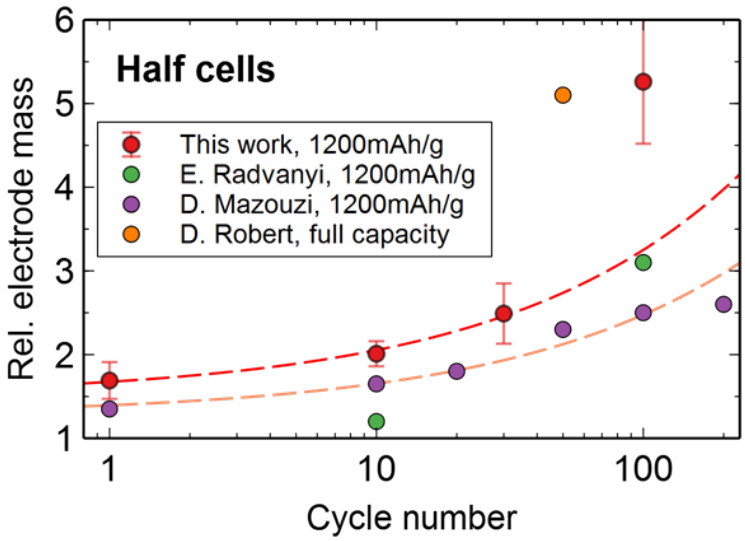

Fig. VI.19: Relative mass of aged electrodes calculated from the volumes obtained by quantification of the STEM-EELS data on electrodes cycled in half-cells. Datapoints from this work are compared to those of D. Mazouzi [26], D.Robert [37] and E. Radvanyi [41] and coworkers.

was significantly different, with only 65% Si, and cycling was carried on at a slow rate of C/20 with a cut at 0.03 V vs Li/Li^+. In addition FEC was not used.

Coming back to the data of Mazouzi, we observe a constant offset downwards compared to our own. Several factors can explain this offset, among which we note: (i) their rinsing of the electrode. Soluble electrolyte products could be eliminated during this step, thus lowering the overall SEI amount and the measured mass. Dedryvère [155], Michan [89] specifically detect that PEO-type oligomers are preferentially rinsed off in XPS and NMR studies respectively. (ii) The silicon powders used in the two studies are not identical. Theirs is fairly monodisperse around 100 nm, whereas ours is polydisperse with a significant portion of small diameter, high specific surface polycrystalline SiNPs (see V.2). An increased specific surface naturally leads to larger SEI buildups. (iii) The accuracy of our method. At the electrode scale, our sample size is extremely reduced and despite our development efforts (see chapter III.2), the technique suffers from intrinsic drawbacks such as its low detection limit. Our considering of the *org* phase is a homogeneous medium of constant density for practical purposes could also introduce significant inaccuracies.

All things considered, this result establishes an important bridge between our local technique and an electrode-scale characterization. In spite of item (iii) and with (i) and (ii) in mind, we believe that the similitude between the trend found in Mazouzi's report and ours highlights the versatility of STEM-EELS, and its ability to probe several length scales at once.

VI.2.2 Chemical changes in the carbonate-organic phase

Molar mass profile from the Faraday equation and STEM-EELS quantification

Our estimation of the mass of aged electrodes can be exploited further. In fact, both fitted curves of figure VI.18 can be used to predict the mass increase at any given cycle number. Therefore Faraday's law (equation VI.3) can be used to estimate the average molar mass of the products responsible for the irreversible capacity up to each cycle, noted here $\overline{M}_{srp}$, for side reaction products. This could allow us to challenge previously formulated hypothesis regarding the density of electrolyte reduction products in full and half cells. Here m^* is the mass increase represented figure VI.18, F is Faraday's constant, and Q_{irr} is the total irreversible capacity plotted figure VI.17.b.

$$\overline{M}_{srp} = \frac{m^* F}{Q_{irr}} \tag{VI.3}$$

To interpret these curves we rely on reduction mechanisms proposed in the literature for the formation of ethylene-oxide based oligomers (PEO) [89] as well as the reduction of FEC, since those are expected to be the principal components of the *org* phase when FEC is used according to the review of chapter I.2.3. Regarding FEC, reports from Nakai [108], Markevitch [103, 252] and Jung [104] have proposed 3 to 4-electrons reduction pathways leading to an assortment of reaction products including Li_2O, LiF, Li_2CO_3 and a partially cross-linked Li-containing polymer (hereby refered to as poly(FEC), see I.2.2) as well as the gases CO_2 and H_2. With these last two excluded, since they will not contribute to the mass increase of the electrode, a review of those works puts the overall reduction of FEC at an average around $\overline{M}_{srp} = 60 g.mol_{e^-}^{-1}$. These values, along with the profiles calculated *via* the Faraday equation, are reported figure VI.21.

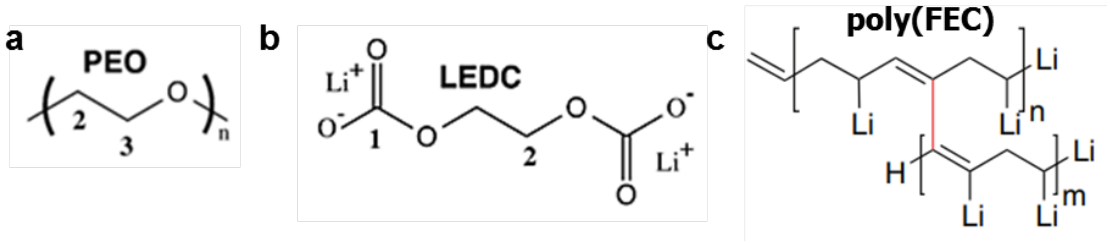

Fig. VI.20: Main SEI components considered in this work: polyethylene oxide (PEO), lithium ethylene dicarbonate (LEDC) and the polymer that results from FEC reduction (poly(FEC)). Edited from [89] (a-b) and [104] (c) respectively.

Three distinct behaviors stand out. Regarding half-cells, we see that for electrode "Half cell L100", which has shown abnormally high irreversible capacities, $\overline{M}_{srp}$ consistently lies below the $20 g.mol_{e^-}^{-1}$ mark after the first cycle. In our system, the only species that could explain this trend would be Li_xSi alloys that were formed irreversibly, e.g. disconnected from either ionic or electronic percolating networks. This matches a previously stated hypothesis that linked the observation of

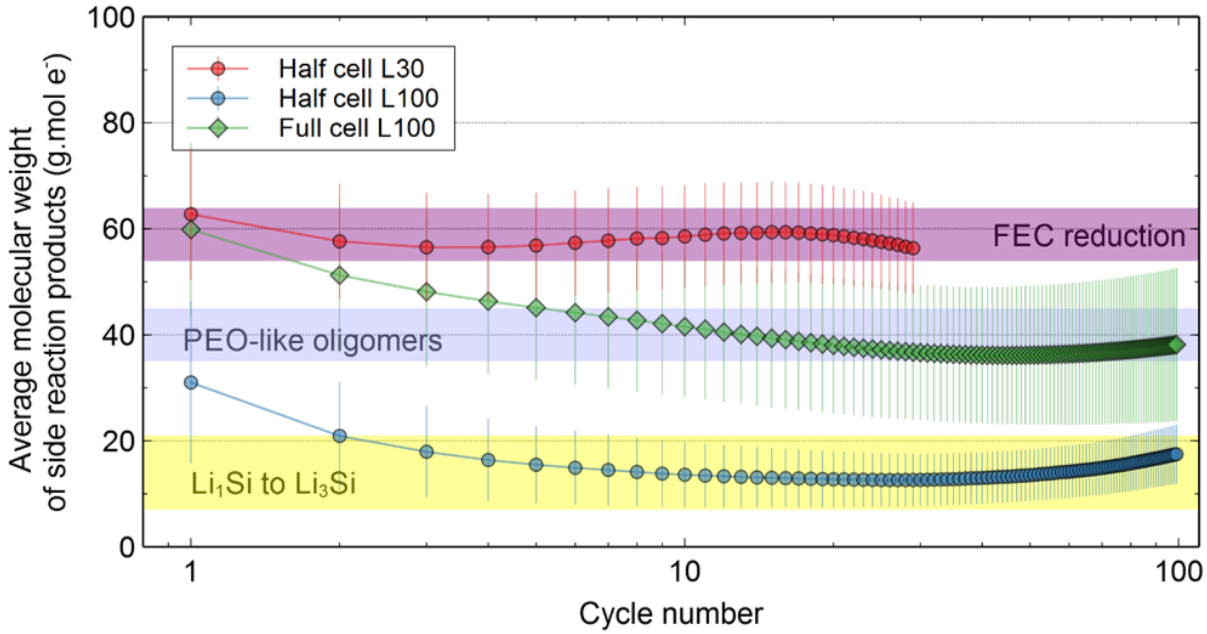

Fig. VI.21: Average molar mass of the side reaction products up to each cycle number, calculated using a prediction of the mass increase extrapolated from STEM-EELS analyses.

amorphous silicon networks in this electrode to an extensive disconnection of the active matter. This is compounded by the fact that this disconnected mass is practically not captured in our STEM-EELS observations, which probably leads to an underestimation of m^* and consequently $\overline{M}_{srp}$. Organic side reaction products should indeed represent a significant portion of this average. Thus we acknowledge that reported $\overline{M}_{srp}$ can appear misleadingly low, but the trend indicates a strong contribution of Li_xSi to the irreversible capacity nonetheless.

As for "Half cell L30", the side reaction products seem to be shared with those of full cells in early cycles, with values in the vicinity of those corresponding to FEC reduction pathways. This supports the idea that FEC is a *sacrificial* additive [104] which systematically reacts first thanks to its lower absolute reduction potential. $\overline{M}_{srp}$ lies in the FEC reduction region throughout the lifetime of "Half cell L30", whereas it quickly drops for "Full cell L100". Our interpretation is that this is a transition from FEC reductions products to PEO-like non lithiated products in later cycles, in line with findings from Dupré and coworkers [115, 118] who show such a transition in full cells. One might ponder why half-cells would be safe from this evolution however, and this warrants further investigation. The trend is most likely linked to the fact that electrolyte reduction does not proceed at the same potential in full and half cells, as detailed at the end of this section (see fig. VI.24).

Evolution of the plasmon peak position E_{max} and the Li-K core-loss edge

There is indeed an ostensibly distinct evolution of the SEI chemistry in full and half cells. This trend suggested by the $\overline{M}_{srp}$ profiles is also reflected in the position of the plasmon peak of EEL

spectra acquired on the *org* phase, E_{max}, which we can quantify on the electrode-scale in a similar fashion to that of the LiF quantities. E_{max} depends on the electronic properties of the specimen and thus its evolution does reflect a modification of the layer's chemistry. Results are reported figure VI.22.

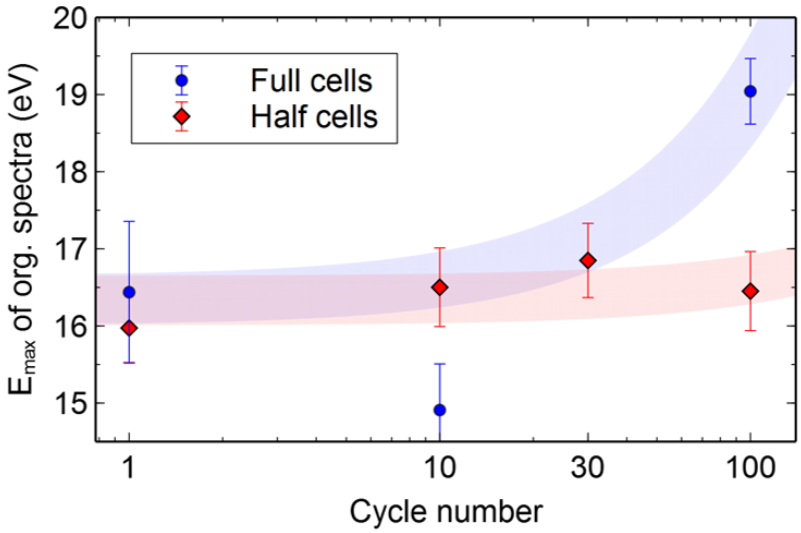

Fig. VI.22: Evolution of the plasmon position of *org* spectra E_{max} for full and half cells. The linear fits are solely shown for visual cues and should not be considered a predictive model. The 10th lithiation in full cell was considered an outlier and excluded.

In half-cells, E_{max} appears almost constant throughout the electrode's lifetime, whereas in full cells it climbs from $\approx$ 16.5 eV to 19 eV. According to our calculations (see III.3.2), higher values indicate PEO-type oligomers while the lower end of the E_{max} range suggests lithiated semi-organic compounds such as LEDC and poly(FEC). Moreover a significant difference is also observed in the lithium content of the *org* phase, which we estimated through the intensity of the Li-K edge. This is illustrated from experimental EELS acquisitions on electrodes stopped at their 100th lithiation in half and full cells respectively, figure VI.23.a-b. Summing and averaging all spectrum images (figure VI.23.d) shows that the average Li-K edge intensity, close to 5000 counts in "Half-cell L30" and "Half-cell L100", is down to about 1500 counts for "Full cell L100". This indicates that the *org* phase is much poorer in lithium when electrodes have cycled extensively in full cells. Unfortunately the quality of the STEM-EELS data acquired on electrodes at their 1st and 10th lithiation was not sufficient to allow us to extract the Li-K intensity in those. As a result the evolution of this quantity across the lifetime of electrodes cannot be directly followed, although $\overline{M}_{srp}$ profiles and E_{max} values give us clues. This is assessed in the summary found below.

Moreover, a closer look at the spectrum images acquired by STEM-EELS on half-cells also reveals the EEL spectra of lithium-containing *org* compounds have a strong tendency to be around $E_{max} \approx 16$ eV. This is shown with the bivariate histogram of figure VI.23, in which each point is a spectrum of the *org* phase.

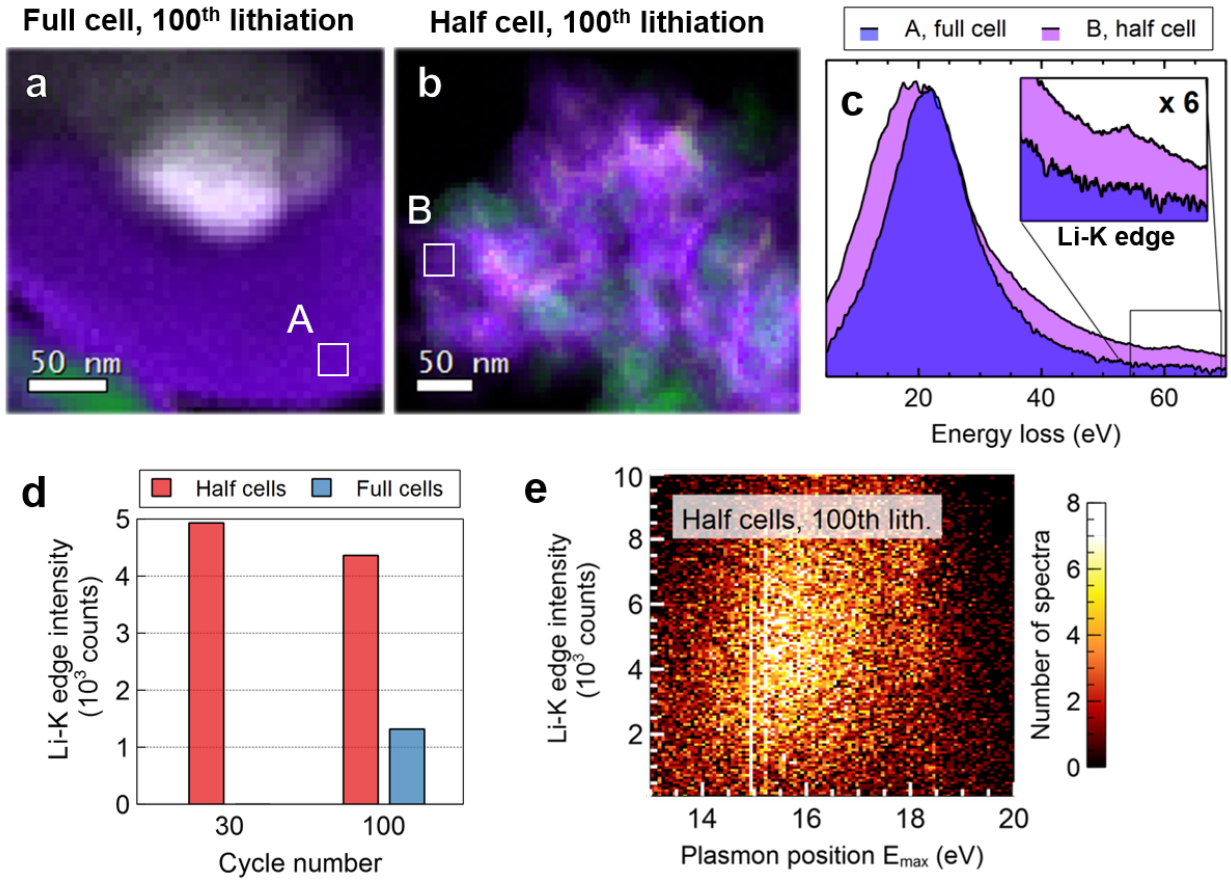

Fig. VI.23: Investigation of the plasmon position E_{max} and the Li-K edge intensity of EEL spectra from the *org* phase of electrodes aged in full and half cells. a-b) Composite thickness maps of the *org* phase (purple), LiF (green) as well as silicon (white) for SEI-covered particles and filaments in full and half cells respectively. c) EEL spectra from positions A and B highlighted in white rectangles in (a) and (b). d) Average intensity of the Li-K edge for all STEM-EELS data in 3 electrodes. e) Bivariate histogram of the Li-K edge intensity and the plasmon position E_{max} for the 91213 EEL spectra acquired on the *org* phase of "Half cell L100".

Interpreting the data in light of the potential evolution of half and full cells

Combining the local measurements of figure VI.23 with the indications drawn from the analysis of the irreversible capacity, figure VI.21, paints the following picture: (i) in half-cells, the composition of the *org* phase is kept relatively unchanged from cycle 1 to 100. From $\overline{M}_{srp}$ profiles, we know that this likely corresponds to an SEI made of FEC reduction products. An in-depth look at our STEM-EELS measurements confirms that the SEI is lithium-rich when electrodes are cycled in half-cells, which matches the established understanding of FEC reduction. Jung and al. in fact report 3 Li atoms in the polymer produced by the reduction of FEC [104]. Naturally the SEI remains chemically diverse, and we can only draw its chemistry in broad strokes. If it were not, points in the bivariate histogram figure VI.23.e would be stacked in a narrow region. They are however dispersed over the full E_{max} range, which is telling of the complexity of the abusively named *org* layer.

(II) In full cells, the SEI formed in early cycle is similar to that of half cells. After 100 cycles however, major discrepancies can be observed. The average molar mass of the side reaction products shows a pronounced drop, which hints at the formation of lithium-poor PEO-like oligomers and polymers, as suggested by Michan, Delpuech and coworkers [89, 115]. As previously stated, this shift proceeds from the fact that electrolyte reduction reactions do not occurs at the same potential in full cells and half cells. In the former configuration, the operating potential of the silicon electrodes will in fact continuously drift upwards throughout aging [27, 28]. That evolution, named *slippage*, is illustrated figure VI.24. As we can see, the operating potential of silicon electrodes climbs in full cells from the 10th cycle whereas in half cells the opposite is true. In "Half cell L100" especially, the potential shows a sharp drop coherent with the disconnection of the active matter and overlithiation phenomenon detailed earlier. Lithium-rich alloys are indeed formed at lower potentials.

Slippage impacts the kinetics of electrolyte reduction two-fold in later cycles. (i) First, lithium-containing species such as LEDC could be unlikely to form from EC reduction at higher potentials according to the work of Ruffo et al. This is arguably a lesser item here since FEC reduction, thought to be the main contributor to the SEI formed in early cycles when the additive is used, can occur at potentials as high as 1 V vs Li/Li^+ [253]. (ii) Mobile Li^+ ions become more scarce as the cathode operating potential soars. Considering that the FEC reduction pathway proposed by Jung et al. involves 4 lithium ions, this is significant. A lithium starved electrochemical environment will naturally favor the formation of lithium poor compounds such as the PEO-like oligomers observed here. This coincides with the views expressed by Dupre et al. from a combination of XPS, NMR and ToF-SIMS analysis in addition to our STEM-EELS contribution [118].

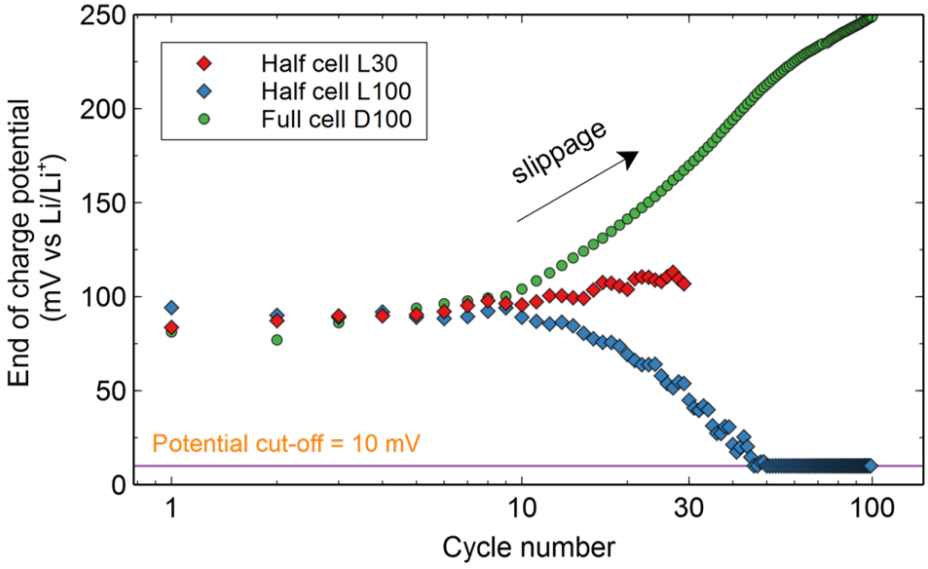

Fig. VI.24: Evolution of the end-of-charge potentials of the silicon electrode of 4 full and half-cells.

VI.2.3 Of the SEI's influence on local lithiation kinetics

In half cells

Now that we have assessed the evolution of both the SEI's chemistry and overall amount across the lifetime of electrodes, we take a step back to the spectrum image level. At this scale, we can take advantage of the versatility of STEM-EELS to investigate how the composition of the SEI affects the lithiation performance of SiNP clusters in electrodes cycled to 1200 $\mathrm{mAh/g}$. $\mathrm{Li_xSi}$ alloys and the SEI are indeed probed simultaneously with low-loss STEM-EELS and the results can be analyzed jointly to outline correlations. We took interest in the following quantities, also the focus of the previous section: (i) the $\mathrm{LiF/Si}$ and *org*/Si volumetric ratios, (ii) the position of the plasmon peak of the EEL spectra of the *org* phase, E_{max}, as well as (iii) the average Li/Si at. ratio, noted x. We have regrouped all 96 STEM-EELS spectrum images this manuscript is built on in 3 classes depending on the electrode they were taken from. First, the 1st and 10th lithiation in half-cells, then those aged in half-cells to their 30th and 100th cycle, and thirdly those aged in full-cells. In each case, we calculate the weighted Pearson correlation coefficient (WPCC) to assess whether a given quantity shows a significant influence on x. It has a value between +1 and -1, where +1 is total positive linear correlation, 0 is no linear correlation, and -1 is total negative linear correlation. On small sample sizes such as the present case, the robustness of WPCC is debatable, but it provides nonetheless a valuable indication. Results for half-cells are reported figure VI.25.

We see here that it is hard to conclude on the influence of either the *org* phase or LiF on lithiation performance from the data of the 10 first cycles (fig. VI.25.a-c), especially given the large standard errors displayed. The wide distribution of points is however indicative of, again, how unevenly phases are distributed in electrodes. Looking at LiF (fig. VI.25.a), we obtain WPCC = -0.003 meaning no influence on the lithiation of each SiNP cluster. With particle-scale observations in mind, this is hardly unexpected. LiF indeed showed a tendency to form segregated domains and does not coat nanoparticles in the first cycles, thus a limited influence on lithiation kinetics as reported here. In aged electrodes however we did reveal LiF morphologies in stark contrast with those of early cycles. Lithium fluoride has been shown to engulf particles, and large amounts of the compounds will logically hinder $\mathrm{Li^+}$ transport, as outlined figure VI.25.d although admittedly through a rather weak negative correlation coefficient (WPCC = -0.45). An even more pronounced effect is observed for the accumulation of the *org* phase, figure VI.25.e. There, trends appear visually as well as through calculation, with WPCC = -0.74, which confirms a severe detrimental effect of large thicknesses of the *org* phase on lithiation kinetics. Here we are reminded of the aging mechanism proposed by Oumellal et al. [151] and reported in the first section of this chapter: the ever-growing SEI will block porosities and ionic transport networks in the electrode. Among the vast array of species that compose this *org* phase, one might ponder which compounds affect lithiation negatively and vice versa. The question can be addressed indirectly by considering the

correlation of the parameter E_{max} to x with figure VI.25.e. A positive slope is explicit and this is reflected by WPCC = 0.63, which means that species that correspond to EEL spectra of higher E_{max} parameters could be associated with higher overall lithium contents in SiNP clusters. The extent of this effect is extremely limited however, given that all E_{max} values for this set are within a narrow band of 17.0 ± 0.5 eV (blue line), which roughly corresponds to FEC reduction products as detailed previously.

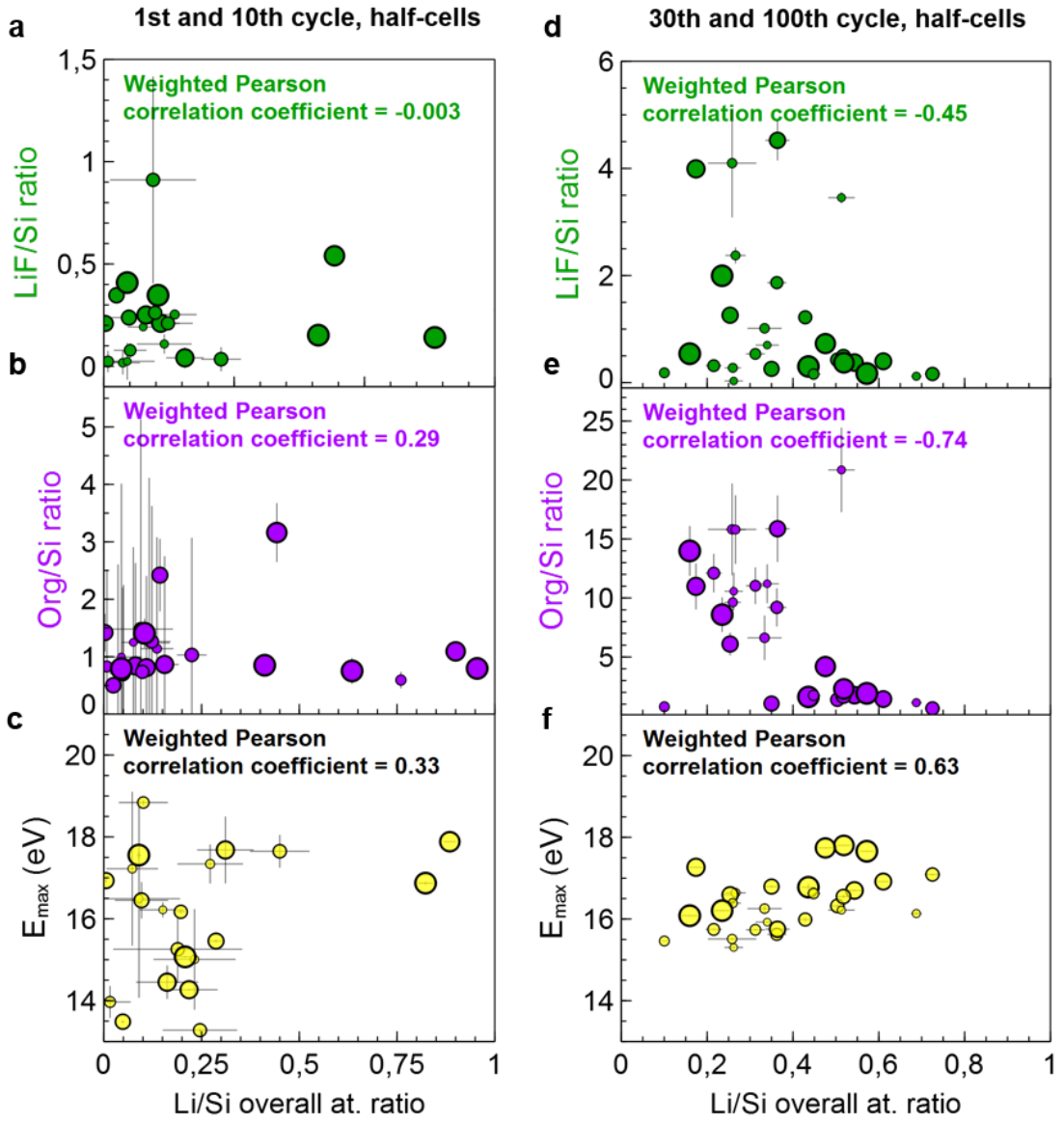

Fig. VI.25: Volumetric ratios for LiF and the *org* phase as well as plasmon peak positions E_{max} calculated from STEM-EELS datasets acquired on electrodes cycled in half-cells. Each marker point represents a spectrum image. Marker sizes correspond to the volume of silicon acquired on relative to the largest spectrum image of the set. (a-c) The left-hand column represents the 1st and 10th cycle, while (d-f) data for aged cells is shown on the right-hand side. Note the difference in the scale of the y-axes between the two columns.

Regarding the effect of the SEI's composition on lithiation performance, beyond the sole content of the *org* phase, we can also look at the relative LiF amount (figure VI.26). In spite of the negative correlation we identified between both those SEI components individually and x, the positive correlation coefficient calculated here between LiF/*org* ratios and x is not insignificant (WPCC = 0.26). This suggests that a particular LiF content in the SEI could be beneficial, or rather least detrimental, to cycling performance, as simulations pointed out. Indeed, Zhang et al. [237] predicted that a higher LiF concentration (calculated up to 50%) would improve ion transport within the SEI.

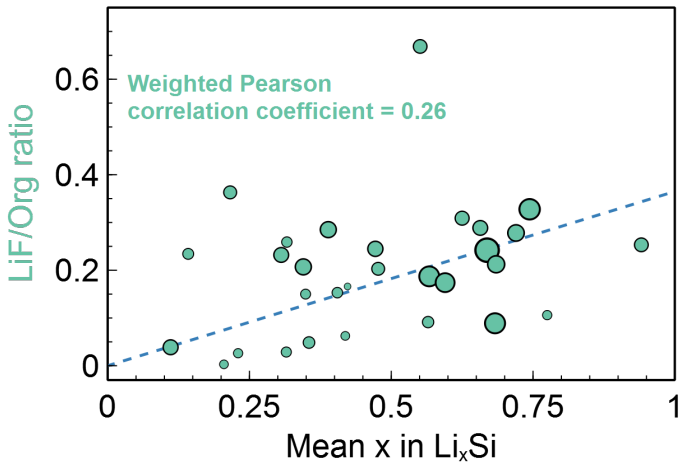

Fig. VI.26: LiF/*org* ratio versus the mean Li/Si at. ratio x for half-cells aged to their 30th and 100th cycle.

Similarities and discrepancies in full cells

We now look towards these same metrics for electrodes aged in full cells. The volumetric ratios LiF/Si, *org*/Si and E_{max} are once more plotted against x to reveal how each influences the other. Results are reported figure VI.27.d-f next to those of aged half cells for comparison purposes. As expected, trends are similar regarding the influence of the overall SEI content on lithiation kinetics: higher amount are detrimental. However this changes once we look at E_{max}, and a peculiar profile is indeed spotted figure VI.27.e. There, the lithium content x drops with increasing E_{max}. This is significant since so far we had only outlined an overall increase in E_{max} in electrodes from full cells in the previous section (fig. VI.22), which we associated with the formation of unlithiated, PEO-like oligomers. We are now able to provide direct, local evidence of the negative correlation of those species to lithiation kinetics, notably through a calculated coefficient of WPCC = -0.74. This analysis can be refined by looking at the intensity of the Lithium K edge of those same EEL spectra E_{max} was extracted from. From the color scheme used in figure VI.27.e, we see that lower E_{max} values are also correlated to smaller Li-K intensities quite strongly (WPCC = -0.63), here in full cells at the spectrum image scale, in line with observations at the individual spectrum scale in half cells figure VI.23.e.

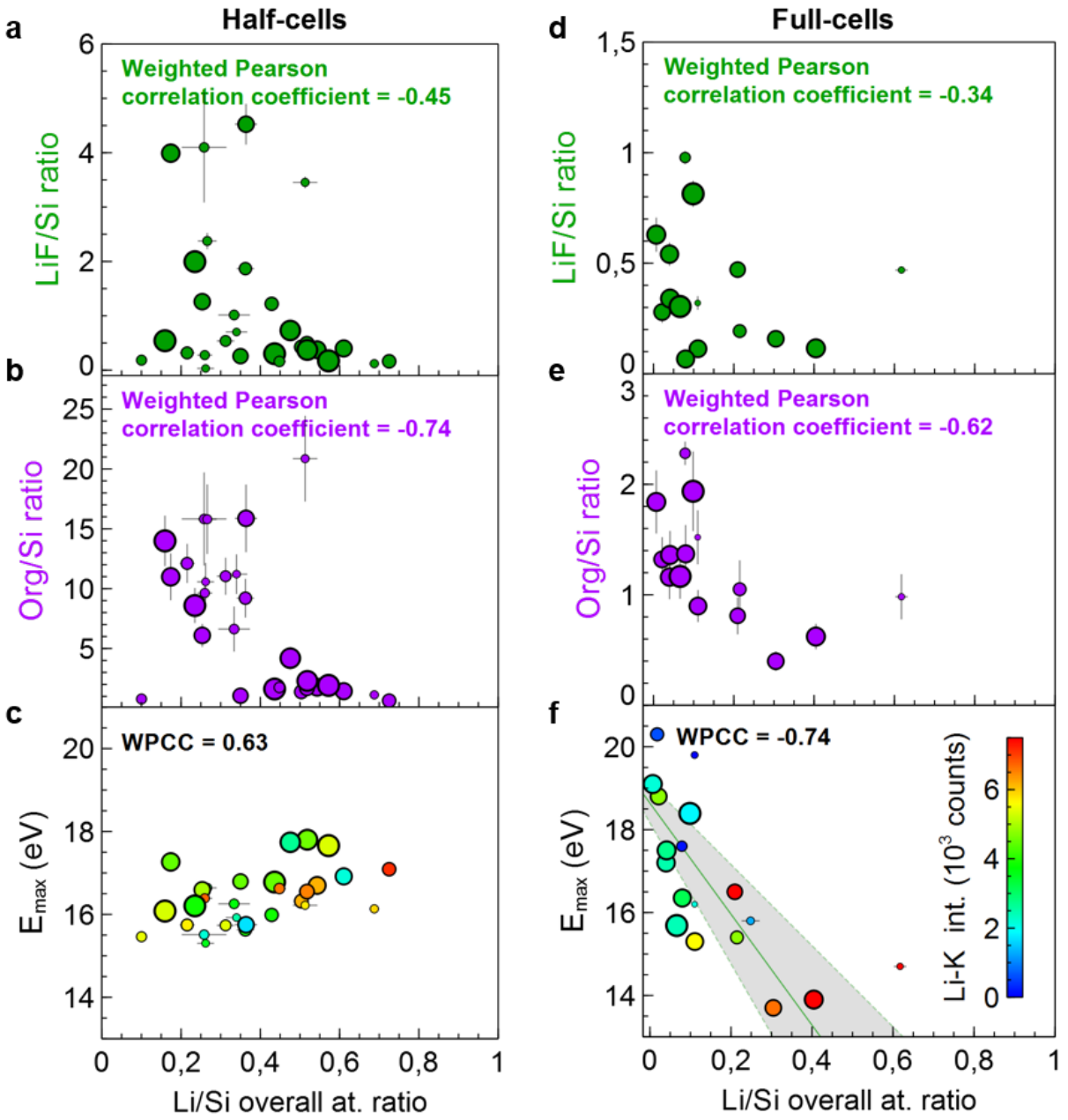

Fig. VI.27: Volumetric ratios for LiF and the *org* phase as well as plasmon peak positions E_{max} calculated from STEM-EELS datasets acquired on electrodes cycled in aged (a-c) half cells and (d-f) full cells. Each marker point represents a spectrum image. Marker sizes correspond to the volume of silicon acquired on relative to the largest spectrum image of the set.

Correlations should not be over-interpreted however. It is unclear whether (i) Li/Si ratios are lower **because** of the prevalence of lithium-poor oligomers in the SEI, which could for hinder the Li^+ diffusivity of the layer or if (ii) the underlying cause of both is simply the potential slippage of the silicon electrode. We have already established that this SEI chemistry is directly linked to the increased operating potential of our electrodes, and this same factor could also directly explain the lower Li/Si ratios observed coincidentally.

VI.3 A summary of electrode aging

As silicon-based electrodes are cycled, aging occurs through two intricately linked degradation phenomena: particle disconnection and SEI accumulation, which cause poor coulombic efficiencies and capacity loss. Both originate from the colossal volume changes that accompanies the lithiation of *Si*. Silicon particles swell then contract upon alloying and subsequent dealloying with lithium, leaving some of them cut-off from the electronic percolating network. STEM-EELS analyses provide local and direct evidence of such scattered, disconnected SiNP clusters, and additionally reveals the presence of lithium trapped in silicon in delithiated electrodes. In electrodes subject to galvanostatic cycling to a limited capacity such as ours (to 30% or 1200 $\mathrm{mAh/g}$), this causes the remainder of connected particles to be charged above that SoC target, and to a faster rate, as the current applied was calculated for the entirety of the initial active silicon mass. That triggers in turn a self-reinforcing effect that promotes irreversible reactions.

Particle disconnection and overlithiation: a negative feedback loop

Over-lithiated nanoparticles will indeed suffer from larger structural damage, causing an ever-increasing number of SiNP to disconnect thus fostering even greater overlithiation in a negative feedback loop. The increased volume expansion that comes with overlithiation increases the risk of particle disconnection as well as current collector delamination [254], and so does the higher lithiation rate as seen on nanowires in chapter 4. The remaining particles that are exceedingly solicited can undergo extreme morphological evolutions, with the formation of silicon dendrites through a mechanism described by Chen and Sieradzki [243] in their *Nature Materials* paper. In one electrode, STEM-EELS thickness mapping revealed that monocrystalline nanoparticles were in fact almost entirely revamped into a network of silicon filament as thin as 10 nm.

In any case, the SEI layer is strained and cracks, forming accrued active surfaces for the continuous reduction of the electrolyte. This is compounded here by the additional stresses brought on by overlithiation. Electrons and mobile lithium ions from the cathode will be irreversibly consumed in an ever-growing SEI. In full cells, this greatly accelerates electrode failure through potential *slippage*. Moreover, the SEI will progressively block porosities and severely hinder Li^+ transport in the electrode. Now, Oumellal [151], Radvanyi [41] and coworkers have proposed that this provokes the overlithiation of the surface of the electrode, setting up the cascade of events we have described. The analysis of FIB cross-sections by ToF-SIMS and STEM-EELS reveals the opposite trend in our case, as electrodes are overlithiated as we approach the current collector. We postulate that this stems from the greater extent of particle disconnection in the electrodes studied in this work. In other words, the lithiation gradient is the result of an electron-starved electrochemical environment rather than a lithium ion-limited one. We summarize our model in the schematic presented below.

A singular SEI chemistry in full cells

Regarding the SEI itself, we are able to quantify the accumulation of both the LiF and the *org* phase, revealing a 2-fold mass increase for electrodes cycled in full cells and 4-fold in half cells. We show that increased SEI amounts are correlated to lower Li/Si ratios locally, which is evidence that lithiation gradients in the electrode can be mediated by lithium diffusion as well. Furthermore in full cells the chemistry of the layer diverges from that of half cells as a result of potential *slippage*. As the silicon electrode's operating potential increases, lithium-poor PEO-like oligomers form and lithium-containing compounds such as LEDC or poly(FEC) are overtaken. In half-cells however, there is no potential evolution and the SEI's chemistry hardly changes across the lifetime of the electrode.

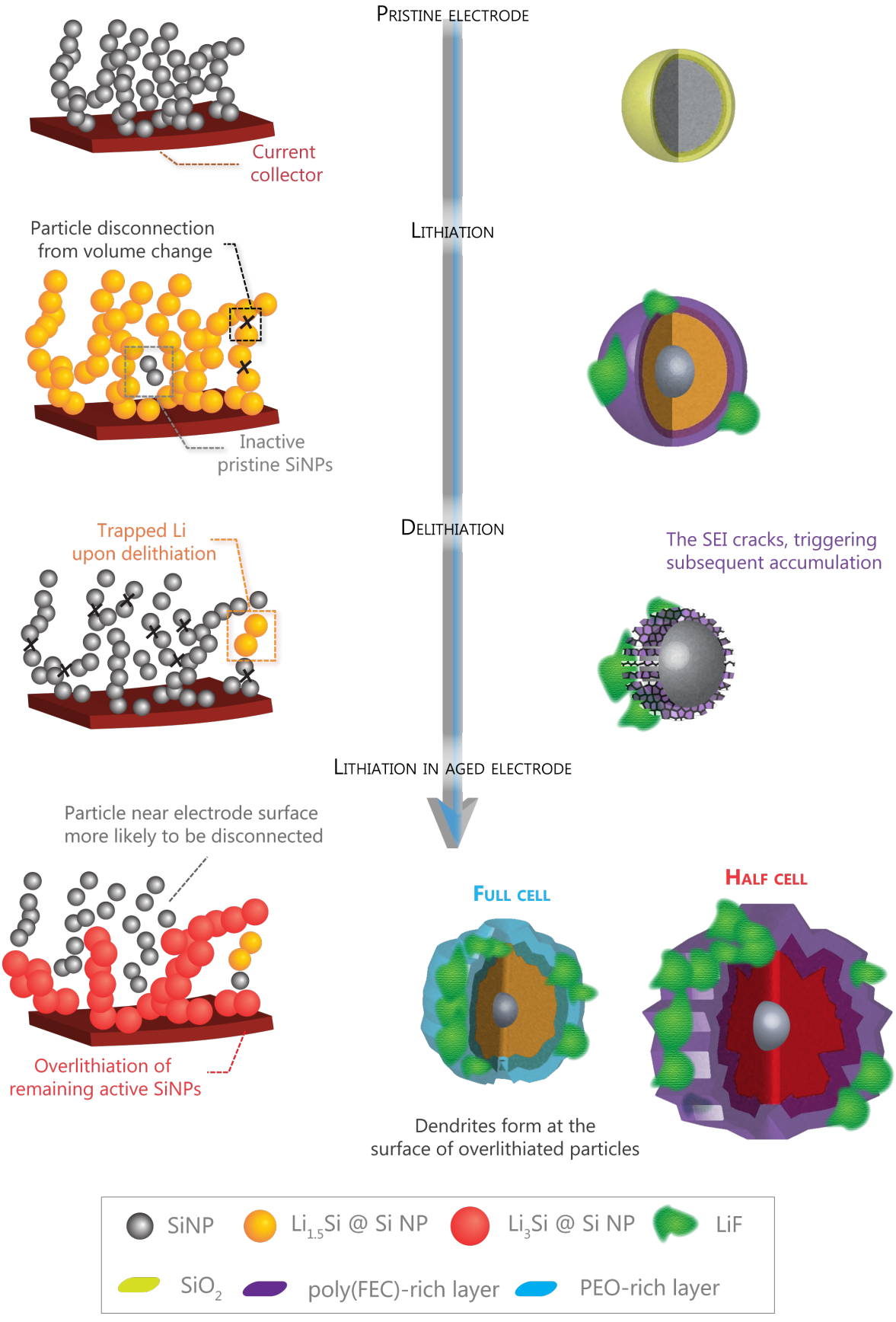

Fig. VI.28: Schematic of the particle disconnection model proposed in the manuscript.

Conclusion

In this thesis work, we have developed transmission electron microscopy techniques to challenge the aging mechanisms of silicon nanoparticle-based negative electrodes at a local scale. Through a review of the characterization work done on this system in **chapter I**, we first identify several key phenomena that ought to be challenged by local observations. In today's state-of-the-art macroscale results, from XRD and NMR studies for example, clues are provided on the overall Li-Si alloy composition, the accumulation of the SEI and the evolution of its chemistry throughout aging. Authors then extrapolate particle-scale models. To check whether these models hold true locally, and offer novel insight on the matter, we have developed low-loss STEM-EELS into a powerful, versatile local spectroscopy tool that is compatible with the great electron sensitivity of the lithiated or organic species of lithiated silicon electrodes.

This effort is described in **chapter III**, starting with an experimental, quantitative study of the degradation of both $\mathrm{Li_xSi}$ alloys and SEI compounds under the electron beam. Simulations of the damage deposited by inelastic scattering complete this picture and allow us to optimize STEM-EELS acquisition protocols to reach the following performance: 15 ms per spectrum, a resolution of 5 nm, for an areal electron dose below $250\,e\,\text{Å}^{-2}$. *Via* the MLLS algorithm, we can then extract the contributions of all the compounds of interest from our heterogeneous system from any experimental EEL spectrum. Individual thickness maps can subsequently be calculated from this fit, making the technique a remarkable phase-mapping tool for composite and heterogeneous systems such as lithiated silicon electrodes. Moreover, we show that multiple STEM-EELS datasets can be summed and averaged to assess quantitatively the preponderance of a given phase in each electrode. Additional insight can also be gathered on the chemistry of the Li-Si and the *org* phase by fitting EEL spectra with the Drude model. Doing so, we extract the parameter E_{max} which we link empirically to either a precise Li/Si atomic ratio, or the crystallinity of silicon in delithiated electrodes. For the *org* phase, it also provides a qualitative indication of whether the layer is rich in PEO, or LEDC/poly(FEC). All of this is obtained simultaneously, offering us the ability to correlate, for example, a local SEI composition with the corresponding Li/Si at. ratio.

With **chapter IV**, we then show that technique development does not stop there, and can be pursued in the design of a custom *operando* experiment. Despite the limited reach of the approach,

our preliminary testing yields important insight on the electrochemisty and *post mortem* morphology of single lithiated silicon nanowires.

Thanks to those novel characterization capabilities, we propose a description of silicon electrodes after their 1st and 10th cycle in **chapter V**. Our ability to simultaneously probe the morphology and chemistry of the $\mathrm{Li_xSi}$ phase is notably put to use to elucidate the first lithiation of crystalline nanoparticles. A local state of charge can in fact be calculated for each particle from our STEM-EELS data, allowing us to show that the lithium content increases as the shell grows from $x \approx 1$ to $x \approx 3$, unlike the biphasic process ($\mathrm{Li_{3.5}Si/c-Si}$) identified for microparticles. This discrepancy stems from a competition between the amorphization process of crystalline silicon and further lithiation of the shell through a solid solution process - a competition mediated by the surface of the reaction front i.e by the particle size. The role of stress in this self-limiting phenomenon is then investigated. In line with the vast body of simulation works out on this system, experimental stress values of 4 ± 2 GPa are reported for the first time in the crystalline core of particles from NPED experiments. Taking a step back to the cluster scale, we observe that lithiation is in fact extremely heterogeneous. Pristine particles clusters remain after 10 cycles, and in lithiated clusters Li is unevenly distributed. We attribute those gradients to a heterogeneous $\mathrm{Li^+}$ transport. Moving on to the SEI, we take advantage of our phase-mapping capabilities to highlight particular morphologies in both the LiF and the *org* phase, and propose a qualitative model. LiF first forms from $\mathrm{LiPF_6}$ reduction into segregated, particle-like domains that can be as thick as 100 nm. In later cycles, layer-like LiF that contain nanocrystals is more prevalent. Those are associated to FEC reduction. Regarding the *org* phase, a conformal morphology is observed with average thicknesses of 15 nm in lithiated electrodes and, importantly, of a lower 11 nm in delithiated ones - a prime evidence of the *breathing* phenomenon.

In **chapter VI**, we apply low-loss STEM-EELS for a systematic analysis of elecrode aging. Foremost among aging symptoms is the disconnection of large portions of the active matter from the percolating network, which leads to the *over*-lithiation of the remainder of active SiNPs. After 100 cycles, SiNPs indeed exhibit tremendous structural damage in the form of silicon dendrites that can completely replace the initially spherical geometry. At the electrode-scale, *over*-lithiation results in concentration gradients in the electrode since particles at the electrode surface are more likely to be disconnected, as evidenced by STEM-EELS and ToF-SIMS on FIB-prepared cross sections. Larger SEI amounts and higher lithium concentrations are indeed observed near the current collector. All of those trends are assessed quantitatively, and the same can be applied to SEI compounds. This allows us to reveal that both LiF and *org* species contribute evenly to a 4-fold and 2-fold accumulation of the SEI after 100 cycles in half and full cells respectively. The volumetric ratio of those two phases is unchanged throughout the electrode's lifetime, at 25 v.%. As to the chemistry of the *org* phase, a significant discrepancy emerges between electrodes cycled in full and half cells. Indeed, potential *slippage* in full cells leads to a Lithium-scarce environment that favors the formation of PEO-like oligomers to the detriment of poly(FEC) and LEDC. Quantifying STEM-EELS in fact allows us

to extrapolate the mass increase of electrodes at each cycle, and plot the average molar mass of irreversible degradation products from our electrochemical data. This, along with major changes in the Li-K edge intensities and E_{max} quantity from electrodes aged in full or half cells, confirms this chemical evolution of the *organic* phase. An extensive and illustrated model is then presented to summarize our findings.

Final words and perspectives

To conclude, we have developed an unparalleled ability for local characterization of sensitive materials. This was used to discuss silicon aging models in Li-ion batteries and propose our own. Thus, as proven in this work, we strongly believe that low-loss STEM-EELS could be applied to solve numerous materials science problems, and that it fills an important niche in TEM-related techniques. Axes to improve the technique include working at 300 kV and combining it with cryo-microscopy so as to mitigate beam damage even further, which could push the achievable resolutions to the nanometer. Correlations with local strain measurements by NPED are also an especially promising development for the study of nano-materials applications. Moreover, the acquisition speed of low-loss STEM-EELS could be leveraged in *in situ* experiments for quick phase mapping. Regarding silicon electrodes themselves, we believe that further study of the concentration gradients detected in FIB-prepared cross-sections is highly warranted to challenge the two opposite scenarios put forward by this work and Oumellal's [41, 151] respectively.

References

(1) Tarascon, J. M.; Armand, M *Nature* **2001**, *414*, 359–67.

(2) Armand, M; Tarascon, J.-M. *Nature* **2008**, *451*, 652–7.

(3) Goodenough, J. B.; Kim, Y. *Chem. Mater.* **2010**, *22*, 587–603.

(4) Bruce, P. G.; Scrosati, B.; Tarascon, J.-M. *Angew. Chem. Int. Ed. Engl.* **2008**, *47*, 2930–46.

(5) Xu, K. *Chem. Rev.* **2004**, *104*, 4303–4417.

(6) Mizushima, K.; Jones, P.; Wiseman, P.; Goodenough, J. *Mater. Res. Bull.* **1980**, *15*, 783–789.

(7) Yazami, R.; Touzain, P. *J. Power Sources* **1983**, *9*, 365–371.

(8) Huggins, R. A. *J. Power Sources* **1999**, *81-82*, 13–19.

(9) Nitta, N.; Yushin, G. *Part. Part. Syst. Charact.* **2014**, *31*, 317–336.

(10) Lee, J. K.; Oh, C.; Kim, N.; Hwang, J.-Y.; Sun, Y.-K. *J. Mater. Chem. A* **2016**, *4*, 5366–5384.

(11) Ryu, J. H.; Kim, J. W.; Sung, Y.-E.; Oh, S. M. *Electrochem. Solid-State Lett.* **2004**, *7*, A306.

(12) Beaulieu, L. Y.; Eberman, K. W.; Turner, R. L.; Krause, L. J.; Dahn, J. R. *Electrochem. Solid-State Lett.* **2001**, *4*, A137.

(13) Timmons, A.; Dahn, J. R. *J. Electrochem. Soc.* **2006**, *153*, A1206.

(14) Graetz, J.; Ahn, C. C.; Yazami, R.; Fultz, B. *Electrochem. Solid-State Lett.* **2003**, *6*, A194.

(15) Wu, H.; Chan, G.; Choi, J. W.; Ryu, I.; Yao, Y.; McDowell, M. T.; Lee, S. W.; Jackson, A.; Yang, Y.; Hu, L.; Cui, Y. *Nat. Nanotechnol.* **2012**, *7*, 310–5.

(16) Wang, J.; Yang, J.; Lu, S. *Nanosci. Nanotechnology-Asia* **2016**, *6*, 3–27.

(17) Li, J.-Y. et al. *Mater. Chem. Front.* **2017**, *1*, 1691–1708.

(18) Dalavi, S.; Guduru, P.; Lucht, B. L. *J. Electrochem. Soc.* **2012**, *159*, A642.

(19) Wei, L.; Chen, C.; Hou, Z.; Wei, H. en *Sci. Rep.* **2016**, *6*, 19583.

(20) Choi, S.; Kwon, T.-W.; Coskun, A.; Choi, J. W. *Science (80-.).* **2017**, *357*, 279–283.

(21) Ashuri, M.; He, Q.; Shaw, L. L. *Nanoscale* **2016**, *8*, 74–103.

(22) Zhang, Z.-l.; Brydson, R.; Aslam, Z.; Reddy, S.; Brown, A.; Westwood, A.; Rand, B. *Carbon N. Y.* **2011**, *49*, 5049–5063.

(23) Liu, N.; Wu, H.; McDowell, M. T.; Yao, Y.; Wang, C.; Cui, Y. *Nano Lett.* **2012**, *12*, 3315–21.

(24) Wu, H.; Cui, Y. *Nano Today* **2012**, *7*, 414–429.

(25) Mazouzi, D.; Lestriez, B.; Roué, L.; Guyomard, D. *Electrochem. Solid-State Lett.* **2009**, *12*, A215.

(26) Mazouzi, D.; Delpuech, N.; Oumellal, Y.; Gauthier, M.; Cerbelaud, M.; Gaubicher, J.; Dupré, N.; Moreau, P.; Guyomard, D.; Roué, L.; Lestriez, B. *J. Power Sources* **2012**, *220*, 180–184.

(27) Delpuech, N.; Dupre, N.; Moreau, P.; Bridel, J. S.; Gaubicher, J.; Lestriez, B.; Guyomard, D. *ChemSusChem* **2016**, *9*, 841–848.

(28) Beattie, S. D.; Loveridge, M. J.; Lain, M. J.; Ferrari, S.; Polzin, B. J.; Bhagat, R.; Dashwood, R. *J. Power Sources* **2016**, *302*, 426–430.

(29) Kasavajjula, U.; Wang, C.; Appleby, A. J. *J. Power Sources* **2007**, *163*, 1003–1039.

(30) Lai, S.-C. *J. Electrochem. Soc.* **1976**, *123*, 1196.

(31) Boukamp, B. A. *J. Electrochem. Soc.* **1981**, *128*, 725.

(32) Li, H *Solid State Ionics* **2000**, *135*, 181–191.

(33) Limthongkul, P.; Jang, Y.-I.; Dudney, N. J.; Chiang, Y.-M. *J. Power Sources* **2003**, *119-121*, 604–609.

(34) McDowell, M. T.; Lee, S. W.; Nix, W. D.; Cui, Y. *Adv. Mater.* **2013**, *25*, 4966–85.

(35) Danet, J.; Brousse, T.; Rasim, K.; Guyomard, D.; Moreau, P. en *Phys. Chem. Chem. Phys.* **2010**, *12*, 220–6.

(36) Key, B.; Morcrette, M.; Tarascon, J.-M.; Grey, C. P. *J. Am. Chem. Soc.* **2011**, *133*, 503–512.

(37) Robert, D. Etude multi-échelle des mécanismes de (dé)lithiation et de d'égradation d'électrodes à base de LiFePO4 et de Silicium pour accumulateurs Li-ion., Ph.D. Thesis, Université Grenobles Alpes, 2014.

(38) Wang, C.; Wu, H.; Chen, Z.; McDowell, M. T.; Cui, Y.; Bao, Z. *Nat. Chem.* **2013**, *5*, 1042–8.

(39) Radvanyi, E.; De Vito, E.; Porcher, W.; Danet, J.; Desbois, P.; Colin, J.-F.; Si Larbi, S. J. *J. Mater. Chem. A* **2013**, *1*, 4956.

(40) Seidlhofer, B. K.; Jerliu, B.; Trapp, M.; Hüger, E.; Risse, S.; Cubitt, R.; Schmidt, H.; Steitz, R.; Ballauff, M. *ACS Nano* **2016**, *10*, 7458–7466.

(41) Radvanyi, E.; Porcher, W.; De Vito, E.; Montani, A.; Franger, S.; Jouanneau Si Larbi, S. *Phys. Chem. Chem. Phys.* **2014**, *16*, 17142–53.

(42) Li, J.; Dahn, J. R. *J. Electrochem. Soc.* **2007**, *154*, A156.

(43) Obrovac, M. N.; Christensen, L. en *Electrochem. Solid-State Lett.* **2004**, *7*, A93–A96.

(44) Nguyen, D.-T.; Kang, J.; Nam, K.-M.; Paik, Y.; Song, S.-W. *J. Power Sources* **2016**, *303*, 150–158.

(45) Ogata, K; Salager, E; Kerr, C. J.; Fraser, A. E.; Ducati, C; Morris, A. J.; Hofmann, S; Grey, C. P. en *Nat. Commun.* **2014**, *5*, 3217.

(46) Ulldemolins, M. **2013**.

(47) Lu, B.; Song, Y.; Zhang, Q.; Pan, J.; Cheng, Y.-T.; Zhang, J. *Phys. Chem. Chem. Phys.* **2016**, *18*, 4721–4727.

(48) Baggetto, L.; Niessen, R. A. H.; Roozehoom, F.; Notten, P. H. L. *Adv. Funct. Mater.* **2008**, *18*, 1057–1066.

(49) Zhao, K.; Pharr, M.; Wan, Q.; Wang, W. L.; Kaxiras, E.; Vlassak, J. J.; Suo, Z. en *J. Electrochem. Soc.* **2012**, *159*, A238–A243.
(50) Beattie, S. D.; Larcher, D; Morcrette, M; Simon, B **2008**, 158–163.
(51) Johari, P.; Qi, Y.; Shenoy, V. B. *Nano Lett.* **2011**, *11*, 5494–5500.
(52) McDowell, M. T.; Ryu, I.; Lee, S. W.; Wang, C.; Nix, W. D.; Cui, Y. *Adv. Mater.* **2012**, *24*, 6034–41.
(53) Liu, X. H.; Fan, F.; Yang, H.; Zhang, S.; Huang, J. Y.; Zhu, T. *ACS Nano* **2013**, *7*, 1495–1503.
(54) Liu, X. H.; Zhong, L.; Huang, S.; Mao, S. X.; Zhu, T.; Huang, J. Y. *ACS Nano* **2012**, *6*, 1522–31.
(55) Xu, R.; Zhao, K. *J. Electrochem. Energy Convers. Storage* **2016**, *13*, 030803.
(56) Zhang, X.; Lee, S. W.; Lee, H.-W.; Cui, Y.; Linder, C. *Extrem. Mech. Lett.* **2015**, DOI: 10.1016/j.eml.2015.04.005.
(57) Zhang, S. *Nat. Comput. Mater.* **2017**, *3*, 7.
(58) Yang, H.; Huang, S.; Huang, X.; Fan, F.; Liang, W.; Liu, X. H.; Chen, L.-Q.; Huang, J. Y.; Li, J.; Zhu, T.; Zhang, S. *Nano Lett.* **2012**, *12*, 1953–1958.
(59) Huang, S.; Fan, F.; Li, J.; Zhang, S.; Zhu, T. *Acta Mater.* **2013**, *61*, 4354–4364.
(60) Brassart, L.; Zhao, K.; Suo, Z. *Int. J. Solids Struct.* **2013**, *50*, 1120–1129.
(61) Sethuraman, V. A.; Chon, M. J.; Shimshak, M.; Srinivasan, V.; Guduru, P. R. *J. Power Sources* **2010**, *195*, 5062–5066.
(62) Chon, M. J.; Sethuraman, V. a.; McCormick, a.; Srinivasan, V.; Guduru, P. R. *Phys. Rev. Lett.* **2011**, *107*, 1–4.
(63) Nadimpalli, S. P. V.; Sethuraman, V. A.; Bucci, G.; Srinivasan, V.; Bower, A. F.; Guduru, P. R. *J. Electrochem. Soc.* **2013**, *160*, A1885–A1893.
(64) Bucci, G.; Nadimpalli, S. P. V.; Sethuraman, V. a.; Bower, A. F.; Guduru, P. R. *J. Mech. Phys. Solids* **2014**, *62*, 276–294.
(65) Chevrier, V. L.; Zwanziger, J. W.; Dahn, J. R. *Rev. Can. Phys.* **2009**, *87*, 625–632.
(66) Shenoy, V. B.; Johari, P.; Qi, Y. *J. Power Sources* **2010**, *195*, 6825–6830.
(67) Chou, C.-Y.; Kim, H.; Hwang, G. S. *J. Phys. Chem. C* **2011**, *115*, 20018–20026.
(68) Kim, H.; Chou, C. Y.; Ekerdt, J. G.; Hwang, G. S. *J. Phys. Chem. C* **2011**, *115*, 2514–2521.
(69) Larche, F; Cahn, J. W. *Acta Metall.* **1973**, *21*, 1051.
(70) Larche, F. C.; Cahn, J. W. *Acta Metall.* **1978**, *26*, 1579–1589.
(71) Sethuraman, V. A.; Srinivasan, V.; Bower, A. F.; Guduru, P. R. *J. Electrochem. Soc.* **2010**, *157*, A1253.
(72) Seo, D. M.; Chalasani, D.; Parimalam, B. S.; Kadam, R.; Nie, M.; Lucht, B. L. en *ECS Electrochem. Lett.* **2014**, *3*, A91–A93.
(73) Peled, E. *J. Electrochem. Soc.* **1979**, *126*, 2047.
(74) Smith, A. J.; Burns, J. C.; Trussler, S.; Dahn, J. R. *J. Electrochem. Soc.* **2010**, *157*, A196.

(75) Gauthier, M.; Carney, T. J.; Grimaud, A.; Giordano, L.; Pour, N.; Chang, H.-H.; Fenning, D. P.; Lux, S. F.; Paschos, O.; Bauer, C.; Maglia, F.; Lupart, S.; Lamp, P.; Shao-Horn, Y. EN *J. Phys. Chem. Lett.* **2015**, DOI: 10.1021/acs.jpclett.5b01727.

(76) Peled, E. *J. Power Sources* **1983**, *9*, 253–266.

(77) Gabano, J.-P.; J.-P. *London New York, Acad. Press. 1983, 467 p.* **1983**.

(78) Peled, E.; Golodnitsky, D.; Ardel, G. *J. Electrochem. Soc.* **1997**, *144*, L208.

(79) Fong, R.; Von Sacken, U.; Dahn, J. R. *J. Electrochem. Soc.* **1990**, *137*, 2009.

(80) Peled, E.; Menkin, S. *J. Electrochem. Soc.* **2017**, *164*, A1703–A1719.

(81) Nazri, G. *J. Electrochem. Soc.* **1985**, *132*, 2050–2054.

(82) Nazri, G.; Muller, R. H. *J. Electrochem. Soc.* **1985**, *132*, 2054–2058.

(83) Aurbach, D.; Daroux, M. L.; Faguy, P. W.; Yeager, E. *J. Electrochem. Soc.* **1987**, *134*, 1611.

(84) Kanamura, K.; Tamura, H.; ichiro Takehara, Z. *J. Electroanal. Chem.* **1992**, *333*, 127–142.

(85) Kanamura, K.; Tamura, H.; Shiraishi, S.; ichiro Takehara, Z. *J. Electroanal. Chem.* **1995**, *394*, 49–62.

(86) Zhuang, G. V.; Xu, K.; Yang, H.; Jow, T. R.; Ross, P. N. *J. Phys. Chem. B* **2005**, *109*, 17567–73.

(87) Kim, H.; Grugeon, S.; Gachot, G.; Armand, M.; Sannier, L.; Laruelle, S. *Electrochim. Acta* **2014**, *136*, 157–165.

(88) Edström, K.; Herstedt, M.; Abraham, D. P. A new look at the solid electrolyte interphase on graphite anodes in Li-ion batteries., 2006.

(89) Michan, A. L.; Leskes, M.; Grey, C. P. *Chem. Mater.* **2016**, *28*, 385–398.

(90) Malmgren, S.; Ciosek, K.; Hahlin, M.; Gustafsson, T.; Gorgoi, M.; Rensmo, H.; Edström, K. *Electrochim. Acta* **2013**, *97*, 23–32.

(91) Alliata, D; Kötz, R.; Novák, P.; Siegenthaler, H. *Electrochem. commun.* **2000**, *2*, 436–440.

(92) Yoshida, T.; Takahashi, M.; Morikawa, S.; Ihara, C.; Katsukawa, H.; Shiratsuchi, T.; Yamaki, J.-i. *J. Electrochem. Soc.* **2006**, *153*, A576.

(93) Chattopadhyay, S.; Lipson, A. L.; Karmel, H. J.; Emery, J. D.; Fister, T. T.; Fenter, P. A.; Hersam, M. C.; Bedzyk, M. J. *Chem. Mater.* **2012**, *24*, 3038–3043.

(94) Chan, C. K.; Ruffo, R.; Hong, S. S.; Cui, Y. *J. Power Sources* **2009**, *189*, 1132–1140.

(95) Lee, Y. M.; Lee, J. Y.; Shim, H.-T.; Lee, J. K.; Park, J.-K. *J. Electrochem. Soc.* **2007**, *154*, A515.

(96) Ban, C.; Kappes, B. B.; Xu, Q.; Engtrakul, C.; Ciobanu, C. V.; Dillon, A. C.; Zhao, Y. *Appl. Phys. Lett.* **2012**, *100*, 243905.

(97) Kim, T.; Park, S.; Oh, S. M. *J. Electrochem. Soc.* **2007**, *154*, A1112.

(98) Guo, B.; Shu, J.; Wang, Z.; Yang, H.; Shi, L.; Liu, Y.; Chen, L. *Electrochem. commun.* **2008**, *10*, 1876–1878.

(99) Philippe, B.; Dedryvère, R.; Allouche, J.; Lindgren, F.; Gorgoi, M.; Rensmo, H.; Gonbeau, D.; Edström, K. *Chem. Mater.* **2012**, *24*, 1107–1115.

(100) Zhang, Y.; Li, Y.; Wang, Z.; Zhao, K. *Nano Lett.* **2014**, DOI: 10.1021/nl503776u.

(101) Choi, N.-S.; Yew, K. H.; Lee, K. Y.; Sung, M.; Kim, H.; Kim, S.-S. *J. Power Sources* **2006**, *161*, 1254–1259.

(102) Elazari, R.; Salitra, G.; Gershinsky, G.; Garsuch, A.; Panchenko, A.; Aurbach, D. *J. Electrochem. Soc.* **2012**, *159*, A1440–A1445.

(103) Markevich, E.; Salitra, G.; Aurbach, D. *ACS Energy Lett.* **2017**, *2*, 1337–1345.

(104) Jung, R.; Metzger, M.; Haering, D.; Solchenbach, S.; Marino, C.; Tsiouvaras, N.; Stinner, C.; Gasteiger, H. a. *J. Electrochem. Soc.* **2016**, *163*, A1705–A1716.

(105) Shkrob, I. A.; Wishart, J. F.; Abraham, D. P. *J. Phys. Chem. C* **2015**, *119*, 14954–14964.

(106) Young, B. T.; Heskett, D. R.; Nguyen, C. C.; Nie, M.; Woicik, J. C.; Lucht, B. L. EN *ACS Appl. Mater. Interfaces* **2015**, *7*, 20004–20011.

(107) Xu, C.; Lindgren, F.; Philippe, B.; Gorgoi, M.; Björefors, F.; Edström, K.; Gustafsson, T. *Chem. Mater.* **2015**, *27*, 2591–2599.

(108) Nakai, H.; Kubota, T.; Kita, A.; Kawashima, A. *J. Electrochem. Soc.* **2011**, *158*, A798.

(109) Etacheri, V.; Haik, O.; Go, Y.; Roberts, G. A.; Stefan, I. C.; Fasching, R.; Aurbach, D. *Langmuir* **2012**, *28*, 965–976.

(110) Schroder, K. W.; Alvarado, J.; Yersak, T. A.; Li, J.; Dudney, N.; Webb, L. J.; Meng, Y. S.; Stevenson, K. J. EN *Chem. Mater.* **2015**, *27*, 5531–5542.

(111) Sina, M.; Alvarado, J.; Shobukawa, H.; Alexander, C.; Manichev, V.; Feldman, L.; Gustafsson, T.; Stevenson, K. J.; Meng, Y. S. *Adv. Mater. Interfaces* **2016**, *3*, 1600438.

(112) Winter, M. *Zeitschrift für Phys. Chemie* **2009**, *223*, 1395–1406.

(113) Kumar, R.; Tokranov, A.; Sheldon, B. W.; Xiao, X.; Huang, Z.; Li, C.; Mueller, T. *ACS Energy Lett.* **2016**, *1*, 689–697.

(114) Kumar, R.; Lu, P.; Xiao, X.; Huang, Z.; Sheldon, B. W. *ACS Appl. Mater. Interfaces* **2017**, acsami.7b06647.

(115) Delpuech, N.; Dupré, N.; Mazouzi, D.; Gaubicher, J.; Moreau, P.; Bridel, J.; Guyomard, D.; Lestriez, B. *Electrochem. commun.* **2013**, *33*, 72–75.

(116) Tavassol, H.; Buthker, J. W.; Ferguson, G. a.; Curtiss, L. a.; Gewirth, A. a. *J. Electrochem. Soc.* **2012**, *159*, A730.

(117) Ruffo, R.; Hong, S. S.; Chan, C. K.; Huggins, R. A.; Cui, Y. *J. Phys. Chem. C* **2009**, *113*, 11390–11398.

(118) Dupre, N.; Moreau, P.; De Vito, E.; Quazuguel, L.; Boniface, M.; Bordes, A.; Rudisch, C.; Bayle-Guillemaud, P.; Guyomard, D. *Chem. Mater.* **2016**, *28*, 2557–2572.

(119) Leroy, S.; Blanchard, F.; Dedryvère, R.; Martinez, H.; Carré, B.; Lemordant, D.; Gonbeau, D. *Surf. Interface Anal.* **2005**, *37*, 773–781.

(120) Fears, T. M.; Doucet, M.; Browning, J. F.; Baldwin, J. K. S.; Winiarz, J. G.; Kaiser, H.; Taub, H.; Sacci, R. L.; Veith, G. M. *Phys. Chem. Chem. Phys.* **2016**, *18*, 13927–13940.

(121) Veith, G. M.; Doucet, M.; Sacci, R. L.; Vacaliuc, B.; Baldwin, J. K.; Browning, J. F. *Sci. Rep.* **2017**, *7*, 6326.

(122) Danet, J. Les alliages LixSi : analyse par spectroscopie de perte d'énergie des électrons et caractérisation électrochimique en accumulateur au lithium., Ph.D. Thesis, 2011.

(123) Boulineau, A.; Simonin, L.; Colin, J.-F.; Bourbon, C.; Patoux, S. *Nano Lett.* **2013**, *13*, 3857–63.

(124) Laffont, L.; Delacourt, C.; Gibot, P.; Wu, M. Y.; Kooyman, P.; Masquelier, C.; Tarascon, J. M. *Chem. Mater.* **2006**, *18*, 5520–5529.

(125) Wang, F.; Graetz, J.; Moreno, M. S.; Ma, C.; Wu, L.; Volkov, V.; Zhu, Y. *ACS Nano* **2011**, *5*, 1190–1197.

(126) Cosandey, F; Su, D; Sina, M; Pereira, N; Amatucci, G. G. *Micron* **2012**, *43*, 22–9.

(127) Zenser, L. P.; Gruehn, R; Liebscher, B. H. *J. Solid State Chem.* **2001**, *157*, 30–39.

(128) Havenbergh, K. V.; Turner, S.; Driesen, K.; Bridel, J.-S.; Tendeloo, G. V. *Energy Technol.* **2015**, *3*, 699–708.

(129) Lin, F.; Markus, I. M.; Doeff, M. M.; Xin, H. L. en *Sci. Rep.* **2014**, *4*, 5694.

(130) Daniels, H. R.; Brydson, R; Brown, A; Rand, B *Ultramicroscopy* **2003**, *96*, 547–58.

(131) Libera, M. R.; Egerton, R. F. *Polym. Rev.* **2010**, *50*, 321–339.

(132) Sigle, W.; Krämer, S.; Varshney, V.; Zern, a.; Eigenthaler, U.; Rühle, M. *Ultramicroscopy* **2003**, *96*, 565–571.

(133) Yurtsever, A.; Weyland, M.; Muller, D. A. *Appl. Phys. Lett.* **2006**, *89*, 151920.

(134) Pfannmöller, M.; Heidari, H.; Nanson, L.; Lozman, O. R.; Chrapa, M.; Offermans, T.; Nisato, G.; Bals, S. *Nano Lett.* **2015**, *15*, 6634–6642.

(135) Moreau, P.; Mauchamp, V.; Pailloux, F.; Boucher, F. *Appl. Phys. Lett.* **2009**, *94*, 123111.

(136) Mauchamp, V.; Boucher, F.; Moreau, P. *Ionics (Kiel).* **2008**, *14*, 191–195.

(137) Robert, D.; Douillard, T.; Boulineau, A.; Brunetti, G.; Nowakowski, P.; Venet, D.; Bayle-Guillemaud, P.; Cayron, C. *ACS Nano* **2013**, *7*, 10887–94.

(138) Adrian, M.; Dubochet, J.; Lepault, J.; McDowall, A. W. *Nature* **1984**, *308*, 32–36.

(139) Leapman, R. D. *Ultramicroscopy* **2017**, *180*, 180–187.

(140) Egerton, R.; Li, P.; Malac, M. *Micron* **2004**, *35*, 399–409.

(141) Aronova, M. A.; Leapman, R. D. *MRS Bull.* **2012**, *37*, 53–62.

(142) Kim, G.; Sousa, A.; Meyers, D.; Libera, M. *Microsc. Microanal.* **2008**, *14*, 459–468.

(143) Yakovlev, S.; Libera, M. *Micron* **2008**, *39*, 734–40.

(144) Yakovlev, S.; Libera, M. *Microsc. Microanal.* **2006**, *12*, 996–997.

(145) Yakovlev, S.; Balsara, N. P.; Downing, K. H. *Membranes (Basel).* **2013**, *3*, 424–439.

(146) Gilman, J. J. *Philos. Mag. B Phys. Condens. Matter; Stat. Mech. Electron. Opt. Magn. Prop.* **1999**, *79*, 643–654.

(147) Monthioux, M; Soutric, F; Serin, V *Carbon N. Y.* **1997**, *35*, 1660–1664.

(148) Egerton, R. F.; Williams, B. G.; Sparrow, T. G. *Proc. R. Soc. A Math. Phys. Eng. Sci.* **1985**, *398*, 395–404.

(149) Williams, D. B.; Edington, J. W. High resolution microanalysis in materials science using electron energy loss measurements., 1976.

(150) Raether, H, *Excitation of plasmons and surface transitions by electrons*, Springer, 1980.

(151) Oumellal, Y.; Delpuech, N.; Mazouzi, D.; Dupré, N.; Gaubicher, J.; Moreau, P.; Soudan, P.; Lestriez, B.; Guyomard, D. en *J. Mater. Chem.* **2011**, *21*, 6201.

(152) Nguyen, B.; Chazelle, S.; Cerbelaud, M.; Porcher, W.; Lestriez, B. *J. Power Sources* **2014**, *262*, 112–122.

(153) Reyter, D.; Rousselot, S.; Mazouzi, D.; Gauthier, M.; Moreau, P.; Lestriez, B.; Guyomard, D.; Roué, L. *J. Power Sources* **2013**, *239*, 308–314.

(154) Delpuech, N.; Mazouzi, D.; Dupré, N.; Moreau, P.; Cerbelaud, M.; Bridel, J. S.; Badot, J.-C.; De Vito, E.; Guyomard, D.; Lestriez, B.; Humbert, B. *J. Phys. Chem. C* **2014**, *118*, 17318–17331.

(155) Dedryvere, R.; Laruelle, S.; Grugeon, S.; Gireaud, L.; Tarascon, J.-M.; Gonbeau, D. *J. Electrochem. Soc.* **2005**, *152*, A689.

(156) Williams, D. B.; Carter, C. B., *Transmission electron microscopy: a textbook for materials science*; 1; Springer: 2009; Vol. 11, p 760.

(157) Egerton, R. F. *Reports Prog. Phys.* **2009**, *72*, 016502.

(158) Egerton, R. F.; Lazar, S.; Libera, M. *Micron* **2012**, *43*, 2–7.

(159) Boniface, M.; Quazuguel, L.; Danet, J.; Guyomard, D.; Moreau, P.; Bayle-Guillemaud, P. *Nano Lett.* **2016**, *16*, 7381–7388.

(160) Egerton, R. F. *Ultramicroscopy* **2007**, *107*, 575–586.

(161) Wan, W.; Zhang, Q.; Cui, Y.; Wang, E. *J. Phys. Condens. Matter* **2010**, *22*, 415501.

(162) Kim, S. P.; Duin, A. C.T. V.; Shenoy, V. B. *J. Power Sources* **2011**, *196*, 8590–8597.

(163) Yoshimura, K.; Suzuki, J.; Sekine, K.; Takamura, T. *J. Power Sources* **2005**, *146*, 445–447.

(164) Wang, L.; Liu, D.; Yang, S.; Tian, X.; Zhang, G.; Wang, W.; Wang, E.; Xu, Z.; Bai, X. *ACS Nano* **2014**, DOI: 10.1021/nn502621k.

(165) Sacci, R. L.; Lehmann, M. L.; Diallo, S. O.; Cheng, Y. Q.; Daemen, L. L.; Browning, J. F.; Doucet, M.; Dudney, N. J.; Veith, G. M. *J. Phys. Chem. C* **2017**, *121*, 11083–11088.

(166) Samarin, S.; Artamonov, O.; Suvorova, A.; Sergeant, A.; Williams, J. *Solid State Commun.* **2004**, *129*, 389–393.

(167) Egerton, R. F. *Microsc. Res. Tech.* **2012**, *75*, 1550–6.

(168) Egerton, R. F.; Lazar, S; Libera, M *Micron* **2012**, *43*, 2–7.

(169) Egerton, R. F.; Malac, M. *Microsc. Microanal.* **2004**, *10*, 1382–1383.

(170) Wu, B.; Neureuther, A. R. *J. Vac. Sci. Technol. B Microelectron. Nanom. Struct.* **2001**, *19*, 2508.

(171) Egerton, R. F. *Ultramicroscopy* **2017**, *180*, 115–124.

(172) Bronsgeest, M. S.; Barth, J. E.; Swanson, L. W.; Kruit, P *J. Vac. Sci. Technol. B Microelectron. Nanom. Struct.* **2008**, *26*, 949.

(173) Egerton, R. F. In *Electron Energy-Loss Spectrosc. Electron Microsc.* Springer US: Boston, MA, 2011, pp 111–229.

(174) Iakoubovskii, K.; Mitsuishi, K.; Nakayama, Y.; Furuya, K. *Phys. Rev. B* **2008**, *77*, 104102.

(175) Malis, T.; Cheng, S. C.; Egerton, R. F. *J. Electron Microsc. Tech.* **1988**, *8*, 193–200.

(176) Gauthier, M. Electrodes négatives à base de silicium pour accumulateurs au lithium mécanisme réactionnel à l'échelle nanométrique., Ph.D. Thesis, 2013.

(177) Donval, G. Modélisation de spectres de perte d'énergie des électrons sur des matériaux d'électrode à base de silicium dans les accumulateurs aux ions lithium., Ph.D. Thesis, 2015.

(178) Su, D.; Yang, B.; Jiang, N.; Sawicki, M.; Broadbridge, C.; Couillard, M.; Reiner, J. W.; Walker, F. J.; Ahn, C. H.; Zhu, Y. *Appl. Phys. Lett.* **2010**, *96*, 94–97.

(179) Kim, K. J.; Wortman, J.; Kim, S. Y.; Qi, Y. *Nano Lett.* **2017**, *17*, 4330–4338.

(180) Ferrari, A. C.; Libassi, A.; Tanner, B. K.; Stolojan, V.; Yuan, J.; Brown, L. M.; Rodil, S. E.; Kleinsorge, B.; Robertson, J. *Phys. Rev. B* **2000**, *62*, 11089–11103.

(181) Penn, D. R. *Phys. Rev.* **1962**, *128*, 2093–2097.

(182) Ingham, J. D.; Lawson, D. D. *J. Polym. Sci. Part A Gen. Pap.* **1965**, *3*, 2707–2710.

(183) Sultanova, N.; Kasarova, S.; Nikolov, I. In *Acta Phys. Pol. A*, 2009; Vol. 116, pp 585–587.

(184) Beaulieu, L. Y.; Hatchard, T. D.; Bonakdarpour, a.; Fleischauer, M. D.; Dahn, J. R. en *J. Electrochem. Soc.* **2003**, *150*, A1457.

(185) Mai, L.; Dong, Y.; Xu, L.; Han, C. *Nano Lett.* **2010**, *10*, 4273–4278.

(186) Hatchard, T. D.; Dahn, J. R. en *J. Electrochem. Soc.* **2004**, *151*, A838.

(187) Liu, X. H. et al. *Nano Lett.* **2011**, *11*, 3312–3318.

(188) Liu, X. H. et al. *Nat. Nanotechnol.* **2012**, *7*, 749–56.

(189) Liu, X. H.; Fan, F.; Yang, H.; Zhang, S.; Huang, J. Y.; Zhu, T. *ACS Nano* **2013**, *7*, 1495–503.

(190) Yuan, Y.; Amine, K.; Lu, J.; Shahbazian-Yassar, R. *Nat. Commun.* **2017**, *8*, 15806.

(191) Gu, M. et al. *Nano Lett.* **2013**, *13*, 6106–12.

(192) Holtz, M. E.; Yu, Y.; Gao, J.; Abruña, H. D.; Muller, D. A. *Microsc. Microanal.* **2013**, *19*, 1027–35.

(193) Den Hertog, M. I.; González-Posada, F; Songmuang, R; Rouviere, J. L.; Fournier, T; Fernandez, B; Monroy, E *Nano Lett.* **2012**, *12*, 5691–5696.

(194) Dupré, N.; Moreau, P.; De Vito, E.; Quazuguel, L.; Boniface, M.; Kren, H.; Bayle-Guillemaud, P.; Guyomard, D. *Chem. Mater.* **2017**, *29*, 8132–8146.

(195) Ferrari, S.; Quartarone, E.; Mustarelli, P.; Magistris, A.; Fagnoni, M.; Protti, S.; Gerbaldi, C.; Spinella, A. *J. Power Sources* **2010**, *195*, 559–566.

(196) Cattaneo, A. S.; Dupke, S.; Schmitz, A.; Badillo, J. P.; Winter, M.; Wiggers, H.; Eckert, H. *Solid State Ionics* **2013**, *249-250*, 41–48.

(197) Tintignac, S.; Baddour-Hadjean, R.; Pereira-Ramos, J.-P.; Salot, R. *Electrochim. Acta* **2012**, *60*, 121–129.

(198) Gentile, P; Solanki, A; Pauc, N; Oehler, F; Salem, B; Rosaz, G; Baron, T; Den Hertog, M; Calvo, V *Nanotechnology* **2012**, *23*, 215702.

(199) Lee, S. W.; McDowell, M. T.; Berla, L. a.; Nix, W. D.; Cui, Y. *Proc. Natl. Acad. Sci.* **2012**, DOI: 10.1073/pnas.1201088109/-/DCSupplemental.www.pnas.org/cgi/doi/10.1073/pnas.1201088109.

(200) An, Y.; Wood, B. C.; Ye, J.; Chiang, Y.-M.; Wang, Y. M.; Tang, M.; Jiang, H. *Phys. Chem. Chem. Phys.* **2015**, *17*, 17718–17728.

(201) Yuk, J. M.; Seo, H. K.; Choi, J. W.; Lee, J. Y. *ACS Nano* **2014**, *8*, 7478–85.

(202) Abellan, P.; Mehdi, B. L.; Parent, L. R.; Gu, M.; Park, C.; Xu, W.; Zhang, Y.; Arslan, I.; Zhang, J.-G.; Wang, C.-M.; Evans, J. E.; Browning, N. D. *Nano Lett.* **2014**, *14*, 1293–9.

(203) Liu, X. H.; Liu, Y.; Kushima, A.; Zhang, S.; Zhu, T.; Li, J.; Huang, J. Y. *Adv. Energy Mater.* **2012**, *2*, 722–741.

(204) Zhao, M. Electrochemical studies of lithium-ion battery anode materials in lithium-ion battery electrolytes., Ph.D. Thesis, 2001.

(205) Obrovac, M. N.; Krause, L. J. *J. Electrochem. Soc.* **2007**, *154*, A103.

(206) Li, J.; Lewis, R. B.; Dahn, J. R. *Electrochem. Solid-State Lett.* **2007**, *10*, A17.

(207) Key, B.; Bhattacharyya, R.; Morcrette, M.; Sezn??c, V.; Tarascon, J. M.; Grey, C. P. *J. Am. Chem. Soc.* **2009**, *131*, 9239–9249.

(208) Bordes, A.; De Vito, E.; Haon, C.; Boulineau, A.; Montani, A.; Marcus, P. *Chem. Mater.* **2016**, *28*, 1566–1573.

(209) Gauthier, M.; Danet, J.; Lestriez, B.; Roué, L.; Guyomard, D.; Moreau, P. *J. Power Sources* **2013**, *227*, 237–242.

(210) Trill, J. H.; Tao, C.; Winter, M.; Passerini, S.; Eckert, H. *J. Solid State Electrochem.* **2011**, *15*, 349–356.

(211) Rohrer, J.; Albe, K. *J. Phys. Chem. C* **2013**, *117*, 18796–18803.

(212) Liu, X. H. et al. *Nat. Nanotechnol.* **2012**, *7*, 749–56.

(213) Chen, L. Q.; Fan, F.; Hong, L.; Chen, J.; Ji, Y. Z.; Zhang, S. L.; Zhu, T.; Chen, L. Q. *J. Electrochem. Soc.* **2014**, *161*, F3164–F3172.

(214) Gao, F.; Hong, W. *J. Mech. Phys. Solids* **2016**, *94*, 18–32.

(215) Zeng, Z.; Liu, N.; Zeng, Q.; Lee, S. W.; Mao, W. L.; Cui, Y. *Nano Energy* **2016**, *22*, 105–110.

(216) Drozdov, A. D.; Sommer-Larsen, P.; deClaville Christiansen, J. *J. Appl. Phys.* **2013**, *114*, 223514.

(217) Zhao, K.; Wang, W. L.; Gregoire, J.; Pharr, M.; Suo, Z.; Vlassak, J. J.; Kaxiras, E. *Nano Lett.* **2011**, *11*, 2962–2967.

(218) McDowell, M. T.; Lee, S. W.; Harris, J. T.; Korgel, B. A.; Wang, C.; Nix, W. D.; Cui, Y. *Nano Lett.* **2013**, *13*, 758–64.

(219) Luo, L.; Wu, J.; Luo, J.; Huang, J.; Dravid, V. P. *Sci. Rep.* **2014**, *4*, 3863.

(220) Tardif, S.; Pavlenko, E.; Quazuguel, L.; Boniface, M.; Marechal, M.; Mareau, V.; Micha, J.-S.; Gonon, L.; Gebel, G.; Bayle-Guillemaud, P.; Rieutord, F.; Lyonnard, S. *ACS Nano* **2017**, *in press*, acsnano.7b05796.

(221) Rouviere, J. L.; Béché, A.; Martin, Y.; Denneulin, T.; Cooper, D. *Appl. Phys. Lett.* **2013**, *103*, 241913.

(222) Hopcroft, M. A.; Nix, W. D.; Kenny, T. W. *J. Microelectromechanical Syst.* **2010**, *19*, 229–238.

(223) Radvanyi, E.; De Vito, E.; Porcher, W.; Jouanneau Si Larbi, S. *J. Anal. At. Spectrom.* **2014**, *29*, 1120.

(224) Karki, K.; Epstein, E.; Cho, J. H.; Jia, Z.; Li, T.; Picraux, S. T.; Wang, C.; Cumings, J. *Nano Lett.* **2012**, *12*, 1392–1397.

(225) Bordes, A. **2016**.

(226) Wang, F.; Wu, L.; Key, B.; Yang, X.-q.; Grey, C. P.; Zhu, Y.; Graetz, J. *Adv. Energy Mater.* **2013**, *3*, 1324–1331.

(227) Buban, J. P.; Ramasse, Q.; Gipson, B.; Browning, N. D.; Stahlberg, H. *J. Electron Microsc. (Tokyo).* **2010**, *59*, 103–12.

(228) Jung, S. C.; Han, Y.-K. *Phys. Chem. Chem. Phys.* **2011**, *13*, 21282.

(229) Chan, M. K. Y.; Wolverton, C.; Greeley, J. P. *J. Am. Chem. Soc.* **2012**, *134*, 14362–14374.

(230) Goldman, J. L.; Long, B. R.; Gewirth, A. A.; Nuzzo, R. G. *Adv. Funct. Mater.* **2011**, *21*, 2412–2422.

(231) Yoon, T.; Nguyen, C. C.; Seo, D. M.; Lucht, B. L. *J. Electrochem. Soc.* **2015**, *162*, A2325–A2330.

(232) Augustsson, A.; Herstedt, M.; Guo, J.; Edström, K.; Zhuang, G. V.; Ross, Jr., P. N.; Rubensson, J.-E.; Nordgren, J. *Phys. Chem. Chem. Phys.* **2004**, *6*, 4185.

(233) Martinez, W. E.; Gregori, G.; Mates, T. *Thin Solid Films* **2010**, *518*, 2585–2591.

(234) Leung, K.; Rempe, S. B.; Foster, M. E.; Ma, Y.; Martinez del la Hoz, J. M.; Sai, N.; Balbuena, P. B. *J. Electrochem. Soc.* **2013**, *161*, A213–A221.

(235) Leung, K.; Soto, F.; Hankins, K.; Balbuena, P. B.; Harrison, K. L. *J. Phys. Chem. C* **2016**, *120*, acs.jpcc.5b11719.

(236) Martin, Y. **2014**.

(237) Lu, P.; Sheldon, B. W.; Zhang, Q.; Pan, J.; Lu, P.; Liu, Z.; Verbrugge, M. W.; Sheldon, B. W.; Cheng, Y.-T.; Qi, Y.; Xiao, X. *Nano Lett.* **2016**, *16*, 2011–2016.

(238) Okuno, Y.; Ushirogata, K.; Sodeyama, K.; Tateyama, Y. en *Phys. Chem. Chem. Phys.* **2016**, *18*, 8643–8653.

(239) Jaumann, T.; Balach, J.; Langklotz, U.; Sauchuk, V.; Fritsch, M.; Michaelis, A.; Teltevskij, V.; Mikhailova, D.; Oswald, S.; Klose, M.; Stephani, G.; Hauser, R.; Eckert, J.; Giebeler, L. *Energy Storage Mater.* **2017**, *6*, 26–35.

(240) Pereira-Nabais, C.; Wiatowska, J.; Chagnes, A.; Gohier, A.; Zanna, S.; Seyeux, A.; Tran-Van, P.; Cojocaru, C. S.; Cassir, M.; Marcus, P. *J. Phys. Chem. C* **2014**, *118*, 2919–2928.

(241) Lee, S. W.; Lee, H.-W.; Ryu, I.; Nix, W. D.; Gao, H.; Cui, Y. en *Nat. Commun.* **2015**, *6*, 7533.

(242) Lee, J. G.; Kim, J.; Lee, J. B.; Park, H.; Kim, H.-S.; Ryu, J. H.; Jung, D. S.; Kim, E. K.; Oh, S. M. *J. Electrochem. Soc.* **2017**, *164*, A6103–A6109.

(243) Chen, Q.; Sieradzki, K. *Nat. Mater.* **2013**, *12*, 1102–1106.

(244) Vickerman, J. C.; Briggs, D, *TOF-SIMS: Materials Analysis by Mass Spectrometry*, 2013, p 732.

(245) Jin, Y. et al. *Energy Environ. Sci.* **2017**, *10*, 580–592.

(246) Tasaki, K.; Goldberg, A.; Lian, J.-J.; Walker, M.; Timmons, A.; Harris, S. J. en *J. Electrochem. Soc.* **2009**, *156*, A1019.

(247) Gao, J.; Shi, S.-Q.; Li, H. *Chinese Phys. B* **2016**, *25*, 018210.

(248) Yamamoto, K.; Iriyama, Y.; Asaka, T.; Hirayama, T.; Fujita, H.; Nonaka, K.; Miyahara, K.; Sugita, Y.; Ogumi, Z. *Electrochem. commun.* **2012**, *20*, 113–116.

(249) Yamamoto, K.; Hirayama, T.; Tanji, T. Development of advanced electron holographic techniques and application to industrial materials and devices., 2013.

(250) Tokranov, A.; Kumar, R.; Li, C.; Minne, S.; Xiao, X.; Sheldon, B. W. *Adv. Energy Mater.* **2016**, *6*, n/a–n/a.

(251) Peled, E.; Patolsky, F.; Golodnitsky, D.; Freedman, K.; Davidi, G.; Schneier, D. *Nano Lett.* **2015**, DOI: 10.1021/acs.nanolett.5b00744.

(252) Markevich, E.; Fridman, K.; Sharabi, R.; Elazari, R.; Salitra, G.; Gottlieb, H. E.; Gershinsky, G.; Garsuch, A.; Semrau, G.; Schmidt, M. A.; Aurbach, D. *J. Electrochem. Soc.* **2013**, *160*, A1824–A1833.

(253) Etacheri, V.; Haik, O.; Goffer, Y.; Roberts, G. A.; Stefan, I. C.; Fasching, R.; Aurbach, D. *Langmuir* **2012**, *28*, 965–76.

(254) Obrovac, M. N.; Chevrier, V. L. Alloy negative electrodes for Li-ion batteries., 2014.

Nanoscale evolution of a silicon electrode for Li-ion batteries by low-loss STEM-EELS

Over the last 25 years, the performance increase of Lithium-ion batteries has been largely driven by the optimization of inactive components. With today's environmental concerns, the pressure for more cost-effective and energy-dense batteries is enormous and new active materials should be developed to meet those challenges. Silicon's great theoretical capacity makes it a promising candidate to replace graphite in negative electrodes in the mid-term. So far, Si-based electrodes have suffered from the colossal volume changes silicon undergoes through its alloying reaction with Li. Si particles will be disconnected from the electrode's percolating network and the solid electrolyte interface (SEI) continuously grows, causing poor capacity retention. A thorough understanding of both these phenomena, down to the scale of a single silicon nanoparticle (SiNP), is critical to the rational engineering of efficient Si-based electrodes. To this effect, we have developed STEM-EELS into a powerful and versatile toolbox for the study of sensitive materials and heterogeneous systems. Using the low-loss part of the EEL spectrum allows us to overcome the classical limitations of the technique. The novel phase-mapping capabilities of low-loss STEM-EELS are then leveraged to outline the morphology and chemistry of the SEI, elucidate the first lithiation mechanism of crystalline SiNPs, and reveal the evolution of the NP morphology under prolonged cycling. Finally, we propose an aging model of our own, based on both local STEM-EELS analyses and the quantitative trends derived from cumulated measurements on more than 1100 particles.

Suivi à l'échelle nanométrique de l'évolution d'une électrode de silicium pour accumulateur Li-ion par STEM-EELS

L'accroissement des performances des accumulateurs Li-ion sur les 25 dernières années découle principalement de l'optimisation de leurs composants inactifs. Aujourd'hui, l'urgence environnementale impose de développer de nouveaux matériaux actifs d'électrode pour proposer la prochaine génération d'accumulateur qui participera à la transition énergétique. A cet effet, le silicium pourrait avantageusement remplacer le graphite des électrodes négatives à moyen terme. Cependant la rétention de capacité des électrodes de silicium est mise à mal par l'expansion volumique que le matériau subit lors sa réaction d'alliage avec le lithium, qui mène à la déconnexion des particules de Si et à une réduction continue de l'électrolyte. Une compréhension de ces phénomènes de vieillissement à l'échelle de la nanoparticule est nécessaire à la conception d'électrodes de silicium viables. Pour ce faire, la technique STEM-EELS a été optimisée de manière à s'affranchir des problèmes d'irradiation qui empêchent l'analyse des matériaux légers d'électrode négative et de la Solid electrolyte interface (SEI), grâce à l'analyse des pertes faibles EELS. Un puissant outil de cartographie de phase est obtenu et utilisé pour mettre en lumière la lithiation cœur-coquille initiale des nanoparticules de silicium cristallin, la morphologie hétérogène et la composition de la SEI, ainsi que la dégradation du silicium à l'issue de cyclages prolongés. Enfin, un modèle de vieillissement original est proposé, en s'appuyant notamment sur un effort de quantification des mesures STEM-EELS sur un grand nombre de nanoparticules.